Self-assembly and Mesocrystal Formation via Non-classical Crystallisation

Dissertation

zur Erlangung des akademischen Grades

Doctor rerum naturalium
(Dr. rer. nat.)

vorgelegt

der Fakultät Mathematik und Naturwissenschaften
der Technischen Universität Dresden

von

Master of Science Lydia Bahrig
geboren am 19.05.1987 in Dresden

Eingereicht am:	02.April 2014
Tag der Verteidigung:	06.Mai 2014
Gutachter:	Prof. Dr. rer. nat. habil. Alexander Eychmüller Prof. Dr. rer. nat. habil. Stefan Kaskel

Die Dissertation wurde in der Zeit von November 2010 bis März 2014 in der Professur für Physikalische Chemie angefertigt.

To my family

Abstract

New materials can be fabricated using small scaled building blocks as a repetition unit. Nanoparticles with their unique size-tuneable properties from quantum confinement can especially be utilised to form two- and three-dimensional ordered assemblies to introduce them into what would normally be considered to be incompatible matrices. Furthermore, new collective properties that derive from the ordered arrangement of the building blocks,are accomplished. Additionally, different materials can be combined by mixing different building blocks during self-assembly, so that size ranges and material combinations that are difficult to achieve by other means can be formed.

The arrangement of small particles into highly ordered arrangements can be realised via self-assembly. To achieve such assemblies, highly monodisperse nanoparticular building blocks with a size distribution below 5% have to be synthesised. The production and variation in the size of both lead chalcogenide and noble metal nanoparticles is presented in this work. Moreover, the syntheses of multicomponential nanoparticles (PbSe/PbS and Au/PbS) are investigated.

Non-classical crystallisation methodologies with their varyious self-assembly mechanisms are used for the formation of highly symmetrical mesocrystals and supracrystals. Analogous to classical crystallisation methods and their formation processes the interparticle interactions, attractive as well as repulsive, determine the resulting crystalline structure. Variation of the environmental parameters consequently leads to structural variation due to the changing interparticle interactions. In contrast to classical crystallisation the length scale of the interparticle forces stays constant as the size dimension of the self-assembled building unit is changed.

Two different non-classical crystallisation pathways are investigated in this work. One pathway focuses on the slow destabilisation of nanoparticles in organic media by the addition of a non-solvent. In this approach optimisation of parameters for the formation of highly symmetrical three-dimensional mesostructures are studied. Furthermore, to shine some light onto the mechanism of self-assembly, the intrinsic arrangement of the building units in a mesocrystal and the steps of non-solvent addition are analysed. The mechanistic investigations explain the differences observed in mesocrystal formation between metal and semiconductor nanoparticles. The lower homogeneity of the building units of the metal nanoparticles leads to smaller and less defined superstructures in comparison to semiconductor building blocks.

Another pathway of non-classical crystallisation is the usage of electrostatic interactions as the driving force for self-assembly and supracrystal formation. Therefore, the building blocks are transferred into aqueous media and stabilised with oppositely charged ligands. The well-know procedure for metal nanoparticles was adapted for semiconductor materials. The lower stability of these nanoparticles in aqueous solution induces an agglomeration of the semiconductor nanoparticles without including oppositely charged metal nanoparticles. The destabilisation effect can be increased by the addition of equally charged metal nanoparticles in a salting out type process.

In comparison to the slow formation of mesocrystals achieved *via* destabilisation in an organic media (up to 4 weeks), the salting out procedure takes place within two hours, but the faster agglomeration causes a less well defined assembly of the building units in the mesocrystals.

Moreover, the arrangement of semiconductor nanoparticles with organic molecules such as polymers and proteins was investigated in order to use the nanoparticles as a light harvesting component. In combination with the directly bound polymer the charge carrier may be directly transferred to the conductive thiophene-based polymer, so that infrared light can be transformed into an electrical signal for use in further applications such as solar cells. The advantage of the nanoparticle-protein system is the self-assembly across a liquid-liquid interface and additionally a Förster resonance energy transfer can occur at this phase boundary. Hence, it is possible to transfer highly energetic photons directly to biological samples without destroying the biological material.

Contents

6. Nanoparticle arrangements in organic matrices and biological systems 141

Abbreviations

0D,1D,2D,3D	zero-dimensional, one-dimensional, two-dimensional, three-dimensional
Ag	Silver
Au	Gold
c.f.	compare to
DLS	Dynamic Light Scattering
DLVO	Deryagin-Landau-Verwey-Overbeek
DMSO	Dimethylsulfoxid
SAED	Electron Diffraction
EOBs	Excitable Oil Bodies
fcc	Face Centred Cubic
FFT	Fast Fourier Transformation
FIB	Focused Ion Beam
FRET	Förster Resonance Energy Transfer
FT-IR Spectroscopy	Fourier Transformation-Infrared spectroscopy
GPC	Gel Permeation Chromatography
hcp	Hexagonal Close Packing
IUCr	International Union of Crystallography
MALDI-TOF	Matrix-assisted laser desorption/ionization-Time of Flight
MEG	Multiple Exciton Generation
ML	Monolayer
MS	Mass Spectroscopy

MUA	11-Mercaptoundecanoic acid
NP	Nanoparticle
ODE	Octadecene
PbSe	Lead selenide
PbS	Lead sulphide
QD	Quantum Dot
TOP	Tri-n-octyl-phosphin
e.g.	for example
SAED	Selected Area Electron Diffraction
SAXS	Small Angle X-ray Scattering
SEM	Scanning Electron Microscopy
SERS	Surface-enhanced Raman Scattering
sh	Simple Hexagonal
SILAR	Successive Ion Layer Adsorption and Reaction
STM	Scanning Tunnelling Microscope
(HR)TEM	(High Resolution) Transmission Electron Microscopy
TGA	Thermogravimetric Analysis
TMA	N,N,N-trimethyl(11-mercaptoundecyl)ammonium chloride
TMS_2S	Bis(trimethylsilylsulphide)
tRFP	Turbo Red Fluorescent Protein
UV	Ultra Violet Light
VDW	Van der Waals
Vis	Visible Light
XRD	X-ray Powder Diffraction

List of Figures

List of Tables

1. Introduction

Crystals have fascinated humankind for centuries because they are beautiful objects and highly aesthetic due to their highly symmetric geometrical shapes. Additionally, crystallisation processes are intimately connected with new technologies and engineering progress.

Already in prehistoric times, the crystallisation of salt by evaporating seawater was used and is an example of one of the oldest traceable technical methods of material transformation in addition to sintering earthenware. The nomenclature "crystal" and "crystallisation" derive from the ancient Greek word *krustallos*, which means ice, iciness and frost, and the term were also commonly used to denote symmetrical, bright and often transparent materials like quartz or glass.

Written documents such as the "Naturalis historia" from Plinius, wherein he mentioned the crystallisation of different salts and vitriols, stretch back to the roman era. In the 12^{th} and 13^{th} century, the alchemists used recrystallisation for purification of substances and to increase their quality. Until the end of the middle ages progress in technology also promoted the various techniques of material production and transformation such as distillation and sublimation in addition to crystallisation. In the 16^{th} century the term crystal, as used by Homer, was adapted from Birringuccio and the Saxonian scientist Agricola in the publication "De re metallica" instead of the terms condensation and coagulation.

Boyle observed the first principles of crystal growth in 1666 and it was at this point that experiments and studies were intensively started to explain crystal formation. Often research was restricted by the resolution of the technical equipment, which slowed down the progress made in this field.

Nowadays, various techniques for the production of different crystalline materials are well known and optimised and they can be used to produce e.g. diamonds for industrial applications or single-crystal materials such as silicon for microelectronics. Nevertheless, after 200 years of systematic scientific work, the knowledge concerning crystallisation and the processes that take place is rather restricted and many aspects need to be investigated further.

In addition to classical crystallisation, as the above described methods are classified as, a new pathway of crystallisation was discovered where analogous to atoms and ions small building units like nanoparticles are arranged similarly to classical crystals. The arrangement of the building blocks is also symmetrical and ordered and the new class of materials are called Mesocrystals with the formation process being described as non-classical crystallisation.

This work is focused on mechanistic investigations of the non-classical crystallisation of lead chalcogenide nanoparticles and noble metal nanoparticles using different methods of non-classical crystallisation to produce highly symmetrical mesocrystals. Therefore, the main principles of classical crystallisation are first introduced before the different pathways of non-classical crystallisation are presented. Thereby, the similarities and contrasts of different crystal forming procedures are revealed. The analogy of the classical and non-classical crystallisation processes is presented and the attractive and repulsive interactions in such systems and their different influences with respect to the length scales involved in crystallisation is reported. Additionally the unique properties and further applications of highly interesting materials that combine nanoparticular properties (quantum confinement) and collective properties that derive from the ordered arrangement are presented.

The second part of the work deals with the synthesis and characterisation of the initial building blocks. Optimisation of the synthesis procedures and new pathways for the production of core-shell materials is reported as is the classical hot-injection method for the production of quasi-spherical semiconductor nanoparticles. Highly monodisperse noble metal nanoparticles are additionally produced in organic media with possible ligand exchange for phase transfer to aqueous media. Monodispersity is defined in this work as narrow size distribution with σ below 5%. For later self-assembly into mesocrystaline materials the surface modification of the single nanoparticles is important and will be determined with different characterisation techniques. The stabilising effects of the ligand shell are investigated during thermal treatment to more fully understand the stability of the ligand shell on top of the nanoparticles during the destabilisation process so that the ligand shell can protect the nanoparticles from fusion during mesocrystal formation.

The third chapter deals with the mesocrystal formation of semiconductor and noble metal mesocrystals using the gas phase diffusion technique with the effects of varying parameters such as temperature, solvent/non-solvent combination and concentration being described. Additionally the formation mechanism at work during the self-assembly process is investigated and the resulting mesocrystaline materials and their nanoparticular internal arrangement are determined. Differences in the size and shape of the semiconductor and metal mesocrystals are studied as are the destabilisation process starting with the equation of the building blocks, and the two dimensional and three-dimensional arrangements are compared. Furthermore, results from the modification of the prepared mesocrystals focusing on attaining higher electrical conductivity for further applications are presented.

Besides the non-classical crystallisation in organic media, the electrostatic self-assembly of oppositely charged nanoparticles in aqueous solution is focused on in the next chapter. The so-called supracrystals are produced analogously to ion based classical crystals via electrostatic interactions. Thus, the combination of different nanoparticle species forming one crystal should be driven by the presence of charge. Structural analysis of the supracrystals and mechanistic investigations of the formation are presented.

The last section of this work deals with more flexible and dynamic systems where the semiconductor nanoparticles act as a light harvesting system and transfer their energy to polymers or biological proteins. Therefore, the nanoparticles have to be located near the energy adapting molecules, which is, in the case of the polymer, realized by direct binding after ligand exchange and in the case of the biological protein over a phase boundary mediated with additional surface-active protein. With this principle, the first Förster resonance energy transfer over a liquid-liquid phase boundary is reported.

2. Mesocrystalline Materials

In this section, the theoretical background to classical and non-classical crystallisation is presented *via* a description of the variety of crystal growth and by presenting the current state of the art in self-assembly research. Thereby, the similarities and contrasts of different crystal forming procedures are revealed. The attractive and repulsive interactions present in such systems and their different influences with respect to the length scales of crystallisation are reported. Additionally, the parameters that influence structure and crystal growth and the various strategies of non-classical crystallisation are presented. Nanoparticles as building blocks, just like atoms or ions, can be arranged into close packed lattices where the resulting structure exhibits single crystal behaviour and unit cell parameters as may be observed within classical crystallisation. The analogy of the resulting structures is examined and the differences of these crystal structures during agglomeration are presented. Moreover, the potential of the new functional materials possessing nanoparticular properties and additionally a crystal structure are shown. New properties of nanoparticular solids and the corresponding possible applications are studied.

2.1. Preface

Crystallisation and crystalline materials play an important role in the areas of science and technology primarily because the inner structure of a material directly influences its properties. A well-known example is of course the different allotropes of carbon. In its diamond modification carbon is a transparent, hard material that does not possess electrical conductivity while in its graphite modification it is black, shows isotropic mechanical behaviour and is conductive within the plane of its covalent bonds.

The differences in the properties of a material brought about by the different orientational arrangement of its component parts is extremely interesting and the controlled fabrication of one modification over another is clearly necessary for applications, as the device function and efficiency are usually based on the properties specific to a particular material modification. This is however but one reason as to why researchers are interested in gaining an understanding of the processes involved in classical crystallisation. Already by the 18^{th} century scientists had learned to use crystallisation for purification and/or isolation of substances and thus as a means to gain access to compounds of high purity. Later the mechanism of single atoms, ions or molecules, which attach to crystalline surfaces during crystallisation, was investigated. In comparison to the model of agglomeration, the processes that work during "real" crystallisation are more complex, and up to now it has proven challenging for researchers to model accurately the theoretical pathways involved and to forecast the results of crystallisation.

In the last decades additional interest has been paid to nanoparticulate materials and their arrangement in solids, as nanoparticles provide an additional class of "building block" that can be designed so as to possess new and tuneable properties caused by the quantum confinement of the electronic wave functions. In biomineralisation, pathways which involve non-classical crystallisation were discovered to exist and intermediates with highly oriented and symmetrically arranged building blocks in the nanometer region were established as being present, which later fuse to form iso-oriented or single crystalline materials. This has subsequently been further developed to encompass the principles of non-classical crystallisation, which embraces new classes of materials such as iso-oriented materials or mesocrystals, which is the highly ordered arrangement of the individual building blocks into a three-dimensional superstructure. Additionally, these materials can be modified and their properties tuned and as such are of great interest for many applications.

To create, modify and optimise materials using methodologies involving non-classical crystallisation first the dominant formation mechanisms need to be identified. One route of particular interest is to mimic the processes involved in bio-mineralisation and superimpose upon their formation nanoparticular building blocks whilst maintaining the coincident arrangement of the building units. The routes that are presented in this chapter are based on first separately producing metal and semiconductor nanoparticles and then their subsequent arrangement into highly ordered superstructures. The pathways of oriented attachment and mesocrystal formation are presented focusing primarily on the advantages of their synthetic fabrication without however going into the details of the mimicry of bio-mineralisation. The various nanoparticular interactions and their role in providing the driving forces for arrangement are illuminated and are placed in context with respect to the different destabilisation methods. First the basic ideas behind classical crystallisation and crystal formation principles are introduced and then oriented attachment and mesocrystal formation is discussed. In a later section the analogy between classical and non-classical crystallisation methods is highlighted and additionally the new properties, which are a combination of the properties of the individual nanomaterials and the new collective properties brought about by their assembly into quantum dot solids and their potential applications are presented.

2.2. Classical Crystal Growth

Before a description of some of the ideas connected with the process of non-classical crystallisation, especially those of oriented attachment and mesocrystal formation, is embarked upon it is perhaps useful to reintroduce a number of the basic mechanisms involved in the description of classical crystallisation. The main principle underlying classical crystallisation is the ordered arrangement of material into a more stable crystalline structure (Ostwald rule of stages).[1,2] This may occur atom by atom, molecule by molecule or, in the case of salts, by the arrangement of ions *via* a precipitation reaction on an organic or inorganic nucleus and, in the case of unstable or metastable phases, *via* reprecipitation. The thermodynamic driving force for this process is solvent supersaturation, which is defined as the dimensionless ratio S (Equation 1):

$$S = \frac{a}{K_{SP}} \tag{1}$$

where S is the relative supersaturation, a represents the concentration or more accurately the activity product of the individual components and K_{SP} represents the equilibrium solubility product.

2.2.1. Nucleation

As mentioned supersaturation plays a major role in the nucleation process. A number of different methods exist for the generation of supersaturated solutions such as influencing the solubility product by means of a temperature reduction or by changes in pressure. Another possibility is to influence the concentration or activity product by changing the pH value, adding a large amount of one of the components or by reducing the solubility of the component(s) through the addition of a non-solvent to the solution.[3,4] During this process nuclei will be created first before the particle growth begins. There are three different nucleation processes that lead to crystal growth: homogeneous nucleation, heterogeneous nucleation and secondary nucleation. We will focus here solely on homogeneous nucleation, which is the simplest case. From a thermodynamic viewpoint, supersaturation, which is an energetically unstable state, is related to the change in chemical potential ($\Delta\mu$) as outlined by equation 2 and therefore related to the overall free energy change involved:

$$\Delta\mu = -kTlnS \tag{2}$$

where k is the Boltzmann constant, T the temperature and S the supersaturation. The change in the overall free energy during the nucleation process (Equation 3) is the sum of the free energy due to the formation of new volume (ΔG_V) and the free energy which is required to create new surface (ΔG_S):

$$\Delta G = \Delta G_V + \Delta G_S = -\frac{4}{3}\pi r^3 p_S T \Delta\mu + 4\pi r^2 \sigma \tag{3}$$

In the above equation σ is the specific free interface, p_s is the density of the solid material and r is the radius of the nucleus. In Figure 2.1 the overall free energy during nucleation is shown and the profile of the function shows a positive maximum which corresponds to the critical radius r^* (Equation 4).

$$r^* = \frac{2}{p_s \left|\Delta\mu\right|} \tag{4}$$

Nuclei sizes with $r > r^*$ will further grow and form stable entities as they can overcome the activation energy barrier at the critical radius. For a given supersaturation (S), the critical radius can be calculated and with a higher degree of supersaturation r^* becomes smaller, as can be shown by combining equation 4 with equation 2.

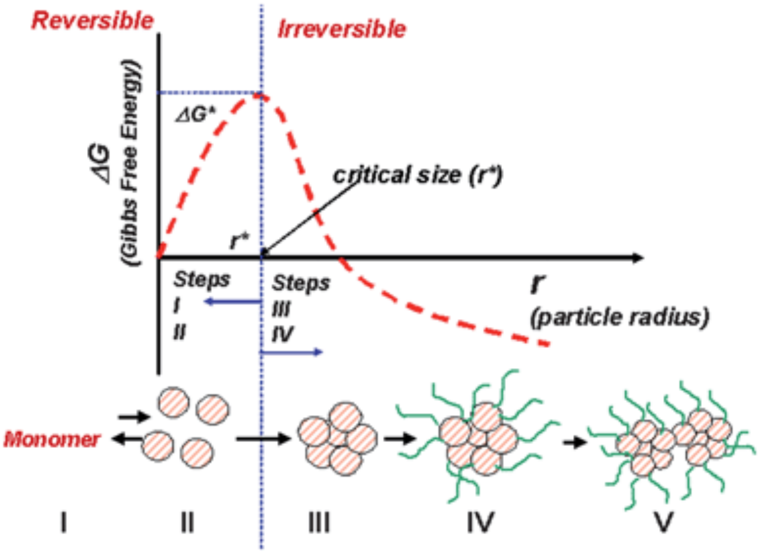

Figure 2.1.: ***Schematic diagram of the nucleation and growth process*** *showing the five stages and the dependence of the Gibbs free energy (G) on the crystal size. Below a critical radius* (r^*)*, a reversible process occurs; for* $r > r^*$ *the process becomes irreversible.*[5]

When the concentration of the growth species decreases below the level where nucleation spontaneously takes place, the nucleation stops and only crystal growth will appear, as is the case described by the LaMer model in Figure 2.2.[6] If the time taken for the spontaneous nucleation is very short and further nucleation is inhibited, particle solutions with small size distributions can be produced, as is often the case in colloidal synthesis. High monodispersity can be achieved in this process through self-focusing of the colloidal size distribution. The smaller particles grow more quickly than the larger ones due to the higher free energy that acts as the driving force in the region of the critical size. Very monodisperse

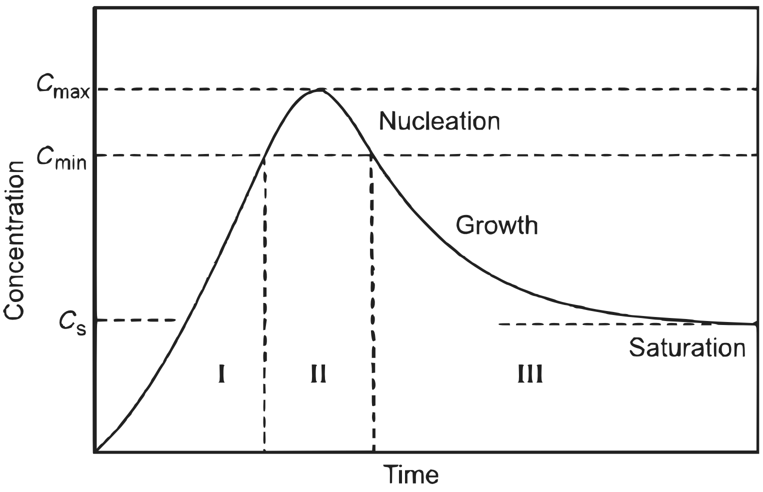

Figure 2.2.: ***LaMer and Dinegar's model*** *used to describe nucleation and nucleus growth*[7]

particle solutions can therefore be produced by quickly stopping the reaction.

For reactions with longer growth periods Ostwald ripening can occur as, due to the decreasing supersaturation occurring in the reaction mixture, the critical radius of the particles is constantly moving towards larger sizes, with the result that stable particles move into the unstable regime and therefore again begin to dissolve. Hence, the larger particles will further grow at the expense of smaller ones which eventually leads to a broader, often bimodal, size distribution.

2.2.2. Crystal growth

For the purposes of this work, the working definition of crystals or crystalline materials as being solids with regularly arranged atoms, molecules or ions will be used. It is of interest to note that the definition of a crystal previous to 1992 was that of a three-dimensional periodically arranged material with the smallest structural unit being the unit cell. While this definition adequately describes single crystalline materials, with the discovery of quasi crystals this definition was no longer deemed to be of sufficient precision. Therefore, in 1992, the International Union of Crystallography (IUCr) defined crystals with respect to their discrete diffraction order i.e. over their long range arrangements and which therefore allowed the inclusion of both polycrystalline materials and quasi crystals.

Single crystalline materials are seldom found in nature due to the inclusion of impurities and grain boundary defects. Even under relatively stringent labora-

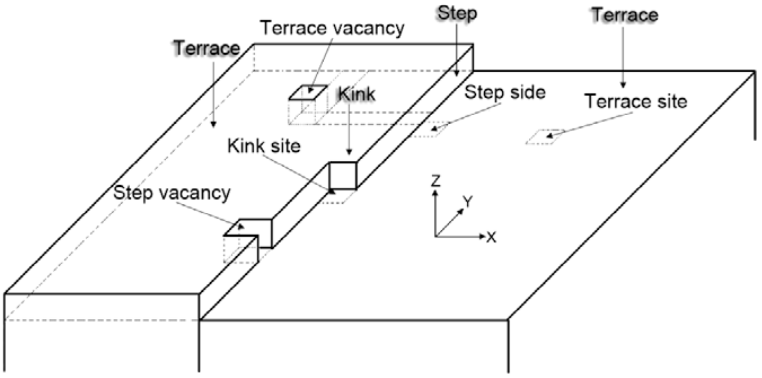

Figure 2.3.: ***Schematic diagram of the substrate surface*** *described by the Kossel-Stranski "terrace-step-kink" model.*[9]

tory conditions single crystalline materials are quiet difficult to produce and often require a high technical outlay for their production.

The unit cell is the smallest repetition unit in a crystalline material and its structure the symmetry of which strongly influences the morphology of the crystal and is always a parallelepiped of precise size and defined angles. The resulting crystals very often possess the habit of polyhedrons with smooth surfaces and fixed angles which, due to the unit cell are constant for any one material. This is as a result of the correspondence principle, where the lattice planes of the crystal are parallel to the crystal surface. The morphology of the resultant crystal can be predicted using Wulffs model, which was established at the beginning of the last century.[8]

Which crystal surface finally dominates depends on the relative rates of growth of the different crystal facets. The more slowly growing facets will be present at the end of the growth period, as the faster growing crystal facets, which have a high surface energy, will have been eliminated. In addition, during crystallisation the physical and chemical environment is important for the resulting habit of the crystal. Different additives or physical parameters influence the rate of growth of the single crystal facets and indirectly influence the morphology, a process known as exomorphism. At the end of the crystallisation process, the single crystal facets have the same vapour pressure and the resulting structure, which is then termed the equilibrium form, is the form that shows the lowest surface energy in comparison to equivalent crystals of the same volume. During the growth process atoms, molecules or ions are arranged on the surface of the crystal structure and hence the building blocks can attach to a number different positions on the crystal face. As is described in the Kossel-Stranski model (see Figure 2.3) the building blocks arrange at a kink or on a step as these are energetically preferred[10] and as a result, the crystal facet will be assembled layer-by-layer resulting in the appearance of flat crystal surfaces at the end of the process.

2.3. Non-classical Pathways

2.3.1. Main Principles

The concepts and ideas behind non-classical crystallisation are an attempt to describe an alternative notion of the formation of crystalline materials, according to which the crystallisation does not undergo the classical pathway of nucleation and crystal growth *via* atom, molecule or ion deposition, but follows a particle mediated aggregation or self-assembly process.[11]

Both pathways start with particle formation induced *via* supersaturation which results in the formation of the initial building blocks and hence the variety of building blocks that may be present is quite large. Not only may crystalline building blocks be used for non-classical crystallisation, but so too can amorphous[12–17] and liquid structures[18–22]. In the case of crystalline building blocks, the classical growth mechanism can be interpreted as being due to the reaction species reaching their equilibrium solubility[23] or the temporary stabilisation of the nanoparticles that have been created such that the classical pathway is inhibited. Different steps within the non-classical crystallisation pathway have been identified and, as we are still in the initial stages of our understanding of the processes involved in non-classical crystallisation, it is quite likely that the list is not as yet complete. The steps identified thus far include:

- the formation of primary building blocks such as intermediary clusters or, as in the case of liquid precursors, phase separation
- the mesoscopic transformation of superstructures, which have formed from amorphous building blocks
- the oriented attachment of nanoparticles
- the formation of three dimensional mesocrystals *via* the self-organization of organic-inorganic nanoparticles

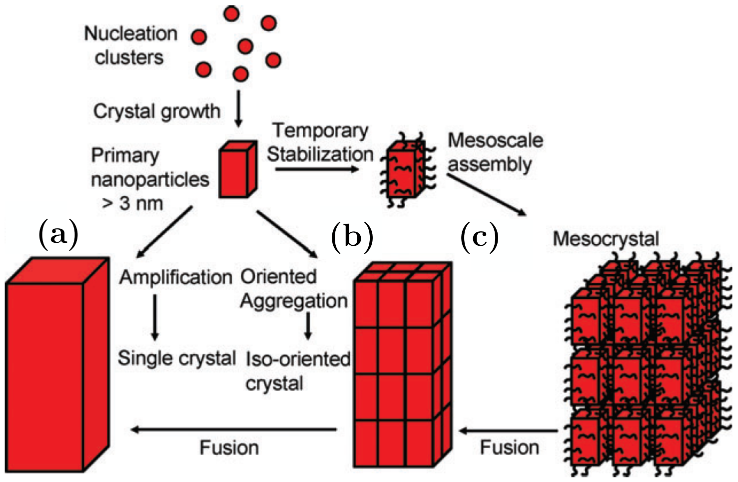

Figure 2.4.: ***Schematic representation of both classical and non-classical crystallisation.*** *(a) Classical crystallisation pathway, (b) oriented attachment of primary nanoparticles forming an iso-oriented crystal upon fusion, (c) mesocrystal formation via self-assembly of primary nanoparticles covered with organics.*[24]

These four steps[11] are illustrated in Figure 2.4 with the classical crystal growth process presented by path (a) where primary nanoparticles when synthesised *via* atom, molecule or ion precipitation grow to afford large single crystals. Path (b) describes the mechanism of oriented attachment where, following post-structuring on the mesoscale, it is possible with mesoscopic transformation to generate single crystals from iso-oriented crystals. For path (c) to occur it is necessary for temporary stabilised building blocks to be present. These inorganic cores with their accompanying organic ligand or stabiliser shell can be structured on the mesoscale in three dimensions. After initial fusion, it is possible to generate iso-oriented crystals and finally single crystals. The production of mesocrystals *via* non-classical crystallisation from a variety of different materials such as PbS[25–27], CdS[28], CdSe[29,30], Au[31], Ag[32], $BaCO_3$[33,34], $CaCO_3$[13,35–43], $CoC_2O_4 \cdot 2H_2O$[44], $CoPt_3$[45] and D,L-alanine[12,46] has been observed and shows a high degree of ordering containing well aligned nanoparticular units. Additionally, these materials have been observed to possess scattering properties that are similar to single crystals.

Non-classical crystallisation occurs predominantly in biological systems where nucleation and growth of the building blocks and their subsequent aggregation into highly ordered and aligned structures can simultaneously take place. Hence, hybrid materials with specific and distinct properties can be generated under ambient conditions. The definition of synthetically prepared mesocrystals not only includes a high degree of ordering of the inorganic-organic hybrid material building blocks but additionally, the alignment of the building blocks along a common crystallographic axis.

In such cases, mesocrystals form a specific class of quantum dot solid in which there is a growing appeal as the interesting properties derived from combining tailored nanoparticular characteristics with properties which derive from the nanoparticle arrangement may provide made-to-measure material solutions in a number of important application fields. Tuneable properties such as photonic band gaps, electronic and optical properties, and high surface area make these materials interesting for applications as diverse as biomedicine, solar energy or energy storage, optoelectronics and heterogeneous catalysis or photocatalysis.[47]

2.3.2. Oriented Attachment

Bottom-up approaches for nanoparticle synthesis are nowadays quiet common and have gained in importance for both materials science research and applications. Therefore the control of the morphology, particle size and size distribution of the prepared colloidal solutions is of great consequence and, as these processes are well described by the classical nucleation and crystal growth theory, theoretical modelling of the crystal growth is possible. With increasing reaction time, the size distribution of the colloidal solution becomes broadened in a process known as Ostwald ripening.

Penn and Banfield have determined that not all growth processes present in nanoparticular solutions can be described using this model.[48–50] For example, TiO_2 particles in hydrothermal synthesis grow together along a crystallographic fashion and form one-dimensional arrangements, the as-synthesised nanoparticles working in this case as building blocks. The driving force for this agglomeration, which is nowadays called oriented attachment, is the reduction in the surface energy achieved by fusion of the facets which possess the highest surface energy. For this process two main principles are postulated (i) fusion can take place after the effective collision of oriented nanoparticles or (ii) coalescence can be induced by particle rotation.[51]

For the first mechanism to occur, the colloidal solutions must be dispersed in order for oriented attachment to be able to take place and high collision rates and free rotation of the nanoparticles must occur. Colloidal solutions are normally kinetically stable with repulsive forces between the particles hindering agglomeration. Under these conditions, the oriented attachment growth rate is related to the number of effective collisions and to the minimisation in the number of high-energy facets *via* the reduction of the surface energy.[52,53] An effective collision is defined as a collision that results in an irreversible oriented attachment. Therefore, the different orientations of the nanoparticles during collision need to be aligned, in order for fusion to a congruent two-dimensional structure at these interfaces to be possible.[54–56] Collisions, where the orientation is not suitable for coalescence or which do not lead to irreversible attachments are termed non-effective collisions.

Superstructures of different dimensionalities can be synthesised through oriented attachment based on nanometer sized building units, which can be treated as zero-dimensional entities, such as spheres, polyhedrons and cubic structures. Thereby, one-dimensional wire or rod like structures, two-dimensional plates and also three-dimensional self-assemblies can be formed *via* arrangement of the nanosised building blocks.[57,58] One-dimensional structures are primarily generated through oriented attachment based on collisions. Hence, interparticle interactions are possible between 0D and 0D particles as are, in the case of the formation of 1D structures, also interactions between 0D and 1D structures and 1D and 1D structures.[11,59] These collision processes are statistical and as a consequence superstructures with different growth directions can be observed.

The second pathway for oriented attachment to occur is not controlled *via* collisions, but rather dominated by particle interactions in the short- and medium-range. In this range, the attractive forces such as Van der Waals forces are greater than the repulsive forces such as electrostatic interactions or steric hindering. Normally these interaction conditions are observed in weakly flocculated colloidal states. The rotational freedom of the single nanoparticles is important to bring about the alignment of the nanoparticles along a crystallographic fashion.

The first step of this reaction path is the interaction of 0D and 0D primary structures to form 1D and 2D architectures. After this formation step, a second phase occurs *via* the formation of 2D (from 1D structures) or 3D structures *via* self-assembly of the 1D and 2D architectures. This hierarchical process can produce mesocrystals in an intermediate state before mesoscopic transformation take place and iso-oriented crystals are formed.[60]

The growth processes described above and the resulting morphologies of the superstructures can be additionally influenced by the presence of organic additives. As is

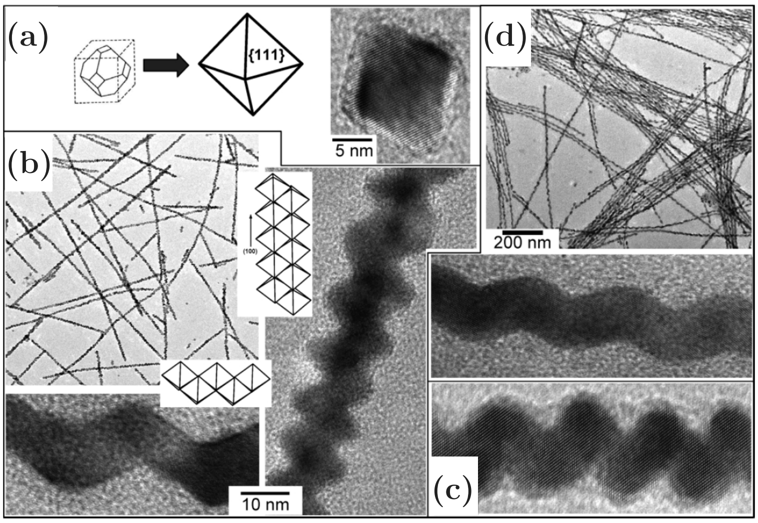

Figure 2.5.: ***Oriented attachment of octahedral PbSe nanoparticles into 1D structures.*** *(a) Octahedral PbSe nanocrystals grown in the presence of HDA and oleic acid. (b) TEM and high-resolution TEM images of PbSe zigzag nanowires grown in the presence of HDA. (c) HRTEM image of single- crystal helical PbSe nanowire grown in oleic acid/HDA/trioctylamine mixture. (d) Helical nanowires formed upon annealing of straight PbSe nanowires in the presence of trioctylamine.*[64]

postulated in Wulffs facet theorem[61], (i.e. at equilibrium the crystal structure with the lowest surface energy by constant volume develops and as a result, the crystal structure reflects the intrinsic symmetry of the lattice) most metals show cubic crystal growth instead of rod like structures.[62,63] As described above the growth rate of the different facets can be altered by influencing the surface energy i.e. by adding organic molecules, through which the crystal morphology can be indirectly influenced. Another possibility by which the morphology can be influenced is by using organic molecules as templates for 2 or 3-dimensional superstructures.

Cho *et al.*[64] reported on nearly defect free PbSe nanowires through assisted assembly using organic molecules. With different combinations of additives straight, helical, branched, tapered and zigzag nanowires can be formed, (shown in Figure 2.5) as can nanorings. Not only was the oriented attachment influenced by these organic molecules but the nanoparticle synthesis was also modified through the addition of long-chained, aliphatic primary amines such as hexadecylamine, dodecylamine and oleylamine and finally octahedrally shaped nanoparticles were synthesised that contained solely {111} facets, see Figure 2.5a.

Using another method Kotov *et al.*[65] have nicely shown the stepwise progress of the oriented attachment of CdTe nanoparticles to highly luminescent crystalline nanowires. Washing steps induce destabilisation of the CdTe nanoparticles by first removal of the stabilizing ligand molecules and subsequent one-dimensional agglomeration. A strong dipole-dipole interaction is believed to be the main driving force for the self-assembly. After arrangement into 1D structures a recrystallisation process from the cubic zinc blend structure to the more stable hexagonal wurtzite structure takes place. This phase transition does not greatly influence the luminescent properties of the as-synthesised nanowires with only a small red shift occurring due to a loss in confinement in the growth direction of the wires.

Not only is oriented attachment possible for semiconductor nanoparticles but it can also be employed in the case of metallic nanoparticle systems. For example, Ravishankar *et al.*[66] have reported on the formation of ultrafine single-crystalline gold nanowires by the controlled removal of primary capping ligands (oleylamine) from the $\{111\}$ facets using ascorbic acid which leads to the destabilisation and resulting aggregation of the gold nanoparticles in one dimension. This method works especially well for gold nanoparticles as the gold-amine binding energy varies for the different facets. The resulting anisotropic structures show convex-concave surfaces with differences in their chemical potential and which leads to a smoothing of the surface along the wire.

The above-mentioned examples highlight only a small selection of the possibilities of employing oriented attachment. In addition to oriented attachment processes involving organic additives, oriented attachment without the help of so called assemblers is also possible. The oriented attachment mechanism is one of the more important non-classical crystallisation pathways as it provides the ability to produce crystal architectures which cannot be produced *via* classical crystallisation methods, opening a wide field of potential applications. Presently, we are far from comprehensively understanding the growth processes and therefore lack the ability to systematically influence them. That is indeed why additional experimental and theoretical research is essential i.e. to shine more light onto these processes in order to enable further design of new materials using this fascinating growth mechanism.

2.3.3. Mesocrystal formation

A second means of non-classical crystallisation is the formation of mesocrystals. Mesocrystals are crystalline materials with crystal facets of some hundred nanometres up to the micrometre size regime. The smallest building units are normally colloidal, crystalline nanoparticles with a core-shell structure, composed of an inorganic core with an organic stabilizing shell. These building blocks are arranged in a unit cell, which forms the entire mesocrystal *via* a translational shift and which results in an inner crystalline structure analogous to that of single crystals. With these nanoparticular superstructures single crystals can be formed during a fusion process *via* the formation of an iso-oriented crystal to produce single crystals as shown in Figure 2.4.[67]

With this distinctive architecture new material properties can be derived because, as mentioned previously, the nanoscopic effects are still present within the individual building blocks of the macroscopic mesocrystal as are new properties which derive from the collective interactions of the building units. It is this combination of properties that is of great interest for many applications, amongst which are those based on photonic band gaps[68] or tuned electronic and optical properties in the case of semiconductor building blocks[69].

Aggregates of particles have been observed since the first crystallisation experiments, but normally they were not observed to display any homogeneous architecture or size and the main focus of the research in this period of time lay in investigating various aspects of the classical pathway. In the last few decades however, partly due to the improved analysis methods, these particle agglomeration processes have been more intensively examined. Amongst the first experiments on mesocrystals without defined habit were undertaken by Matijevic *et al.* and were concerned with various Ce(IV)-salts in a crystallisation study in the absence of organic additives[70], where it was observed that the elongated, and also plate-like nanoparticles, orient themselves along one axis to form a one-dimensional superstructure. Earlier, Pedres *et al.* investigated geometrically shaped mesocrystalline $BaSO_4$ architectures containing a porous inner structure, which would normally be expected to exhibit growth according to classical crystallisation principles similar to that of a single crystalline material. Studies on different materials such as CuO[71,72], CeO_2[70], MgO[73,74], Fe_3O_4[75] and Eu_3O_4[76,77] show the variety of possible structures. In addition to the aforementioned materials, $CaCO_3$ was also observed to form mesocrystalline materials. This $CaCO_3$ structure, which was synthesised in silica gel and known as the "sheaf-of-wheat", was described by Dominquez *et al.*[78] in which calcite rhombohedra orient along the c-axis. The complete structure behaves as a single crystal under a polarisation microscope, which can be used to visualise the perfect arrangement of the rhombohedra building units.

Nevertheless, not only are one-dimensional arrangements and two-dimensional nanoparticular arrays[79–85] possible, but so too are three-dimensional mesocrystals. Busch and Kniep demonstrated a nearly perfectly arranged 3D fluorapatite mesocrystal, synthesised in gelatin.[86–91] The resulting elongated hexagonal mesocrystals showed typical single crystalline properties, which makes it difficult to determine the arrangement of the building blocks. Only with perpendicular thin cuts could the mesocrystalline structure be proven. The growth mechanism of these fluorapatite crystals was not influenced by the 2%wt. of intracrystal gelatin, which was found between the building blocks.

The particular growth mechanism for these kinds of arrangements has not presently been fully elucidated. However, the growth of mesocrystals in gels seems to be appropriate, as in gels the local supersaturation is very high[92], which leads to the formation of the primary building blocks. The high viscosity present in these media slows down mass transport processes such as convection and other processes that influence crystallisation and thus promotes the undisturbed orientation of the building blocks along their preferred interaction direction to obtain an energy-minimised structure.

Formation methods

Beside the synthesis of mesocrystals in gels,[43,91] there are a variety of alternative methods to bring about the ordering of organic ligand shell containing spherical nanoparticles, especially with respect to metal and semiconductor building blocks. The obvious starting point for these methods is the correct synthetic protocol to provide the required nanoparticles in sufficient quantity and monodispersity and in a solvent environment which can subsequently be used to bring about their controlled arrangement on the mesoscale.

Murray *et al.* have shown that with their layering technique the gentle destabilisation of nanoparticle solutions by a slow diffusion of non-solvent into the solution leads to 3D crystalline structures.[3,69] During destabilisation, the solution is kept in the dark and left until precipitation is complete thus ensuring that intermixing of the phases and convection effects are minimised, a process which is analogous to the use of gels as solvent. The solvent/non-solvent pair, the polarity of the non-solvent and the temperature are amongst the more important factors that influence the destabilisation rate. A modification to the technique employed by Talapin *et al.* introduces a buffer-layer, which is normally a weaker acting non-solvent than the non-solvent layer above, between the solvent and non-solvent.[30] The buffer-layer acts to slow down the destabilisation rate, due to the fact that the time taken for the first agglomeration of nanoparticles to occur is protracted, which results in better quality mesocrystals with respect to their size and their higher symmetry. In a step taken towards the optimisation of the gentle destabilisation method a recent additional study, in which it was shown that a capillary microfluidic platform, where the destabilisation *via* non-solvent forms nanoliter microfluidic plugs, can be used for the self-assembly of inorganic nanoparticles into 3D superstructures and where additionally the growth kinetics could be studied, should be mentioned.[93]

It is not always necessary to destabilise the nanoparticles using a non-solvent in order to arrange them into ordered crystalline materials. Zheng *et al.* have used the inherently low stability of the nanoparticles in their reaction solution after the synthesis.[94] In this study the nanoparticles were kept in the reaction flask without the application of the clean-up procedure and the low solubility at reduced temperature lead to agglomeration and growth of the first nanoparticle arrangements over two days. A further method based on supersaturation methods is the slow and controlled evaporation of the solvent. Normally this method is quiet common for the preparation of 2D structures[24,83,95–99], but a number of examples exist where it has been employed to form 3D architectures[100–102].

To create oriented and ordered architectures, electrostatic interactions can also be used as has been shown by Grzybowski *et al.*[103–107] In these studies oppositely charged nanoparticles were slowly destabilised *via* solvent evaporation. At first an equal amount of oppositely charged nanoparticles is established by titration of the nanoparticles of interest. Then a number of cleaning procedures follow and the precipitate is dissolved in a mixture of solvent and non-solvent. During the slow evaporation of the lower boiling solvent, destabilisation of the nanoparticles is initiated and the structural arrangement is driven by the oppositely charged ligand shell of the nanoparticles. In this destabilisation method nanoparticles made of different materials can be arranged into macroscopic mesocrystals or, as they have been called in this case, supracrystals. This method has so far only been reported in aqueous solution as it is based on charge pairing and is therefore limited to polar solvents as otherwise the surface charge on the ligands will be lost.

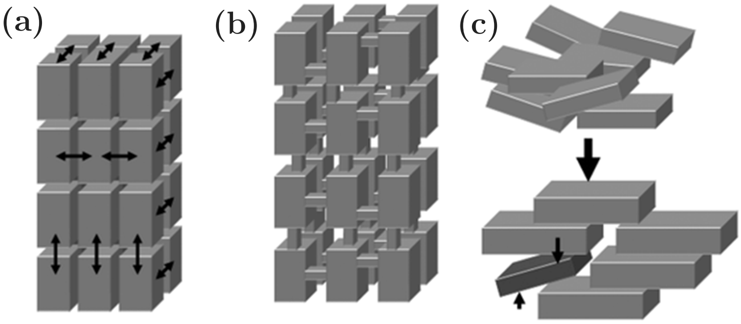

Figure 2.6.: ***Three principal possibilities to explain the three-dimensional mutual alignment of nanoparticles into mesocrystal*** *(a) nanoparticle alignment by physical fields or mutual alignment of identical crystal faces; (b) epitaxial growth of nanoparticle employing a mineral bridge connecting the two nanoparticles; and (c) nanoparticle alignment by spatial constrains, i.e. an entropy-driven mechanism.*[11]

Interparticle interactions

The methods thus far mentioned are based on the slow destabilisation of nanoparticles in order to provide sufficient time for the building blocks to arrange. If the agglomeration occurs too quickly the resulting structures are usually not highly ordered but often non-ordered or porous. The particle arrangement during slow precipitation primarily takes place through interparticle interactions. As reported by Cölfen *et al.*, there are different possible mechanisms for mesocrystal formation. First, processes may be classified as to whether they are dynamic or static, with the above mentioned methods all falling under the heading of dynamic processes. During a static process, an organic matrix determines the outer shape of the mesocrystal formed and the building blocks assemble along the structures present. In dynamic pathways, which are more prevalent, the building blocks assemble freely into three-dimensional mesocrystals and, as is shown in Figure 2.6, three different main pathways can be used to describe their formation.

The first route is based on vectored physical interactions such as electrostatics and investigated by Grzybowski *et al.*[108] Other forces such as Van der Waals interactions, magnetic interactions, entropic effects, attractive depletion forces, dipole interactions and a host of others can also influence the resulting structures during the agglomeration of the building blocks. The second mechanism is based on the three-dimensional arrangement through the formation of interparticle mineral bridges. These bridges occur after the classical crystallisation of the nanoparticles has stopped thereby allowing the temporary stabilisation in the form of ligand molecules to take place. Mineral bridges can then grow on defects in the ligand shell. A new nanoparticle can grow on the newly induced surface, up to the point of complete stabilisation and resulting equilibrium. The growth mechanism between nanoparticle formation and defect induced mineral bridge growth varies.[109–112] The third pathway only occurs in the case of anisotropic building blocks and is based on the Onsager-theory of lyotropic liquids, where entropic forces result in ordered arrangements.

To understand the arrangement of nanoparticles with respect to the above mentioned preparation techniques, it is necessary to focus on the physical interparticle interactions as it is these that are important for the first pathway. Therefore, the different length scales and magnitudes of the interparticle forces will now be the main focus of the discussion before further examining the specific types of interparticle interactions.

The Lennard-Jones potential function is the predominant model used in predicting the interactions between atoms and small molecules, where the attractive interactions such as Van der Waals act to counter the repulsive interactions which are mostly electrostatic in nature. The length scales of the attractive and repulsive forces are of the same magnitude as the atomic, molecular or ionic building units to be used in the assembly. If we consider nanoparticular building blocks, this condition is no longer valid as while the length scales over which the interactions are effective remains constant the size of the building blocks has drastically increased. In principle, it would be possible to calculate the potential over all constituent atoms of the nanoparticle and their interactions with other nanoparticles, but this would be costly and likely to contain many errors because of the necessary oversimplification of the interactions or in the estimation of their numerical values.[108]

The varying ratio of the length scales of the interactions with respect to the particle sizes plays an important role during self-assembly. To influence self-assembly, the attractive forces need to be strong enough to overcome the entropic effects such as the loss of translational and rotational movement of the building blocks. Initially, the attractive interactions induce cluster formation and the early stage of this aggregation can be described within the equilibrium theory of physical clusters,[113] where the average numbers of n-sized clusters can be estimated. Additional agglomeration then follows, so that mesocrystals are formed. The agglomeration is an interplay between the length scale and the magnitude of all of the interactions involved. On the one hand short range interactions of high magnitude induce self-assembly whilst on the other long range interactions of small magnitude result in ordered arrangements. Exceeding a value of magnitude and interaction length within this ideal range results in the particle agglomeration occurring too quickly and consequently only non-ordered structures or those with short range order precipitate.[108] This interplay of the length scale and the magnitude leads to the different destabilisation methods as have been presented above and the different interaction potentials lead to different equilibrium morphologies and structures of the resulting colloidal mesocrystals.

Now the most commonly observed interaction occurring between matter, namely the Van der Waals (VdW) interactions will be focused on. These non-covalent interactions are based on the electromagnetic variation within molecules or bulk materials. Normally, the VdW interactions are attractive and their magnitude can range from being quite small up to hundreds of kT, with the magnitude of their interaction decreasing as a function of the sixth power of their separation. Generally three different types of VdW interactions are distinguished:

- Keesom interactions (dipole - dipole interaction)
- Debye interactions (dipole - induced dipole interaction)
- London dispersion interactions (induced dipole - induced dipole interaction)

The VdW interactions are always present between materials and molecules and can lead to unintentional agglomeration between nanoparticles, which is why normally charges or ligands, which are employed to sterically stabilise the nanoparticular building blocks, are required. By contrast, this phenomenon can also be used for the controlled assembly of the nanoparticular units, as described in the works of Murray *et al.*[69] where fcc packed 50 μm large superlattices composed of 2 nm sized CdSe nanoparticles are formed mainly by VdW interactions. Talapin *et al.*[99] have demonstrated that the dipole-dipole interactions influence the ordering of the nanoparticles and it was revealed that while antiferroelectric arrangements of dipoles is unusual for bulk materials, this type of arrangement can be found in the case of nanoparticular superlattices as is shown in Figure 2.7. Goubet *et al.*[114] have also investigated Au nanoparticles that arrange with the help of VdW interactions during solvent evaporation and have found that these are not the sole interactions that influence the agglomeration process. Besides the VdW forces

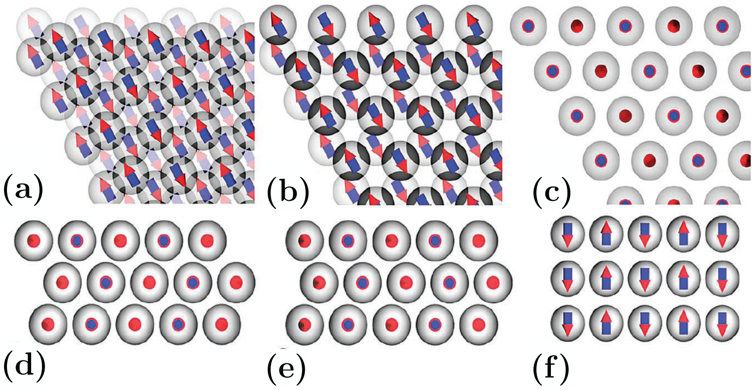

Figure 2.7.: ***Dipole ordering in nanoparticle superlattices.*** *Top view ([0001] plane) of (a) horizontal antiferroelectric ordering in fcc, (b) horizontal antiferroelectric ordering in hcp, and (c) vertical antiferroelectric ordering in sh lattices. Panels (d), (e), and (f) show side views ([1h2 h] plane) of fcc, hcp, and sh structures, correspondingly.*[99]

electrostatic forces and ligand-solvent interactions also control the assembly and resulting morphology.

In addition to the VdW interactions, the sum of which is normally attractive, electrostatic interactions, which provide attractive forces between oppositely charged building units and repulsive between like-charged nanoparticles, are also present. The intensity of these interactions during the self-assembly can be influenced by the concentration of nanoparticles in the solution, their charge and also by the dielectric constant of the solvent. Grzybowsi *et al.*[103–107] have investigated this in a number of self-assembly experiments involving gold and silver nanoparticles with oppositely charged ligands. In these experiments Au and Ag nanoparticles of the same size were modified by ligand exchange with 11-mercaptoundecanoic acid (MUA) and N,N,N-Trimethyl(11-mercaptoundecyl) ammonium chloride (TMA). After titration to achieve a 1:1 ratio, the nanoparticles were redissolved in a mixture of distilled water and a nonpolar non-solvent (DMSO). During heating of this mixed nanoparticle solution at 70°C over 12 h the water evaporates and the nanoparticles slowly precipitate, so that the dielectric constant (ϵ) of the mixed solution changes. As is presented in equation 5, when the water, which has a relative dielectric constant of 78, evaporates in the mixture the dielectric constant slowly changes to that of DMSO, which is 65 at 25°C. Hence, the charge screening is reduced and slow agglomeration starts until the point of complete precipitation is reached.

$$F = \frac{1}{4\pi\epsilon} \cdot \frac{q_1 q_2}{r^2} \tag{5}$$

During their investigations they have also focused on the length scale of the electrostatic interactions. The synthesised mesocrystals crystallise in a diamond like lattice, i.e. every nanoparticle is surrounded by 4 nearest neighbours. This relatively inefficient close packing is as a result of short range interactions; the screening length κ_C^{-1} calculated using Deryagin-Landau-Verwey-Overbeek (DLVO) theory is ≈2.7 nm. Additionally, they observed that screening helps the ordered assembly during destabilisation because in polydisperse samples smaller particles can stabilise those which are larger so that the long range interactions between them are reduced to the point where flocculation no longer takes place. Too high a polydispersity leads to the complete stabilisation of the solution without self-assembly as is shown in Figure 2.8.

In addition, external fields such as electrostatic and magnetic fields can also induce self-assembly as polarisation forces and permanent dipole moments can orient within such fields. Normally anisotropic nanoparticles arrange along these external fields and form 1D and 2D structures and have even been observed to form 3D structured films.[115–117] The same 1D[118–121], 2D[122,123] and 3D[124,125] structured superlattices are also observed by applying magnetic fields. In addition to the one-dimensional wires, chains of rings can also be formed. However, as no symmetrical three-dimensional nanoparticle arrangements have so far been reported to form in such cases this assembly method will not be focused upon further.

While the hard sphere model is used to describe the effects of Van der Waals, electrostatic, magnetic and dipole interactions within systems composed of nanoparticles, they are better described as core shell systems consisting of a nearly hard inorganic core surrounded by an organic ligand shell. Interactions involving the ligand shell differ from those entailing core-core interactions. Usually, the ligands are organic molecules with different functionalities which can interact with the neighbouring molecules on the same nanoparticle, with molecules on adjacent nanoparticles and/or with solvent molecules. Generally, these interactions are short range, being on the length scale of Angstroms or nanometres, such as covalent bonds, dipole interactions, donor-acceptor interactions and hydrogen bonds to name but a few. These interactions, when separately considered, are weak interactions but

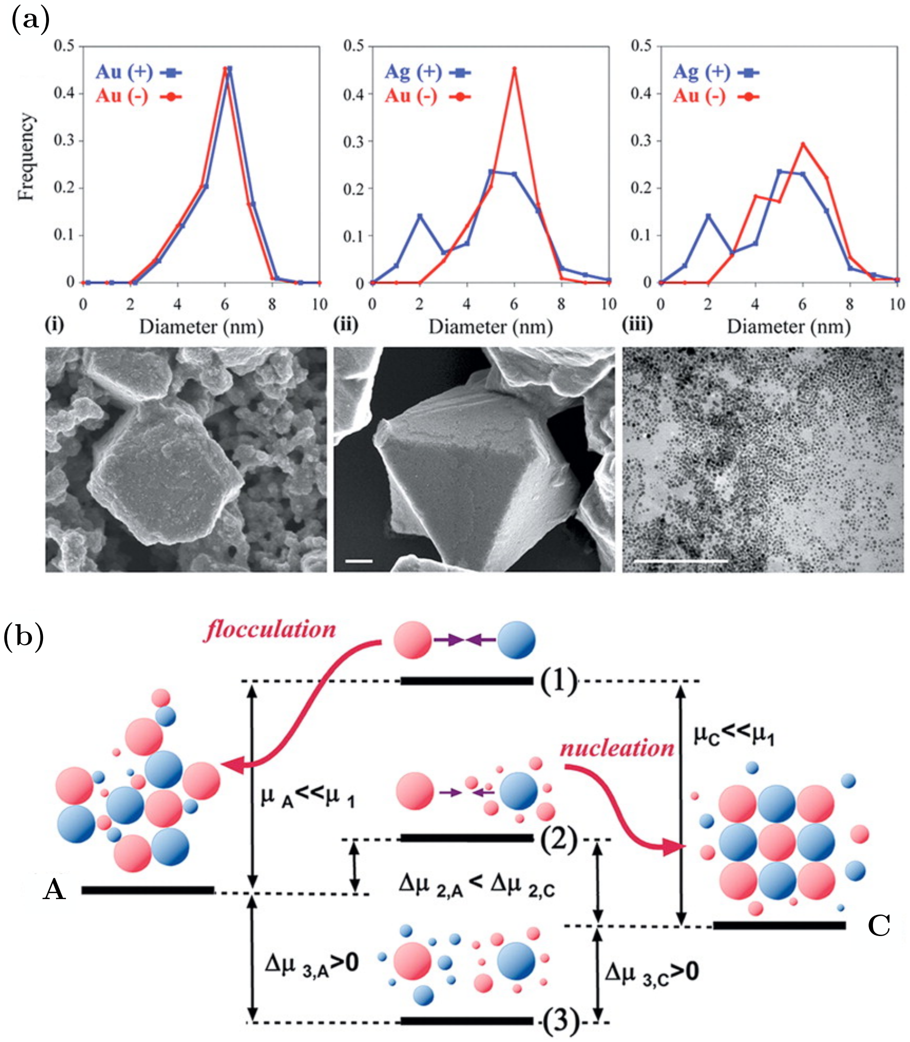

Figure 2.8.: ***Electrostatic interactions as driving force for crystallisation.*** *(a) Effect of NP polydispersity on the quality of crystals. Graphs (i) to (iii) give normalised size distributions of the metallic cores of oppositely charged NPs used in crystallisation experiments; typical outcomes of these experiments are illustrated by SEM or TEM images shown in the bottom row (scale bars 200 nm). (b) Effect of small particles on the stability of the dispersed, large NPs. In the absence of small particles (1), large NPs of opposite charges interact by relatively strong electrostatic forces resulting in high chemical potential and the NPs instantly flocculate to form amorphous aggregates (A). Small NPs of one type surround large NPs of the opposite charge and effectively screen electrostatic interactions between them (2) so that slow and ordered nucleation takes place. If small NPs of both types are present in the suspension (3), all large NPs are screened and interact very weakly remaining stable solutions.*[103]

their summation over all nanoparticles results in them having a relatively strong effect. As previously described, the solvent influences the magnitude of the interactions, e.g. the dipole-dipole interaction of cis-azobenzene in toluene is $\epsilon_{dd} \approx 2.7kT$ but in water it is $\epsilon_{dd} \approx 0.08kT$, which is as a result of more effective screening due to the higher dielectric constant of water. Hence the molecular dipole interactions of cis-azobenzene in water are too weak to cause significant interaction and therefore charges (not dipoles) are required to induce significant electrostatic interactions.[108] In some cases, these interactions can induce temporary assembly on the mesoscale through changes in environmental conditions or may lead to redissolution of the nanoparticular units. In contrast to the non-directed dipole interactions, donor-acceptor interactions are more specific and hence it is possible to interlink nanoparticles using DNA or other donor-acceptor pairs.[126–129] Hydrogen bonding is also well documented as being able to provide interactions between ligand molecules and which are stronger in aprotic solvents.[130] In all the above methods the interactions between the ligand molecules play an important role and consequently can influence the mesocrystal morphology. Observations concerning the degree of flexibility of the ligands suggest that stiffness within the ligands may also be important for the formation of ordered and/or non-ordered assemblies induced *via* varying the temperature.[131]

Not only can attractive and repulsive interactions influence mesocrystal formation, but so too can entropic effects. These so called depletion forces and confinement effects (not to be confused with the quantum confinement effects that may be present in the individual building blocks) can be either repulsive or attractive. The repulsive forces, which are due to the presence of the ligand shell, are primarily due to steric interactions and act to hinder the particles from coming together and therefore prevent their self-assembly.[132,133] These repulsion forces depend on the length and the amount of ligand present at the nanoparticle surface. Attractive entropic interactions result due to the depletion force. Here, hard spheres come together because smaller hard spheres, ligand molecules or solvent molecules are present in the solution, and hence assembly by the bigger nanoparticles is entropically preferred. The force active in keeping the particles together is the osmotic pressure, which acts to push the particles together due to the excluded molecules in between them. This excluded volume or gained volume depends on the size of the depletant.[134,135]

As can be seen the variety of particle interactions that may be present in such systems is large and consequently nearly every interaction leads to new possible mechanistic pathways in the formation of mesocrystals. Also this variety adds a further layer of complexity in trying to understand the formation processes because the self-assembly process always results from interplay between the different attractive and repulsive forces. Some methods such as that of Grzybowski *et al.* are focused on using electrostatic interactions, others such as those of Talapin and Pileni use Van der Waals interactions as well as entropic and ligand interactions. The optimisation of the methods employed depends on the combination of nanoparticles, ligand shell, solvent and physical environmental influences such as pressure, temperature and ionic strength of the solvent amongst others. This makes it quite challenging to reproducibly synthesise mesocrystalline materials and a large variation in morphology is present even within the same synthetic batch.

Analogy to Atoms

The analogy of forming a classical crystal from its atomic or molecular components to that of the formation of mesocrystals due to the agglomeration of single nanoparticles into a macroscopic structure is obvious. Despite the fact that the driving forces and the interactions present during the assembly process are somewhat different the resulting structures are nevertheless very similar, as also is the observed growth mechanism. In classical crystallisation the first phase in mesocrystal formation is agglomeration caused by supersaturation, with the nanoparticles being destabilised by the addition of non-solvents or the evaporation of solvent. Bodnarchuk *et al.*[93] have observed the in-situ crystal growth process of CdSe, PbS, Au and $CoFe_2O_4$ mesocrystals within a nanoliter microfluidic plug. The nanoparticles are dissolved in an ethanol/toluene droplet and over the time of the toluene evaporation the nanoparticle solution is stable. Only when the nucleation threshold is reached is crystalline material achieved. After this first agglomeration the growth process of these crystals goes on until the solution is completely clear and colourless and as a result mesocrystals were produced that can have different crystalline structures and morphologies. Goubet and Pileni[136] as well as Kalsin *et al.*[103] have demonstrated the analogy between the morphology that results from mesocrystals composed of nanoparticles and that of classical crystals. The mesocrystals show the same crystal facets and angles as the components of classical crystals in the same crystal lattice. Also twinning effects, which occur in classical crystallisation are also found during the self-assembly of mesocrystals. Rupich *et al.*[26] describe the dependence of twinning with respect to the particle size of the constituent PbS nanoparticles and have calculated that with increasing size the twinning becomes more favourable. PbS nanoparticles with a size below 4 nm do not exhibit twinning in the resulting structure. However, by contrast, PbS particles larger than 7 nm in size form multiply twinned face-centred cubic superlattices with decahedral and icosahedral symmetry, exhibiting crystallographically forbidden five-fold symmetry elements. They have also reported that the interparticle potential during agglomeration becomes "softer", which also causes the higher degree of twinning. Nanoparticle arrangements in colloidal crystals suggest that the principle of maximum space filling is in operation, so that in many experiments an optimised nanoparticle arrangement is observed.[137–142] Experimental data using octahedrally shaped nanoparticles allows the formation of particle arrays, which depend on the composition of the organic ligand shell.[112,137–141,143,144] Four phenomenological models for this observation are proposed:

- anisotropic nanocrystals without or with just a small ligand shell
- hard spheres with small organic shell as compared to the core size
- hard spheres with large organic shell as compared to the core size
- small hard spheres with a very large organic shell, which is deformable and soft[25]

The nanoparticle arrangement between the different models differs and for the nanocrystals without or with a small ligand shell a bcc arrangement is preferred.[141,145] By increasing the coverage of the nanoparticle surface with organic ligand molecules the form of the nanoparticles is smoothened, so that defects in the orientation inside of the super lattice occur. This smoothened surface acts so as to change the packaging from bcc to fcc.[137–139] If small inorganic cores are covered with a thick shell of organics the orientational ordering becomes almost completely lost and the spheres, which can be deformed, arrange in a bcc structure.[140,143] Typically, the crystal structure of mesocrystals can be determined using SAXS measurements however, using this method it is not completely clear if the mesocrystal has an overall crystalline structure or if it also contains amorphous portions within the middle of a partially crystalline structure. Only by cutting through the crystal and visualizing the inner structure with HRTEM can one unambiguously determine the internal arrangement. Kniep *et al.*[91] reported on fluorapatite-gelatine-nanocomposites and their internal structure. The basis for the branched growth is a hexagonal elongated prism-like core of apatite. After the fractal growth has finished the hexagonal structure grows to form a spherical structure. The inner arrangement cannot be estimated only by consideration of the outer shape. Kniep *et al.* presented the first focused ion beam cuts on such structures to gain a deeper understanding of the arrangement and of the growth mechanism.

Properties and Applications

There presently exist a number of new and interesting applications based opportunities grounded on the structure of the mesocrystals. Before some examples are introduced, it is important to understand the internal structure of the mesocrystalline materials. Zhou and O'Brien have postulated that for general classification purposes three basic types of mesocrystals may be considered.[146] The first structures consist of nanoparticles separated by organic molecules, the second consists of nanoparticles connected by mineral bridges and additionally surrounded by organic ligands and in the third type of mesocrystal the nanoparticles are connected only by mineral bridges but without the presence of organic ligands. These different architectures influence the properties of the single mesocrystal entities, such as the electronic properties and the surface area of the nanoparticles, drastically.

Mesocrystals with bare surfaces show highly accessible surface areas and are well suited for heterogeneous catalysis and photocatalysis as shown by Zeng *et al.*[147], Tartaj *et al.*[148] and Yu *et al.*[149]. Zeng *et al.* used CoO and $Zn_{1-x}Co_xO/Co_{1-y}Zn_yO$ nanocomposites to catalyse, in a heterogeneous catalytic reaction, the oxidation of CO to CO_2. Both materials exhibit catalytic activity already at a relatively low temperature of 60°C, whichincreases up to temperatures of 120-140°C. The high surface area of the synthesised mesocrystalline material and the surface decoration with hydroxyl groups, which are essential for the CO adsorption, are responsible for the high catalytic activity. Yu *et al.* reported on an NO removal *via* a photocatalytic reaction at the surface of TiO_2 nanowires. The mesocrystaline rutile nanowires show a high catalytic activity because the nanowires have a high aspect ratio, which allows a fast charge transport, a large surface area with many open pores for the diffusion of NO and the efficient penetration of light.

Not only are catalytic reactions on the high surface area of the mesocrystaline materials possible, but in addition these materials are appropriate electrode materials. Pang *et al.*[150] synthesised $W_{18}O_{49}$ mesocrystals, which show good electrochemical properties and have a high electron-proton transport rate. In addition, they show large pseudocapacitive capacitance and a superior stability, which makes them potential materials for use as supercapacitors.

Mesocrystals which possess an organic ligand shell around them and whose preparation was described above, are usually not suitable for use in catalytic approaches as the surfaces are relatively inaccessible but do possess other interesting properties such as closed intracrystalline pores, which is advantageous for thermal and dielectric insulation.

Zhu *et al.* have reported on superstructures and the SERS properties of gold nanocrystals of different shapes.[151] These noble-metal nanocrystal materials possess a plasmon resonance and have many potential applications in e.g. optical waveguides, superlensing, photon detection and surface-enhanced Raman scattering (SERS) for sensing and imaging applications.[151] The SERS sensitivity is highly dependent on the structure of the Au mesocrystals so that the hotspots and the strength of the antenna effect vary. Not only do the size, shape and type of the single building blocks influence the SERS signal, the interparticle distance in the nanoparticle arrangement also changes the signal intensity. The difficulty in this reported study was the production of highly monodisperse Au nanoparticles of different shapes and their controlled assembly into 3D structures. Single-crystalline rhombic dodecahedral nanoparticles arranged into an fcc triangular superstructure showed the highest SERS effect. Additionally, the SERS effect was measured to be stronger along the edges and corners than in the middle of the superstructures. The presence of a higher number of hotspots makes these materials especially interesting as chemical and biological sensors, as immunosensors and for analytical measurements due to their high sensitivity. The SERS effect was also observed for Ag nanoparticle arrangements as described by Fendler.[152] Additional collective properties of Ag nanoparticles deriving from their shifted resonances in absorption spectroscopy due to Lorentz field effects and changes in reflectance measurements have also been described.[153]

The arrangement of magnetic nanoparticles into ordered superstructures opens up a class of materials with unique magnetic properties. The ferromagnetic nanoparticles so arranged are potential candidates for magnetic storage media. The idea is that each ferromagnetic nanoparticle corresponds to one bit of information. Up to now, there are several challenges to overcome before their application becomes a reality, such as their limited thermal fluctuation and their superparamagnetism at room temperature.[154] Magnetic nanoparticles capped with organic ligands and arranged into mesocrystals show collective behaviour caused by long-range dipolar interactions because contact between the nanoparticles is hindered by the ligand shell so that exchange interactions are neglected.[155] When 3-D ordered and non-ordered arrangements of magnetic nanoparticles are compared, the ordered assemblies possess a more square-like hysteresis loop and a higher blocking temperature, with the consequence that superparamagnet behaviour occurs at higher temperatures. Due to the higher ordering present within mesocrystals, the coupling constant between the nanoparticles increases with decreasing interparticle distance, which corresponds directly to the increase in dipolar interactions.[154] For applications of these magnetic 3D superstructures the interactions between the magnetic nanoparticles and their complicated underlying behaviour need to be investigated further.

The magnetic properties of such mesocrystals can also be used in biomedical and targeting applications. Ge *et al.* have reported on a method by which water soluble Fe_3O_4 mesocrystals that still exhibit superparamagnetism may be produced, which is normally limited in Fe_3O_4 nanoparticles to a domain size of approximately 30 nm.[156] Additionally the magnetic response to external magnetic fields, which is caused by the higher magnetization per particle into the arrangement, is much stronger than that of the single magnetic nanoparticles. Coating the mesocrystals with a silica shell allows the coupling *via* specific silane chemistry ligands to surfaces and molecules.[157]

Another field of application is in the area of photonic crystals. The 3D arrangement of spherical particles into macroscopic ordered structures leads to spatially periodic structures. The nanoparticle sizes need to be in the range of the photon wavelength to influence the propagation of electromagnetic waves. Using template free fabrication of photonic crystals has many advantages e.g. the easily tuneable photonic bandgap *via* size variation of the building blocks and relatively inexpensive fabrication. An inherent disadvantages are the imperfect structures that result from 3D self-assembly and, as is often observed, the absence of a full photonic band gap.

In addition, electronic properties of the isolated nanoparticle arrangements are of great interest. Yang *et al.* investigated the electronic properties of 3D Au colloidal crystals with scanning tunnelling microscope (STM).[158] The STM tip required higher bias voltages because of the insulating organic layers around the nanoparticular building blocks which resulted in a lower effective voltage. Additionally, conductance due to the collective nature of the structure could be observed. In contrast to the conductance of any one given nanocrystal a slight additional modulation was witnessed to be superimposed on the collective conductance background, which mimics the Coulomb staircase structure normally observed from isolated nanoparticles. As most experiments on the electronic behaviour of nanoparticles are made on layers with a defined thickness and size it was also possible to determine that the application of a thermal treatment increases the conductivity[159], which brings these structures one step closer to being used in promising applications involving low-cost, high-performance energy conversion and storage technologies.

The mechanical properties of mesocrystals are also of interest with respect to potential applications and therefore it is necessary to understand them with respect to device integration and such parameters as robustness and durability. Measurements have been performed with PbS mesocrystals in the group of Shevchenko *et al.* where the collective mechanical response of the material was undertaken, and which has been reported to be in the range between hard sphere colloidal crystals and opals.[27,160,161] The observed response can be compared with that of hard and stiff polymers, but shows a greater degree of hardness. This increased hardness comes from the dense packing of the spheres, which distributes the stress over the complete material and this results in an increased hardness and modulus. However, the fracture toughness is significantly diminished as only ligand-ligand interactions keep the inorganic cores inside of the material. The ligand-ligand interactions lead to a behaviour which is analogous to stiffness and elasticity in polymers. Podsiadlo *et al.* have also shown the dependence of increasing nanoparticle size on hardness (H) and elasticity (E). If the NP size increases in H then E also increases. The combination of the organic-inorganic core-shell material makes the material behave like nanoparticle-filled polymers. Thus, the mechanical properties can be influenced by ligand-ligand interactions and can be optimized through further investigation. Not only were the mechanical properties of PbS mesocrystals undertaken but also those of Au mesocrystals were measured and it was reported that the formation processes influence the Youngs modulus of the different structures.[162] Consequently, the relatively high stiffness combined with the elasticity caused by the nanoparticular structure is in accordance with the embedding and integration of these functional materials into technical devices.

All the examples presented here make it clear that the properties of mesocrystals depend on the internal structure of the mesocrystals and hence it is possible to vary and optimize the properties as required for different applications. Both mechanical stability and electrical conductivity are very important characteristics for the integration of the functional materials into devices and first procedures to optimize the materials regarding their conductivity and hardness have been undertaken. It is important for many applications that the mesocrystalline materials are not static materials as is the case for bulk materials. With small changes such as a different ligand shell, the properties can be widely varied and it is possible to optimize the properties with the end application field in mind.

2.4. Résumé

Briefly the latest state of the art of classical crystal growth and non-classical nanoparticle arrangement is presented. Thereby, the synthetic pathways of oriented attachment and non-classical crystallisation with firstly synthesised nanoparticles as building blocks are focused. Especially, the analogies of classical crystal lattices to those of nanoparticles are impressive and in some cases the inner structure of macroscopic solids can only be identified with thin cut techniques or focused ion beam experiments because of the single crystal behaviour of the resulting crystals. Besides the self-assembly mechanism and its parameters the properties of the mesocrystals, which are a sum of the nanoparticular properties and the unique collective properties, which derive from the highly ordered nanoparticle arrangement are presented and the corresponding possible applications, too.

2.5. References

1. Dirksen, J. & Ring, T. Fundamentals of crystallization: Kinetic effects on particle size distributions and morphology. *Chemical Engineering Science* **46,** 2389–2427 (1991).
2. Van Santen, R. A. The Ostwald step rule. *The Journal of Physical Chemistry* **88,** 5768–5769 (1984).
3. Murray, C. B., Kagan, C. R. & Bawendi, M. G. Synthesis and Characterization of Monodisperse Nanocrystals and close-packed Nanocrystal Assemblies. *Annual Review of Materials Science* **30,** 545–610 (2000).
4. Peng, X., Wickham, J & Alivisatos, A. P. Kinetics of II-VI and III-V Colloidal Semiconductor Nanocrystal Growth: “Focusing” of Size Distributions. *Journal of the American Chemical Society* **120,** 5343–5344 (1998).
5. Dalmaschio, C. J., Ribeiro, C. & Leite, E. R. Impact of the colloidal state on the oriented attachment growth mechanism. *Nanoscale* **2,** 2336–45 (2010).
6. LaMer, V. K. & Dinegar, R. H. Theory, production and mechanism of formation of monodispersed hydrosols. *Journal of the American Chemical Society* **72,** 4847–4854 (1950).
7. Goesmann, H. & Feldmann, C. Nanoparticulate functional materials. *Angewandte Chemie (International ed.)* **49,** 1362–95 (2010).
8. Wulff, G. Zur Frage der Geschwindigkeit des Wachsthums und der Auflösung der Krystallflächen. *Zeitschrift für Kristallographie* **34,** 449–480 (1901).
9. Zhang, J.-H., Zhang, Y., *et al.* Comparative study of Cu_{13} and Co_{13} clusters deposition and diffusion on the Cu(001) surface. *Computational Materials Science* **48,** 250–257 (2010).
10. Kossel, W. Zur Energetik von Oberflächenvorgängen. *Annalen der Physik* **413,** 457–480 (1934).
11. Cölfen, H. & Antonietti, M. *Mesocrystals and Nonclassical Crystallization* (Wiley New York, 2008).
12. Ma, Y., Cölfen, H. & Antonietti, M. Morphosynthesis of alanine mesocrystals by pH control. *The journal of physical chemistry. B* **110,** 10822–8 (2006).
13. Yu, S.-H. & Cölfen, H. Bio-inspired crystal morphogenesis by hydrophilic polymers. *Journal of Materials Chemistry* **14,** 2124 (2004).

14. Tlatlik, H., Simon, P., *et al.* Biomimetische Fluorapatit-Gelatine-Nanokomposite: Vorstrukturierung von Gelatine-Matrices durch Ionenimprägnierung und Auswirkungen auf die Formentwicklung. *Angewandte Chemie* **118,** 1939–1944 (2006).
15. Gehrke, N., Nassif, N., *et al.* Retrosynthesis of Nacre via Amorphous Precursor Particles. *Chemistry of Materials* **17,** 6514–6516 (2005).
16. Balz, M., Therese, H. A., *et al.* Crystallization of Vaterite Nanowires by the Cooperative Interaction of Tailor-Made Nucleation Surfaces and Polyelectrolytes. *Advanced Functional Materials* **15,** 683–688 (2005).
17. Qi, L., Cölfen, H. & Antonietti, M. Formation of $BaSO_4$ fibres with morphological complexity in aqueous polymer solutions. *Chemistry-a European Journal,* 3526–3532 (2001).
18. Faatz, M., Gröhn, F. & Wegner, G. Amorphous Calcium Carbonate: Synthesis and Potential Intermediate in Biomineralization. *Advanced Materials* **16,** 996–1000 (2004).
19. Faatz, M., Gröhn, F. & Wegner, G. Mineralization of calcium carbonate by controlled release of carbonate in aqueous solution. *Materials Science and Engineering: C* **25,** 153–159 (2005).
20. DiMasi, E., Kwak, S.-Y., *et al.* Complementary Control by Additives of the Kinetics of Amorphous $CaCO_3$ Mineralization at an Organic Interface: In-Situ Synchrotron X-Ray Observations. *Physical Review Letters* **97,** 045–503 (2006).
21. Gower, L. & Tirrell, D. Calcium carbonate films and helices grown in solutions of poly(aspartate). *Journal of Crystal Growth* **191,** 153–160 (1998).
22. Addadi, L. & Weiner, S. Control and Design Principles in Biological Mineralization. *Angewandte Chemie International ed.* **31,** 153–169 (1992).
23. Cao, G. *Nanostructures and Nanopmaterials - Synthesis, Properties and Applications* (Imperial College Press, London, 2004).
24. Niederberger, M. & Cölfen, H. Oriented attachment and mesocrystals: non-classical crystallization mechanisms based on nanoparticle assembly. *Physical chemistry chemical physics : PCCP* **8,** 3271–87 (2006).

25. Simon, P., Rosseeva, E., *et al.* PbS-organic mesocrystals: the relationship between nanocrystal orientation and superlattice array. *Angewandte Chemie* **51,** 10776–81 (2012).

26. Rupich, S. M., Shevchenko, E. V., *et al.* Size-dependent multiple twinning in nanocrystal superlattices. *Journal of the American Chemical Society* **132,** 289–96 (2010).

27. Podsiadlo, P., Krylova, G., *et al.* The role of order, nanocrystal size, and capping ligands in the collective mechanical response of three-dimensional nanocrystal solids. *Journal of the American Chemical Society* **132,** 8953–60 (2010).

28. Vossmeyer, T, Reck, G, *et al.* A "Double-Diamond Superlattice" Built Up of $Cd_{17}S_4(SCH_2CH_2OH)_{26}$ Clusters. *Science (New York, N.Y.)* **267,** 1476–9 (1995).

29. Murray, C. B., Sun, S., *et al.* Colloidal synthesis of nanocrystals and nanocrystal superlattices. *IBM Journal of Research and Development* **45,** 47–56 (2001).

30. Talapin, D. V., Shevchenko, E. V., *et al.* A New Approach to Crystallization of CdSe Nanoparticles into Ordered Three-Dimensional Superlattices. *Advanced Materials* **13,** 1868 (2001).

31. Fang, J., Ma, X., *et al.* Nanoparticle-aggregated 3D monocrystalline gold dendritic nanostructures. *Nanotechnology* **17,** 5841–5845 (2006).

32. Fang, J., Ding, B. & Song, X. Self-assembly mechanism of platelike silver mesocrystal. *Applied Physics Letters* **91,** 083108 (2007).

33. Yu, S.-H., Cölfen, H., *et al.* Tectonic arrangement of $BaCO_3$ nanocrystals into helices induced by a racemic block copolymer. *Nature materials* **4,** 51–5 (2005).

34. Guo, X.-H. & Yu, S.-H. Controlled Mineralization of Barium Carbonate Mesocrystals in a Mixed Solvent and at the Air/Solution Interface Using a Double Hydrophilic Block Copolymer as a Crystal Modifier. *Crystal Growth & Design* **7,** 354–359 (2007).

35. Xu, A.-W., Antonietti, M., *et al.* Uniform Hexagonal Plates of Vaterite $CaCO_3$ Mesocrystals Formed by Biomimetic Mineralization. *Advanced Functional Materials* **16,** 903–908 (2006).

36. Page, M. G. & Cölfen, H. Improved Control of $CaCO_3$ Precipitation by Direct Carbon Dioxide Diffusion: Application in Mesocrystal Assembly. *Crystal Growth & Design* **6,** 1915–1920 (2006).
37. Wang, T., Antonietti, M. & Cölfen, H. Calcite mesocrystals: ”morphing” crystals by a polyelectrolyte. *Chemistry (Weinheim, Germany)* **12,** 5722–30 (2006).
38. Zhan, J., Lin, H.-P. & Mou, C.-Y. Biomimetic Formation of Porous Single-Crystalline $CaCO_3$ via Nanocrystal Aggregation. *Advanced Materials* **15,** 621–623 (2003).
39. Olaf Grassman, Neder, R. B., *et al.* Biomimetic control of crystal assembly by growth in an organic hydrogel network. *American Mineralogist* **88,** 647–652 (2003).
40. Grassmann, O. & Löbmann, P. Biomimetic nucleation and growth of $CaCO_3$ in hydrogels incorporating carboxylate groups. *Biomaterials* **25,** 277–282 (2004).
41. Grassmann, O., Müller, G. & Löbmann, P. OrganicInorganic Hybrid Structure of Calcite Crystalline Assemblies Grown in a Gelatin Hydrogel Matrix: Relevance to Biomineralization. *Chemistry of Materials* **14,** 4530–4535 (2002).
42. Wang, T., Cölfen, H. & Antonietti, M. Nonclassical crystallization: mesocrystals and morphology change of $CaCO_3$ crystals in the presence of a polyelectrolyte additive. *Journal of the American Chemical Society* **127,** 3246–7 (2005).
43. Grassmann, O. & Löbmann, P. Morphogenetic control of calcite crystal growth in sulfonic acid based hydrogels. *Chemistry (Weinheim, Germany)* **9,** 1310–6 (2003).
44. Pujol, O., Bowen, P., *et al.* Growth and Self-assembly of Nanostructured CoC_2O_4 $2H_2O$ Particles. *The Journal of Physical Chemistry B* **108,** 13128–13136 (2004).
45. Shevchenko, E. V., Talapin, D. V., *et al.* Colloidal synthesis and self-assembly of $CoPt_3$ nanocrystals. *Journal of the American Chemical Society* **124,** 11480–5 (2002).

46. Wohlrab, S., Pinna, N., *et al.* Polymer-induced alignment of DL-alanine nanocrystals to crystalline mesostructures. *Chemistry (Weinheim, Germany)* **11,** 2903–13 (2005).

47. Zhou, L. & O'Brien, P. Mesocrystals - Properties and Applications. *The Journal of Physical Chemistry Letters* **3,** 620–628 (2012).

48. Banfield, J. F. Aggregation-Based Crystal Growth and Microstructure Development in Natural Iron Oxyhydroxide Biomineralization Products. *Science* **289,** 751–754 (2000).

49. Penn, R. L. Imperfect Oriented Attachment: Dislocation Generation in Defect-Free Nanocrystals. *Science* **281,** 969–971 (1998).

50. Penn, R. & Banfield, J. F. Morphology development and crystal growth in nanocrystalline aggregates under hydrothermal conditions: insights from titania. *Geochimica et Cosmochimica Acta* **63,** 1549–1557 (1999).

51. Lee, E. J. H., Ribeiro, C., *et al.* Oriented attachment: an effective mechanism in the formation of anisotropic nanocrystals. *The journal of physical chemistry. B* **109,** 20842–6 (2005).

52. Leite, E. R., Giraldi, T. R., *et al.* Crystal growth in colloidal tin oxide nanocrystals induced by coalescence at room temperature. *Applied Physics Letters* **83,** 1566 (2003).

53. Polleux, J., Pinna, N., *et al.* Ligand functionality as a versatile tool to control the assembly behavior of preformed titania nanocrystals. *Chemistry (Weinheim, Germany)* **11,** 3541–51 (2005).

54. Ribeiro, C., Lee, E. J. H., *et al.* A kinetic model to describe nanocrystal growth by the oriented attachment mechanism. *Chemphyschem : a European journal of chemical physics and physical chemistry* **6,** 690–6 (2005).

55. Penn, R. L. Kinetics of Oriented Aggregation. *The Journal of Physical Chemistry B* **108,** 12707–12712 (2004).

56. Zhang, J., Huang, F. & Lin, Z. Progress of nanocrystalline growth kinetics based on oriented attachment. *Nanoscale* **2,** 18–34 (2010).

57. Yang, H. G. & Zeng, H. C. Self-Construction of Hollow SnO_2 Octahedra Based on Two-Dimensional Aggregation of Nanocrystallites. *Angewandte Chemie* **116,** 6056–6059 (2004).

58. Zeng, H. C. Synthetic architecture of interior space for inorganic nanostructures. *Journal of Materials Chemistry* **16,** 649 (2006).

59. Zhang, J., Lin, Z., *et al.* A multistep oriented attachment kinetics: coarsening of ZnS nanoparticle in concentrated NaOH. *Journal of the American Chemical Society* **128,** 12981–7 (2006).

60. Yuwono, V. & Burrows, N. Oriented aggregation: formation and transformation of mesocrystal intermediates revealed. *Journal of the American Chemical Society* **132,** 2163–5 (2010).

61. John A. Venables. *Introduction to Surface and Thin Film Processes* (Cambridge University Press, 2000).

62. Kudera, S., Carbone, L., *et al.* Selective growth of PbSe on one or both tips of colloidal semiconductor nanorods. *Nano letters* **5,** 445–9 (2005).

63. Chernov, A. Stability of faceted shapes. *Journal of Crystal Growth* **24-25,** 11–31 (1974).

64. Cho, K.-S., Talapin, D. V., *et al.* Designing PbSe nanowires and nanorings through oriented attachment of nanoparticles. *Journal of the American Chemical Society* **127,** 7140–7 (2005).

65. Tang, Z., Kotov, N. A. & Giersig, M. Spontaneous organization of single CdTe nanoparticles into luminescent nanowires. *Science (New York, N.Y.)* **297,** 237–40 (2002).

66. Halder, A. & Ravishankar, N. Ultrafine Single-Crystalline Gold Nanowire Arrays by Oriented Attachment. *Advanced Materials* **19,** 1854–1858 (2007).

67. Cölfen, H. & Antonietti, M. Mesocrystals: inorganic superstructures made by highly parallel crystallization and controlled alignment. *Angewandte Chemie (International ed.)* **44,** 5576–91 (2005).

68. Soukoulis, C. M. Photonic band gap materials: the ”semiconductors” of the future? *Physica Scripta* **T66,** 146–150 (1996).

69. Murray, C., Kagan, C. & Bawendi, M. Self-organization of CdSe nanocrystallites into three-dimensional quantum dot superlattices. *Science* **270,** 1335–1338 (1995).

70. Hsu, W., Ronnquist, L. & Matijevic, E. Preparation and properties of monodispersed colloidal particles of lanthanide compounds. 2. Cerium (IV). *Langmuir* **17,** 31–37 (1988).

71. Lee, S.-H., Her, Y.-S. & Matijević, E. Preparation and Growth Mechanism of Uniform Colloidal Copper Oxide by the Controlled Double-Jet Precipitation. *Journal of Colloid and Interface Science* **186,** 193–202 (1997).

72. Zhang, Z., Sun, H., *et al.* Three-Dimensionally Oriented Aggregation of a Few Hundred Nanoparticles into Monocrystalline Architectures. *Advanced Materials* **17,** 42–47 (2005).

73. Ball, M. & Taylor, H. The dehydration of brucite. *Mineralogical Magazine,* 754–766 (1961).

74. Thangaraj, N., Westmacott, K. & Dahmen, U. HVEM studies of the sintering of MgO nanocrystals prepared by $Mg(OH)_2$ decomposition. *Ultramicroscopy* **37,** 362–374 (1991).

75. Bernal, J., Dasgupta, D. & Mackay, A. Oriented transformations in iron oxides and hydroxides. *Nature* (1957).

76. Bärnighausen, H. LiEu3O4 Eine neue, mit $LiSr_2EuO_4$ isotype Europium (II, III)-verbindung. *Zeitschrift für anorganische und allgemeine Chemie* **349,** 280–288 (1967).

77. Bärnighausen, H. Die Kristallstruktur von $LiEu_3O_4$. *Zeitschrift für anorganische und allgemeine Chemie* **374,** 201–224 (1970).

78. Dominguez Bella, S. & Garcia-Ruiz, J. Textures in induced morphology crystal aggregates of $CaCO_3$: Sheaf of wheat morphologies. *Journal of Crystal Growth* **79,** 236–240 (1986).

79. Collier, C. P., Vossmeyer, T & Heath, J. R. Nanocrystal superlattices. *Annual review of physical chemistry* **49,** 371–404 (1998).

80. Schliehe, C., Juarez, B. H., *et al.* Ultrathin PbS sheets by two-dimensional oriented attachment. *Science (New York, N.Y.)* **329,** 550–3 (2010).

81. Wang, Z., Schliehe, C., *et al.* Correlating superlattice polymorphs to internanoparticle distance, packing density, and surface lattice in assemblies of PbS nanoparticles. *Nano letters* **13,** 1303–11 (2013).

82. Talapin, D. V., Shevchenko, E. V., *et al.* Quasicrystalline order in self-assembled binary nanoparticle superlattices. *Nature* **461,** 964–7 (2009).

83. Urban, J. J., Talapin, D. V., *et al.* Self-assembly of PbTe quantum dots into nanocrystal superlattices and glassy films. *Journal of the American Chemical Society* **128,** 3248–55 (2006).

84. Stoeva, S. I., Prasad, B. L. V., *et al.* Face-Centered Cubic and Hexagonal Closed-Packed Nanocrystal Superlattices of Gold Nanoparticles Prepared by Different Methods. *The Journal of Physical Chemistry B* **107,** 7441–7448 (2003).

85. Andres, R. P., Bielefeld, J. D., *et al.* Self-Assembly of a Two-Dimensional Superlattice of Molecularly Linked Metal Clusters. *Science* **273,** 1690–1693 (1996).

86. Kniep, R. & Busch, S. Biomimetic Growth and Self-Assembly of Fluorapatite Aggregates by Diffusion into Denatured Collagen Matrices. *Angewandte Chemie International ed.* **35,** 2624–2626 (1996).

87. Busch, S., Dolhaine, H., *et al.* Biomimetic Morphogenesis of Fluorapatite-Gelatin Composites: Fractal Growth, the Question of Intrinsic Electric Fields, Core/Shell Assemblies, Hollow Spheres and Reorganization of Denatured Collagen. *European Journal of Inorganic Chemistry* **1999,** 1643–1653 (1999).

88. Busch, S., Schwarz, U. & Kniep, R. Morphogenesis and Structure of Human Teeth in Relation to Biomimetically Grown FluorapatiteGelatine Composites. *Chemistry of Materials* **13,** 3260–3271 (2001).

89. Busch, S., Schwarz, U. & Kniep, R. Chemical and Structural Investigations of Biomimetically Grown Fluorapatite-Gelatin Composite Aggregates. *Advanced Functional Materials* **13,** 189–198 (2003).

90. Simon, P., Schwarz, U. & Kniep, R. Hierarchical architecture and real structure in a biomimetic nano-composite of fluorapatite with gelatine: a model system for steps in dentino- and osteogenesis? *Journal of Materials Chemistry* **15,** 4992 (2005).

91. Kniep, R. & Simon, P. Fluorapatite-Gelatine-Nanocomposites: Self-Organized Morphogenesis, Real Structure and Relations to Natural Hard Materials. *Biomineralization I,* 73–125 (2007).

92. Putnis, A., Prieto, M. & Fernandez-Diaz, L. Fluid supersaturation and crystallization in porous media. *Geological Magazine* **132,** 1 (2009).

93. Bodnarchuk, M. I., Li, L., *et al.* Three-dimensional nanocrystal superlattices grown in nanoliter microfluidic plugs. *Journal of the American Chemical Society* **133,** 8956–60 (2011).

94. Zheng, N., Fan, J. & Stucky, G. D. One-step one-phase synthesis of monodisperse noble-metallic nanoparticles and their colloidal crystals. *Journal of the American Chemical Society* **128,** 6550–1 (2006).

95. Courty, A. Silver Nanocrystals: Self-Organization and Collective Properties. *The Journal of Physical Chemistry C* **114,** 3719–3731 (2010).

96. Bodnarchuk, M. I., Kovalenko, M. V., *et al.* Energetic and entropic contributions to self-assembly of binary nanocrystal superlattices: temperature as the structure-directing factor. *Journal of the American Chemical Society* **132,** 11967–77 (2010).

97. Evers, W. H., De Nijs, B., *et al.* Entropy-driven formation of binary semiconductor-nanocrystal superlattices. *Nano letters* **10,** 4235–41 (2010).

98. Overgaag, K., Evers, W., *et al.* Binary superlattices of PbSe and CdSe nanocrystals. *Journal of the American Chemical Society* **130,** 7833–5 (2008).

99. Talapin, D. V., Shevchenko, E. V., *et al.* Dipole-dipole interactions in nanoparticle superlattices. *Nano letters* **7,** 1213–9 (2007).

100. Liao, C.-W., Lin, Y.-S., *et al.* Formation of diverse supercrystals from self-assembly of a variety of polyhedral gold nanocrystals. *Journal of the American Chemical Society* **135,** 2684–93 (2013).

101. Goubet, N, Richardi, J, *et al.* How to Predict the Growth Mechanism of Supracrystals from Gold Nanocrystals. *The Journal of Physical Chemistry Letters* **2,** 417–422 (2011).

102. Goubet, N., Portalès, H., *et al.* Simultaneous growths of gold colloidal crystals. *Journal of the American Chemical Society* **134,** 3714–9 (2012).

103. Kalsin, A. M., Fialkowski, M., *et al.* Electrostatic self-assembly of binary nanoparticle crystals with a diamond-like lattice. *Science (New York, N.Y.)* **312,** 420–4 (2006).

104. Kowalczyk, B., Kalsin, A. M., *et al.* Size selection during crystallization of oppositely charged nanoparticles. *Chemistry (Weinheim, Germany)* **15,** 2032–5 (2009).

105. Kowalczyk, B., Walker, D. A., *et al.* Nanoparticle supracrystals and layered supracrystals as chemical amplifiers. *Angewandte Chemie (International ed.)* **49,** 5737–41 (2010).

106. Bishop, K. J. M. & Grzybowski, B. "Nanoions": fundamental properties and analytical applications of charged nanoparticles. *Chemphyschem : a European journal of chemical physics and physical chemistry* **8,** 2171–6 (2007).

107. Orlik, R., Mitus, A., *et al.* Computer simulation of self-assembly (crystallization) of oppositely charged nanoparticles with various size distributions. *Journal of Non-Crystalline Solids* **355,** 1360–1369 (2009).

108. Bishop, K. J. M., Wilmer, C. E., *et al.* Nanoscale forces and their uses in self-assembly. *Small (Weinheim, Germany)* **5,** 1600–30 (2009).

109. Oaki, Y, Kotachi, A, *et al.* Bridged Nanocrystals in Biominerals and Their Biomimetics: Classical Yet Modern Crystal Growth on the Nanoscale. *Advanced Functional Materials* **16,** 1633–1639 (2006).

110. Miura, T., Kotachi, A., *et al.* Emergence of Acute Morphologies Consisting of Iso-Oriented Calcite Nanobricks in a Binary Poly(Acrylic Acid) System. *Crystal Growth & Design* **6,** 612–615 (2006).

111. Oaki, Y. & Imai, H. Nanoengineering in echinoderms: the emergence of morphology from nanobricks. *Small (Weinheim, Germany)* **2,** 66–70 (2006).

112. Harfenist, S. A., Wang, Z. L., *et al.* Highly Oriented Molecular Ag Nanocrystal Arrays. *The Journal of Physical Chemistry* **100,** 13904–13910 (1996).

113. Hill Terrell, L. *Statistical mechanics / principles and selected applications* 432 (New York : McGraw-Hill, 1956).

114. Goubet, N., Richardi, J., *et al.* Which Forces Control Supracrystal Nucleation in Organic Media? *Advanced Functional Materials* **21,** 2693–2704 (2011).

115. Ryan, K. M., Mastroianni, A., *et al.* Electric-field-assisted assembly of perpendicularly oriented nanorod superlattices. *Nano letters* **6,** 1479–82 (2006).

116. Smith, P. A., Nordquist, C. D., *et al.* Electric-field assisted assembly and alignment of metallic nanowires. *Applied Physics Letters* **77,** 1399 (2000).

117. Van der Zande, B. M. I., Koper, G. J. M. & Lekkerkerker, H. N. W. Alignment of Rod-Shaped Gold Particles by Electric Fields. *The Journal of Physical Chemistry B* **103,** 5754–5760 (1999).

118. Tanase, M., Silevitch, D. M., *et al.* Magnetic trapping and self-assembly of multicomponent nanowires. *Journal of Applied Physics* **91,** 8549 (2002).

119. Tanase, M., Felton, E. J., *et al.* Assembly of multicellular constructs and microarrays of cells using magnetic nanowires. *Lab on a chip* **5,** 598–605 (2005).

120. Tripp, S. L., Pusztay, S. V., *et al.* Self-Assembly of Cobalt Nanoparticle Rings. *Journal of the American Chemical Society* **124,** 7914–7915 (2002).

121. Tripp, S. L., Dunin-Borkowski, R. E. & Wei, A. Flux closure in self-assembled cobalt nanoparticle rings. *Angewandte Chemie (International ed.)* **42,** 5591–3 (2003).

122. Wiedwald, U., Spasova, M., *et al.* Ferromagnetic resonance of monodisperse Co particles. *Journal of Vacuum Science & Technology A: Vacuum, Surfaces, and Films* **19,** 1773 (2001).

123. Lalatonne, Y, Richardi, J & Pileni, M.-P. Van der Waals versus dipolar forces controlling mesoscopic organizations of magnetic nanocrystals. *Nature materials* **3,** 121–5 (2004).

124. Pileni, M.-P. Nanocrystal Self-Assemblies: Fabrication and Collective Properties. *The Journal of Physical Chemistry B* **105,** 3358–3371 (2001).

125. Sun, S. & Murray, C. B. Synthesis of monodisperse cobalt nanocrystals and their assembly into magnetic superlattices. *Journal of Applied Physics* **85,** 4325 (1999).

126. Alivisatos, A. P., Johnsson, K. P., *et al.* Organization of 'nanocrystal molecules' using DNA. *Nature* **382,** 609–11 (1996).

127. Yan, H., Park, S. H., *et al.* DNA-templated self-assembly of protein arrays and highly conductive nanowires. *Science (New York, N.Y.)* **301,** 1882–4 (2003).

128. Braun, E, Eichen, Y, *et al.* DNA-templated assembly and electrode attachment of a conducting silver wire. *Nature* **391,** 775–8 (1998).

129. Mirkin, C. A., Letsinger, R. L., *et al.* A DNA-based method for rationally assembling nanoparticles into macroscopic materials. *Nature* **382,** 607–9 (1996).

130. Steiner, T. The hydrogen bond in the solid state. *Angewandte Chemie International ed.* (2002).

131. Born, P., Murray, E. & Kraus, T. Temperature-induced particle self-assembly. *Journal of Physics and Chemistry of Solids* **71,** 95–99 (2010).

132. Currie, E., Norde, W & Cohen Stuart, M. Tethered polymer chains: surface chemistry and their impact on colloidal and surface properties. *Advances in Colloid and Interface Science* **100-102,** 205–265 (2003).

133. Milner, S. Polymer brushes. *Science* **251,** 905–914 (1991).

134. Oosawa, F. On Interaction between Two Bodies Immersed in a Solution of Macromolecules. *The Journal of Chemical Physics* **22,** 1255 (1954).

135. Baranov, D., Fiore, A., *et al.* Assembly of colloidal semiconductor nanorods in solution by depletion attraction. *Nano letters* **10,** 743–9 (2010).

136. Goubet, N & Pileni, M.-P. Analogy Between Atoms in a Nanocrystal and Nanocrystals in a Supracrystal: Is It Real or Just a Highly Probable Speculation? *The Journal of Physical Chemistry Letters* **2,** 1024–1031 (2011).

137. Quan, Z. & Fang, J. Superlattices with non-spherical building blocks. *Nano Today* **5,** 390–411 (2010).

138. Choi, J. J., Bealing, C. R., *et al.* Controlling nanocrystal superlattice symmetry and shape-anisotropic interactions through variable ligand surface coverage. *Journal of the American Chemical Society* **133,** 3131–8 (2011).

139. Bian, K., Choi, J. J., *et al.* Shape-anisotropy driven symmetry transformations in nanocrystal superlattice polymorphs. *ACS nano* **5,** 2815–23 (2011).

140. Goodfellow, B. W. & Korgel, B. a. Reversible solvent vapor-mediated phase changes in nanocrystal superlattices. *ACS nano* **5,** 2419–24 (2011).

141. Zheng, R., Gu, H., *et al.* Self-Assembly and Self-Orientation of Truncated Octahedral Magnetite Nanocrystals. *Advanced Materials* **18,** 2418–2421 (2006).

142. Glotzer, S. C. & Solomon, M. J. Anisotropy of building blocks and their assembly into complex structures. *Nature materials* **6,** 557–62 (2007).

143. Korgel, B. a., Fullam, S., *et al.* Assembly and Self-Organization of Silver Nanocrystal Superlattices: Ordered Soft Spheres? *The Journal of Physical Chemistry B* **102,** 8379–8388 (1998).

144. Whetten, R. L., Shafigullin, M. N., *et al.* Crystal Structures of Molecular Gold Nanocrystal Arrays. *Accounts of Chemical Research* **32,** 397–406 (1999).

145. Agarwal, U. & Escobedo, F. a. Mesophase behaviour of polyhedral particles. *Nature materials* **10,** 230–5 (2011).

146. Zhou, L. & O'Brien, P. Mesocrystals: a new class of solid materials. *Small (Weinheim, Germany)* **4,** 1566–74 (2008).

147. Yao, K. X. & Zeng, H. C. Architectural Processes and Physicochemical Properties of CoO/ZnO and $Zn_{1-x}Co_xO/Co_{1-y}Zn_yO$ Nanocomposites. *The Journal of Physical Chemistry C* **113,** 1373–1385 (2009).

148. Tartaj, P. Sub-100 nm TiO_2 mesocrystalline assemblies with mesopores: preparation, characterization, enzyme immobilization and photocatalytic properties. *Chemical communications* **47,** 256–8 (2011).

149. Zhang, D., Li, G., *et al.* Green synthesis of a self-assembled rutile mesocrystalline photocatalyst. *CrystEngComm* **12,** 1759 (2010).

150. Wang, D., Li, J., *et al.* Hexagonal mesocrystals formed by ultra-thin tungsten oxide nanowires and their electrochemical behaviour. *Chemical communications* **46,** 7718–20 (2010).

151. Zhu, Z., Meng, H., *et al.* Superstructures and SERS properties of gold nanocrystals with different shapes. *Angewandte Chemie (International ed.)* **50,** 1593–6 (2011).

152. Fendler, J. H. in *Nanocrystals Forming Mesoscopic Structures* 279–293 (Wiley-VCH Verlag GmbH & Co. KGaA, Weinheim, 2005).

153. Brioude, A., Courty, A. & Pileni, M.-P. in *Nanocrystals Forming Mesoscopic Structures* 213–229 (Wiley-VCH Verlag GmbH & Co. KGaA, Weinheim, 2005).

154. Petit, C., Motte, L., *et al.* in *Nanocrystals Forming Mesoscopic Structures* 251–278 (Wiley-VCH Verlag GmbH & Co. KGaA, Weinheim, 2005).

155. Chantrell, R., Walmsley, N., *et al.* Calculations of the susceptibility of interacting superparamagnetic particles. *Physical Review B* **63,** 024410 (2000).

156. Song, R.-Q. & Cölfen, H. Mesocrystals-ordered nanoparticle superstructures. *Advanced Materials* **22,** 1301–30 (2010).

157. Ge, J., Hu, Y., *et al.* Superparamagnetic magnetite colloidal nanocrystal clusters. *Angewandte Chemie* **46,** 4342–5 (2007).

158. Yang, P., Arfaoui, I., *et al.* Unexpected electronic properties of micrometer-thick supracrystals of Au nanocrystals. *Nano letters* **12,** 2051–5 (2012).

159. Hanrath, T. Colloidal nanocrystal quantum dot assemblies as artificial solids. *Journal of Vacuum Science & Technology A: Vacuum, Surfaces, and Films* **30,** 030802 (2012).

160. Tam, E., Podsiadlo, P., *et al.* Mechanical properties of face-centered cubic supercrystals of nanocrystals. *Nano letters* **10,** 2363–7 (2010).

161. Podsiadlo, P., Lee, B., *et al.* High-pressure structural stability and elasticity of supercrystals self-assembled from nanocrystals. *Nano letters* **11,** 579–88 (2011).

162. Yan, C., Arfaoui, I., *et al.* Soft Supracrystals of Au Nanocrystals with Tunable Mechanical Properties. *Advanced Functional Materials* **23,** 2315–2321 (2013).

3. Nanoparticular Building Blocks

The mesocrystal building blocks and their synthesis are focused upon in this chapter. Thereby, the synthesis and the optimisation methods for the production of highly monodisperse, quasi-spherical nanoparticles in the size range of 2-15 nm are presented. Semiconductor, metal and core-shell nanoparticles are prepared as nanoparticular building units and are favoured as they can achieve the criteria of high monodispersity by their syntheses in organic media. In some cases the optimisation procedure and the influence of parameters such as the injection temperature, reaction duration and the reactivity of the precursor molecules are regarded. An important point for later self-assembly is the surface modification of the single nanoparticles and their coating ligands as during the formation process of mesocrystalline materials the special properties which derive from materials at the nanodimension should be maintained in the macroscopic structure, with the implication that the nanoparticles have to be protected against fusion during the self-assembly procedure. Hence, Fourier transform infrared spectroscopy is used for the characterisation of surface ligands. Additionally, thermogravimetric analysis coupled with mass spectroscopy is implemented to gain information concerning the stability of the nanoparticles. Moreover, spectroscopic measurements are undertaken and (HR)TEM measurements are carried out in order to characterise the optical properties and the habitus of the nanoparticles and their ability to form two dimensional ordered arrangements.

3.1. Preface

Based on the continuing trend towards device miniaturisation in industry, it is indispensable for scientists to improve and develop strategies to successfully deliver materials, which can achieve this aim. The synthesis of colloidal nanoparticles especially represents one field where a wide variety of materials with low size distribution, high crystallinity and optimised optical properties can be reproducibly manufactured.[1,2]

Therefore, two main approaches exist; the top-down and the bottom-up strategies. In the conventional semiconductor technology and microfabrication industry the production of new nanodimensional materials is done by size reduction of bulk material. The typically "top-down" approach for microelectronics is based on highly clean surfaces and bulk materials with homogeneous properties and mostly continuous crystal structure, which increases the cost for the initial bulk materials. Additionally, the patterning of these bulk materials can only be done stepwise and in two dimensions where which every step combines many individual operations. This concept is problematic during the production of complex structured monodisperse materials because the process runs stepwise and high standards of cleanness have to be guaranteed over the whole production period.[3] The "top-down" approach of synthesizing small nanoparticles is based on physical methods such as milling and grinding. The disadvantages of this approach are the broad size distribution of the synthesised nanoparticles and the low size and shape control. Nevertheless, a big advantage of these methods are the large quantities which can be produced.[4,5]

The "bottom-up" approach can be regarded as a self-assembling process of small molecules, atoms or ions, which interact with each other and form agglomerates or are deposited in defined structures. Therefore, techniques for organic and inorganic synthesis are used. Common techniques are gas phase synthesis[6] and wet chemical processes[7–11], in which the properties of the produced nanoparticles can vary, which is caused by differences in crystallinity and surface modifications, despite using the same materials. Especially for these methods a small size distribution, suppression of agglomeration and controlled surface modification are possible and are big advantages. Gas phase syntheses are continuous processes with relatively high reaction temperatures so that crystalline nanoparticles with bare surfaces occur. The high temperatures sometimes tend to towards agglomeration of the nanoparticles and cause a broad size distribution. The reactions are normally thermodynamically driven so that it is difficult to synthesise metastable nanoparticles with special morphologies.

For that purpose, the wet chemical processes are more favourable because they are kinetically driven. With the principle of LaMer and the knowledge about critical nucleus formation, the size distribution and the particle formation can be easily varied by changing the reaction conditions.[12] Presently, a high oversaturation induces nucleus formation within a short time window and after this period of time the nucleus formation is inhibited caused by too low reactant concentrations. The resulting metastable nuclei are capped with functionalised organic molecules, which stabilise the nanoparticles in solution and prevent particle agglomeration. The nanoparticle surface can be covered with hydrophobic organic monolayers[13,14] that sterically hinder the agglomeration or the nanoparticles are charge separated by using positively or negatively charged organic monolayers as ligands[15–17]. Additionally, polymers or biological molecules like proteins can be directly bound on the nanoparticle surface to make them stable in special environments like the human body[18–22]. The surface substantially determines the chemical reactivity and the solubility of the nanoparticles in solution[23]. In general, the nanoparticles inherit the same solubility behaviour as imposed by the solution exposed ligand. In addition, the immobilisation of the ligands can result in new properties that the ligands did not show before and so the ligands can directly influence the reactivity and stability of the nanoparticles. To introduce new functional groups or surface properties it is in most cases possible and necessary for later applications[23] to exchange ligands without changing the core properties.

The properties of the inorganic core make the nanomaterials unique because of the presence of the quantum-size effect and it is this that explains the altered properties from those of the bulk materials after size reduction. In this context, semiconductor nanoparticles belong to a class of increasingly interesting materials as their optical and electronic properties are size dependent[24,25]. This results in larger band gaps once the nanoparticle has reached that of the Bohr radius of the material as the electron-hole pair is restricted in their spatial dimensions leading to energy quantisation. The relationship of nanoparticle size and bandgap energy is described for semiconductor nanoparticles in the Brus-equation[26].

Noble metal nanoparticles also show size dependent electronic behaviour which influences the plasmon resonance and thereby the optical properties.[27] The plasmon resonance frequency is affected by the nanoparticle material, its electron density and also by the surrounding media. Hence a change in the ligand shell or solvent can shift the plasmon resonance to different values depending on the dielectric constant of the surrounding media.[28] In 1908 Mie calculated the surface plasmon resonance for the first time by solving the Maxwell equations for small spherical particles which interact with an electromagnetic field.[29] However, this model only describes spherical metal nanoparticles but for particles with different morphologies, anisotropic effects were observed.[30] While the changing optical properties of metal nanoparticles are interesting, nowadays the high surface areas of the metallic nanoparticles, which are important for catalytic applications[31], also receive a great deal of attention, particularly, nanoparticle arrangements with low surface coverage which are needed to realise high catalytic activity.

Another method to tune the optical and electronic properties of nanomaterials is the synthesis of colloidal core-shell nanoparticles, which contain at least two inorganic materials in an onion-like structure.[32,33] the shell providing a physical barrier that acts as passivation layer to make the core less sensitive for the surrounding media. In addition, the shell can enhance the quantum yield, tune the lifetime of semiconductor nanoparticles and influence their optical properties. Semiconductor core-shell materials are well reported and their resulting properties depend on the relative positions of electronic energy levels of the materials involved.[33] Figure 3.1 shows the different configurations, which are possible to form between two different semiconductor materials. The location of the electron-hole pair within the different structures is important in determining the resulting properties. In type I structures the exciton is located in the core, in reversed type I structure it is located in the shell and in type II structures the electron-hole pair is separated into the different core-shell regions. For the case of semiconductor materials, the electronic structure of the core-shell materials are reasonably well known, but the combination of metal and semiconductor materials is somewhat more complex. Additionally, it is challenging to synthesise metal-semiconductor core-shell materials due to the complex synthetic routes that have to be chosen as consequence of the high lattice mismatches in the crystalline structure of metals and semiconductors, so that epitaxial growth is very difficult to realise.[34] Therefore, new synthetic strategies must be developed to produce defined core-shell hybrid structures.

With regard to further applications, the manipulation of single nanoparticles is not easy to implement in such a way that they can be contacted or introduced as functional individual units into devices. Hence, it is currently expected that two

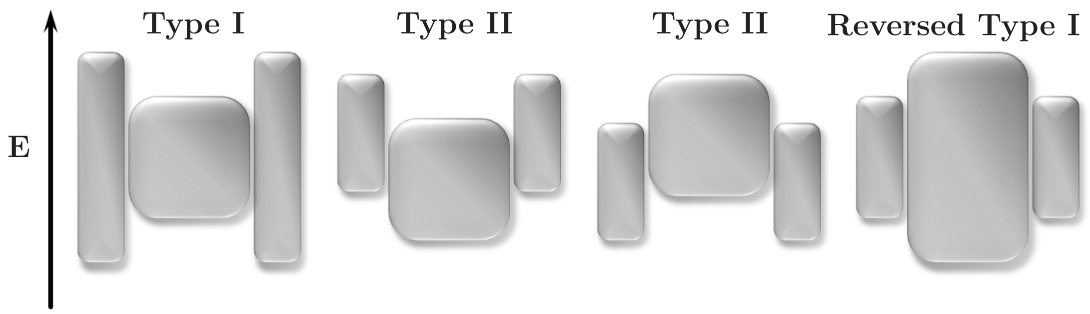

Figure 3.1.: ***Schematic representation of the relative energy-level alignment of the bandgap in different core/shell systems realised with semiconductor NCs.*** *The conduction and valence band edges correspond to the upper and lower edges of the rectangles.*[33]

dimensional and 3D arrangements will most likely be employed for applications if they are to become an essential part of modern nanotechnology.[35] For the arrangement of highly symmetrical 3D mesocrystals, the nanoparticular building blocks have to fulfil special conditions in order to make the implementation of the building units into these ordered crystalline structures possible. For that matter, low size distributions of the as-synthesised nanoparticles have to be achieved and they should be less than 5% to minimise stacking faults and defects in the crystalline structure of the resulting superstructures. Additionally, to control the crystallisation of the nanoparticles, these building blocks have to have a defined surface modification so that later it is possible to control the conditions for self-assembly.

3.2. Semiconductor nanoparticles - PbS and PbSe

Semiconductor nanoparticles belong to a class of increasingly interesting materials because their optical and electronic properties are size dependent.[24,25] The IV-VI semiconductors, in particular lead sulphide and lead selenide nanoparticles, hold much potential, as they possess unique intrinsic properties. In their macroscopic form they crystallise in the rock-salt structure (cubic) and have a narrow direct bandgap of 0.41 to 0.28 eV respectively at 300 K.[36] Due to their relatively high dielectric constants of ϵ_∞ =18.0-24.0 and their low effective hole and electron masses, excitons with relatively large Bohr radii are generated (a_B(PbS) = 20 nm[37], a_B(PbSe) = 46 nm[36]). Particles, with sizes below the Bohr radius, show typical changes in their properties because of the quantum size effect, which is a consequence of the steric restriction of the electron-hole pair. The Brus-equation describes the relationship between the particle size and bandgap energy due to the quantum size effect and using well optimised synthetic routes the bandgap of PbS and PbSe nanoparticles is extendable to reach 1.55 eV (800 nm).[38] Due to their electronic structure the optical properties of the lead chalcogenide materials leads them to absorb and emit in the near-infrared and mid-infrared spectral region. In addition, the fact that they have large exciton radii of about 18 nm or greater allows one to tune their bandgaps at room temperature to between 500-3000 nm.[9,38–40] Therefore, lead chalcogenides have the potential to be employed in a wide range of devices as optically active components and hence could be beneficial in such applications as solar cells, IR lasers and detectors and as fluorophores in the field of telecommunications.[37,41] In addition, lead chalcogenide nanoparticles have been reported to be capable of efficient multiple exciton generation (MEG)[42–44], which makes them especially attractive for photovoltaic applications.

3.2.1. Lead sulphide nanoparticles[*]

Modified syntheses of Nagel *et al.*[37] are the basis for the preparation of monodisperse lead sulphide nanoparticles and for small PbS nanoparticles the synthesis of Hines *et al.*[38,46] has been used. The syntheses described therein provide quantum dots in the size range of 2-14 nm. The yield of the as-synthesised nanoparticles varies strongly and depends heavily on the synthesis method used and on the reaction conditions. The main difference between the production of small and big nanoparticles can be found in the sulfur precursor used. It is helpful in synthesising small nanoparticles to choose highly reactive sulfur sources to achieve a high supersaturation within a short period of time, as outlined by LaMer theory. Consequently, a high concentration of highly reactive nuclei will be formed and thus a fast depletion of the sulfur precursor will be realised and a stagnancy in the growing process of the nuclei will occur resulting in a size limitation of the nanoparticles. Bigger nanoparticles can be easily synthesised by using less reactive sulfur sources, but the sulfur precursor has to decompose thermally at a defined rate, so that supersaturation takes place and only a low amount of nuclei are formed which grow over a longer period of time (minute range) by using the sulfur precursor left and forming highly facetted nanoparticles.

---

[*] Parts of this section have already been published.[45]

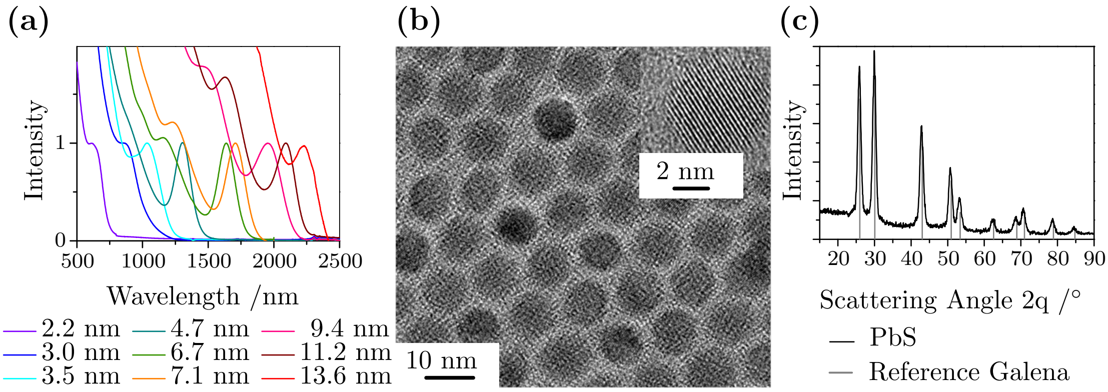

Figure 3.2.: ***Optic, size, shape and crystal structure characterisation of PbS nanoparticles.*** *Absorption spectra of various PbS nanoparticle sizes with their typical and size tuneable band-to-band transitions (a), TEM investigations on single crystalline 8 nm sized quasi-spherical PbS nanoparticles (b) and X-ray powder diffraction analysis of the crystalline structure, which shows same reflexes like bulk PbS (c).*

The evolution of the growing nanoparticle species is shown in Figure 3.2a in the absorption spectra. On the basis of the first absorption maximum the monodispersity of the nanoparticles can be estimated by comparing the broadening of the first maximum. For bigger nanoparticles the second up to the fourth transition is observable. The spectra possess sharp and well-resolved blue shifted transition bands with respect to the bulk material, indicating both the occurrence of the size quantisation effect and the presence of a narrow size distribution. The higher band transitions of small nanoparticles are not observable.

Typically, in the investigations of the formation process of the mesocrystals presented later, the nanoparticle building blocks were chosen to be in the size range of 5-10 nm. As is shown in Figure 3.2b and 3.2c, these nanoparticles have a single crystalline structure analogue to the normal PbS galena configuration having a cubic crystal structure of the Fm$\bar{3}$m space group. Because of their nearly equal size and morphology, the nanoparticles can be easily assembled into two-dimensional layers as it is shown in Figure 3.2b. Using high-resolution TEM (HRTEM) images of single nanoparticles the habitus of the PbS quantum dots was investigated. To separate the nanoparticles for morphology analysis, a colloidal crystal was soaked with epoxide monomer. After partial swelling and consequent diluting of the nanoparticles the epoxide becomes hard. Thin cuts made *via* focused ion beam were prepared and measured using HRTEM as is shown in Figure 3.3 a,e. With fast Fourier transformation (FFT) the crystal facets can be determined

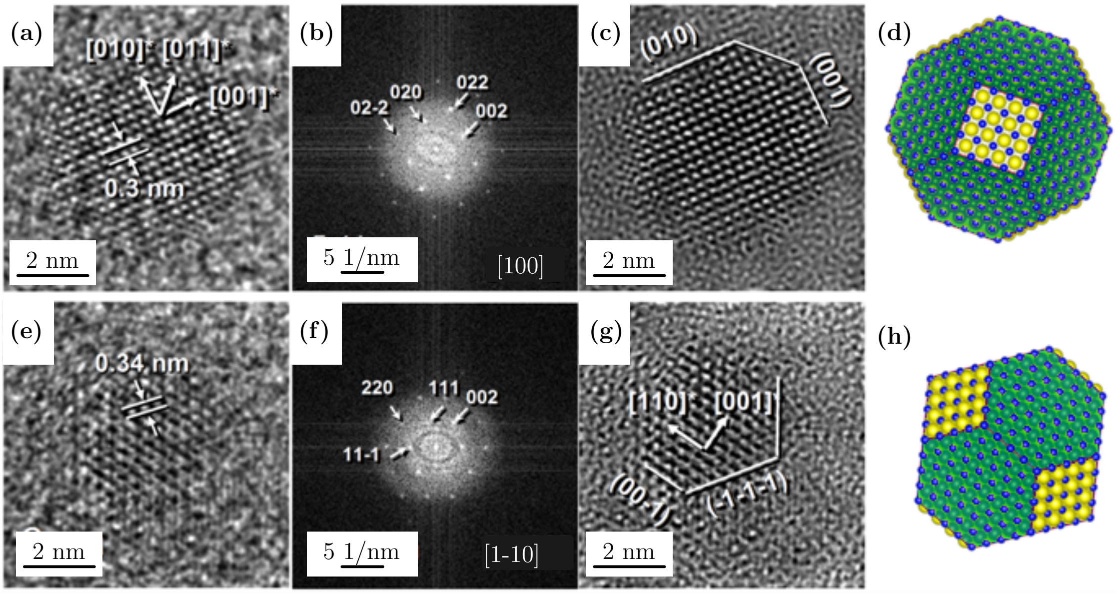

Figure 3.3.: ***HRTEM images of single PbS nanoparticles.*** *The particles are viewed along [100]PbS (a) and [1-10]PbS (e) direction. (b,f) shows the corresponding FFT and (c,g) the filtered images. (d,h) represent the simulated nanoparticular morphology as truncated octahedrons.*[45]

(Figure 3.3 b,f) and this is represented in Figure 3.3 c,g in the filtered image. By combining the two projections the resulting habit of the filtered representations can be approximated to a truncated octahedron. Additionally, the morphology expresses the galena preferred crystal facets {100}, {111} and {110} and in combination with the corresponding FFTs the space group Fm$\bar{3}$m and the unit cell parameter a = 5.936 $\mathring{A}$ can be confirmed.[47]

In order to study the properties of the ligand shell, Fourier transformed IR spectroscopy measurements were done. During preparation of the PbS quantum dots, oleic acid and n-tri-octyl-phosphine (TOP) were used as ligands. The oleic acid forms a highly soluble oleate-complex with the relatively insoluble lead acetate to provide the appropriate lead species as precursor. Additionally, oleic acid acts as a stabilizing ligand during and after synthesis. The role of the TOP is highly complex and not fully understood until now.[48] During synthesis, it influences the morphology of the nanoparticles and stabilises them in solution. Syntheses of bigger nanoparticle sizes without using TOP results in a high polydispersity of the produced nanoparticles and additionally agglomeration during the formation process. In the literature it is reported, that only oleic acid, but not TOP can be found as the surface stabiliser on lead chalcogenides.[49,50] To confirm these assumptions

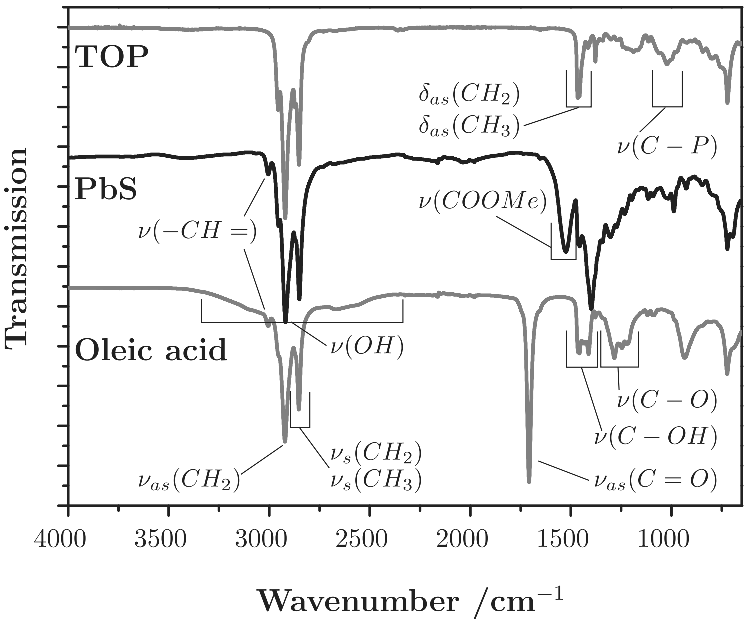

Figure 3.4.: ***FT-IR spectra of the surface ligands and PbS nanoparticles.*** *Oleic acid can be confirmed as a surface ligand in contrast to the n-tri-octyl-phosphine.*

also for the synthesis employed here, FT-IR measurements were carried out. In Figure 3.4 the spectra of TOP, oleic acid and ligand-capped PbS quantum dots are presented. In the region between 2800-3000 cm^{-1} the spectra of all three components look similar because they all contain -CH$_2$ and -CH$_3$ groups which accounts for the stretching vibrations shown there. Additionally, the oleic acid and the PbS nanoparticle spectra have a peak at 3007 cm^{-1}, which belongs to the stretching vibration associated with -CH= groups. The intense peak at 1758 cm^{-1} in the oleic acid spectrum is conspicuous, representing the -C=O vibration. The -C=O vibration could not be observed in the nanoparticle spectra, which is as the result of the absence of oleic acid on the nanoparticle surface or a result of changing inductive effects during binding to the nanoparticle surface. The fingerprint region of the spectra with the -C-P stretching vibrations (1030-1170 cm^{-1}) is less significant, so that a concrete statement about TOP as surface ligand is difficult to make. In the nanoparticle spectra a new peak at 1544 cm^{-1} arises and can be assigned to the resonance frequency of the carboxylic acid salt.[51] As result of a chemical reaction of oleic acid and the nanoparticle surface a bond between the carboxylic group and the lead-ions is possible. The inductive effect, arising from the electron-donating metal-ion, reduces the force constant of the bond, resulting in a lower wavenum-

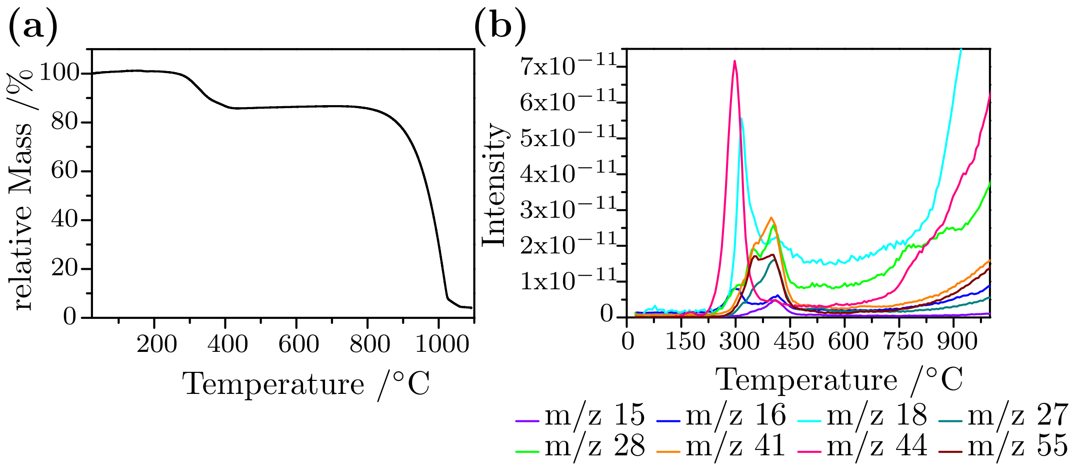

Figure 3.5.: ***TGA-MS measurements of PbS nanoparticles showing two mass losses (a) and the corresponding MS spectra (b).*** *The first mass loss is caused by degradation of ligand molecules and the second one additionally by removing PbS units.*

ber for the absorbance of the carboxylic group. The inductive effects also affect the neighbour -C-OH group, inducing a change in the transmission intensity. The FT-IR spectrum shows explicitly the binding of oleic acid to the particle surface, which supports the literature published results. Moreover, it is reported that PbS nanoparticles are covered with lead-ions as a final monolayer on all of the charged facets, which supports the existence of an oleic acid ligand shell.[52,53] In addition to the FT-IR measurements, P-NMR measurements were performed. These experiments did not show any changes in the nanoparticles, so that TOP on the nanoparticle surface can be excluded.

Thermogravimetric analysis (TGA) was undertaken from 25 to 1000°C in an inert atmosphere using argon. Two mass losses between 200 and 1000°C are observed. In a first step, 18.39% of the total mass leaves the structure between 200°C and 450°C, see Figure 3.5a. With regard to the mass spectroscopy (MS) of the removed molecules, two main fractions can be determined. The first fraction starting at 200°C and present up to 350°C is dominated by M/z peaks of 44 and above 250°C a M/z signature of 18 is observed (Figure 3.5b). There, CO_2^+-species and H_2O^+-molecules are removed, which indicates a residual humidity is present in the structure and also a degree of unbound oleic acid molecules. This may occur because, while the carboxylic group is normally bound to the nanoparticle surface, it may also be arranged such that the head group sticks out from the ligand shell. From 300°C on up to 450°C M/z peaks representing $C_xH_y^+$ and $C_xH_yO_z^+$-species (15, 16, 27, 28, 41 and 55) increase in intensity as result of the degradation along the length of the oleic acid molecules. Higher M/z values only occur with low intensities because the electron bombardment ionisation is conducive to molecule fragmentation. Moreover, M/z values indicative of water and CH_2 groups leaving the structure are also observed at higher temperatures than 450°C. The second main mass loss starts at 750°C with increasing M/z values of 18, 28 and 44, so water and CH_2-groups and additionally CO_2^+ from the bound carboxylic groups are leaving the structure. In total, the mass reduction of the second step is 85.51%, which cannot be realised by ligand molecules alone. The ligand shell left on top of the nanoparticle surface is bound *via* carboxylic group to the Pb-units and stabilises the nanoparticles, but the high temperatures remove the stabilizing ligand shell, so that bare surfaces remain. The lower melting points of nanoparticular units result in melting and additional evaporation of PbS species. The detection of these species is difficult because only positively charged ions can be measured, so sulfur ions are not observable with this measurement setup. Accordingly, the particles are partially stabilised up to 750°C with ligand molecules and so the amount of organic stabilizing material cannot be easily distinguished with TGA.

3.2.2. Lead selenide nanoparticles

Lead selenide nanoparticles were synthesised using a modified preparation technique from Houtepen *et al.*[54] and Brumer *et al.*[36]. Monodisperse PbSe nanoparticles in a size range of 3.3-11.2 nm can be synthesised with quasi-spherical morphology. Size calculations are done by means of the Brus-equation using the first transition maximum of the absorption peak, see Figure 3.6a. Size variation can be achieved by using different solvents and amounts of n-tri-octyl-phosphine, and by variation of the reaction temperature and time. Hence, the nanoparticle concentration and also the yield diversify with every changed parameter. The as-synthesised nanoparticles are monodisperse and single crystalline as for the PbS nanoparticles and also show a truncated octahedron morphology. The crystal lattice is equivalent to the PbSe bulk material and reveals the typical reflexes of clausthalite in the X-ray powder diffraction, see Figure 3.6b and 3.6c.[55]

FT-IR measurements show analogous results to that of PbS nanoparticles so that oleic acid as a stabilizing ligand can be assumed to be present on the nanoparticle surface.

Also the results of TGA-MS analysis are nearly equal to those obtained for the

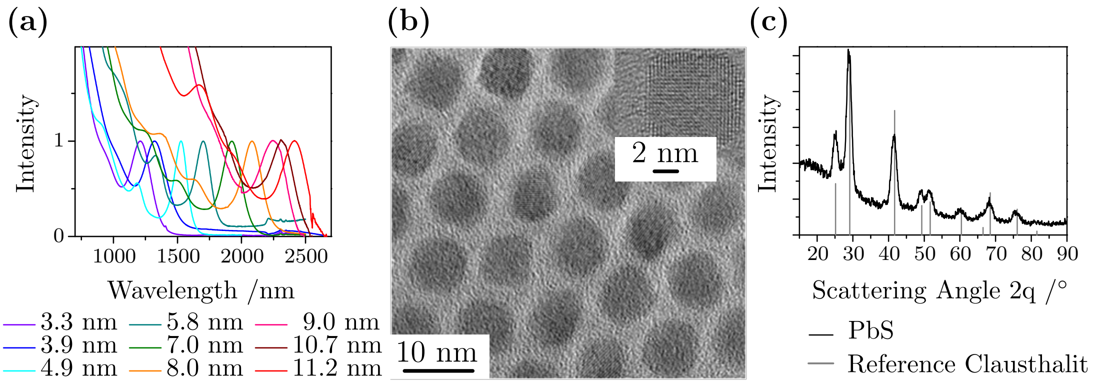

Figure 3.6.: ***Optical, size, shape and crystal structure characterisation of PbSe nanoparticles.*** *Absorption spectra of various PbSe nanoparticle sizes with their typical and size tuneable band transitions (a), TEM investigations on single crystalline 8 nm sized quasi-spherical PbSe nanoparticles (b) and X-ray powder diffraction analysis of the crystalline structure, which shows same reflexes like bulk PbSe (c).*

PbS nanoparticles, see Figure 3.7. Mass loss occurs stepwise in two steps, where the first mass loss is about 18.25% and the second about 70.26%. The water and CO_2^+-species start to evaporate in this case at 250°C. The degradation of the alkyl chain starts at 300°C. From 450-750°C only low amounts of water and parts of the alkyl chain are removed. Above 750°C the parts of oleic acid that were left are removed until the surface of the particle is no longer stable and melting and evaporation of inorganic material takes place.

3.3. Noble metal nanoparticles - Au and Ag

Metal nanoparticles are, from a historical point of view the longest used nanomaterials in spite of the fact that the size of the used materials was not known at that point in time. Already in the late antiquity, glass was coloured using a gold sol which gave them the characteristic red shades such as red-violet, magenta and wine-red of colloidal gold. Thus, gold nanoparticles found applications in the production of coloured glass and also as a painting colour for porcelain at an early stage.[4]

The reasons for the red colour of gold nanoparticles are their plasmonic properties. Not only nanodimensional gold shows this behaviour, but so too do other noble metal materials such as silver, palladium and platinum which can interact with incident electromagnetic radiation of the appropriate wavelength.[56] The electro-

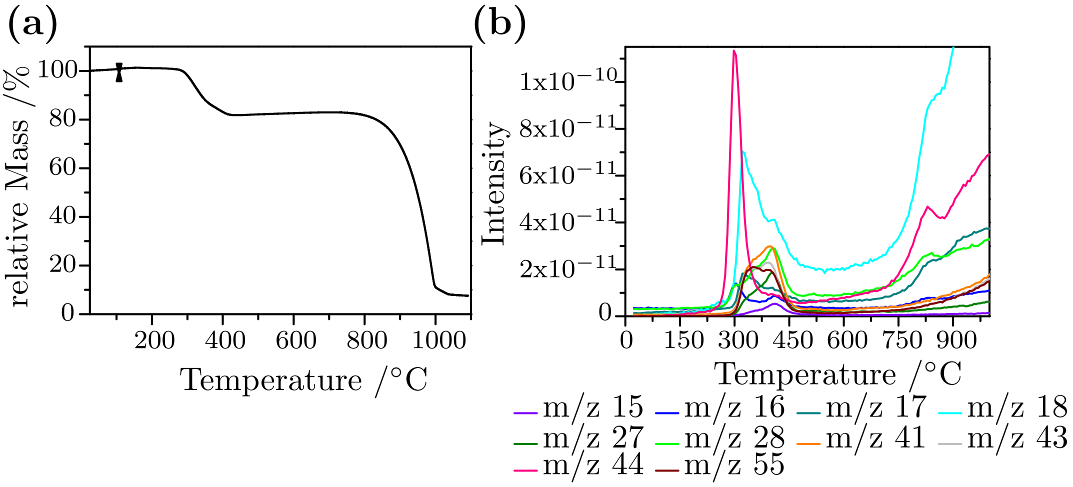

Figure 3.7.: ***TGA-MS measurements of PbSe nanoparticles*** *showing the two areas of mass loss (a) and the corresponding MS spectra of the removed parts over the temperature range.*

magnetic radiation initiates collective vibrations of the electron gas in the particles as it is shown in Figure 3.8.[28] If the resonance frequency of the plasmonic vibrations is in the spectral region of visible light, the particles absorb these wavelengths and as a result the particle solution is coloured. As is described in the introduction of this chapter the plasmon resonance frequency can be influenced by many parameters. It depends on the nanomaterial used as well on the refraction index of the surrounding media, e.g. the ligand shell and also the solvent. The shape influences the plasmonic resonance strongly. So, spherical gold nanoparticles show only one maximum in the absorption spectrum. In elongated structures a second maximum at longer wavelength occurs.[57] In comparison to semiconductor nanoparticles and their quantum confinement, the resonance frequency of the plasmon is less dramatically affected by size.

Besides the changes in the optical properties of noble metal nanoparticles, the thermal properties are also influenced by size. With decreasing radii of the particles the melting point of the materials decreases. As an example, gold nanoparticles with a diameter of 10 nm melt at 1200°C, but particles with 2 nm in diameter have a melting point of 700°C.[58] In contrast to that, their high chemical resistance is not affected, which makes the noble-metal nanoparticles good candidates in medical and biological applications.[59,60] Silver nanoparticles with their antibacterial and antiviral properties are especially well suited for this task. The large surface areas and the high curvature of the particle surface make the atoms more reactive and so

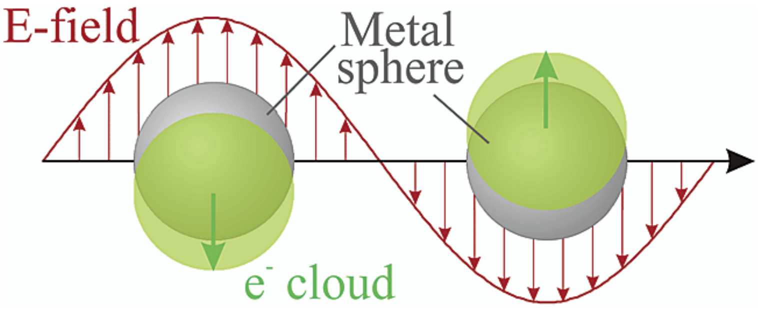

Figure 3.8.: ***Schematic representation of the plasmon resonance.*** *Incoming light with a specific resonance frequency excites the electrons to a coherent surface vibration, the so called plasmon.*[28]

noble-metal nanoparticles may be attractive for catalytic applications.[31] A problem with such systems may arise if they are requited for high temperature reactions because of their reduced melting point. Due to their special optical properties, they are also good candidates for surface enhanced Raman scattering and fluorescence amplification.[61,62] Arranged into 2D or 3D structures and with their high electrical conductivity the noble metal nanoparticles find applications as building units in nanoelectronics and sensor technology.[63]

3.3.1. Gold nanoparticles for organic solvents[†]

The synthesis of gold nanoparticles is achieved using the method of Peng *et al.*[65]. Spherical and monodisperse nanoparticles in the size range of 2.4-9.5 nm can be produced *via* variation of the reaction temperature between 2-40°C and follows a nearly linear trend, see Figure 3.9a. The synthesis is done in organic solvents to minimise size distribution effects in comparison to the aqueous synthesis and the as-synthesised nanoparticles are nearly monodisperse (standard deviation 5%). In addition to the reaction temperature as parameter, the stirring rate also influences the size distribution. As a result of slower mixing of the components during injection, different regions of supersaturation are generated and so the size distribution increases with decreasing stirring rate. In such a case bigger particle sizes are generated and additional network like structures are formed. To exclude influences generated by a changing mixing rate, the reaction parameters for the production of 5 nm sized gold nanoparticles are fixed at a stirring rate of 750 rpm and reaction

---

[†] The results of this chapter were partly obtained within the framework of the bachelor thesis written by M.Sc. Danny Haubold[64] under the mentoring of the author.

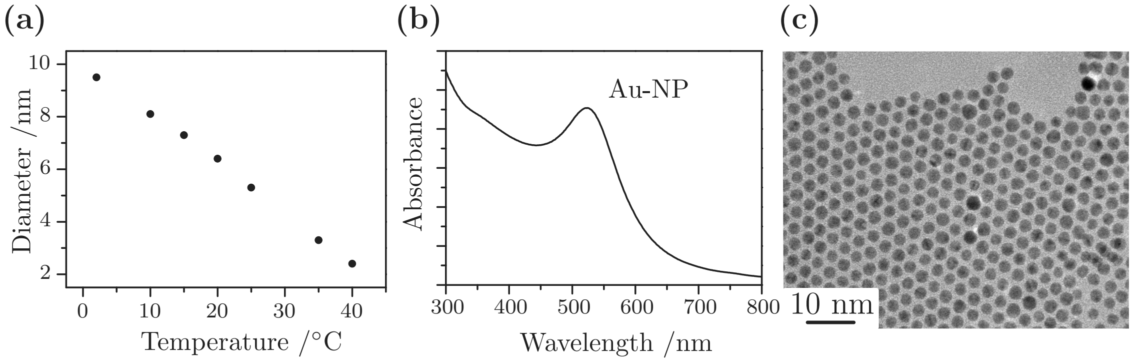

Figure 3.9.: ***Temperature dependent size variation of the diameter during gold nanoparticle synthesis, absorption spectrum of gold NPs and TEM investigations on their morphology.*** *Size determination of the as-synthesised particles could not be achieved with the surface plasmon resonance frequency. Therefore, TEM measurements are necessary and they show the morphology and the twinning of the nanoparticles additionally.*

temperature of 20°C.

The optical properties of the as-synthesised nanoparticles are measured using absorption spectroscopy. The absorption maximum is 520 nm, which correlates well with the dark red coloured nanoparticle solution observed. The precipitated and dried nanoparticles show the typical metallic radiance of the bulk material. As it is shown in Figure 3.9b, the absorption spectrum contains only one maximum as a result of the spherical morphology. In comparison to semiconductor nanoparticles, qualitative information about size and size distribution are not included in the spectra. Furthermore, TEM measurements show well-arranged 2D hexagonal densely packed nanoparticle monolayers with an average particle size of 5 nm (Figure 3.9c). A closer look at the nanoparticle morphology in the HRTEM images show that they exhibit a mostly twinned crystal structure, in Figure 3.10 the gold nanoparticles and their multidomain structure are presented. In literature, defects and twinning effects in gold nanoparticles are well described and it is observed that these structures show a high amount of [111] facets.[65] Baletto *et al.*[66] reported that the [100] facets have a higher surface energy in contrast to the [111] facets of the gold structure so that icosahedral structures are preferentially formed. Single crystalline gold nanoparticles are also observed, but their separation from the nanoparticle solution is not possible. Additionally, in Figure 3.10 the X-ray powder diffraction (XRD) of the gold nanoparticles with their face centred cubic crystal structure is shown. The increased intensity of the [111] facet is caused by

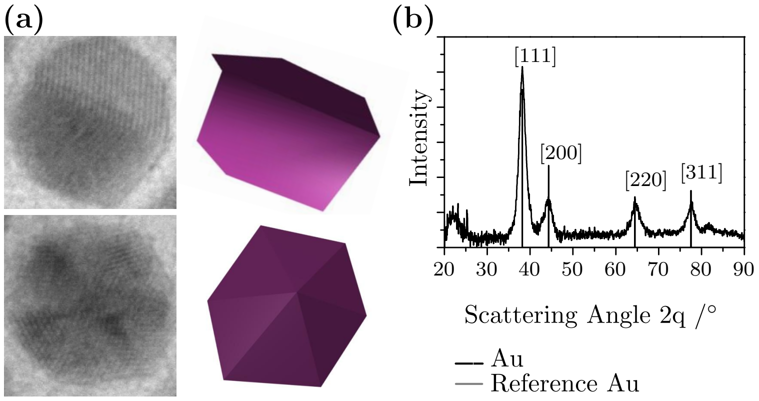

Figure 3.10.: ***Twinned morphologies of gold nanoparticles synthesised using the method of Peng et al.[67] and corresponding XRD measurements of the particles.*** *The [111] facet is pronounced because of the favoured formation of this facet.[55]*

the twinning effects of [100] facets described above.

As oleylamine is used as the surface ligand the amine group should be attached to the particle surface. In Figure 3.11 the FT-IR spectra of the gold nanoparticles and of oleylamine is shown. The -CH_2 and -CH_3 vibrations of both spectra are quite similar, which is not surprising as oleylamine is the only stabiliser molecule used. The peak for the -NH_2 group shows low intensity, so that the binding of this group on the surface of the particle cannot be proven. Oleylamine was chosen as the stabiliser because of its structural similarity to oleic acid, which is used as the ligand for the semiconductor nanoparticles. The thermal behaviour of the stabilizing ligands and that of the gold core were investigated by thermogravimetric measurements, see Figure 3.11. At 175°C, it is expected that similar fragments to those observed in the TGA-MS analysis of the PbS and PbSe nanoparticles, will be detected. This is indeed the case and a 13% mass loss is observed to occur between 175-375°C. The following plateau shows the stability of the gold nanoparticles for the remainder of the ligand shell. Above 800°C a second mass loss takes place, where the remaining parts of the ligand shell are removed from the particles. Simultaneously, the heat flow shows an endothermic process that describes the slow melting of the gold nanoparticles. After thermal treatment, the gold nanoparticles are molten together to macroscopic gold nuggets as a result of the absence of the stabilizing molecules.

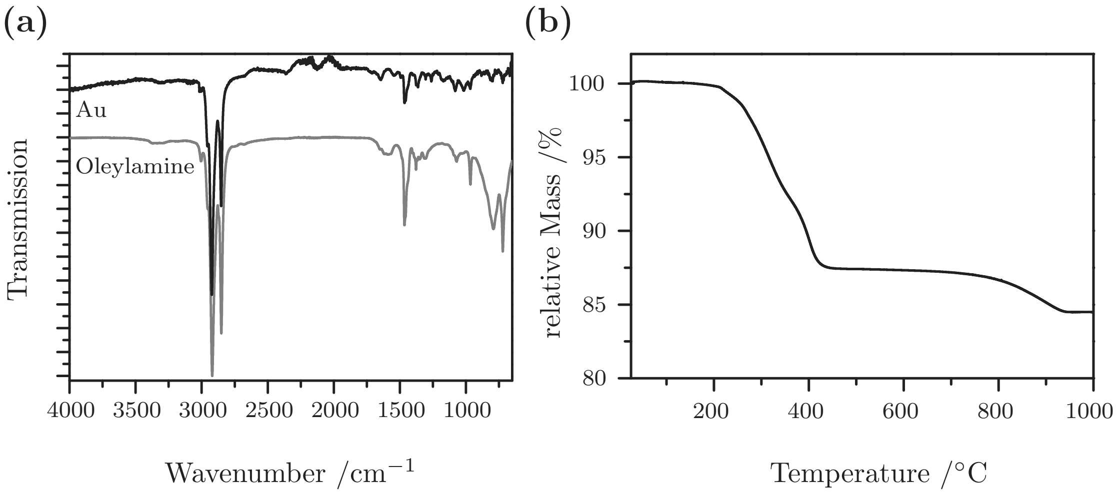

Figure 3.11.: ***FT-IR and TGA measurements of the gold nanoparticles.*** *Oleylamine stabilises the particle surface and keeps the particles soluble in organic media. To remove the ligands, temperatures above 200° C are necessary. However, too high temperatures also remove the first surface atoms.*

3.3.2. Gold and silver nanoparticles for aqueous solvents

To produce noble metal nanoparticles soluble in aqueous solution, a synthesis procedure from Jana *et al.*[67] was used. Depending on the particle size the synthesis varies in the number of preparation steps. 2-4 nm sized Au seeds and also 5-7 nm sized silver particles can be synthesised *via* a one-step synthesis. Bigger nanoparticles are prepared by a seeded growth procedure using the prepared core particles. For the later three-dimensional arrangement, the particle size should be in the range of 5-10 nm. For silver nanoparticles this can be realised with a one-step synthesis but in the case of Au nanoparticles a second synthesis step is necessary. Both syntheses follow the principle of reducing a silver or gold salt in organic media in the presence of a very weak stabilizing ligand. Before the cleaning procedure of the synthesis is done the particles are stabilised by ligand exchange with an ω-functionalised alkane thiol like 11-mercaptoundecanoic acid (MUA) or with N,N,N-trimethyl(11-mercaptoundecyl)-ammonium chloride (TMA). After ligand exchange the nanoparticles are soluble in aqueous solution.

The optical properties of such particles are similar to the properties of the above described metal nanoparticles. The seed nanoparticles of gold show very broad absorption spectra because of the large size distribution, see Figure 3.12. By comparison, the spectra of the seeded growth gold nanoparticles show a distinct plas-

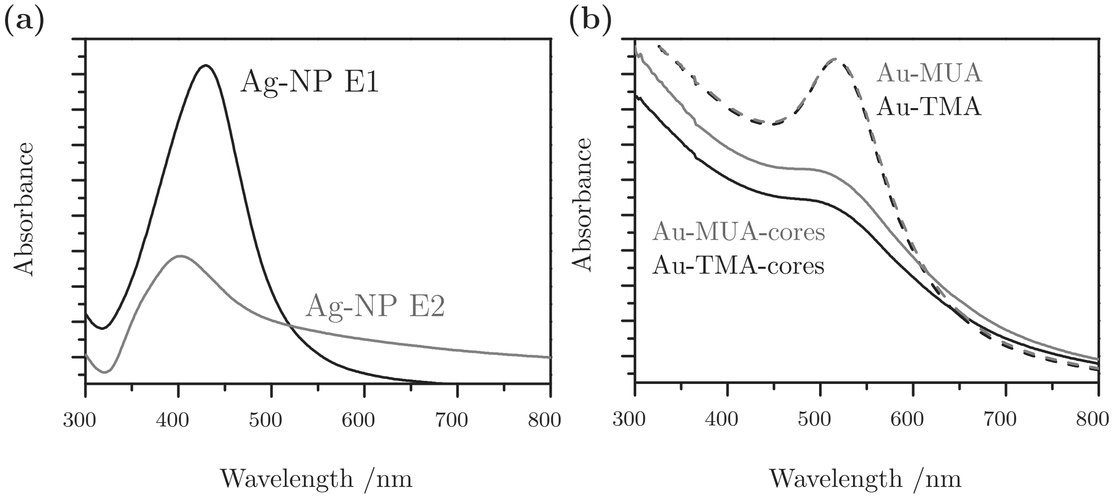

Figure 3.12.: ***Absorption spectra of aqueous gold and silver nanoparticles,*** *which show the plasmon peaks of the particles and the size distribution of the samples. The lower stability of the silver nanoparticles causes agglomeration during synthesis and is apparent as a declining branch in the absorption spectra.*

mon resonance at 516 nm. The different stabilizing ligands were exchanged after dividing the reaction solution into two parts, so that the inorganic part and the size distribution of both solutions are equal. The lower stability of the silver nanoparticles results in agglomeration during the synthesis and so size selective precipitation follows to separate the fractions. Fraction E1 has a plasmon resonance at 430 nm and exactly one maximum so that the morphology of the silver nanoparticles is spherical. In Fraction E2 the maximum is shifted to smaller wavelength and the maximum possesses a tail at higher wavelengths, which represents the variety of agglomerates formed. For later investigations only fraction E1 is used.

The size distributions, an indication for which can be glimpsed from the peak broadening of the absorption spectra, can be confirmed with TEM measurements. As is shown in Figure 3.13, the synthesised gold seeds have a size of around 2 nm and few bigger particles of sizes up to 6 nm. In comparison to that, the gold nanoparticles formed from seeded growth show spherical morphology and a size of 5.1 0.7 nm analogous to the silver nanoparticles with a size of 5.5 0.5 nm. The size distribution is higher in comparison to the gold nanoparticles synthesised *via* the method of Peng *et al.*[65] described above, but the twinning of the single nanoparticles can also be observed. The surface ligands do not influence the particle morphology or size because they have been added after particle growth was

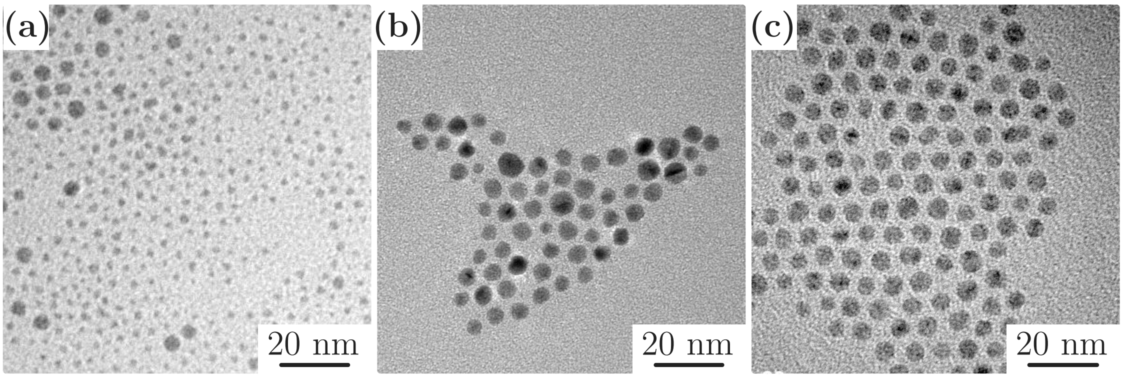

Figure 3.13.: ***TEM images of the synthesised seeds and seeded-growth particles.*** *The size distribution of the small Au-TMA nanoparticles (a) of around 2 nm is higher than that of the 5 nm sized ones (b). The silver nanoparticles covered with TMA (c) show also small size-distribution. The stabilisation with TMA or MUA does not influence the inorganic core material.*

completed.

FT-IR measurements show (Figure 3.14) that the weak stabilizing ligand didodecylamine used during synthesis, is completely replaced by the anionic MUA stabiliser and the cationic TMA. The -OH stretching vibration of the carboxylic group of the MUA is shifted from 3000 cm^{-1} to higher wavenumbers because the carboxylic dimers and their hydrogen bonds are formed in solids. The TMA ligand has a vibration at 2400 cm^{-1} that cannot be explained with the structure of the molecule and may be a result of impurities within the reagents. These impurities do not attach to the surface of the nanoparticles and can be removed during the cleaning procedure. All other vibrations reinforce the existence that the ligands have been exchanged on the nanoparticle surface.

3.4. Core-shell nanoparticles - PbSe/PbS and Au/PbS

Heterogeneous nanostructures and their preparation are an important field in current research. New developments in colloidal chemistry enable the synthesis of multicomponent nanoparticles such as core-shell, dumbbell or Janus structures with different material combinations e.g. metal-metal[68], metal-semiconductor[27,69] and semiconductor-semiconductor[70–72] components. The aim of the synthesis of

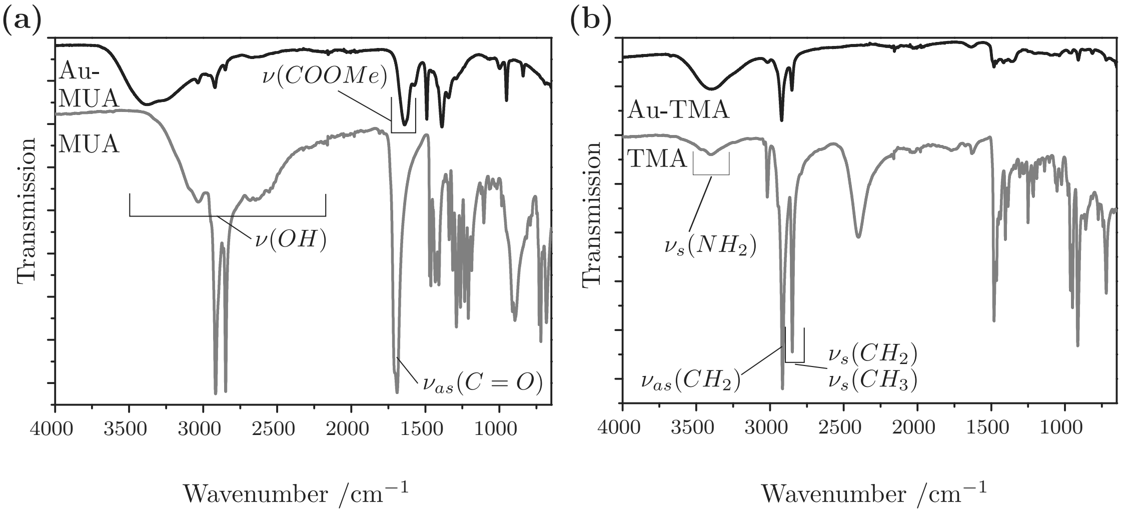

Figure 3.14.: ***FT-IR investigations of the bound surface ligands.*** *The carboxylic group of the MUA binds on the nanoparticle surface, which is confirmed by the increasing carboxylate vibration with the particle present (a). The amine shows impurities that can be removed during ligand exchange (b).*

PbSe/PbS and Au/PbS core-shell structures is to arrange them into three dimensional structures to form crystals, which theoretically have the potential to be highly efficient thermoelectric materials. Dresselhaus *et al.*[73–75] postulated in a theoretical study that the figure of merit of thermoelectric materials increases by the combination of two nanomaterials with dimensions of about the phonon wavelength as a result of phonon scattering at the grain boundaries while electron transport is not influenced by this. Furthermore, they undertook calculations for lead chalcogenides, which revealed 5 nm as an optimal size to achieve highest efficiencies. For the combination of two semiconductor materials in core-shell structures, the shell structure normally grows epitaxially on the core surface. During this process the surface traps of the cores are filled with new inorganic material, which often leads to a higher quantum yield of the core-shell nanoparticles due to the passivation of the cores. The relative position of the bandgaps is used as a classification for semiconductor core-shell structures, with the three existing types described in the introduction.[32,33] Lead selenide/sulphide nanoparticles belong to a quasi-type I structure because the valence-band edges of both materials are nearly equal, see Figure 3.15, so that the hole wave function is smeared out over the whole structure while the electron is located in the core.[76]

It is important for the preparation of heterogeneous materials that both materials

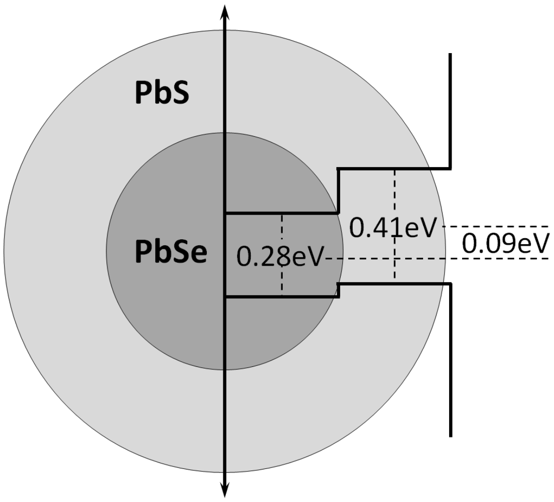

Figure 3.15.: ***Bandgap structure of PbS and PbSe in a core-shell material.*** *The small difference between the valence bands broadens the wave function of the hole. Core-shell structures with this speciality are quasi-type I structures.*

show the same crystal structure, in this case NaCl-type, and have a minimal lattice mismatch, here 1.3%.[36,70] In contrast to semiconductor-semiconductor core-shell nanoparticles with a small lattice mismatch, heterostructures combining metal and semiconductor materials are challenging to synthesise. Their large lattice mismatch and the differences in their crystal structure reduce the tendency of epitaxial growth drastically so that during shell growth defects, cracks and disordered aggregation occur. In Table 3.1 the lattice mismatches of different semiconductor materials combined with gold are shown, calculated with the denoted equation.[34]

The combination of metal-semiconductor hybrid materials enables a new field of functional materials because the combination of plasmonic resonance and semicon-

Table 3.1.: Lattice parameters of the [111] facet of gold and selected semiconductor materials and their lattice mismatch.[34]

Crystal facet Metal (Core_{CF})	Crystal facet Semiconductor (Shell_{CF})	Lattice mismatch [%] (LM) $LM = \frac{Shell_{CF} - Core_{CF}}{Core_{CF}} \cdot 100\%$
Au (111)	PbS (111)	45.6
Au (111)	CdTe (111)	58.9
Au (111)	CdS (111)	42.7
Au (111)	ZnS (111)	32.9

ductor bandgap allows new unique properties.[27] Metal nanoparticles can influence the optical properties of semiconductor particles as Shimizu *et al.*[77] reported. The coupling of CdSe(ZnS) particles onto a metal surface enhances their fluorescence. Hirakawa *et al.*[78] reported on the electron-hole separation in hybrid nanoparticles and their ability to increase their photocatalytic activity. Yang *et al.*[69] described the charge separation in hybrid nanostructures, e.g. the electrons are located in the metal core and the holes stay in the semiconductor shell, which increases the electron-transfer rate as a function of increasing shell thickness.

3.4.1. PbSe/PbS core-shell nanoparticles[‡]

As the basis for the core-shell nanoparticles, PbSe core particles are synthesised as described in section 3.1.2. The chosen core diameters have an average size of 5 nm and are capped with oleic acid surface ligands. The shell synthesis using a single injection of shell material did not result in hybrid structures. The high amount of injected sulfur precursor leads to supersaturation, which is higher than the homogeneous nucleation energy and this result in nucleation and formation of new particles. The existing PbSe core particles dissolve during the process and PbS nanoparticles are formed, which is confirmed by EDX measurements. Based on the results of single injection experiments a new synthesis strategy for shell formation was used. In the literature, the successive ion layer adsorption and reaction (SILAR) technique as an alternative to multiple injections is often reported.[80] There, alternating cationic and anionic precursors for each monolayer are added and so distinct shells are grown. Adapting this method and using an excess of lead-oleate in the reaction solution, which stabilises the PbSe core particles, a multiple injection method is obtained. During the shell growth the concentration of the added sulfur precursor is so low that homogeneous nucleation cannot take place. To grow a crystal shell of 2.5 nm around the core, five monolayers of PbS are needed. The theoretical shell thickness is based on the work of Dresselhaus *et al.*[75] to produce later on arrangements of 5 nm PbSe and 5 nm PbS sections analogously to Figure 3.16.

To optimise the shell growth and size distribution of the hybrid nanoparticles, the injection temperature is varied between 50 and 140°C. As shown in Figure 3.17a, higher reaction temperatures result in broader absorption peaks up to a complete

---

[‡] The results of this chapter were partly obtained within the framework of the bachelor thesis written by B.Sc. Elke Schade[79] under the mentoring of the author.

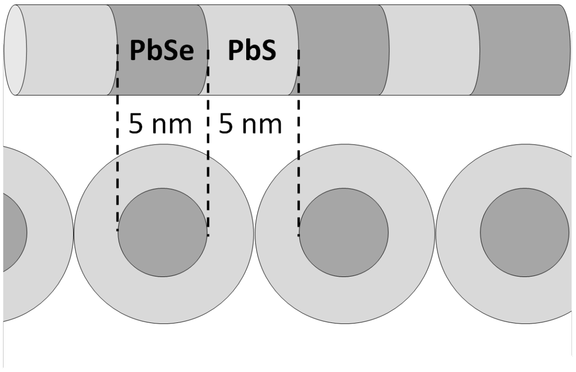

Figure 3.16.: ***Schematic diagram of the postulated superlattice nanowires from Dresselhaus et al.[74].*** *To realise these nanowires core-shell structures with 5 nm core diameter and 2.5 nm shell thickness are required.*

scattering of the sample at 140°C. With increasing amount of monolayers (ML), defects and stacking faults broaden the size distribution, so that only with an injection temperature of 60°C can five monolayers of PbS be grown on top of the PbSe cores with an acceptable size distribution. The temperature dependent agglomeration of the hybrid nanoparticles is shown in Figure 3.17b-d and it indicates that higher temperatures induce faster shell growth and less ordered arrangements of monolayers so that nanoparticles are growing together. By reducing the reaction temperature below 60°C the reactivity of the thioacetamide precursor is strongly reduced so that only partial shell growth occurs. The addition of shell material can be measured with absorption spectroscopy because the absorption wavelength is red-shifted as a consequence of the larger particle size. Calculation of the exact diameter of the hybrid nanoparticles with the Brus-equation cannot be done because this equation is only valid for monocomponential particles. TEM investigations show the increasing size of the hybrid materials the number of monolayers increases. The assumed shell thickness from calculation can be assessed using TEM measurements. Per monolayer the diameter of the nanoparticle increases by 1 nm, so that after addition of 5 MLs 10 nm sized core-shell nanoparticles result.

To reduce the size distribution of the hybrid material, chloride-ions in form of lead-chloride (2% referred to lead acetate) have been added to the reaction solution because it has been reported that chloride-ions can act as a ripening agent.[81] Consequently, the shell growth appears homogenous, which results in a lower size distribution and a more defined absorption maximum. In addition to the injection temperature, the solvent that the core nanoparticles are in influences the shell

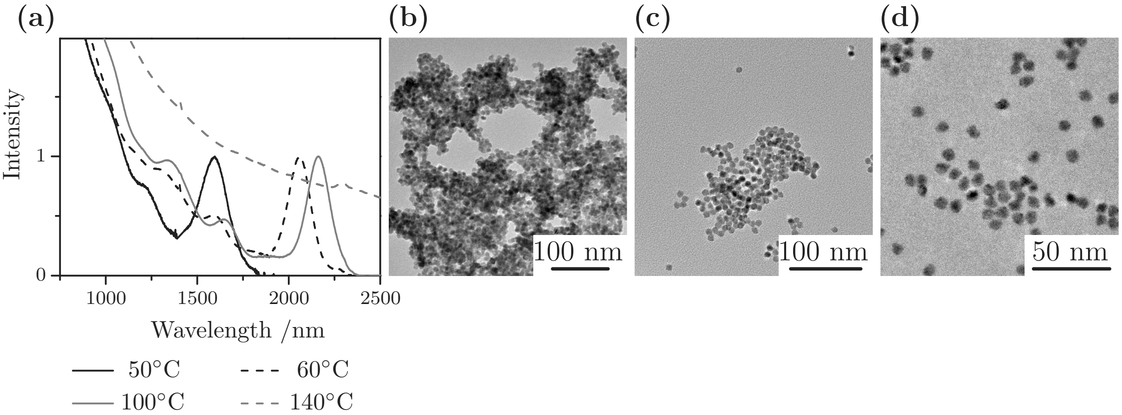

Figure 3.17.: ***Influence of the injection temperature during shell growth and resulting core-shell structures.*** *Higher temperatures lead to inhomogeneous shell growth and agglomeration, the intergrowth of the particles during shell synthesis can be observed additionally from TEM images showing nanoparticles synthesised by the different injection temperatures.*

growth. The core nanoparticle solutions are mixed with octadecene (ODE) as solvent. To remove the initial solvent, the solution is evacuated at 60°C. In comparison to the initial solvent, the shell growth differs strongly. If dried nanoparticles are redissolved in ODE or core nanoparticles in toluene solution are used the resulting hybrid materials scatter strongly and show a large amount of agglomerates. In comparison to that, core solutions with chloroform or hexane show controlled shell growth. During the evaporation of hexane boiling retardation occurs so that chloroform is used as the solvent for the PbSe nanoparticles. The background and the reaction mechanism of these observations are not completely understood until now and similar results are not reported in literature.

Scale-up of the synthesis is necessary to provide sufficient material for the later formation of 2D and 3D arrangements of the nanoparticles. Therefore, two and fourfold synthesis were tried. Though, the twofold synthesis worked best because agglomerates, which are formed in the normal approach, do not occur presumably due to the higher mixing rate and so more homogenous shell growth is observed. In the 4-times basic approach, the particle formation works as well as in the doubled approach with only the absorption peak becoming broadened by a small amount of dimer-formation of the nanoparticles. Consequently, the optimal synthesis parameters are 60°C with core particles dissolved in chloroform with an addition of 2% lead chloride as additive. Additionally, the doubling of the amounts used in the

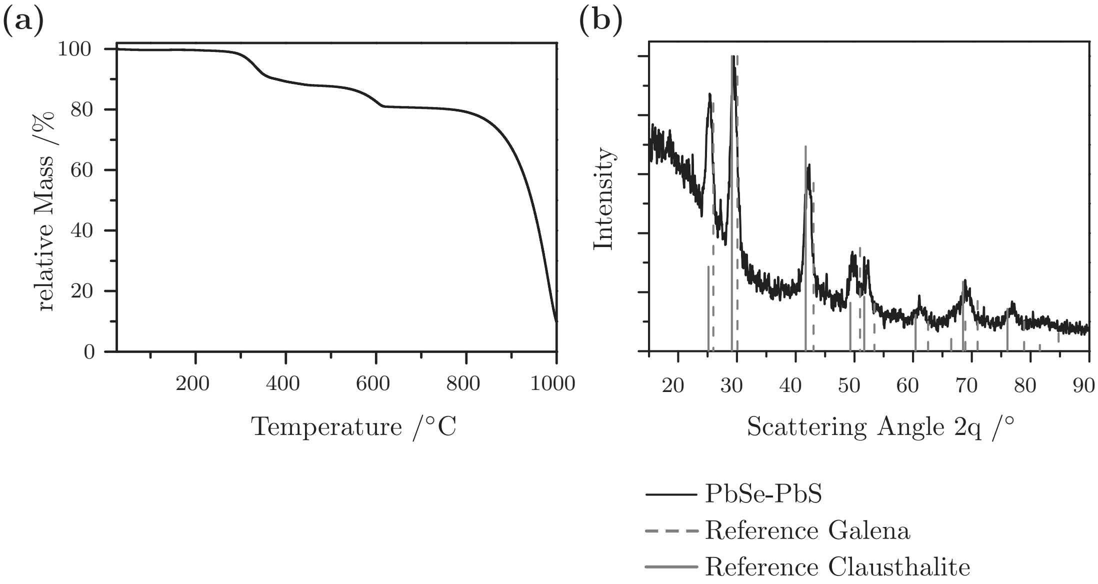

Figure 3.18.: ***TGA study of PbSe-PbS core-shell particles and their corresponding XRD.*** *As a result of the lattice deformation during shell growth new lattice parameters between the galena and the clausthalite structure are formed.*

basic approach results in hybrid structures with low size distributions. The characterisation of the hybrid materials shows that surface stabilizing ligands are the same for PbS as for PbSe nanoparticles (measured with FT-IR). Thermal analysis, see Figure 3.18a, exhibits a new step between the ligand removal (250-400°C) and the evaporation of the core material (>750°C) at 500-600°C associated with oleic acid degradation. The crystalline structure of the hybrid material shows reflexes between the crystal structures of PbSe and PbS bulk materials, which is as a result of lattice deformation during shell growth, see Figure 3.18b.

3.4.2. Au/PbS core-shell nanoparticles[§]

Based on the gold nanoparticles, that are described in section 3.2.1 with a diameter of 5 nm and oleylamine as capping ligand and preferential [111] facets, lead sulphide is a potential candidate to be used as a shell material to form metal-semiconductor hybrid materials as a new class of functional materials. In the literature, there are only few reports about centrosymmetric Au-PbS nanoparticle syntheses. A two step strategy is reported by Lee *et al.*[83], where firstly gold nanoparticles are

---

[§] The results of this chapter were partly obtained within the framework of the master thesis written by M.Sc. Danny Haubold[82] under the mentoring of the author.

synthesised and in the second step the shell material is grown on top of the core. Another method is reported by Zhang *et al.*[34] in a four step process. A big benefit of this method is that single crystalline PbS shells can be solely grown on top of the gold core which is not reported in the synthesis of Lee *et al.*[83]. Firstly, a silver shell is grown on top of the gold core, then exchanged to an amorphous silver sulphide shell and afterwards transformed *via* cation exchange reaction to a single crystalline PbS shell. A third method is that of Yang *et al.*[84], which uses PbS nanoparticles as cores onto which gold dots were grown at special facets on top of the PbS core. All three syntheses were tried with the result that only the synthesis of Lee *et al.*[83] shows optimisation potential because PbS nanoparticles are formed as a side product and the heterogeneous nucleation is partially inhibited as is known from PbSe-PbS core-shell synthesis. The other synthesis strategies did not show any shell growth and in this case more optimisation steps are required.

Before optimisation of the synthesis of Lee *et al.*[83] is done the reasons for the homogeneous nucleation of PbS and the inhibited heterogeneous nucleation should be considered. The main reason is the high lattice mismatch, which is 45.6% between the [111] facets of PbS and Au. During nucleation three different energies are important. One is the homogeneous growth energy ($E_{hom-growth}$), which represents the aggregation of similar atoms and ions with the core material or nucleus. The second energy is the homogeneous nucleation energy ($E_{hom-nuc}$), in the case of the Au-PbS system this represents the formation of new PbS nuclei, and the third energy is the heterogeneous nucleation energy ($E_{het-nuc}$), which accompanies the attachment of PbS on top of the gold core surface. Heterogeneous nucleation strongly varies with the lattice mismatch. As is shown in Figure 3.19, the homogeneous nucleation and growth energy of PbS remains independent of the lattice mismatch and only the heterogeneous nucleation energy varies. If the lattice mismatch is small, e.g. PbSe-PbS, heterogeneous nucleation is favoured because the formation of new nuclei shows an energy barrier. In the energy region between the homogeneous and heterogeneous nucleation (grey arrow) the parameters of the synthesis can be varied and core-shell nanoparticles will result. Below the heterogeneous nucleation energy no nucleation can occur and above the homogeneous nucleation energy both nucleation steps take place simultaneously. The high lattice mismatch shifts the heterogeneous nucleation energy closer to the homogeneous nucleation energy so that the energy region within which parameter variation is feasible gets smaller. The heterogeneous nucleation energy is still lower than the

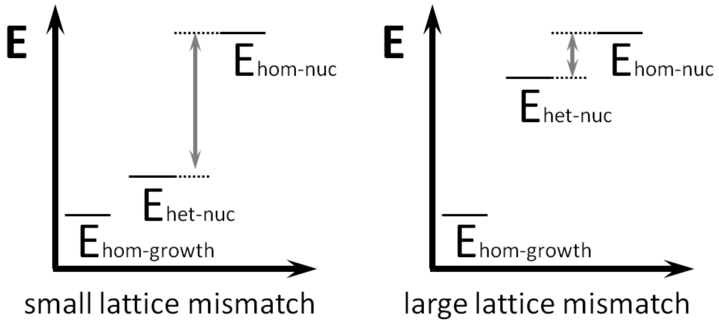

Figure 3.19.: ***Lattice mismatch dependent nucleation and growth energy levels.*** *Raising the lattice mismatch increases the heterogeneous nucleation energy level so that the region of parameter variation (grey arrow) is reduced and shell growth becomes more challenging.*

homogeneous nucleation energy because energetically the reduction of surface energy during agglomeration on existing cores is favoured in contrast to the formation of new surfaces. The calculation of the absolute energy level of the shown energies is difficult because parameters like reaction temperature, local concentrations and stirring rate influence the energy levels. For the Au-PbS core-shell synthesis the reaction parameters have to be chosen first in the region of the heterogeneous nucleation energy and then have to be reduced to homogeneous growth conditions for homogeneous shell growth.

On the basis of the synthesis of Lee *et al.*[83] and with the theoretical background information about the nucleation energies a new synthetic route for the formation of centrosymmetric core-shell nanoparticles was developed. Additionally, Janus particles as hybrid structures can be synthesised by parameter variation.

The synthesised gold cores with a diameter of 5 nm in section 3.2.1 and the weak oleylamine ligands represent the nucleation points for heterogeneous nucleation. Their variation in morphology results in differently shaped core-shell structures caused by changes in the shell growth. As precursors for shell formation, lead oleate and bis(trimethylsilylsulphide) (TMS_2S) were used. The high reactivity of the sulfur source is needed to overcome the energy level of heterogeneous nucleation and to induce multiple nucleation on top of the gold nanoparticles to form centrosymmetric core-shell structures. Less reactive sulfur precursors would cause Janus particles as is reported by Shi *et al.*[85]. Additionally, the reduction in sulfur precursor concentration also generates Janus particles. With the highly reactive TMS_2S the reaction could be done at room temperature, but under these consider-

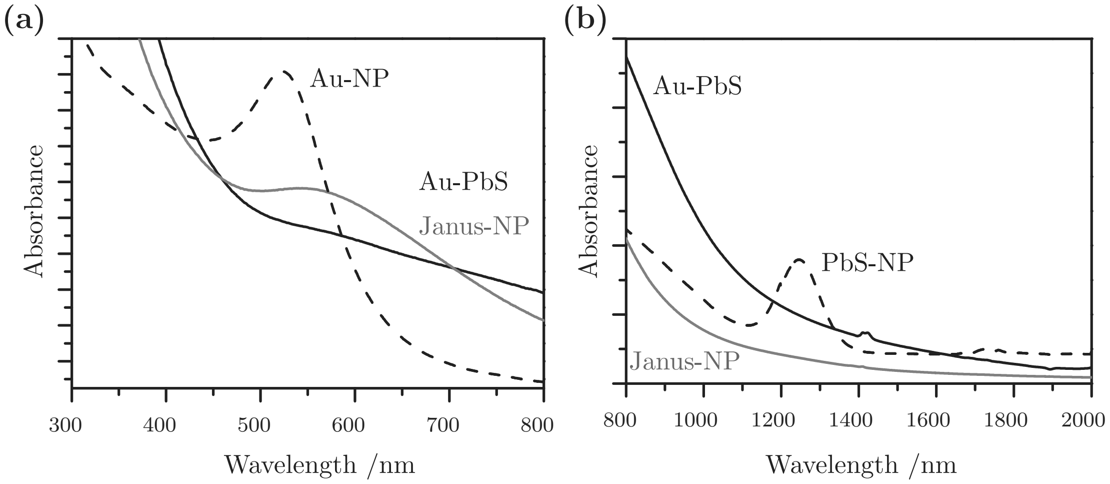

Figure 3.20.: ***Absorption spectra of hybrid Au-PbS nanoparticles in the UV/VIS and IR region.*** *The Au plasmon frequency is shifted due to the changing dielectric constant of the surrounding media during shell growth. The absorption maximum of PbS nanoparticles is broadened as a consequence of a large size distribution of the domains in the shell.*

ations homogeneous nucleation is preferred so that PbS nanoparticles are formed as side product. With increasing reaction temperature, heterogeneous nucleation is favoured and so core-shell particles are formed. It is a fact that the lattice vibrations of the core material are stronger at higher temperatures and it may be that this increases the tolerance between the Au and PbS lattice during nucleation. Additionally, the injection speed influences the concentration profile of thermally decomposed TMS_2S and also affects the reaction kinetics. Fast injection promotes homogeneous nucleation and therefore injections over 15 seconds are done to generate hybrid materials. The ratio of lead and sulfur precursor to the amount of gold nanoparticles present influences the morphology of the hybrid structure. By reducing the lead and sulfur amount to 1/6 of the initial concentration Janus particles can be formed. Characterisation of the Janus particles and the hybrid structures is done using absorption spectroscopy in the UV/VIS and in the IR region. As it is shown in Figure 3.20, the plasmon resonance of the gold core is shifted to higher wavelengths and is also broader than the core spectrum. The red-shift is as a consequence of the changed dielectric constant in the surroundings of the partially or completely oleylamine covered PbS shell. The decreasing intensity and the broadening of the peak are results of the higher polydispersity and the differences

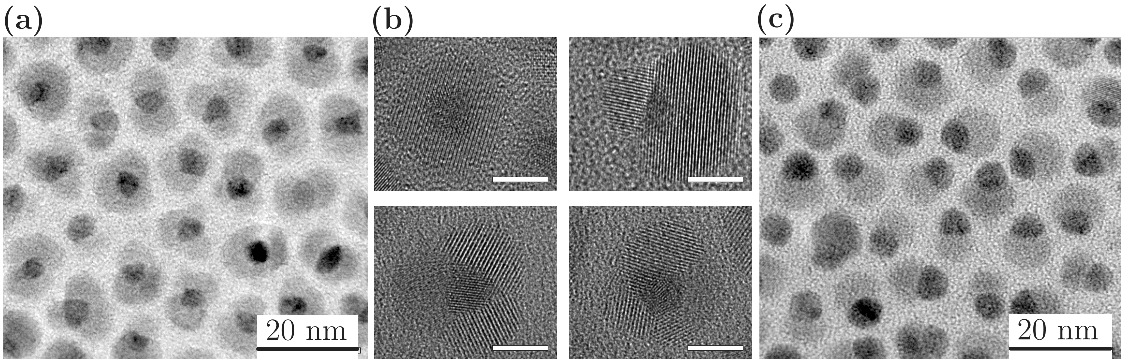

Figure 3.21.: ***HRTEM and overview images of core-shell and Janus Au-PbS nanoparticles.*** *While Janus particles always show only one nucleation point the amount of domains of core-shell particles varies. Seldomly is only one domain expressed; mostly 2-4 domains are observed because of multiple parallel nucleation and twinned gold cores.*

in the PbS domains in the shell material. In the IR region, the absorption peak of lead sulphide particles is completely diminished and only a broad absorption can be measured as a consequence of the variances in domain dimensions of PbS in the shell material. Hence, a broadening of the single absorption peaks can be observed as shown in the spectra.

The morphology of the Janus and the core-shell particles is shown in Figure 3.21 including the multidomains of the core-shell nanoparticles. The averaged shell thickness of both particle types varies between 3-5 nm depending on their morphology. Besides single crystalline shells, also two and three domain core-shell particles are formed during synthesis with a higher amount than the single crystalline ones. By means of fast Fourier transformation (FFT) the relative orientation of the core crystal lattice and the shell crystal lattice can be determined. The FFTs of the gold cores show the preferential [111] crystal facet of these particles is as Baletto *et al.*[66] postulated. 85% of the gold cores show the [111] facets and only 15% have other crystal facets. The relative orientations of the PbS crystal facets to the [111] gold facet were determined, but a favoured crystal lattice orientation could not be found. Only trends could be determined, e.g. the angle between $[111]_{PbS}$ and gold is always between 60-90° and analogously the angle of $[200]_{PbS}$ varies between 35-60°. The complex morphology also complicates the analysis of the orientation and the twinning of the gold nanoparticle cores. XRD measurements only show the reflexes of the gold cores; the PbS domains were not expressed in any signal because of the small amount of arranged scattering lattice planes.

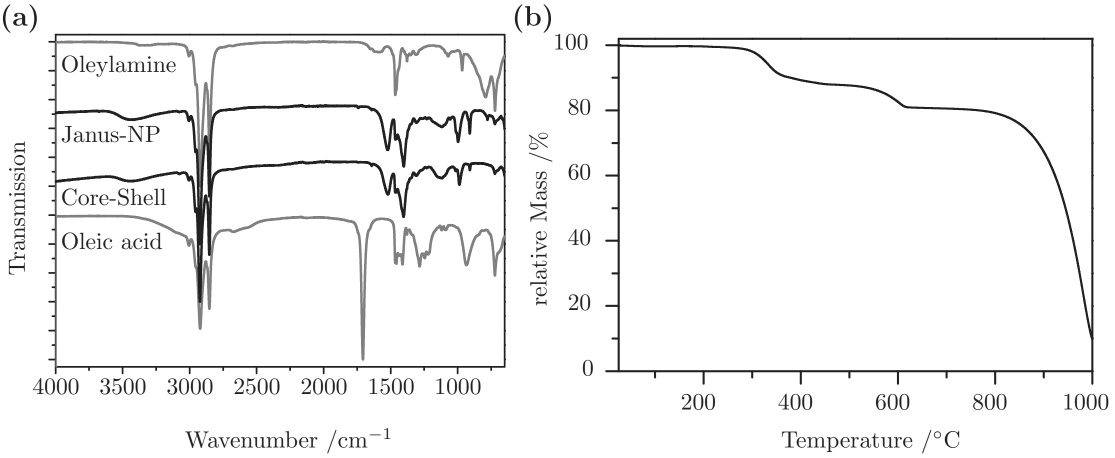

Figure 3.22.: ***FT-IR of oleylamine and oleic acid capped hybrid nanoparticles and their TGA spectra.*** *Oleic acid stabilises the PbS domains of the hybrid particles. Ligand removal takes place starting at 150°C.*

Surface stabilisation of the as-synthesised nanoparticles is done with oleylamine and oleic acid, where oleylamine binds to the gold surface and oleic acid to the lead species. The FT-IR measurements, see Figure 3.22, show the particles and their ligands. The -CH_3 and -CH_2 vibrations of both ligands are the same and can be found between 2800-3000 cm^{-1}. The missing C=O vibration at 1706 cm^{-1} in the particle spectra and the increase in the peak at 1500-1550 cm^{-1} represents the carboxylic vibration, see detailed information in section 3.1.1, and suggests the binding of oleic acid to the PbS part of the particle surface. The amine vibration of oleylamine at 3400-3350 cm^{-1} has a low intensity and so it cannot be determined in the particle spectrum. Based on the fact that oleylamine is a better ligand for gold nanoparticles than oleic acid, it is expected that it still stabilises the gold surface.

TGA experiments show nearly the same results as observed for PbS nanoparticles. Between 150-400°C a mass loss of 30% is observed where at first parts of the ligands are removed from the nanoparticle surface. From 600°C on an endothermic process takes place and above 800°C the remaining ligand molecules are removed and the first lead sulphide parts evaporate after first melting of the shell and parts of the core (endothermic process). The as-synthesised and characterised hybrid structures are soluble in tetrachloroethylene and only the Janus particles are soluble in toluene.

3.5. Résumé

Having considered all the presented issues the synthesis of monocomponential materials and monodisperse quasi-spherical nanoparticles can be realised. The optimisation of the different preparation techniques results in high reproducibility and high yields of nanoparticle solution. For semiconductor nanoparticles the absorption spectra can be taken as a measure for quality control. For metallic nanoparticles TEM measurements are necessary. The covering of the nanoparticle surface with oleic acid and oleylamine results in long-term stability of the nanoparticle solution. Heat treatment of the nanoparticles is possible, but ligand degradation starts at 200°C. In this case, metallic nanoparticles are more stable than semiconductor nanoparticles with respect to evaporation. Electrostatic capping ligands like MUA and TMA transfer the metallic nanoparticles into aqueous solution and stabilise them for a long period of time. In contrast to the low reactivity of gold nanoparticles and with respect to environmental influences, silver nanoparticles have to be kept in the dark as otherwise light induced oxidation will take place and this results in the destabilisation of the nanoparticle solution. All in all, the as-synthesised nanoparticles are highly monodisperse so that 2D and 3D crystalline arrangements with an ordered inner structure and high symmetry are possible. In contrast, the core-shell nanoparticles are inappropriate for highly symmetrical 3D assemblies. The PbSe-PbS nanoparticles show high monodispersity and good 2D packaging, but the received amounts per synthesis are too low to form mesocrystalline materials. The combination of several syntheses tends to result in larger size distributions so that stacking faults and point defects occur in the 3D structures. However, while Au-PbS structures are producible in high yields, their size distribution and their variation in habitus is too extreme for ordered arrangements, so that the core-shell nanoparticles are best suited for aerogel formation or layer-by-layer deposition.

3.6. References

1. Eychmüller, A. Structure and Photophysics of Semiconductor Nanocrystals. *The Journal of Physical Chemistry B* **104,** 6514–6528 (2000).
2. Alivisatos, A. P. Perspectives on the Physical Chemistry of Semiconductor Nanocrystals. *The Journal of Physical Chemistry* **100,** 13226–13239 (1996).
3. Kraus, T. *Assembly and printing of micro and nano objects* PhD thesis (2007).
4. Goesmann, H. & Feldmann, C. Nanoparticulate functional materials. *Angewandte Chemie (International ed.)* **49,** 1362–95 (2010).
5. Zhang, Q., Kano, J. & Fumio, S. in *Handbook of Powder Technology* 07, 509–528 (Elsevier, 2007).
6. Gutsch, A., Mühlenweg, H. & Krämer, M. Tailor-made nanoparticles via gas-phase synthesis. *Small (Weinheim, Germany)* **1,** 30–46 (2005).
7. Park, J., Joo, J., *et al.* Synthesis of monodisperse spherical nanocrystals. *Angewandte Chemie (International ed.)* **46,** 4630–60 (2007).
8. Pinna, N. & Niederberger, M. Surfactant-free nonaqueous synthesis of metal oxide nanostructures. *Angewandte Chemie (International ed.)* **47,** 5292–304 (2008).
9. Hickey, S. G., Gaponik, N. & Eychmüller, A. Synthesis and characterisation of NIR-emitting nanocrystals for photonic and optoelectronic applications. *Photonics and Nanostructures - Fundamentals and Applications* **5,** 113–118 (2007).
10. Nizamoglu, S., Mutlugun, E., *et al.* White emitting CdS quantum dot nanoluminophores hybridized on near-ultraviolet LEDs for high-quality white light generation and tuning. *New Journal of Physics* **10,** 23026 (2008).
11. Eychmüller, A., Gaponik, N., *et al. NIR-emitting nanocrystals for photonic applications* in *Proceedings of SPIE* (SPIE, 2007), 67282P–67282P–9.
12. LaMer, V. K. & Dinegar, R. H. Theory, production and mechanism of formation of monodispersed hydrosols. *Journal of the American Chemical Society* **72,** 4847–4854 (1950).
13. Badia, A., Singh, S., *et al.* Self-Assembled Monolayers on Gold Nanoparticles. *Chemistry - A European Journal* **2,** 359–363 (1996).

14. Brust, M, Fink, J, *et al.* Synthesis and reactions of functionalised gold nanoparticles. *Journal of the Chemical Society, Chemical Communications,* 1655 (1995).

15. Templeton, A. C., Chen, S., *et al.* Water-Soluble, Isolable Gold Clusters Protected by Tiopronin and Coenzyme A Monolayers. *Langmuir* **15,** 66–76 (1999).

16. Yao, H., Momozawa, O., *et al.* Stepwise Size-Selective Extraction of Carboxylate-Modified Gold Nanoparticles from an Aqueous Suspension into Toluene with Tetraoctylammonium Cations. *Chemistry of Materials* **13,** 4692–4697 (2001).

17. Bishop, K. J. M. & Grzybowski, B. "Nanoions": fundamental properties and analytical applications of charged nanoparticles. *Chemphyschem : a European journal of chemical physics and physical chemistry* **8,** 2171–6 (2007).

18. Clapp, A. R., Medintz, I. L., *et al.* Fluorescence resonance energy transfer between quantum dot donors and dye-labeled protein acceptors. *Journal of the American Chemical Society* **126,** 301–10 (2004).

19. Halpert, J. E., Tischler, J. R., *et al.* Electrostatic Formation of Quantum Dot/J-aggregate FRET Pairs in Solution. *The Journal of Physical Chemistry C* **113,** 9986–9992 (2009).

20. Miyazaki, A. & Nakano, Y. Morphology of Platinum Nanoparticles Protected by Poly(N -isopropylacrylamide). *Langmuir* **16,** 7109–7111 (2000).

21. Chechik, V. & Crooks, R. M. Monolayers of Thiol-Terminated Dendrimers on the Surface of Planar and Colloidal Gold. *Langmuir* **15,** 6364–6369 (1999).

22. Teranishi, T., Kiyokawa, I. & Miyake, M. Synthesis of Monodisperse Gold Nanoparticles Using Linear Polymers as Protective Agents. *Advanced Materials* **10,** 596–599 (1998).

23. Perepichka, D. F. & Rosei, F. Metal nanoparticles: from "artificial atoms" to "artificial molecules". *Angewandte Chemie (International ed.)* **46,** 6006–8 (2007).

24. Henglein, A. Small-particle research: physicochemical properties of extremely small colloidal metal and semiconductor particles. *Chemical Reviews* **89,** 1861–1873 (1989).

25. Weller, H. Colloidal Semiconductor Q-Particles: Chemistry in the Transition Region Between Solid State and Molecules. *Angewandte Chemie International ed.* **32,** 41–53 (1993).

26. Brus, L. E. Electronelectron and electron-hole interactions in small semiconductor crystallites: The size dependence of the lowest excited electronic state. *The Journal of Chemical Physics* **80,** 4403 (1984).

27. Achermann, M. Exciton-Plasmon Interactions in Metal-Semiconductor Nanostructures. *The Journal of Physical Chemistry Letters* **1,** 2837–2843 (2010).

28. Kelly, K. L., Coronado, E., *et al.* The Optical Properties of Metal Nanoparticles: The Influence of Size, Shape, and Dielectric Environment. *The Journal of Physical Chemistry B* **107,** 668–677 (2003).

29. Mie, G. Beiträge zur Optik trüber Medien, speziell kolloidaler Metallösungen. *Annalen der Physik* **330,** 377–445 (1908).

30. Barnes, W. L., Dereux, A. & Ebbesen, T. W. Surface plasmon subwavelength optics. *Nature* **424,** 824–30 (2003).

31. Daniel, M.-C. & Astruc, D. Gold nanoparticles: assembly, supramolecular chemistry, quantum-size-related properties, and applications toward biology, catalysis, and nanotechnology. *Chemical reviews* **104,** 293–346 (2004).

32. Ghosh Chaudhuri, R. & Paria, S. Core/shell nanoparticles: classes, properties, synthesis mechanisms, characterization, and applications. *Chemical reviews* **112,** 2373–433 (2012).

33. Reiss, P., Protière, M. & Li, L. Core/Shell semiconductor nanocrystals. *Small* **5,** 154–68 (2009).

34. Zhang, J., Tang, Y., *et al.* Nonepitaxial growth of hybrid core-shell nanostructures with large lattice mismatches. *Science (New York, N.Y.)* **327,** 1634–8 (2010).

35. Whitesides, G. M. & Grzybowski, B. A. Self-assembly at all scales. *Science (New York, N.Y.)* **295,** 2418–21 (2002).

36. Brumer, M, Kigel, A, *et al.* PbSe/PbS and PbSe/PbSe$_x$S$_{1-x}$ Core/Shell Nanocrystals. *Advanced Functional Materials* **15,** 1111–1116 (2005).

37. Nagel, M, Hickey, S. G., *et al.* Synthesis of Monodisperse PbS Nanoparticles and Their Assembly into Highly Ordered 3D Colloidal Crystals. *Zeitschrift für Physikalische Chemie* **221,** 427–437 (2007).
38. Hines, M. & Scholes, G. Colloidal PbS Nanocrystals with Size-Tunable Near-Infrared Emission: Observation of Post-Synthesis Self-Narrowing of the Particle Size Distribution. *Advanced Materials* **15,** 1844–1849 (2003).
39. Wise, F. W. Lead Salt Quantum Dots: the Limit of Strong Quantum Confinement. *Accounts of Chemical Research* **33,** 773–780 (2000).
40. Dutta, A. K., Ho, T., *et al.* Nucleation and Growth of Lead Sulfide Nano- and Microcrystallites in Supramolecular Polymer Assemblies. *Chemistry of Materials* **12,** 1042–1048 (2000).
41. Schaller, R. & Klimov, V. High Efficiency Carrier Multiplication in PbSe Nanocrystals: Implications for Solar Energy Conversion. *Physical Review Letters* **92,** 186601 (2004).
42. Schaller, R. D., Sykora, M., *et al.* Seven excitons at a cost of one: redefining the limits for conversion efficiency of photons into charge carriers. *Nano letters* **6,** 424–9 (2006).
43. Ellingson, R. J., Beard, M. C., *et al.* Highly efficient multiple exciton generation in colloidal PbSe and PbS quantum dots. *Nano letters* **5,** 865–71 (2005).
44. Murphy, J. E., Beard, M. C., *et al.* PbTe colloidal nanocrystals: synthesis, characterization, and multiple exciton generation. *Journal of the American Chemical Society* **128,** 3241–7 (2006).
45. Simon, P., Rosseeva, E., *et al.* PbS-organic mesocrystals: the relationship between nanocrystal orientation and superlattice array. *Angewandte Chemie* **51,** 10776–81 (2012).
46. Bakueva, L, Musikhin, S, *et al.* Size-tunable infrared (1000-1600 nm) electroluminescence from PbS quantum-dot nanocrystals in a semiconducting polymer. *Applied Physics Letters* **82,** 2895 (2003).
47. Wernick, J. H. Constitution of the $AgSbS_2$-PbS, $AgBiS_2$-PbS, and $AgBiS_2$-$AgBiSe_2$ systems MS. *Am. Mineral. J. H. Wernick 1960 45 591* **45,** 591 –598 (1960).

48. Evans, C. M., Evans, M. E. & Krauss, T. D. Mysteries of TOPSe revealed: insights into quantum dot nucleation. *Journal of the American Chemical Society* **132,** 10973–5 (2010).

49. Dai, Q., Zhang, Y., *et al.* Ligand Effects on Synthesis and Post-Synthetic Stability of PbSe Nanocrystals. *The Journal of Physical Chemistry C* **114,** 16160–16167 (2010).

50. Moreels, I., Justo, Y., *et al.* Size-tunable, bright, and stable PbS quantum dots: a surface chemistry study. *ACS nano* **5,** 2004–12 (2011).

51. Bealing, C. R., Baumgardner, W. J., *et al.* Predicting nanocrystal shape through consideration of surface-ligand interactions. *ACS Nano* **6,** 2118–27 (2012).

52. Dai, Q., Wang, Y., *et al.* Size-dependent composition and molar extinction coefficient of PbSe semiconductor nanocrystals. *ACS nano* **3,** 1518–24 (2009).

53. Moreels, I., Lambert, K., *et al.* Composition and Size-Dependent Extinction Coefficient of Colloidal PbSe Quantum Dots. *Chemistry of Materials* **19,** 6101–6106 (2007).

54. Houtepen, A. J., Koole, R., *et al.* The hidden role of acetate in the PbSe nanocrystal synthesis. *Journal of the American Chemical Society* **128,** 6792–3 (2006).

55. Swanson HE, Tatge E, F. R. Standard X-ray Diffraction Powder Patterns. *Physics Today* **7,** 22 (1954).

56. Zhang, J. Z. & Noguez, C. Plasmonic Optical Properties and Applications of Metal Nanostructures. *Plasmonics* **3,** 127–150 (2008).

57. Noguez, C. Surface Plasmons on Metal Nanoparticles: The Influence of Shape and Physical Environment. *Journal of Physical Chemistry C* **111,** 3806–3819 (2007).

58. Dick, K., Dhanasekaran, T, *et al.* Size-dependent melting of silica-encapsulated gold nanoparticles. *Journal of the American Chemical Society* **124,** 2312–7 (2002).

59. Dreaden, E. C., Mackey, M. a., *et al.* Beating cancer in multiple ways using nanogold. *Chemical Society reviews* **40,** 3391–404 (2011).

60. Choi, W. I., Sahu, A., *et al.* Photothermal cancer therapy and imaging based on gold nanorods. *Annals of biomedical engineering* **40,** 534–46 (2012).

61. Tam, F., Goodrich, G. P., *et al.* Plasmonic enhancement of molecular fluorescence. *Nano letters* **7,** 496–501 (2007).

62. Chen, G., Wang, Y., *et al.* Measuring ensemble-averaged surface-enhanced Raman scattering in the hotspots of colloidal nanoparticle dimers and trimers. *Journal of the American Chemical Society* **132,** 3644–5 (2010).

63. Joseph, Y., Guse, B. & Nelles, G. Aging of 1,ω-Alkyldithiol Interlinked Au Nanoparticle Networks. *Chemistry of Materials* **21,** 1670–1676 (2009).

64. Haubold, D. *Synthese und Charakterisierung von Gold- und Gold-Blei(II)-sulfid-Nanokristallen und deren Anordnung in Superstrukturen* 2011.

65. Peng, S., Lee, Y., *et al.* A facile synthesis of monodisperse Au nanoparticles and their catalysis of CO oxidation. *Nano Research* **1,** 229–234 (2008).

66. Baletto, F., Ferrando, R., *et al.* Crossover among structural motifs in transition and noble-metal clusters. *The Journal of Chemical Physics* **116,** 3856 (2002).

67. Jana, N. R. & Peng, X. Single-phase and gram-scale routes toward nearly monodisperse Au and other noble metal nanocrystals. *Journal of the American Chemical Society* **125,** 14280–1 (2003).

68. Pellegrino, T., Fiore, A., *et al.* Heterodimers based on $CoPt_3$-Au nanocrystals with tunable domain size. *Journal of the American Chemical Society* **128,** 6690–8 (2006).

69. Yang, T.-T., Chen, W.-T., *et al.* Interfacial Charge Carrier Dynamics in CoreShell Au-CdS Nanocrystals. *The Journal of Physical Chemistry C* **114,** 11414–11420 (2010).

70. Sashchiuk, A, Langof, L, *et al.* Synthesis and characterization of PbSe and PbSe/PbS coreshell colloidal nanocrystals. *Journal of Crystal Growth* **240,** 431–438 (2002).

71. Dabbousi, B. O., Rodriguez-Viejo, J, *et al.* (CdSe)ZnS Core/Shell Quantum Dots: Synthesis and Characterization of a Size Series of Highly Luminescent Nanocrystallites. *The Journal of Physical Chemistry B* **101,** 9463–9475 (1997).

72. Hines, M. A. & Guyot-Sionnest, P. Synthesis and Characterization of Strongly Luminescing ZnS-Capped CdSe Nanocrystals. *The Journal of Physical Chemistry* **100,** 468–471 (1996).

73. Dresselhaus, M. S., Chen, G, *et al.* New Directions for Low-Dimensional Thermoelectric Materials. *Advanced Materials* **19,** 1043–1053 (2007).

74. Lin, Y.-M. & Dresselhaus, M. S. Thermoelectric properties of superlattice nanowires. *Physical Review B* **68,** 75304 (2003).

75. Dresselhaus, M. S., Chen, G, *et al.* New composite thermoelectric materials for energy harvesting applications. *JOM* **61,** 86–90 (2009).

76. Bartnik, A., Wise, F., *et al.* Electronic structure of PbSe-PbS core-shell quantum dots. *Physical Review B* **75,** 245424 (2007).

77. Shimizu, K., Woo, W., *et al.* Surface-Enhanced Emission from Single Semiconductor Nanocrystals. *Physical Review Letters* **89,** 117401 (2002).

78. Hirakawa, T. & Kamat, P. V. Charge separation and catalytic activity of Ag@TiO_2 core-shell composite clusters under UV-irradiation. *Journal of the American Chemical Society* **127,** 3928–34 (2005).

79. Schade, E. *Synthese und Charakterisierung von Blei(II)-Selenid/ Blei(II)-Sulfid-Kern/Schale-Nanopartikeln und deren Anordnung in Überstrukturen* 2012.

80. Li, J. J., Wang, Y. A., *et al.* Large-scale synthesis of nearly monodisperse CdSe/CdS core/shell nanocrystals using air-stable reagents via successive ion layer adsorption and reaction. *Journal of the American Chemical Society* **125,** 12567–75 (2003).

81. Saruyama, M., Kanehara, M. & Teranishi, T. Drastic structural transformation of cadmium chalcogenide nanoparticles using chloride ions and surfactants. *Journal of the American Chemical Society* **132,** 3280–2 (2010).

82. Haubold, D. *Synthese und Charakterisierung von Gold- und Gold-Blei(II)-sulfid-Nanopartikeln und deren Anordnung in zwei- und dreidimensionale Superstrukturen* MA thesis (2013).

83. Lee, J.-S., Shevchenko, E. V. & Talapin, D. V. Au-PbS core-shell nanocrystals: plasmonic absorption enhancement and electrical doping via intraparticle charge transfer. *Journal of the American Chemical Society* **130,** 9673–5 (2008).

84. Yang, J., Elim, H. I., *et al.* Rational synthesis, self-assembly, and optical properties of PbS-Au heterogeneous nanostructures via preferential deposition. *Journal of the American Chemical Society* **128,** 11921–6 (2006).
85. Shi, W., Zeng, H., *et al.* A general approach to binary and ternary hybrid nanocrystals. *Nano letters* **6,** 875–81 (2006).

4. Non-classical crystallisation of highly symmetrical three-dimensional mesocrystals

In the present chapter the formation of highly symmetrical and ordered three-dimensional superstructures, so called mesocrystals, will be presented. After introduction to the destabilization technique used and the presentation of the new and optimized gas-phase diffusion technique the focus is initially maintained on ordered self-assembly of lead sulphide and lead selenide mesocrystals. A description regarding the building blocks and their ripening processes under air and ambient conditions is followed by a description of the optimization of formation parameters. Here, temperature, nanoparticle concentration, and solvent/non-solvent combinations are examined and optimized to receive large and symmetrically shaped mesocrystals. Furthermore, the destabilization process is investigated using dynamic light scattering experiments in order to follow the agglomeration process. Also, temperature effects on the ligand shell are determined. In addition to the arrangement of semiconductor nanoparticles the self-assembly procedure from gold nanoparticles into mesocrystals is described. The optimization procedure of mesocrystal formation for metallic nanoparticles is presented along the lines of that as for the PbS and PbSe nanoparticles. Differences in the size and shape of the semiconductor and metal mesocrystals are regarded during comparison of the destabilization process starting with the equation of the building blocks, and for the two dimensional and three-dimensional arrangement. Consequently, the differences in the destabilization process are highlighted. For further applications in thermoelectric and electronic devices, conductivity measurements are undertaken and the optimization of the conductivity using various methods is presented.

4.1. Preface

The manipulation of single nanoparticles is not easy to implement in such a way as to contact them or to introduce them as individual functional units into devices. Therefore, it is currently expected that 2 dimensional and 3D arrangements will most likely be employed for applications if they are to become an essential part of modern nanotechnology.[1] In these arrangements the properties of the single nanoparticle building blocks are still evident but are present within a macroscopic bulk material which can subsequently be incorporated into devices with already existing techniques. Important for applications involving these quantum dot solids is the retention of the special size tuneable properties of the nanoparticular building blocks. For the production of quantum dot solids self-assembly methods are commonly applied whereby the spontaneous organisation of the building blocks into periodically packed structures is used to advantage. Normally, direct interactions such as interparticle forces, indirect forces such as templating or external forces drive particle agglomeration where the modulation of thermodynamic forces influences the structuring by reaching different local equilibria.[2] Mesocrystals form a special class of quantum dot solid, where the size-dependent properties of the individual nanoparticles are maintained in the macroscopic structure and additionally there are new features that derive from the unique collective properties afforded by the arrays of ordered particles. Further, mesocrystalline materials display similar behaviours to single crystalline materials because the nanoparticles are arranged along a common crystallographic fashion.[3]

In the literature there are only a few strategies for the production of highly ordered 3D nanoparticle arrangements. The most common technique for their formation is the so called three-layer supersaturation technique which makes use of a slow nanoparticle destabilisation in a gradient solvent system of different polarity.[4–7] A variant on this is the preparation of ordered structures in small droplets which employs the slow precipitation of the nanoparticular building blocks with the slow diffusion of a non-solvent.[8] Another commonly employed method is solvent evaporation, where a number of different optimised techniques have been reported.[9–13] A further template-free approach for dynamic self-assembly is the use of a mixture of oppositely charged nanoparticles for the formation of colloidal crystals.[14,15] Additional control over the modulation of the interparticle forces, under equilibrium and non-equilibrium conditions in this system can be provided by external

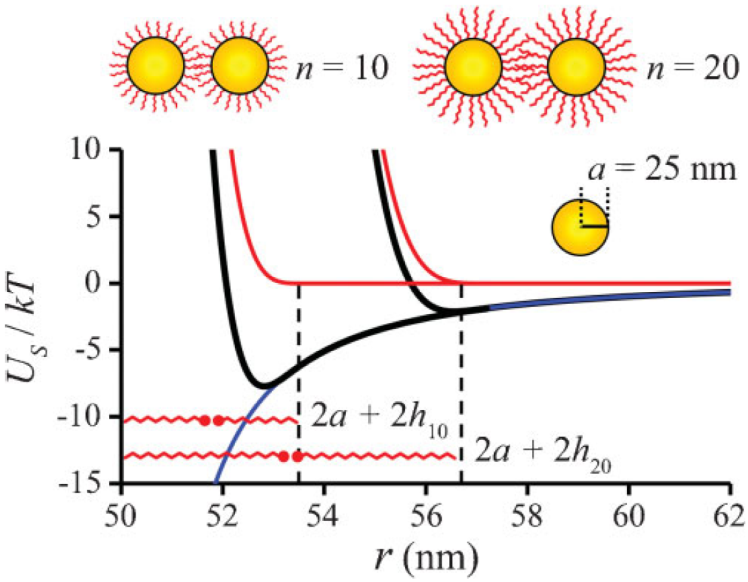

Figure 4.1.: ***Engineering interparticle interactions with steric repulsion*** *The plot shows the total interparticle potential (black) between two 50 nm gold NPs derived as the sum of both van der Waals interactions (blue) and steric repulsions (red) due to polyethylene glycol ligands of two different lengths. Due to the compression of the ligands, the minimum energy separation is smaller than that of the extended ligands (h), r-2a < 2h.*[17]

stimuli.[16]

The nanoparticle self-assembly process is not only interesting for further applications in the fields of magnetic storage, biomedicine diagnostics, optoelectronics, light emitting devices, photonics, photovoltaics and sensors[18] but there is also great interest in the formation process itself and its analogy to the atomic arrangements in crystalline structures.[12] As a consequence the destabilisation process during crystal formation and the forces that are present during this process are analyzed by parameter variation and experiments on different time scales. Further, the analogy to atoms and their arrangement mechanisms depending on the interplay of different interparticle forces and space filling are regarded in the context of length scale variation because the length scale of the forces stay constant in contrast to the increasing size of the nanoparticles, see Figure 4.1. Hence, size variation of nanoparticles can result in completely different crystalline structures by keeping all parameters in the system constant and only diversifying indirectly the length scale of the driving forces.

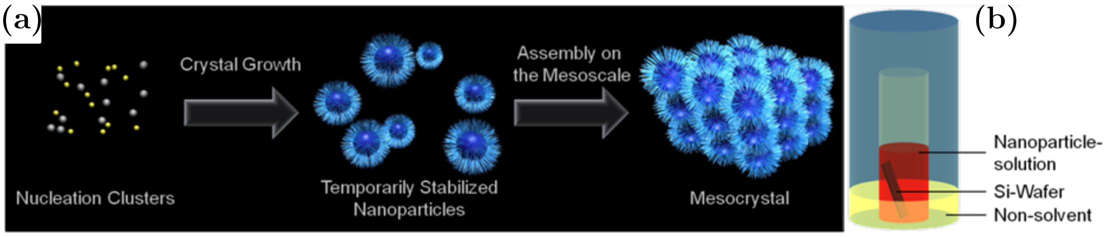

Figure 4.2.: ***Pathway of non-classical crystallisation and developed experimental setup.*** *(a) pathway of non-classical crystallisation with the steps of temporary stabilisation of nanoparticles and slow structuring on the mesoscale and (b) experimental setup for the slow destabilisation of nanoparticle solution with non-solvents over the gas phase using the principle of non-classical crystallisation with temporally stabilised nanoparticular building blocks.*

4.2. Non-classical crystallisation via gas-phase diffusion technique

To construct superstructures composed of nanoparticles on the mesoscale is challenging and therefore the route of non-classical crystallisation as first described by Clfen et al.[19] has been implemented. As is presented in Figure 4.2a the nucleation clusters at first form temporally stabilised nanocrystals which, for the purposes of this study, equates to the process of nanoparticle synthesis and is focused on in the chapter dealing with the nanoparticular building blocks. Subsequently, the as-synthesised building blocks can be used for assembly on the mesoscale.

These arrangement processes takes place via the slow destabilisation of the temporally stabilised nanocrystals using non-solvents diffusing into the nanoparticle solution and induce a change in solvent polarity and consequently precipitate the nanoparticles. In order to achieve this, the principle of ether diffusion as used in supramolecular chemistry was adapted and optimised to bring about the gentle destabilisation of the nanoparticulate building blocks. As using this method the non-solvent is transferred via a gas phase diffusion step through the nanoparticle containing solution; the intermixing is more gentle than that of the usually applied liquid layer procedure[5,20], where the non-solvent stays directly in contact over a liquid-liquid phase boundary or is separated by a buffer layer. This direct contact of the solvent-non-solvent layer is avoided and in the following procedure the mixing of solvents or solutions of nearly the same density can be more effectively controlled and thus the need for a buffer layer is eliminated. The advantage of

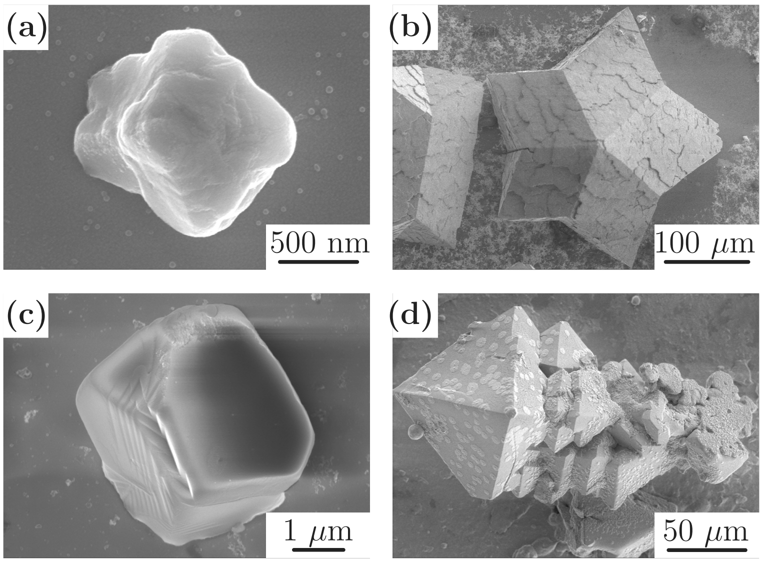

Figure 4.3.: ***Mesocrystals of PbS and PbSe nanoparticles prepared with the liquid-layer technique and the newly developed gas phase destabilisation technique.*** *The resulting structures from the liquid-layer technique (a,c) are smaller and less symmetrical due to the intermixing during overlay of non-solvent on top of the nanoparticle solution. The gas-phase diffusion technique overcomes this problem and a more controlled destabilisation follows from this (b,d).*

the new method is that on the one hand a better control of the phase boundary and hindering of the intermixing is achieved and on the other, the presupposed density gradient that is important for the liquid-layer technique is unnecessary, see Figure 4.3. However, the vapour pressure of the non-solvent needs to be higher than for the nanoparticle solution otherwise the solvent transport takes place in the inverted direction. To overcome this parameter limitation a buffer layer can be introduced into the system, but this is not required for the destabilisation experiments with PbS, PbSe and Au nanoparticles. Many parameters such as the solubility of the non-solvent in the NP solution, vapour pressure and temperature influence the destabilisation rate during mesocrystal formation. The exceptional advantage of the resulting structures is that they are ordered macroscopic materials with nanoscopic properties which are derived from the nanoparticular building blocks. The organic ligand shell surrounding the quantum dots inhibits the nanoparticles from merging during agglomeration and therefore helps to retain the advantageous properties of the microscopic building blocks whilst present in the macroscopic material.

4.3. Self-assembly of PbS and PbSe nanoparticles and mesocrystal formation

For the formation of highly ordered, periodic three dimensional structures from nanoparticles the building blocks play an important role having the potential to influence each stage of the formation process. For the destabilisation process introduced here we focus on highly monodisperse, nanocrystalline oleic acid capped PbS and PbSe building blocks. For 3D superlattice formation the monodispersity of the nanoparticles is fundamentally important in order to obtain a perfectly ordered close-packed arrangement. Kowalczyk et al.[15] have investigated crystalline arrangements formed using polydisperse building blocks and have reported that a size selective process occurs during the crystallisation of oppositely charged nanoparticles. In addition to the increasing polydispersity the amount of stacking faults and packing defects in the structures also increases while the size of the superstructures formed decreases. To avoid this, in the systems reported upon here, samples of very monodisperse PbS and PbSe nanoparticles have been used. To create single crystalline quantum dot solids, where the nanoparticles are arranged along a common crystallographic direction and possess a crystallographically hierarchical structure, as is the case for mesocrystals, such crystalline building blocks are ideally required. The building blocks must be single crystalline and without twinning as this influences the later atomistic-like arrangement within the single crystalline superstructure (superlattice)[21].

For the formation of PbS and PbSe mesocrystals the building blocks with an average size between 5-10 nm are synthesised (see chapter 3.1 for further details). During the complete destabilisation procedure the nanoparticles must remain stable under ambient conditions, which mean remaining stable in solvents such as toluene and octane in a temperature range of -23°C up to 45°C and under air. Absorption measurements of the nanoparticles over one week show (Figure 4.4a) a ripening process which is initialised by exposure with air. The monodispersity of the already quite uniformly sized nanoparticles increases over time. During this process the nanoparticle size becomes smaller resulting in the first and second transition bands sharpening and becoming blue-shifted (see Figure 4.4a). A plot of the radius versus time (Figure 4.4b) shows a first, but only temporary, increase in size during the first 8 hours for the samples exposed to ambient conditions and after this a continuous ripening process occurs. This process is only observed in

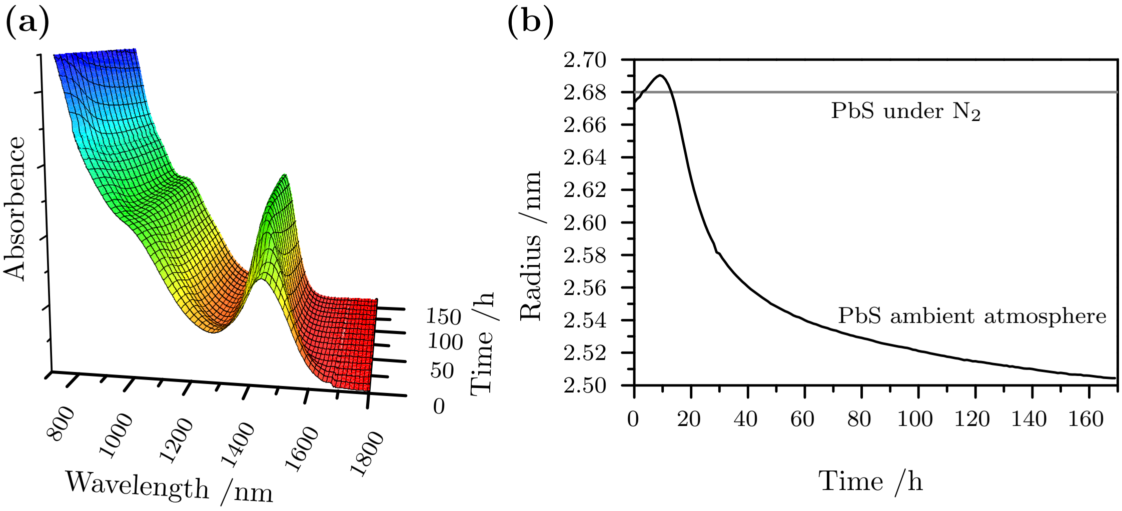

Figure 4.4.: ***Time dependent ripening process of the initial nanoparticles under air. (a) Absorbance measurements over time under air.*** *Peak sharpening of the first and second transition bands is observed which leads to a higher monodispersity of the building blocks. (b) NP radius over time visualizing the size change during the air induced ripening process. After increasing size the radius first quickly decreases and then slow down to approximatly a fixed value.*

samples exposed to air and takes place in a number of different solvents while samples under inert gas, but with all other measurement conditions the same, do not show this ripening process. It can therefore be assumed that during the ripening process ligands are removed from the surface and the mobility of ions and surface molecules increases. The size change observed is approximately in the range of two ionic radii of sulfur (1.84 $\AA$)[22] or lead (1.19 $\AA$)[22] or in the range of one PbS unit so that it appears likely that reactive species present in the samples exposed to air induce surface movement of single ions which may lead to the reduction of defects on the surface of the quantum dots, and which is energetically preferred for the minimisation of the surface energy. This process has also been observed in previous studies[23] where oxygen acts as a mediator but presently the reason for the ripening process is poorly understood and is still under investigation.

4.3.1. Destabilisation parameters

To optimise the production of ordered close-packed 3D structures the effects that the temperature, nanoparticle concentration and solvent/non-solvent pair have on the crystallisation process were investigated. In such systems temperature influences many parameters such as the solubility of the non-solvent in the nanoparticle solution, vapour pressure and inter-diffusivity rate to mention just a few. In addition the solubility of the nanoparticles increases as the temperature is increased. In this study three different temperatures have been investigated, -23°C (250 K), room temperature (25°C/298 K) and 45°C (318 K, see Figure 4.5). At 45°C it is observed that the diffusion of the non-solvent into the solvent occurs very quickly and hence the rate of destabilisation is relatively high. The agglomerates so produced therefore display few if any signs of ordering and do not form highly symmetrical architectures. Instead the precipitated particles form porous layers on the silicon wafer in the case of PbSe or only small non-ordered architectures in the case of PbS. By reducing the temperature the destabilisation rate is decelerated and the particles have more time to align and order during agglomeration. However, there appears to be a limit to this advantageous temperature effect as at -23°C symmetrical ordered structures can again no longer be found. Born et al.[24] have previously described an analogous phenomenon with gold nanoparticles where agglomerates of gold nanoparticles were formed only when a certain temperature is exceeded and the agglomeration rate was found not to influence the crystallinity of the agglomerates so created. Also when the agglomeration was slow non-ordered agglomerates were present. In dynamic light scattering (DLS) measurements, described later in the text, such large agglomerates were not observed at reduced temperatures but a broadening of the hydrodynamic radius and the presence of the first small aggregates of nanoparticles was observed at 2°C, see Figure 4.7. At lower temperatures it is likely that the ligands experience an enhanced stiffness which is expected given the fact that oleic acid has a melting point of 17°C and as a result the ligands can no longer easily bind together during agglomeration.[24–27] This lower flexibility hinders the rearrangement of the inorganic nanoparticle cores from the point that it hinders the surface diffusion of the nanoparticles with respect to one another. Furthermore, the attractive Van der Waals interactions of the ligand chains act to reduce the surface diffusion and they are one component, additional to the reduced ligand flexibility and others, of the energy barrier for the rearrangement of the nanoparticles. As a result the ligands are unable to form a well arranged superlattice as has been shown by Wang et al.[28] and hence only small, non-ordered architectures are formed. At room temperature larger ordered and facetted agglomerates can be found and as such this temperature appears to be conducive in combining a slower agglomeration rate, minimizing the formation

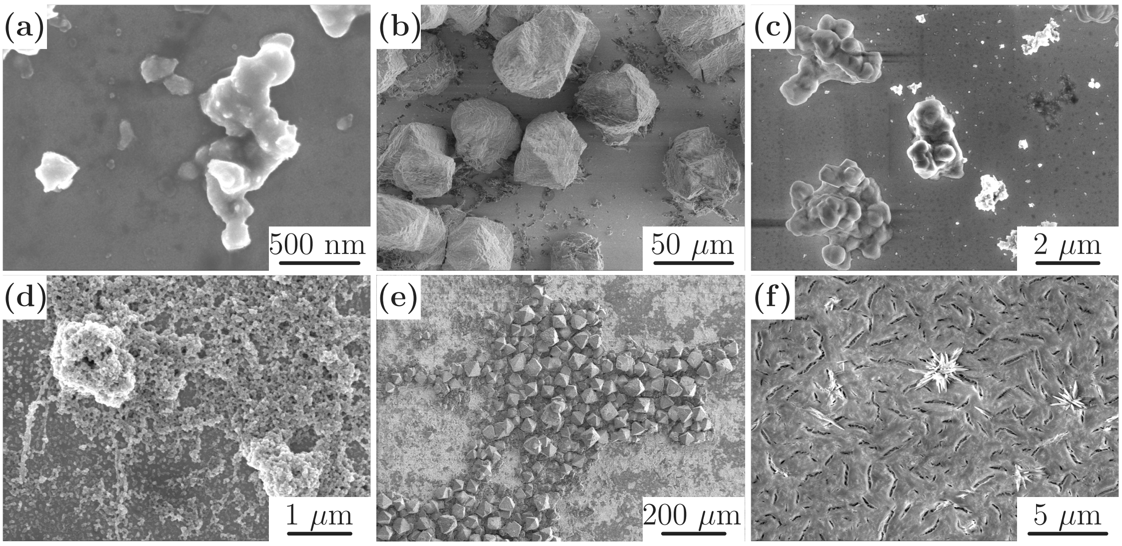

Figure 4.5.: ***Temperature influences on the destabilisation time and the mesocrystal architecture.*** *Low temperatures increase the ligand stiffness and hinder the ordered agglomeration; increasing temperature accelerates the destabilisation and enables ligand movement during agglomeration so that at room temperature the destabilisation rate is optimum. Higher temperature induces higher destabilisation rates that reduces the time scale of ordered self-assembly.*

of unordered agglomerates (c.f. 45°C) and providing a greater flexibility of the ligands so that interparticle rearrangement after first agglomeration is possible (c.f. -23°C) which is optimal for mesocrystal formation.

In addition to temperature effects the resulting architectures are also greatly influenced by the nanoparticle concentration. In solution the particle concentration impacts upon the mean free path and hence the degree of collision. The rate of agglomeration in a highly concentrated solution is therefore higher than in solutions with lower amounts of particles. These studies have revealed that a minimum particle concentration of 1 mg/ml of 5-10 nm sized nanoparticles is required for mesocrystal formation, with lower particle concentrations resulting in the formation of small amounts of porous non-ordered structures. The influence of the mass concentration was studied using 5, 10 and 15 mg/ml and two main trends were observed: i) the mesocrystal size increases at higher concentrations, but in a number of cases the superstructures merge together and ii) the amount of mesocrystals formed increases as the concentration is increased. Ordered architectures were achieved from all nanoparticle solutions containing between 5-15 mg/ml of nanoparticles. Using this effect to our advantage we were then able to optimise the process and synthesise structures in the size range from 15-350 μm. Another important parameter investigated was the solvent in which the nanoparticles were dissolved. For the gas phase method the vapour pressure of the solvent must be smaller than that of the non-solvent, otherwise the vapour transport is predominantly from the solution phase to the non-solvent phase. As representative solvents toluene and octane were used. In toluene both kinds of nanoparticles (PbS and PbSe) are very soluble and highly concentrated solutions are found to be stable over long periods of time. In octane the solubility of PbSe nanoparticles is less than in toluene with the result that the resulting stable concentration of these nanocrystals is much lower than for toluene. As a result after the addition of the precipitation agent (acetone, methanol, ethanol, 2-propanol or 1-propanol) a quicker destabilisation occurs and thick layers composed of PbSe nanoparticles without long-range order can be easily formed. By contrast however, PbS nanoparticles have a high solubility in octane and a slower destabilisation rate in comparison to toluene and therefore the formation of well faceted and symmetrical mesocrystals were observed. If one focuses on PbS nanoparticles formed using octane as solvent and acetone as non-solvent a change in the habitus of the mesocrystals formed can clearly be observed (see Figure 4.6). With a concentration of 5 mg/ml the main architectures that result are trigonal truncated pyramidal shapes. As the concentration is increased to 15 mg/ml twinning plays an important role and the main habitus is octahedral. It may also be observed that the crystalline structures formed have grown together, but in the correct crystallographic fashion. Twinning is in this case not only a function of particle size as Rupich et. al[6] have described it, but it is also a function of particle concentration and the combination of solvent/non-solvent pair used during the destabilisation process. For example, methanol as non-solvent is not an optimal non-solvent to use in combination with octane because of its low solubility in this solvent. As result the precipitation is attenuated and cannot be completed within the timescales employed here. In contrast to methanol, ethanol, 2-propanol and 1-propanol all behave in a similar fashion with respect to the mesocrystal habitus after destabilisation with all three non-solvents resulting in the formation of symmetrically shaped octahedral structures with very distinct facets. The destabilisation rate follows the same trend as expected with respect to the boiling points of the different non-solvents. The structural variety of the structures formed is lowest for acetone and the resulting architectures are not influenced by the nanoparticle concentration. The largest structural variety can be found when ethanol is

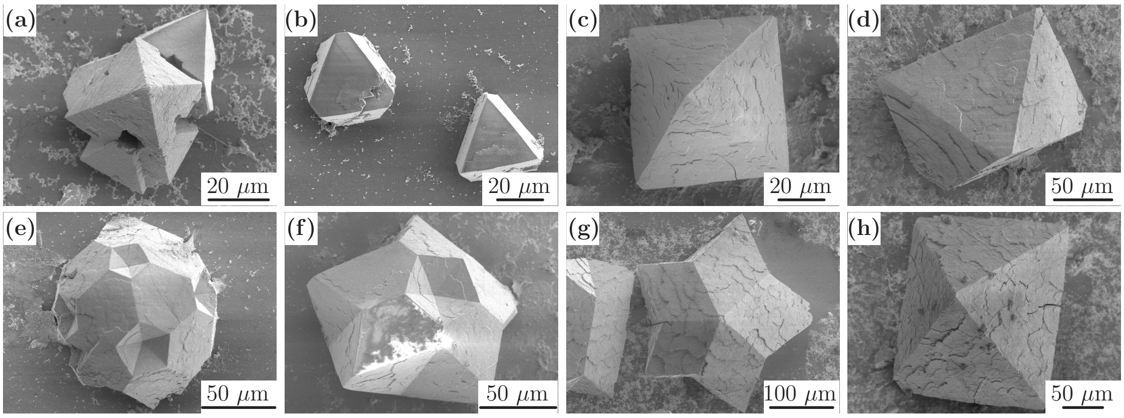

Figure 4.6.: ***Non-solvent changes lead to different mesocrystal architectures,*** *shown are the preferential morphologies obtained for the single octane/non-solvent pairs of PbS (a,b) acetone, (c,d) ethanol, (e,f) 2-propanol and (g,h) n-propanol*

employed as the destabilisation agent, where octahedral, truncated trigonal pyramidal, five armed star-like structures and Buckyball structures can be observed, and hence ethanol as non-solvent does not appear to act as a dominant structure determining medium. By contrast 2-propanol and n-propanol do appear to influence the habitus of the mesocrystalline structures. When 2-propanol is used as non-solvent only twinned structures, Buckyball structures and five-armed stars can be observed, while n-propanol shows less twinning than 2-propanol with octahedral and a small amount of five armed star structures being found on the substrate. The branched structure of 2-propanol may account for the higher propensity for twinning, but the influence of the non-solvent on the structure of the mesocrystals is still under investigation.

4.3.2. Mechanistical investigations of the destabilisation process

To understand the formation processes that give rise to such ordered mesostructures in more detail the evolution of the destabilisation process was monitored in-situ using DLS. It is not possible to directly measure the destabilisation process with DLS for all non-solvent systems studied here due to the accompanying changes in the refractive index of the solvent/non-solvent mixtures. It was necessary that the refractive index match the solvent/non-solvent pair in order to observe any changes due to the first steps of agglomeration and therefore a PbS nanoparticle

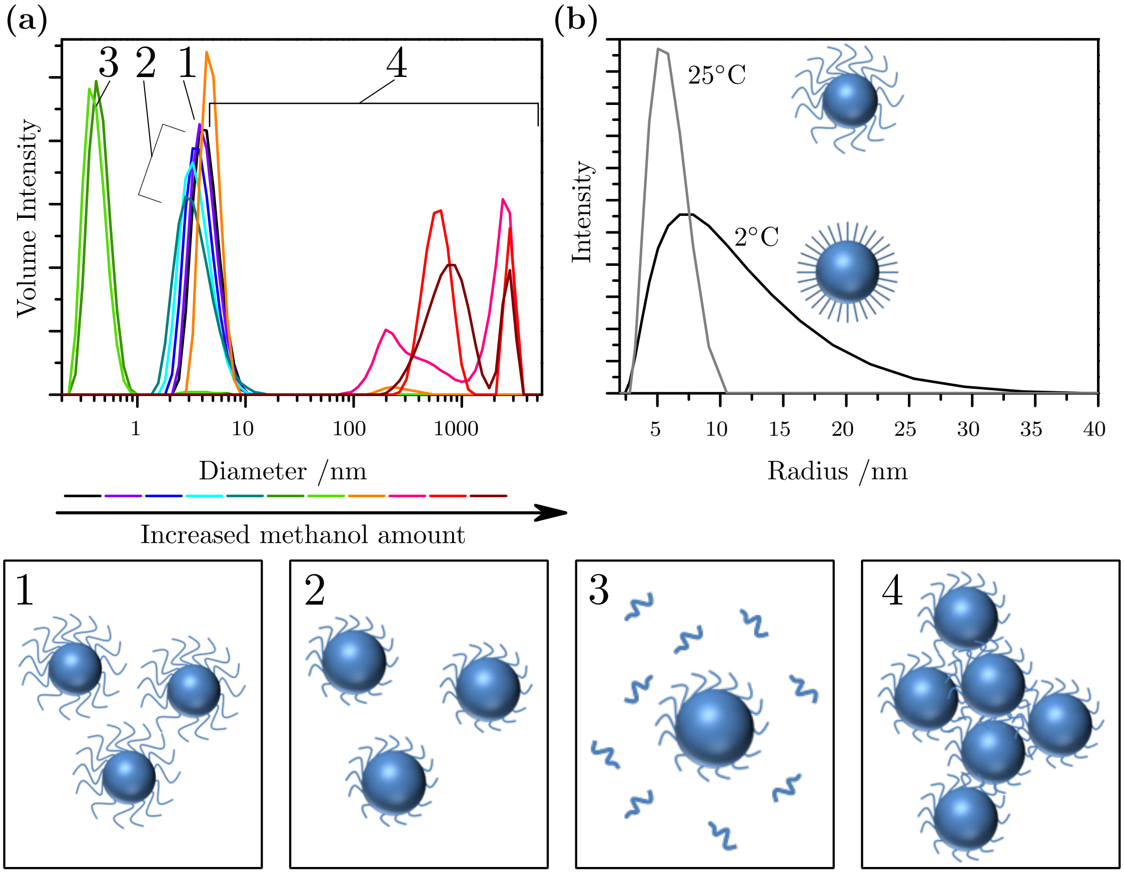

Figure 4.7.: ***Slow destabilisation of PbS nanoparticles with methanol during DLS measurements*** *show the ligand non-solvent interaction and the following ligand removal which results in agglomeration and temperature influences on the ligand flexibility and the hydrodynamic size of the NPs*

solution in toluene was slowly destabilised by the drop wise addition of methanol as non-solvent. In this scheme the nanoparticles may be considered as an inorganic core surrounded by a bound organic ligand shell, composed of oleic acid and tri-n-octylphosphine, these ligands behaving in a manner similar to the polymer chains of polymer brushes due to the limited space present at the nanoparticle surface.

Before the addition of the non-solvent, the pure solvent (toluene) acts as a good solvent for the aliphatic hydrocarbon chains of the oleic acid and tri-n-octylphosphine i.e. the interaction between the hydrocarbon segments with the solvent molecules is favoured (Figure 4.7-1). Upon the progressive addition of the non-solvent the polymer-solvent interaction becomes less favourable due to the changing solvent polarity which in turn results in the self-interaction between the ligand hydrocarbon chains becoming increasingly more preferred. The significance of this is that the polymer chains on the surface of the nanoparticle interact more strongly with their neighbouring ligand chains and consequently bind closer together (Figure 4.7-2). This unfavourable change in the solvent polarity also results in a closer packed ligand shell due to ligand contraction towards the nanoparticle surface and this in turn results in the reduction of the hydrodynamic radius as is shown in Figure 4.7. Upon further addition of non-solvent ligands are stripped off from the nanoparticle surface and can be found as single molecules in solution (Figure 4.7-3). This ligand removal results in further nanoparticle destabilisation and causes the formation of the first small nanoparticle agglomerates. Through the ongoing addition of non-solvent the ligand molecules stripped from the surface precipitate due to being less soluble in the resulting solvent mixture. In addition the lowered ability of any ligand shell left remaining on the nanoparticle surface to provide sufficient stabilisation causes agglomeration (Figure 4.7-4) because of the thermodynamic driving forces which result due to the higher surface energy of the unadorned nanoparticles and which can be minimised by the formation of agglomerates. The strongest attractive force during the slow arrangement occurs between the (111) facets of the single nanoparticles. Seen without ligands the (111) facet has the highest surface energy because of the presence of uncompensated charge.[29] The driving force towards destabilisation is the minimisation of the surface energy and is favoured in order to stabilise the structure. This results in a face-to-face arrangement inside the crystalline structure being preferred and this can be observed in the resulting structure discussed later in the section Crystal structure and internal arrangement of PbS mesocrystals. The complete agglomeration process can be followed for agglomeration sizes smaller than 6 μm as larger sized objects are out of the detector range or will quickly precipitate.

Additionally, temperature influences on the ligand shell can be studied with DLS. Reducing the sample temperature and keeping it constant over a short period of time results in an increased hydrodynamic radius. Born et al.[24] described analogous results with gold nanoparticles. The ligand shell, which behaves as do polymers, is stiffer at lower temperatures and so the interactions with the solvent molecules are limited and the polymer chains are inflexible so that the hydrodynamic radius increases. Unbound oleic acid molecules crystallise at 17°C. Bound to the nanoparticles the effect of lower ligand flexibility is observable at 5°C and below. The measurement range is limited by our particular DLS equipment because cooling below 0°C was not possible. As has been shown from the DLS measurements and also by Bodnarchuk et al.[8], during destabilisation at first agglomerates are formed in solution and these agglomerates act as nuclei for further crystal growth. While the processes involved in the positioning of these agglomerates is presently not fully understood, it is however clear that agglomerates are attached to the silicon wafer surface and crystal growth takes place there. After their deposition on the silicon substrate the nuclei agglomerates grow with additional nanoparticles being deposited from solution via destabilisation. We have observed in these studies that the crystals formed at the bottom of the vertically standing silicon wafer are normally larger in size. This may be rationalised by the fact that during destabilisation the non-solvent front is moving from the top of the solution through to the bottom so that the rate of destabilisation at different depths of the solvent and hence on different positions of the silicon wafer varies. Therefore at the top of the silicon wafer the nanoparticles have the shortest period of time to arrange while those at the bottom positions have the longest. As a consequence of this, and as Figure 4.8 shows, the effect of the destabilisation rate can be observed by examining the structures that occur at different depths (vertical positions) along the substrate as a function of time. At the beginning of the destabilisation process i.e. the top of the substrate, the agglomerates that are formed are not as symmetrical as those found further down. The agglomerates formed consist of only a small number of nanoparticles and so vacancies inside the structure can be found as defects and kinks, which are caused by the short agglomeration time and smaller amounts of material. It appears that the time range is too short for rearrangement of the nanoparticles and the force to minimise the surface energy of the mesocrystaline structures is too weak which is given further credence by the presence of only a small amount of nanoparticle arrangements. In the intermediate phase of the destabilisation i.e. the middle of the vertical standing silicon wafer, the structures are larger than those present at the top and begin to display the first presence of facets and a recognisable crystalline habitus. Compared to the structures observed at the top of the substrate an additional deposition of nanoparticles has taken place in order to form the crystalline materials observed. The nanoparticle arrangement is obviously driven by the minimisation of surface energy of the whole crystalline structure which results in a face-to-face arrangement of the single nanoparticles into the supercrystal.

The facets with the higher surface energy, due to their lower ligand coverage, are

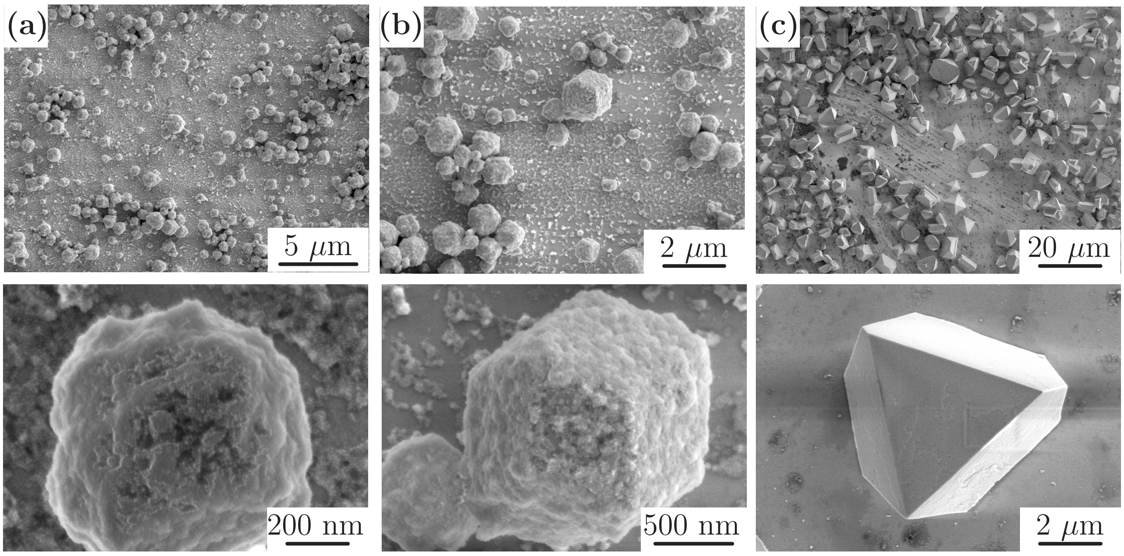

Figure 4.8.: ***Mesocrystal growth on different wafer positions*** *and so variation of the destabilisation time scale from (a) Si-Wafer top, (b) middle and (c) bottom*

the 111 facets as described by Bealing et al.[30] and so the arrangement of the 111 facets through a face-to-face orientation is plausible. Hence, the defects and vacancies observed at the top of the substrate are filled with nanoparticles. The effect of surface energy minimisation across every single nanoparticle leads to a highly symmetrical (face-to-face) arrangement which leads to the formation of the first facetted mesocrystalline structures. At the bottom of the silicon substrate highly symmetrical and well facetted crystalline structures of PbS and PbSe mesocrystals can be observed (see Fig. 4.8). The concentration of the ordered agglomerates on the bottom is significantly higher than at the top and variations in the habitus may also be observed.

4.3.3. Crystal structure and internal arrangement of PbS mesocrystals*

To investigate the inner structure of the PbS mesocrystals different techniques can be used. Non-destructive examinations are radiation based techniques. Here, octahedral shaped mesocrystals like that shown in Figure 4.9a have been investigated with X-ray diffraction. Small angle X-ray scattering (SAXS) will provide information concerning the nanoparticle arrangement within the mesocrystal while

---

*Parts of this section have already been published.[21]

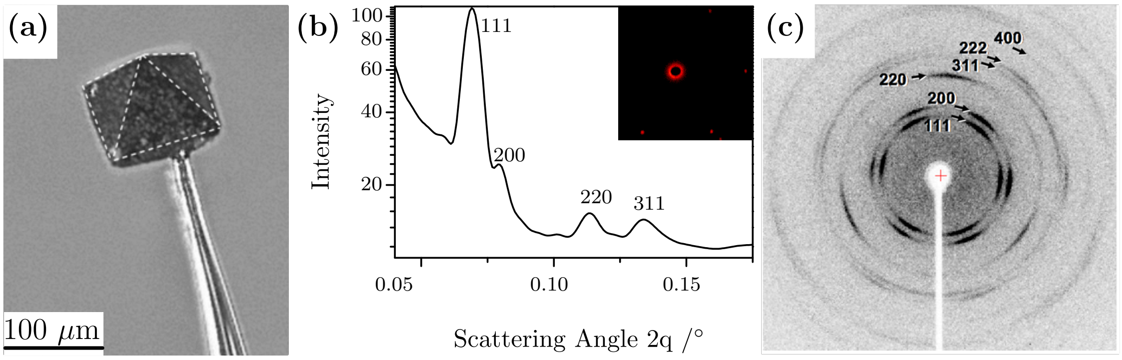

Figure 4.9.: ***SEM image of octahedral shaped PbS mesocrystal and corresponding X-ray diffraction pattern.*** *(b) shows SAXS results with the fcc packaging of the nanoparticular units and (c) represents the X-ray diffraction of the galena structure inside a mesocrystal illustrating the oriented arrangement along the [111] and [110] directions of the galena structure.*[21]

X-ray diffraction of the whole mesocrystal probes the crystal structure of the single nanoparticles, and in this case the reflexes are consistent with the galena structure. Figure 4.9b illustrates the arrangement of the single nanoparticles into a face centred cubic (fcc) crystal structure, which is not surprising for these kind of structures and has also been reported in literature.[6,7] Particular attention should be paid to the X-ray scattering data because as the Bragg part of the diffraction suggests the presence of a texture-dominated material with a high degree of ordering of the single nanoparticle units being necessary (Figure 4.9c) in order to receive such a diffraction pattern. Statistically arranged crystalline building blocks should show circular scattering. Here, single reflexes can be determined by X-ray diffraction recorded along the [111] direction of the octahedral mesocrystal, which indicates a long-range ordering of the single nanoparticles to each other. In the Figure are shown the (111) and the (200) reflexes of the galena structure, which should be absent in the X-ray scattering of a single crystalline galena structure along the [111] direction. The broadening of the (111), (200) and the (220) reflexes of the galena is 15-20°. Both effects, the broadening and the presence of the (111) and (200) reflexes, suggest a preferred but not perfectly aligned nanoparticle arrangement along the [111] and the [110] direction of the galena structure.

In contrast to non-destructive methods polishing and cutting procedures can also be used to investigate the inner structure of the mesocrystals. One advantage of this is the visual control of these analyses. The non-destructive techniques

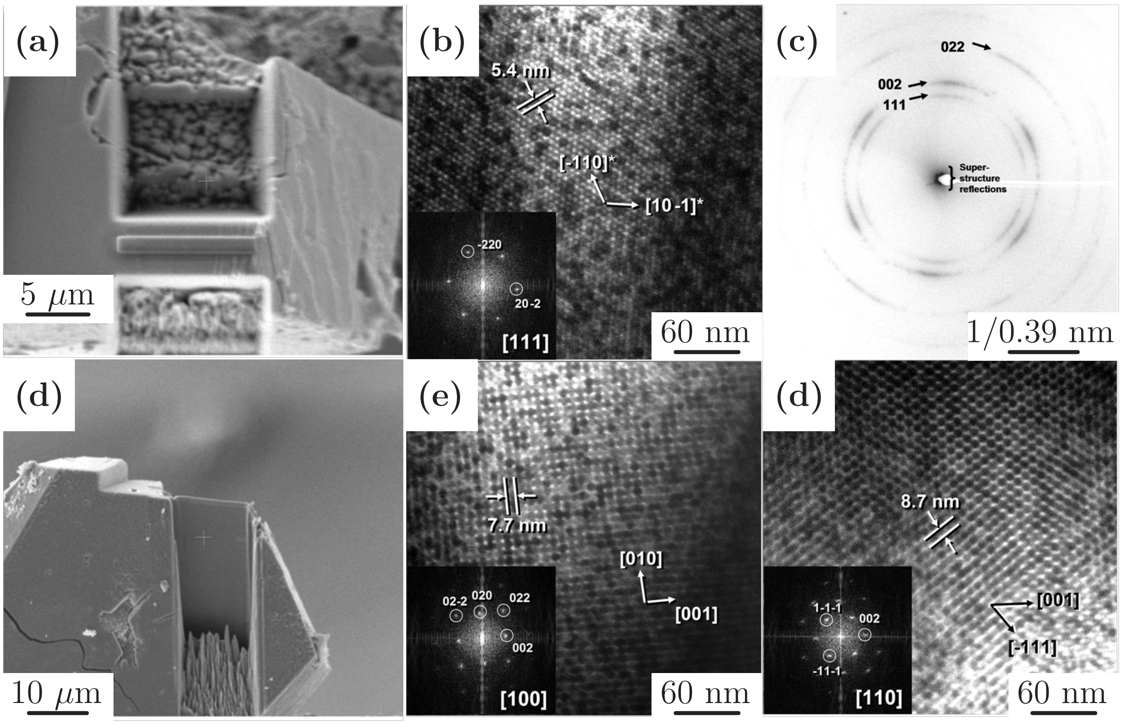

Figure 4.10.: ***FIB cuts and HRTEM investigation of the inner structure.*** *The TEM images with FFT inlays representing the different crystal orientations. (c) Electron diffraction pattern corresponding to (b) showing the galena and the superstructure ordering.*[21]

are only capable of determining crystalline structures, so that possible amorphous inner parts may remain undetected. To get a first impression of the sample homogeneity, polishing of the mesocrystals showed that their internal structure was without cracks and grain boundaries on the length scale of micrometers. Additionally the homogeneous inner structure can then be imaged. For measurements with HRTEM polishing of the structures is not sufficient and so thin cuts via focused ion beam (FIB) techniques are used to prepare nanoparticle monolayers (Figure 4.10). Conventional methods such as diamond cutting techniques could introduce artefacts into the structure, which result from the mechanical stress during preparation. FIB techniques avoid this mechanical stress so that the internal structure can be investigated without having introduced artefacts. Inserting epoxide monomers into the structure, to harden it before cutting, lead to uncontrolled swelling and deformation of the mesocrystaline structure. With the help of three different orientations of superlattice [111], [100] and [110] (Figure 4.10) measured after FIB cut and identifying the orientation of the nanoparticular building units

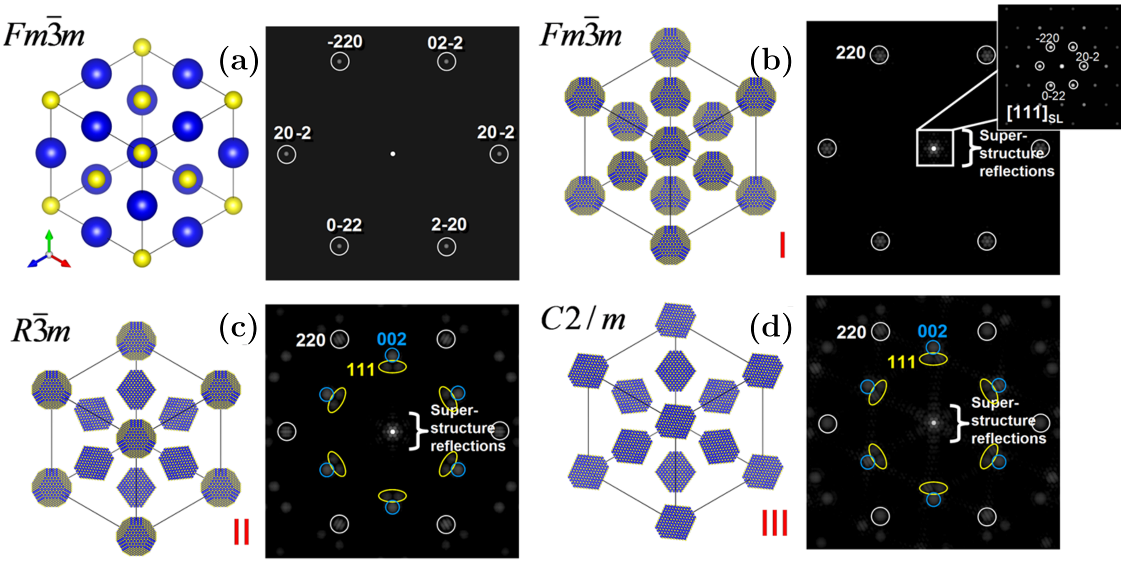

Figure 4.11.: ***Simulated arrangements of nanoparticles using different models.*** *(a) [111] Projection of galena (PbS) crystal structure with corresponding simulated SAED pattern; (b, c, d) Projections along the [111] of simulated PbS mesocrystals (models I, II, III) with corresponding simulated SAED patterns, illustrating orientational relationship between superstructure and PbS (galena) nanocrystals reflections. The sets of equidistant 220, 002 and 111 PbS Bragg reflections are marked with white, blue and yellow circles, respectively.*[21]

as being fcc, the unit cell of the superstructure was determined as $a_{Mesocrystal}$=15.4 nm. This stands in good agreement with the approximated value calculated for 5.5 nm sized nanoparticles with a ligand shell containing 1.8 nm long oleic acid molecules.[31] Upon examination of the thin cut of the [111] zone in more detail the FFT shows only (220) reflexes that represent hexagonal symmetry with a lattice distance of $d_{220} \approx 5.4$ nm. The corresponding electron diffraction pattern looks similar to the X-ray diffraction in the wide angle region. Additionally, the small angle region of the electron diffraction presents the diffraction pattern of the superlattice arrangement and shows hexagonal reflexes because of the highly ordered nanoparticle arrangement (Figure 4.10).

The PbS mesocrystals presented here are unique and their internal structure is different from the previous structurally characterised systems reported in literature.[31–33] Here, the truncated octahedral PbS nanoparticles self-assemble into a fcc superlattice with long-range orientation of the building units while keeping their preferred crystallographic orientation limited to shorter ranges.

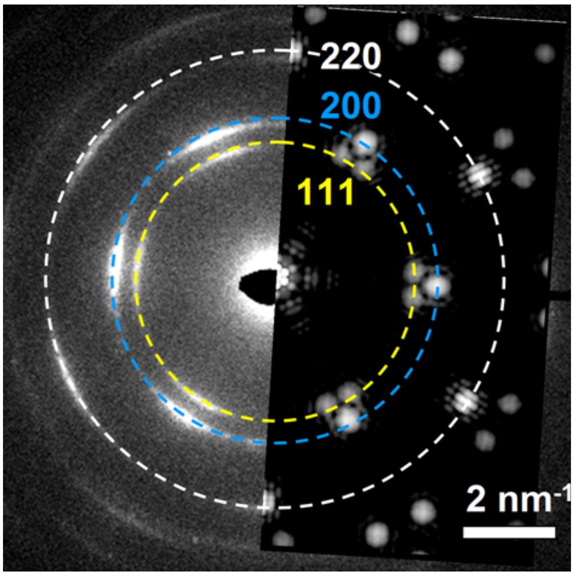

Figure 4.12.: ***Comparison of experimental and simulated SAED pattern recorded along [111]of PbS-mesocrystal.*** *Simulated SAED was obtained by superposition of ED patterns calculated using proposed models I, II and III.*[21]

To gain deeper understanding of the mesocrystaline arrangement the internal structure has been simulated using model structures focussing on the different orientational alignment of the PbS nanoparticles. The basic model represents the arrangement of truncated octahedral PbS nanoparticles as they are described in the section on nanoparticular building blocks on an fcc $Fm\bar{3}m$ structure with unit cell parameter of 15.4 nm. The crystallographic orientation of the nanoparticles is kept coaxial to the fcc lattice that maintains the initial symmetry of the galena crystal lattice. The simulated electron diffraction pattern differs strongly in the wide angle region from the experimental data so that additional modifications such as particle rotation are required to fulfil the orientational correlation $[111]_{Mesocrystal} \parallel [110]_{Galena}$. In model II the nanoparticles only in the centre of the unit cell and in model III additionally at the vertices are rotated. The space-group symmetries of the colloidal nanocrystal superlattices for models II and III are $R\bar{3}m$ and $C2/m$, respectively. The results presented in Figure 4.11 are already closely related to the experimental electron diffraction patterns, see Figure 4.12. This allows us to interpret the electron diffraction patterns from the experimental data as being a superposition of the electron diffractions of the simulated model structures. Both models represent a close approximation of the single-domains within the multidomain structure of the PbS mesocrystals. Furthermore, a systematic analysis of the orientational relationships between the single truncated PbS nanoparticles indicates a face-to-face arrangement within the closed packed layers while keeping a certain degree of orientational mismatch.

4.4. Mesocrystaline arrangement of gold nanoparticles[†]

Analogous to the destabilisation of PbS and PbSe nanoparticles the gold nanoparticles are also self-assembled. The gas-phase diffusion method with optimised parameters as determined for semiconductor nanoparticles is adapted for the slow destabilisation and arrangement of gold nanoparticles. The as-synthesised gold nanoparticles described in chapter 3.3.1 with an average diameter of 5 nm and oleylamine as stabilizing ligand have been used. In comparison to lead chalcogenide nanoparticles the gold particle morphology is highly twinned and as result cannot be considered as homogeneous.

4.4.1. Destabilisation parameters

Instead of oleic acid as stabilizing ligand oleylamine is bound to the gold nanoparticle surface. These two ligands only vary in their head group which bounds to the nanoparticle surface. Hence, the presumption of nearly equal ligand behaviour is close observed but needs to be confirmed. After testing the temperature dependence of the destabilisation of oleylamine capped gold nanoparticles it was found that the results are similar to those obtained for the lead chalcogenide destabilisation. As is shown in Figure 4.13, increasing temperature results in an increase in the destabilisation rate and shortens the self-assembly time. Destabilisation at 40°C takes 2 days on average in comparison to destabilisation at 22°C which needs 1 week and at 8°C and -10°C takes several weeks. As was observed for the previous optimisation conditions the best 3D arrangements are possible between 8-22°C. Higher temperatures hinder a controlled agglomeration due to the high destabilisation rate and too short a time for rearrangement. Too low a temperature induces a higher ligand stiffness and so a reduced ordered agglomeration resembling to sit-

---

[†] The results of this chapter were partly obtained within the framework of the bachelor thesis written by M.Sc. Danny Haubold[34] under the mentoring of the author.

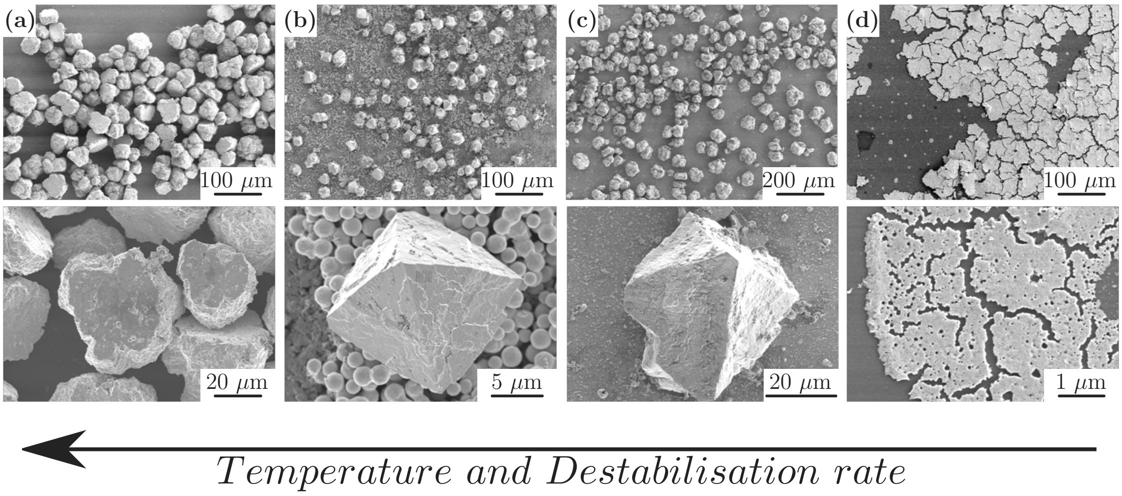

Figure 4.13.: ***Temperature dependence of mesocrystal formation with gold nanoparticles.*** *Increasing temperature results in increasing destabilisation rate reducing the ordered self-assembly. Below the melting temperature of oleylamine the stiffness of the ligands increases so that rearrangement is hindered by entanglements.*

uation for the oleic acid capped nanoparticles. Analogous to oleic acid, oleylamine as a molecule freezes below 21°C. In the temperature range between 8 and 22°C the degree of completely arranged mesocrystals present accelerates with increasing temperature in the same way as that observed for oleic acid capped nanoparticles with room temperature providing the best results.

The nanoparticle concentration in toluene or octane as solvent influences the interparticle interactions during mesocrystal formation because the strength of the single forces mostly decrease non-linearly with interparticle distance. Therefore, it is indispensable for mesocrystal formation to overcome a critical formation concentration. For lead sulphide and lead selenide the concentration is 1 mg/ml and gold nanoparticles must also exceed this critical concentration. Experiments with higher concentrations, like 5 mg/ml, show highly symmetrical mesocrystals with sizes in the range of 15-30 μm. Many of the self-assembled structures are not complete and only few of these crystals are observed on top of the silicon wafer, while at the end of the formation process the amount of dissolved nanoparticles is too low to end up forming ordered structures. By increasing the mass concentration of the solution mesocrystals of the same size, but nevertheless completed are determined. Additionally, on the wafer there are many small nuclei that have also precipitated and which would have been formed at the end of the formation pro-

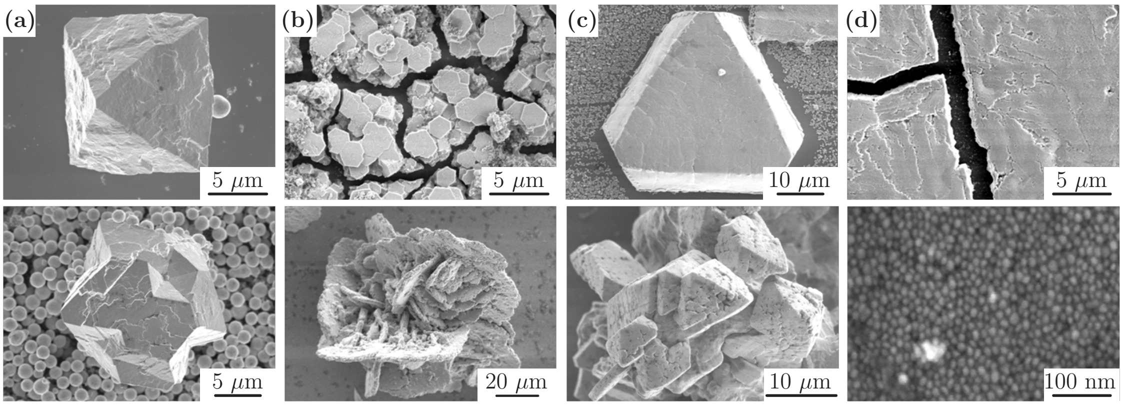

Figure 4.14.: ***SEM images of gold mesocrystals and layers.*** *(a) toluene/-ethanol, (b) toluene/n-propanol, (c) octane/n-propanol and (d) octane/acetone, methanol, n-butanol.*

cess had the amount of nanoparticles remaining in solution been sufficient to grow them into bigger structures. Near the saturation concentration of the solutions (15 mg/ml) less ordered but bigger agglomerates, in the size range of 10 μm up to 1 mm, are assembled. Most agglomerates show an intergrowth that results in these big structures.

As is described for PbS and PbSe nanoparticles the solvent/non-solvent pair influences the destabilisation rate via the vapour pressure and polarity of the non-solvent. The lower polarity of the n-octane seems to stabilise the gold nanoparticles less effectively than the more polar toluene. Consequently, the destabilisation with n-octane as solvent delivers mostly homogeneous layers with cracks occurring during the drying procedure (Figure 4.14). Only n-octane/n-propanol form mainly trigonal planar structures that intergrow from time to time. Better results for three-dimensional ordered agglomerations are observable using toluene as solvent and ethanol or n-propanol as non-solvent. The variety of as-prepared structures ranging from octahedral mesocrystals through hexagonal structures up to twinned structures such as five-armed stars, so called “stella quinquangula” (Figure 4.14). The tendency of ordered arrangements decline below 0°C and layer arrangements increases. In comparison to lead chalcogenide mesocrystals the sizes of the gold mesocrystals (5-30 μm) are much smaller than those of the semiconductors. In addition, the tendency for twinning and intergrowth is higher for the gold nanoparticles possibly caused by the multidomain structure of the initial nanoparticles. Moreover, the combination of toluene and n-propanol leads to rosette-like structures which formed with plate-like structures. All in all the destabilisation parameter optimisation does not appear to increase the structure size and hinder the twinning and intergrowth of the formed mesocrystals.

4.5. Comparison of the destabilisation of lead chalcogenide and gold nanoparticles‡

The resulting mesocrystals produced using the lead chalcogenide and gold nanoparticles differ mainly in their size and degree of twinning. To get a deeper understanding of the formation process and of the inner nanoparticular arrangement all three steps of mesocrystal formation are considered and compared.

Starting with the nanoparticular building blocks, the size of the zero dimensional formation units used to form the later structures are regulated so that the dimension of both sets of particles is similar having an average diameter of 5 nm. Only the capping ligands vary in their binding head group, for lead chalcogenides it is oleic acid and for gold nanoparticles oleylamine. Both sets of nanoparticles possess an alkyl chain that is equal so that the melting point and Van der Waals interactions between the molecules should be similar. That this may be the case is also indicated by what is observed in the temperature studies of the formation process and the thermogravimetric analysis of the building blocks. The main difference between the building blocks is their crystal structure. The lead chalcogenide nanoparticles are single crystalline and all show the same truncated octahedron morphology. The gold nanoparticles have a large degree of structural variety ranging from single crystalline particles up to multidomained, twinned structures. Consequently the morphology of the single gold nanoparticles is diverse and so too is the interparticle forces associated with every morphology which could lead to twinned mesocrystals.

To form and examine two dimensional structures, the nanoparticles are placed on a TEM grid. With the help of FFT the particle orientation of each particle can be determined. For PbS nanoparticles orientations along the [110], [112], [100] and [111] are observed on the TEM grid. The simulated morphology is shown in Figure 4.15. Furthermore, the orientational ordering of the single nanoparticles corresponding to the FFTs is presented. 70% of the investigated nanoparticles possesses the [110] orientation and 10% the [111] orientation. All other orientations represent interme-

---

‡Parts of this section have already been accepted in Advanced Materials[35] and the results of this chapter were partly obtained within the framework of the master thesis written by M.Sc. Danny Haubold[36] under the mentoring of the author.

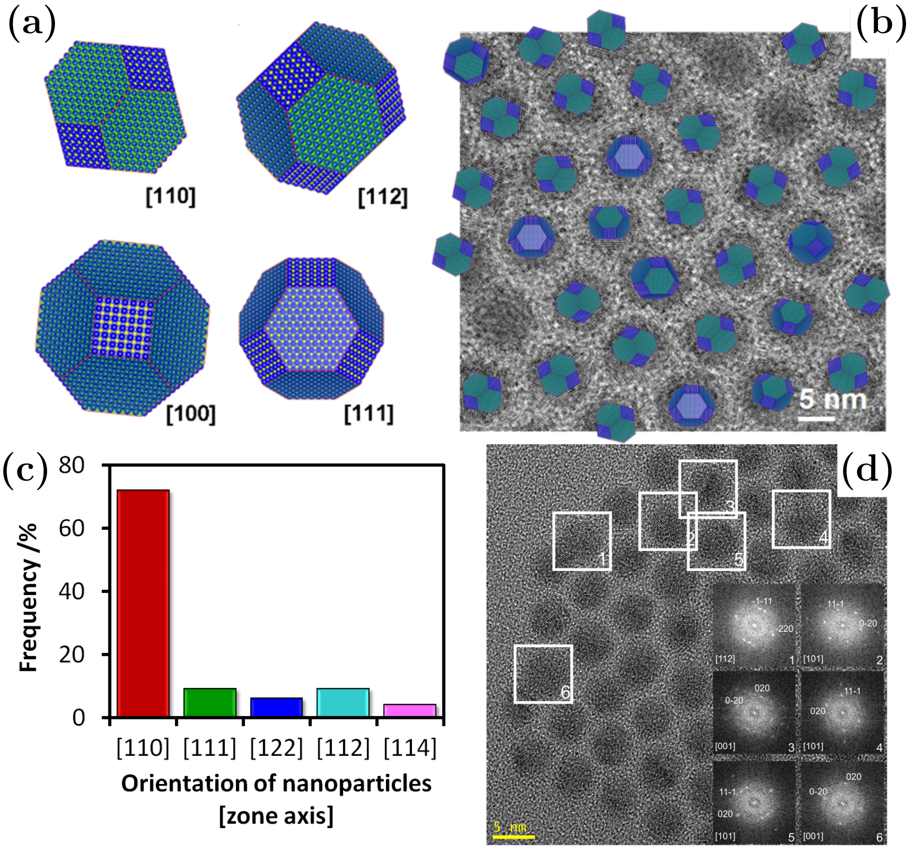

Figure 4.15.: ***Comparison of the alignment of PbS and Au 2D nanoparticular layers.*** *(a) represents the observed orientations of PbS nanoparticles, which are present in the 2D layer (b). (c) Statistical overview of the orientations present in the PbS nanoparticle layer. (d) TEM image with the corresponding FFTs of a 2D gold nanoparticle layer.*[35]

diates between these two configurations with a tilting of 20-30°. It can be seen that in such a 2D arrangement the PbS nanoparticles align in the preferred face-to-face orientation, which can be also found in the 3D mesocrystals. By contrast, the arrangement of gold nanoparticles is difficult to determine because the nanoparticles are multidomained and the orientation of the single particles cannot be analysed from the FFTs. Only a few particles show interpretable reflexes in the FFT, but sometimes also twinning is observed inside the structure. An analysis of the FFTs of the single particles reveals a random distribution of their relative orientation, which is in contrast to the reported arrangement of PbS.

The face-to-face orientation of the PbS nanoparticles seen in the two dimensional assembly is also observed in the 3D mesocrystals. The uniformity of the single nanoparticles and the apparently similar forces that drive the assembly towards the face-to-face orientation that derive from this are able to form highly ordered mesocrystals with a lower amount of defects. Gold nanoparticles with highly intrinsic twinning in their gold crystal structure are less uniform and so a lot of defects are introduced into the structure during self-assembly and as result less symmetric mesocrystals are formed. The smaller sizes can be an effect of the higher nucleation rate of the gold nanoparticles during destabilisation because the energy of the different facets varies strongly depending on the morphology of the nanoparticle. Fewer stabilised facets of higher energy will form agglomerates earlier than stable facets so that it is possible that mesocrystal growth stops with a coverage of highly stabilised nanoparticle facets in comparison to the energy levels of destabilised facets present in solution.

4.6. Mesocrystal modifications for conductivity measurements

For later application as thermoelectric material the conductivity of the initial mesocrystals have to be characterised. Thus, the mesocrystals with their sizes between 10-350 μm have to be contacted via electrodes. Standard equipment for contacting these 3D samples is not available so that modified techniques have to be used. One method for contacting the mesocrystals is using interdigitated gold-electrodes with distances below 50 μm and with macroscopic contacts (Figure 4.16). The mesocrystals are suspended in a methanol solution to remove some of the surface ligands and then drop cast from solution on top of the electrodes. Methanol evaporates and only the mesocrystals are left on top of the gold contacts. Applying a voltage between the contacts not give any meaning results as the currents measured were too small. The mesocrystals can be easily removed from the electrode surface because the only interaction between the mesocrystals and the gold electrodes is their inherent adhesion. To enhance the effective forces between the crystals and the gold electrode linker molecules were utilised, with dithiol-functionalised molecules being especially favourable for this application. As linkers 1,2-Dithiolethane, 1,6-Dithiolhexane and 1,4- Dithiolbenzene are used as was previously reported by Joseph et al.[37] for interconnection of gold nanoparticles. The gold electrodes are covered with the thiol molecules at a pH<7 to activate the thiol group. After a number of washing steps the mesocrystals are added to the solution and kept to

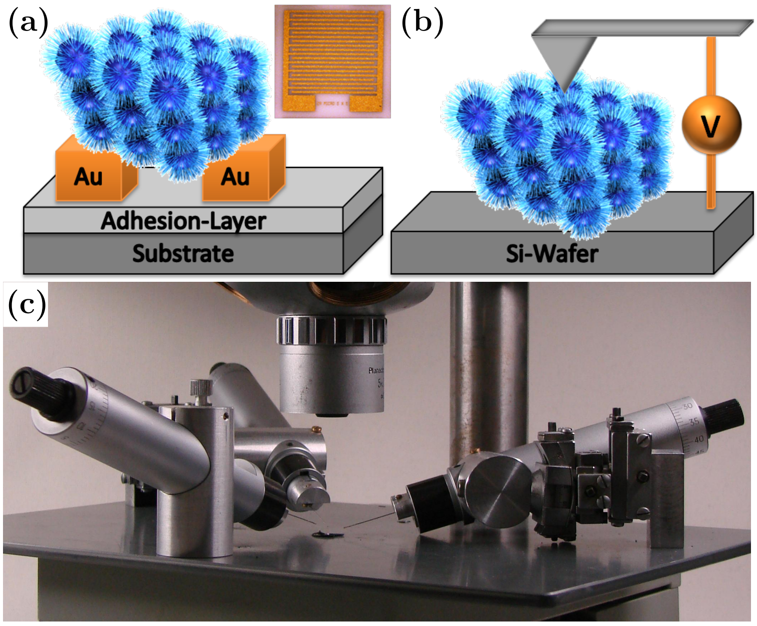

Figure 4.16.: ***Types of electrode connections on mesocrystals.*** *(a) showing interdigitated gold-electrodes, (b) AFM measurements in contact mode and (c) using micrometer screws for electrode connection.*

react overnight. After solvent removal the measurements were initiated, but the resistivity of the mesocrystals is too high or the electrode contact insufficient to measure conductivity.

Conductivity measurements, done with atomic force microscopy in contact mode, also provided results showing a high resistivity, similar to the interdigitated gold-electrodes. Another possibility is to use micrometer screws and an optical microscope to contact the mesocrystal manually using two electrodes (Figure 4.16). Unlike the case of the interdigitated gold-electrode the distances of the electrodes are undefined and additionally, the mesocrystal slightly deforms during contacting process. Here measurements of the PbS and PbSe mesocrystals show a high resistivity being very near to the limit of detection of the measurement setup. The high resistivity of the mesocrystals is most likely as a result of the coverage of the nanoparticle surface with long-chained organic ligands, which hinder electron transport through the structure.

To reduce the resistivity removal of these surface stabilisers can be achieved in two ways. One is ligand exchange with conductive and short ligands and the second pathway is to apply a heat treatment and so decompose the long-chained organic ligands.

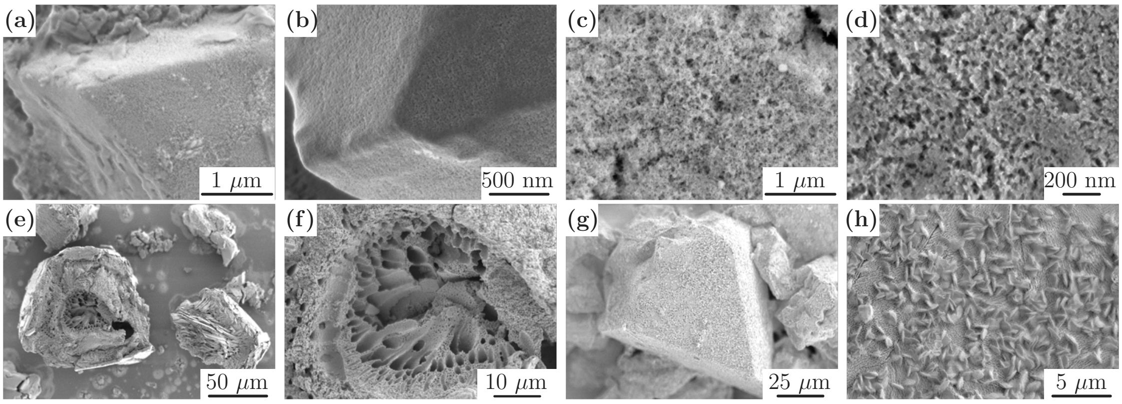

Figure 4.17.: ***Mesocrystals after ligand exchange*** *with (a-d) formic acid in time steps of 10, 30, 90 and 180 minutes and (e, f) with acetic acid and (g, h) with oxalic acid.*

Ligand exchange experiments were carried out with short-chained carboxylic acid ligands, e.g. formic acid, acetic acid and oxalic acid, see Figure 4.17. The ligand exchange has been reported on 2D quantum dot films in the literature.[38] Therefore concentrations of 1 mM up to 10 mM acid solutions are used for the ligand exchange. As reported in the literature oxalic acid shows the highest capability to exchange the oleic acid ligands completely, but for all three ligand solutions too long an exposure time and high concentrations of ligand molecules induce etching at the nanoparticle surface. Hence, different concentrations and exchange times were tried to optimize the ligand exchange for the 3D mesocrystals. The longest exposure time was 18 hours with 10 mM carboxylic acid solution in acetonitrile. All samples show etching and only sponge-like structures are observed after this treatment. Lowering the concentration to 2 mM and varying the reaction-time with surface etching of the nanoparticles still possible to determine after 10 minutes even with formic acid, the substance of lowest reactivity. After 3 hours the whole structure has completely interacted with carboxylic ligands, and only a fragile sponge-like structure is left. Consequently, the ligand exchange with short-chained carboxylic acids cannot be adapted from 2D films to mesocrystals because the surface etching and related destruction of the highly ordered arrangement take place. Also ligand exchange experiments with ligands like butylamine and ammonium sulphide does not work because the interparticle regions within the whole structure and not only the surface region must undergo exchange with the new ligands which influences strongly the stability of the mesocrystaline arrangement.

Another pathway for ligand removal is heat treatment of the mesocrystals. The

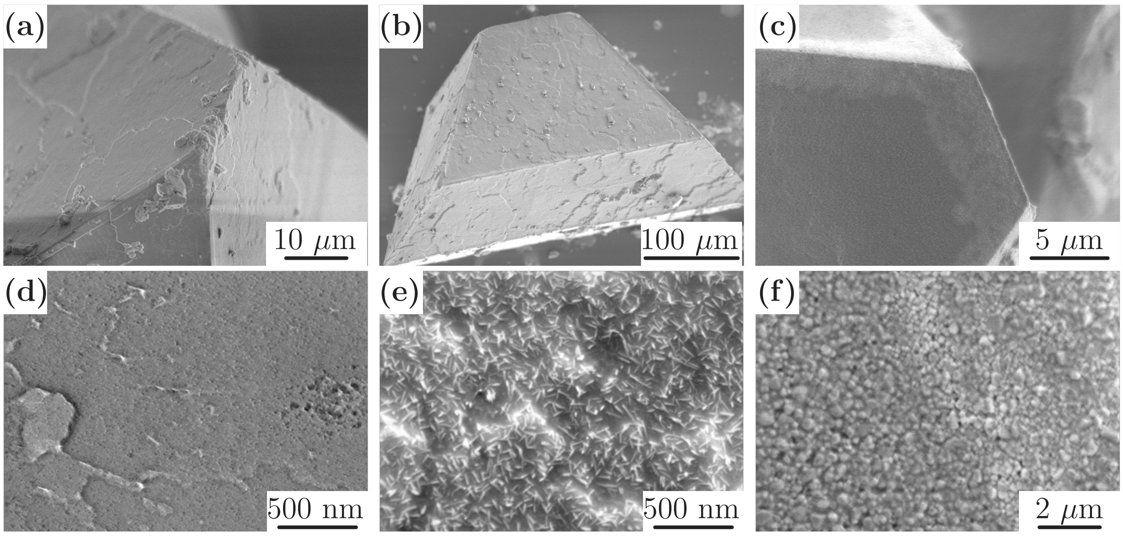

Figure 4.18.: ***Thermal treatment of PbS mesocrystals.*** *All SEM images show mesocrystals after a reaction time of 30 minutes with (a) 200°C, 350°C, and 500°C.*

TGA-MS measurements of the PbS and PbSe nanoparticles show ligand degradation starting at 200°C. Heat treatment at 200°C, 350°C and 500°C with reaction times of 10, 20 and 30 minutes were investigated (Figure 4.18). All samples heated to 200°C and 350°C possess high resistivity values as measured using a two electrode method. Only the samples at 500°C and 30 minutes removal time shows some degree of conductivity, but SEM images show the mesocrystal surface to have melted , and the nanoparticles to have formed bigger crystalline domains. Already at 350°C the domain formation starts after longer exposure times (30 minutes), but under such conditions the conductivity was not influenced. The TGA-MS experiments show the part decomposition of the protecting and insulating ligand shell and the partially removed ligands presumably destabilise the surface of the single building blocks so that PbS and PbSe units are able to move along the nanoparticle surface and so larger domains that remain insulating are formed, which remains low in conductivity after partial intergrowth of the whole mesocrystaline structure. Higher temperatures induce faster and more frequent intergrowth of the nanoparticular units so that a percolation length over the whole structure is built and so the conductivity increases. Additionally, holes can be found on the molten mesocrystal surface that may be pathways, through which the decomposed ligands of the inner nanoparticles leave the structure as gaseous products. A more gentle heat treatment on 2D nanoparticle arrangements were initiated to see if any changes

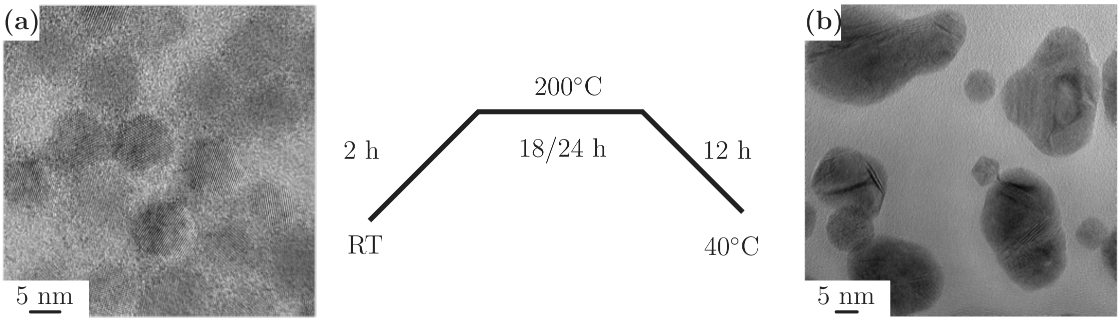

Figure 4.19.: ***Heat treatment of 2D nanoparticular layers.*** *PbS nanoparticles keep their shape and size and start to align along one orientation (a). First intergrowth can be observed. Gold nanoparticle arrangements melt together to form bigger sizes while detached nanoparticles kept their shape and size (b).*

in the crystallinity and/or ligand removal occurred over time using TEM imaging. Thus, TEM grids with nanoparticle arrangements were heated under an argon atmosphere for 24 hours at 200°C. As is shown in Figure 4.19, the nanoparticles are still present in their "initial" form only the interparticle distances are reduced. Some nanoparticles start to grow together so that longer heat treatment would likely lead to bigger particle domains. The same experiment for gold nanoparticles, but with 18 hours heating at 200°C shows big particle domains, where 2D nanoparticle arrangements had been previously present. Single nanoparticles are not influenced by the heat treatment because here the higher surface mobility of the atoms cannot induce intergrowth. Consequently, the experiment shows that the barrier to surface movement of single gold atoms in comparison to PbS or PbSe units is lower. Further experiments, are planned to determine more precisely the conditions under which this occurs.

4.7. Résumé

It could be shown, that the new gas-phase diffusion technique is suitable to form highly symmetrical and ordered three-dimensional superstructures with semiconductor and metal nanoparticles. Thus the building blocks and their intrinsic crystal structure influences the mesocrystal formation mainly because during the formation process not only do nanoparticles arrange into a crystal lattice but additionally the nanoparticles are aligned along a crystallographic fashion. The single crystalline PbS and PbSe nanoparticles are able to form large and highly symmetric mesocrystals by face-to-face arrangement of the single building blocks. In comparison gold nanoparticles, with their internal multidomain structure, only form smaller and less symmetrical mesocrystals with a higher amount of defects and twinning caused by the differences in the morphology of the building units. Furthermore, DLS measurements shine some light into the formation process and the temperature dependence of this process with respect to ligand flexibility. Low temperatures increase the ligand stiffness and as a consequence, the ordering during agglomeration gets lost through entanglement of the ligands. Moreover, the temperature also influences the destabilization rate and too high a temperature induces agglomeration too quickly so that ordering on this time-scale is no longer possible. Additionally the influence of the nanoparticle concentration and solvent/non-solvent pair has been examined. The internal structure of the PbS mesocrystals gives us a deeper understanding of the formation and also stabilization of the mesocrystals. The differences observed in the 2D arrangements of gold and lead chalcogenide nanoparticles compared to those of the 3D structures, possessing different sizes and degrees of defect formation, can be explained from the knowledge gained from the 0D and 2D experiments. The 2D arrangement with the differences in nanoparticular alignment gives additional hints as to the smaller sizes and less symmetrical shapes of mesocrystals that can be formed with gold nanoparticles. At the end, the modification of the mesocrystals via ligand exchange and thermal treatment was presented to realize a higher conductivity for further applications. The long-chained organic ligands of the mesocrystals act as insulators resulting in a high resistivity of the structures. In fact as no commercially available standard measurement setups were suitable, a number of different techniques have been used for the conductivity measurements. Only a thermal treatment of the mesocrystals increased the conductivity, but the nanoscopic properties are destroyed by surface melting and so bigger domain sizes result. A more gentle thermal treatment was undertaken with 2D arrangements in order to follow the merging process.

4.8. References

1. Whitesides, G. M. & Grzybowski, B. A. Self-assembly at all scales. *Science (New York, N.Y.)* **295,** 2418–21 (2002).
2. Grzelczak, M., Vermant, J., *et al.* Directed self-assembly of nanoparticles. *ACS nano* **4,** 3591–605 (2010).
3. Cölfen, H. & Antonietti, M. *Mesocrystals and Nonclassical Crystallization* (Wiley New York, 2008).
4. Kagan, C., Murray, C. & Bawendi, M. Long-range resonance transfer of electronic excitations in close-packed CdSe quantum-dot solids. *Physical Review B* **54,** 8633–8643 (1996).
5. Talapin, D. V., Shevchenko, E. V., *et al.* A New Approach to Crystallization of CdSe Nanoparticles into Ordered Three-Dimensional Superlattices. *Advanced Materials* **13,** 1868 (2001).
6. Rupich, S. M., Shevchenko, E. V., *et al.* Size-dependent multiple twinning in nanocrystal superlattices. *Journal of the American Chemical Society* **132,** 289–96 (2010).
7. Podsiadlo, P., Krylova, G., *et al.* The role of order, nanocrystal size, and capping ligands in the collective mechanical response of three-dimensional nanocrystal solids. *Journal of the American Chemical Society* **132,** 8953–60 (2010).
8. Bodnarchuk, M. I., Li, L., *et al.* Three-dimensional nanocrystal superlattices grown in nanoliter microfluidic plugs. *Journal of the American Chemical Society* **133,** 8956–60 (2011).
9. Disch, S., Wetterskog, E., *et al.* Shape induced symmetry in self-assembled mesocrystals of iron oxide nanocubes. *Nano letters* **11,** 1651–6 (2011).
10. Liao, C.-W., Lin, Y.-S., *et al.* Formation of diverse supercrystals from self-assembly of a variety of polyhedral gold nanocrystals. *Journal of the American Chemical Society* **135,** 2684–93 (2013).
11. Goubet, N., Richardi, J., *et al.* Which Forces Control Supracrystal Nucleation in Organic Media? *Advanced Functional Materials* **21,** 2693–2704 (2011).

12. Goubet, N & Pileni, M.-P. Analogy Between Atoms in a Nanocrystal and Nanocrystals in a Supracrystal: Is It Real or Just a Highly Probable Speculation? *The Journal of Physical Chemistry Letters* **2,** 1024–1031 (2011).
13. Goubet, N, Richardi, J, *et al.* How to Predict the Growth Mechanism of Supracrystals from Gold Nanocrystals. *The Journal of Physical Chemistry Letters* **2,** 417–422 (2011).
14. Kalsin, A. M., Fialkowski, M., *et al.* Electrostatic self-assembly of binary nanoparticle crystals with a diamond-like lattice. *Science (New York, N.Y.)* **312,** 420–4 (2006).
15. Kowalczyk, B., Kalsin, A. M., *et al.* Size selection during crystallization of oppositely charged nanoparticles. *Chemistry (Weinheim, Germany)* **15,** 2032–5 (2009).
16. Fialkowski, M., Bishop, K. J. M., *et al.* Principles and implementations of dissipative (dynamic) self-assembly. *The journal of physical chemistry. B* **110,** 2482–96 (2006).
17. Bishop, K. J. M., Wilmer, C. E., *et al.* Nanoscale forces and their uses in self-assembly. *Small (Weinheim, Germany)* **5,** 1600–30 (2009).
18. Zhou, L. & O'Brien, P. Mesocrystals - Properties and Applications. *The Journal of Physical Chemistry Letters* **3,** 620–628 (2012).
19. Niederberger, M. & Cölfen, H. Oriented attachment and mesocrystals: non-classical crystallization mechanisms based on nanoparticle assembly. *Physical chemistry chemical physics : PCCP* **8,** 3271–87 (2006).
20. Murray, C. B., Kagan, C. R. & Bawendi, M. G. Synthesis and Characterization of Monodisperse Nanocrystals and close-packed Nanocrystal Assemblies. *Annual Review of Materials Science* **30,** 545–610 (2000).
21. Simon, P., Rosseeva, E., *et al.* PbS-organic mesocrystals: the relationship between nanocrystal orientation and superlattice array. *Angewandte Chemie* **51,** 10776–81 (2012).
22. Lide, D. R. *CRC handbook of chemistry and physics, Internet version 2005* (CRC Press, Boca Raton, FL, 2005).
23. Hines, M. & Scholes, G. Colloidal PbS Nanocrystals with Size-Tunable Near-Infrared Emission: Observation of Post-Synthesis Self-Narrowing of the Particle Size Distribution. *Advanced Materials* **15,** 1844–1849 (2003).

24. Born, P., Murray, E. & Kraus, T. Temperature-induced particle self-assembly. *Journal of Physics and Chemistry of Solids* **71,** 95–99 (2010).

25. Wuister, S. F., van Houselt, A., *et al.* Temperature antiquenching of the luminescence from capped CdSe quantum dots. *Angewandte Chemie (International ed.)* **43,** 3029–33 (2004).

26. Wuister, S. F., de Mello Donegá, C. & Meijerink, A. Luminescence temperature antiquenching of water-soluble CdTe quantum dots: role of the solvent. *Journal of the American Chemical Society* **126,** 10397–402 (2004).

27. de Mello Donegá, C., Bode, M. & Meijerink, A. Size- and temperature-dependence of exciton lifetimes in CdSe quantum dots. *Physical Review B* **74,** 085320 (2006).

28. Wang, Z., Schliehe, C., *et al.* Correlating superlattice polymorphs to internanoparticle distance, packing density, and surface lattice in assemblies of PbS nanoparticles. *Nano letters* **13,** 1303–11 (2013).

29. Schliehe, C., Juarez, B. H., *et al.* Ultrathin PbS sheets by two-dimensional oriented attachment. *Science (New York, N.Y.)* **329,** 550–3 (2010).

30. Bealing, C. R., Baumgardner, W. J., *et al.* Predicting nanocrystal shape through consideration of surface-ligand interactions. *ACS Nano* **6,** 2118–27 (2012).

31. Choi, J. J., Bealing, C. R., *et al.* Controlling nanocrystal superlattice symmetry and shape-anisotropic interactions through variable ligand surface coverage. *Journal of the American Chemical Society* **133,** 3131–8 (2011).

32. Quan, Z. & Fang, J. Superlattices with non-spherical building blocks. *Nano Today* **5,** 390–411 (2010).

33. Bian, K., Choi, J. J., *et al.* Shape-anisotropy driven symmetry transformations in nanocrystal superlattice polymorphs. *ACS nano* **5,** 2815–23 (2011).

34. Haubold, D. *Synthese und Charakterisierung von Gold- und Gold-Blei(II)-sulfid-Nanokristallen und deren Anordnung in Superstrukturen* 2011.

35. Simon, P., Bahrig, L., *et al.* Interconnection of Nanoparticles within 2D Superlattices of PbS/Oleic Acid Thin Films. *Advanced materials* (2014).

36. Haubold, D. *Synthese und Charakterisierung von Gold- und Gold-Blei(II)-sulfid-Nanopartikeln und deren Anordnung in zwei- und dreidimensionale Superstrukturen* MA thesis (2013).

37. Joseph, Y., Guse, B. & Nelles, G. Aging of 1,ω-Alkyldithiol Interlinked Au Nanoparticle Networks. *Chemistry of Materials* **21,** 1670–1676 (2009).

38. Zarghami, M. H., Liu, Y., *et al.* p-Type PbSe and PbS quantum dot solids prepared with short-chain acids and diacids. *ACS nano* **4,** 2475–85 (2010).

5. Nanoparticular Supracrystals via electrostatic self-assembly in aqueous media

In this chapter non-classical crystallisation *via* electrostatic interactions between nanoparticular building units is presented. The basis of the work presented here are the publications of the Grzybowski group. All experiments were done during an internship in this working group and so the same techniques and preparation methods were used. The supracrystals, prepared by electrostatic self-assembly, normally contain silver and gold nanoparticles. The purpose of the internship was to apply the published procedures to semiconductor nanoparticles in order to generate highly ordered hybrid three-dimensional superstructures. The starting point of the studies was the nanoparticles with their charged ligand shell. For silver and gold nanoparticles the syntheses and characterisations are described in the chapter dealing with nanoparticular building blocks. The semiconductor nanoparticles have an oleic acid stabilising shell and hence the ligand exchange and stability experiments are presented. After characterisation of the initial nanoparticles the electrostatic self-assemble procedure and the different material combinations are discussed. Optimisation of the parameters which influence the structuring on the mesoscale is determined. Hereby, parameters such as the concentration of nanoparticles, ratio of oppositely charged nanoparticles, solvent/non-solvent ratio and pH are investigated. Furthermore, the structuring effect of polydisperse nanoparticle solutions has been reported in the literature. This effect was also investigated during the studies. Subsequently, the supracrystals which are formed are characterised using HRSEM, elemental mapping and small angle X-ray scattering (SAXS) to determine the internal structure. In addition the destabilisation process is examined and the effects of polydispersity in this special case are considered.

5.1. Preface

For applications such as optoelectronics[1], catalysis[2], biological sensing[3], high-density data storage[4], IR lasers and detectors and solar cells[5] based on nanomaterials it is inevitable that nanoparticular arrangements in two or three dimensions will be utilised. Because of this it is especially necessary to develop further the research field for dealing with controlled agglomeration and self-assembly of metallic and/or semiconductor nanoparticles. The focus of attention is primarily to preserve the unique nanoscopic properties of the nanoparticles during the formation of the macroscopic nanoparticular solids. Besides the arrangement techniques relying on attractive Van der Waals or hard-sphere interactions, the means of assembly using electrostatic interactions establishes new possibilities and methodologies for the formation of highly ordered arrangements. The strategy is based on the usage of oppositely charged ligand molecules stabilizing the nanoparticles in solution and operates *via* the long-range organisation of matter at the nanoscale in the presence of anionicly and cationicly stabilised nanoparticles.[6] With this technique, the possibility exists to overcome the limitations of the all-attractive nature of the interparticle interactions and their usual arrangement in closed-packed structures.[7–10]

With oppositely charged metal nanoparticles diamond-like lattices were assembled by Kalsin *et al.*[11]. Therefore, equally sized gold and silver nanoparticles capped with ω-functionalised alkane thiols like 11-mercaptoundecanoic acid (MUA) as anionic stabilizing ligand and N,N,N-trimethyl(11-mercaptoundecyl)ammonium chloride (TMA) as cationic analogue can be assembled, see figure 5.1a.[12] The packed crystal structure follows from the interplay between the thickness of the screening layer and the dimensions of the assembling nanoparticles. Precipitation and agglomeration takes place at the point of charge compensation so that titration as a preparation technique can be easily and advantageously used.[13] Inferentially it can be said, that *via* the variation of the controlled ligand ratio charged/uncharged on top of the nanoparticles the amount of positively to negatively charged nanoparticles can be influenced and so presumably changes in nanoparticle arrangement of the “nano-ions” can occur in a controlled fashion.

Furthermore, Kolny *et al.*[15] and also Shevchenko *et al.*[7] have reported on binary lattices assembled *via* electrostatic interactions. The binary nanoparticle superlattices contain different combinations of metallic, semiconductor and magnetic nanoparticles. So arrangements of such colloidal particle combinations, which have been

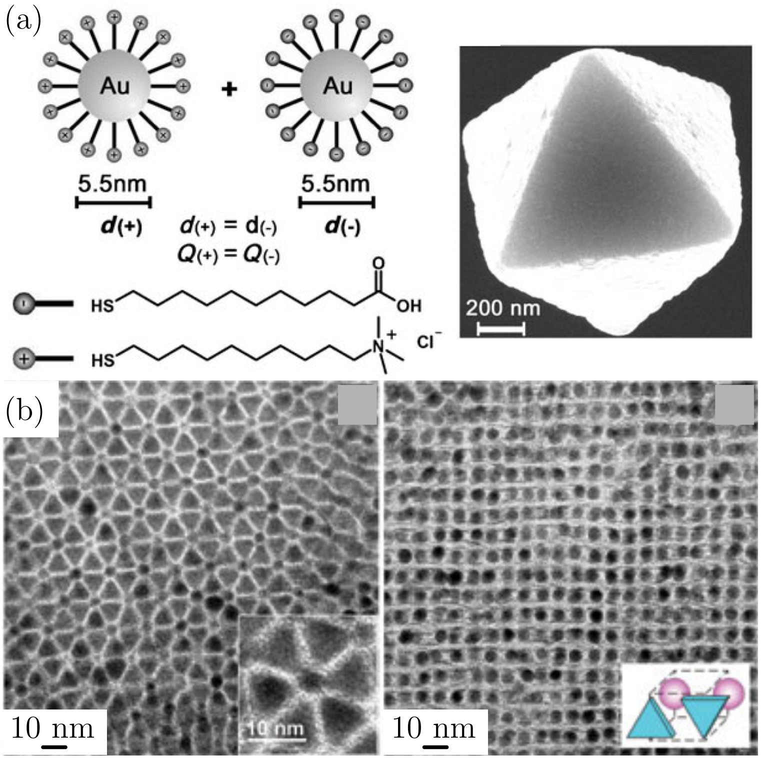

Figure 5.1.: ***Arrangement of supracrystals and binary nanoparticle superlattices.*** *(a) Schematic representation of oppositely charged Au and Ag nanoparticles capped with ω-functionalised alkane thiols and a supra crystal assembled with the shown nanoparticles.*[14] *(b) TEM images of binary superlattices assembled with triangular LaF*$_3$ *nanoplates and spherical gold nanoparticles.*[7]

reported first by Shevchenko *et al.*[7], are possible and new structures with tuneable properties can be assembled. Additionally, the arrangement on various length scales from nanometer sized particles up to the micrometer-scale[16,17] are shown and also shape variation of the building blocks is a powerful tool to create new assemblies, as shown in figure 5.1c,d. Leunissen *et al.*[16] also reported the arrangement of oppositely charged nanoparticles into superlattices. They determined by parameter variation, that charge neutrality does not dictate the stoichiometry of the resulting structures as is observed in atomic systems. Moreover, they proved the existence of oppositely charged nanoparticles inside of the superlattices by melting them in electric field. All systems regarded in the literature, reported on the concomitance of electrostatic, Van der Waals, dipolar and steric repulsion interactions during particle arrangement. Additionally, entropic factors like space-filling influence the self-assembly process. The non-equilibrium nature of the self-assembly results from the evaporation process during the arrangement and introduces additional complexity into the system.[18]

5.2. Ligand exchange and nanoparticle modification for electrostatic self-assembly

The starting point for electrostatic self-assembly are charged nanoparticles. Gold and silver nanoparticles with charged surface ligands, their synthesis and characterisation are described in the chapter on nanoparticular building blocks in section 3.3.2. The gold nanoparticles with their average size of 5.1 nm, dispersity (σ) of 13.7% and the silver nanoparticles with their average size of 5.5 nm, dispersity of 9.1% and the gold cores with sizes of about 2 nm are covered with the stabilising ligands 11-mecaptoundecanoic acid and N,N,N-trimethyl(11-mercaptoundecyl)ammonium chloride. Self-assembled monolayers of these ligands have a thickness of 1.63 nm for MUA and 1.9 nm for TMA.[19] With the stabilising ligands on the nanoparticle surface the nanoparticles are soluble in aqueous solution and are stable and unaggregated. Nanoparticle solutions containing MUA as ligand have a pH of nearly 10 so that the carboxylic function is deprotonated. To affirm the results of TEM measurements and determine the surface charge dynamic light scattering (DLS) experiments were utilised. Gold nanoparticles covered with MUA show a hydrodynamic diameter of 9.4 nm and a charge of -16.5 mV; the TMA capped gold nanoparticles have a hydrodynamic diameter of 7.4 nm and show 22.8 mV as the surface charge and the silver TMA species are 8.5 nm in diameter and have a charge of 21 mV. The averaged hydrodynamic diameter of the gold-cores with 6.2 nm (Au-MUA-cores) and 7.1 nm for Au-TMA-cores is smaller than the hydrodynamic diameter of the gold nanoparticles.

Semiconductor nanoparticle synthesis as presented in chapter 3 always results in oleic acid stabilised nanoparticles soluble in nonpolar solvents so that for electrostatic arrangement the ligand shell must be exchanged. Similar to the gold and silver nanoparticles the ligands 11-mecaptoundecanoic acid and N,N,N-trimethyl(11-mercaptoundecyl)ammonium chloride are used. To characterise the newly formed compounds absorption spectra in the near-infrared region, TEM measurements, DLS and zeta potential investigations were applied. Thus, the absorption of the lead sulphide and lead selenide nanoparticles does not change with ligand exchange because the core material is stable during this procedure and only the carboxyl

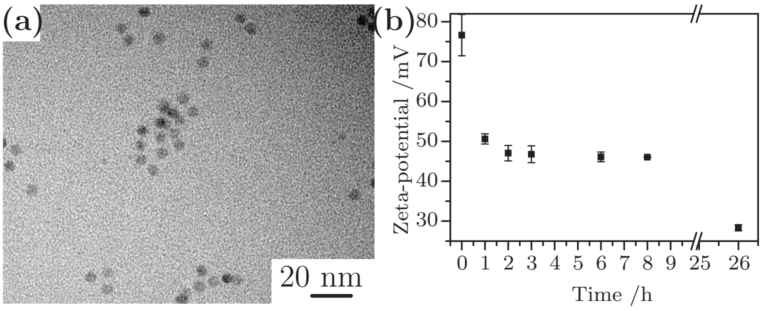

Figure 5.2.: ***TEM image of PbSe-TMA nanoparticles and zeta potential of PbS-TMA nanoparticles.*** *Over time the zeta potential is reduced and the nanoparticles precipitate.*

group is removed from the nanoparticle surface and replaced by the thiol functionality. Furthermore, TEM measurements (see Figure 5.2) show that the nanoparticles keep their size, but large ordered 2D arrangements cannot be found on the TEM grid as consequence of the repulsive interactions of the ligand shell. By probing PbS-MUA and PbSe-MUA nanoparticles using DLS, aggregates of up to 100 nm can be observed, but these agglomerates are stable over time at pH 10. By contrast PbS-TMA with average hydrodynamic radius of 7.85 nm and PbSe-TMA nanoparticles with a size of 7.1 nm can be measured. Thereby, the stability of the TMA aggregates is limited and they precipitate over a 24 hour period. Following the process by measuring the zeta potential and the hydrodynamic radius the zeta potential is reduced over time and simultaneously bigger agglomerates are formed, see Figure 5.2 and 5.3. The agglomerates are not uniformly sized and are amorphous structures without any long- or short-range orientation. Increasing the nanoparticle stability with pH control or different techniques of ligand exchange *via* oleic acid removal with hydrazine and then addition of the TMA ligands were not successfully.

5.3. Supracrystal formation with oppositely charged nanoparticles

For the following discussion the following term convention will be used In order to avoid the permanent mention of the corresponding ligand to nanoparticle core. Therefore it is taken that the first term used always belongs to the MUA-capped nanoparticles and the second to TMA-capped particles, e.g. PbS:PbSe means

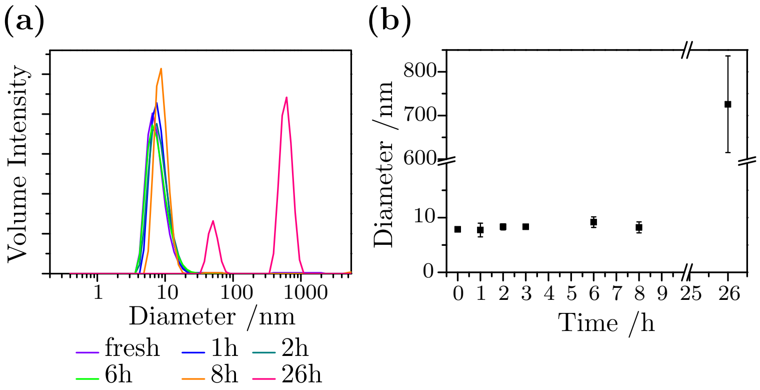

Figure 5.3.: ***Size distribution of the PbS-TMA nanoparticles over time measured with DLS.*** *Initially the nanoparticles remain separate, but with decreasing zeta potential agglomeration take place.*

PbS-MUA:PbSe-TMA. As reported in literature, the electrostatic interactions are strongest at the point of charge equality and so the combinations, PbS:PbSe, PbSe:PbS, PbSe:Au, PbS:Ag, PbS:Au, Au:PbSe and Au:PbS were investigated and titration experiments were done to identify the point of charge compensation. All compositions behave similarly and precipitation is detected at equal molar amounts of the nanoparticles. The precipitate was washed and it was then attempted to redissolve the precipitate, as earlier published. However the nanoparticular building units only partially return to the solution phase so that as first step of the reported procedure, i.e. titration and redissolving, was exchanged for direct agitation which causes precipitation during 24 hours.

5.3.1. PbS:Au

Variation of the parameters mentioned above influences the combination of PbS:Au and the crystallisation process of the supracrystal formation. During the destabilisation and supracrystal formation a number of different parameters can be optimised. Keeping the destabilisation temperature constant at 65°C the nanoparticle concentration, the ratio of charged nanoparticles, the amount of H_2O to dimethylsulfoxide (DMSO), the pH and the influence of size can be varied. As an initial starting point the formation of ordered 3D arrangements with a concentration of 1 μmol PbS and 1 μmol Au nanoparticles and a ratio of H_2O:DMSO of 2:2 was first undertaken. As presented in Figure 5.4, the supracrystals are not symmetric and are small in size. Changing the H_2O:DMSO ratio to values above two results in layers and unordered structures because a higher amount of DMSO, which acts

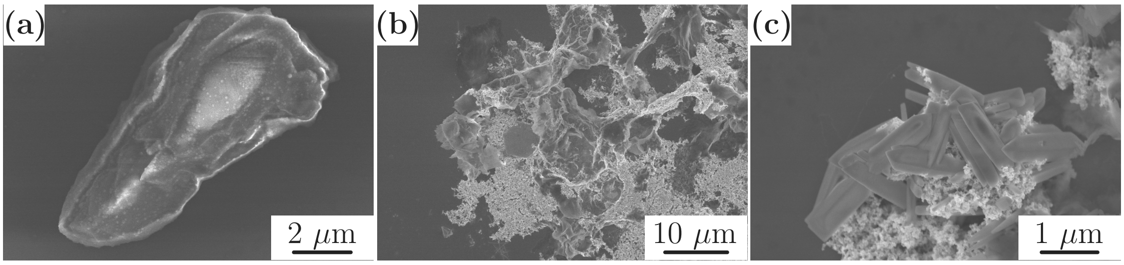

Figure 5.4.: ***SEM images of PbS:Au supracrystals.*** *(a) shows the initially formed supracrystals with low symmetry, (b) represents the variation of* H_2O*:DMSO variation to 3:1 and so the formation is not influenced by non-solvent and (c) shows the destabilisation with a higher nanoparticle concentration. Highly symmetrical supracrystals are formed besides a side product.*

as a non-solvent for the nanoparticles, initiates the precipitation. Above the ratio of two the agglomeration is not influenced by DMSO and even without the addition of DMSO the reaction rate is still the same. The same phenomenon with respect to the DMSO influence is observed during the variation of the concentration (Figure 5.4). Higher concentrations lead to more symmetric aggregates as a consequence of a shorter particle distance and so higher agglomeration rate without depletion around the aggregation centres (Figure 5.4). Variations in the ratio of concentration from 1:1 to 2:1 PbS:Au changes the agglomeration mechanism resulting in one-dimensional agglomeration and unordered self-assembly. Nanowires with thicknesses of 100 nm are formed of different lengths. Influencing additional parameters keeps the 1D assembly without changing the size or shape. As the purpose was to produce 3D structures further experiments in that direction were not investigated.

Moreover, the pH value of the mixed solution can be varied to affect higher stability of the nanoparticle solution. Higher pH values should completely deprotonate the carboxyl functions of the MUA ligands and so repulsion of the single MUA-capped nanoparticles should increase and the agglomerates of the initial solution dissipate. Raising the pH value up to 13 shortens the reaction time of the mixtures from nearly 24 hours to only 2 hours while bigger agglomerates occur. The deprotonation of the MUA ligands not only dissolves the agglomerates, additionally the electrostatic interactions between the TMA and MUA ligands increase and cause faster supracrystals formation. Kalsin *et al.*[11] have also reported on the stabilising effect of polydispersity. In experiments with gold and silver nanoparticles it was

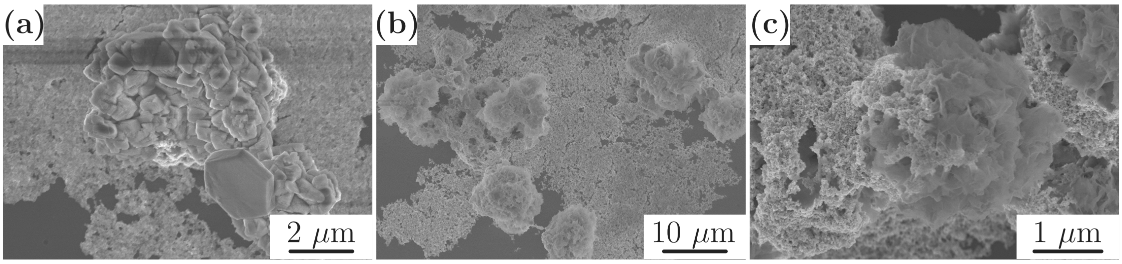

Figure 5.5.: ***SEM images of PbS:Au supracrystals with variation of Au-TMA-core concentration.*** *The core concentration decreases from left to right from 0.5 /0.25 /0.1 mol and the structures that are generated below a certain core-concentration are amorphous.*

pointed out that equally sized oppositely charged nanoparticles instantly flocculate and form amorphous aggregates caused by attraction forces which are too high. Smaller particles can screen the electrostatic field around the bigger nanoparticles and so can decelerate the reaction up to the point where completely stable mixed solutions result. Consequently, only one component should show a bimodal size distribution to reduce the electrostatic interaction of equally sized nanoparticles in a way that allows controlled agglomeration to take place. The addition of Au-TMA-cores to the PbS:Au solution (0.5/0.25/0.1 μmol) slightly stabilises the mixture by increasing the amount of highly ordered hexagonally shaped supracrystals and also multiple twinned structures with clear crystal facets. Decreasing the amount of TMA-cores results in decreasing the symmetry of supracrystals, see Figure 5.5. In comparison to TMA-cores, MUA-cores slow down the self-assembly process and reduce the symmetry of supracrystals, so that the facets that are present only can be guessed at.

5.3.2. Au:PbS

The supracrystal formation process that results from the combination of Au-MUA nanoparticles with PbS-TMA particles is investigated and optimised. Concentration of the nanoparticle solution as the first parameter change is considered. When this is done, higher concentrations are found to induce the growth of hexagonally shaped plates. Reduction of the particle concentration results in more three-dimensional growth but with the formation of smaller and less symmetrical ordered arrangements (Figure 5.6). To optimise the precipitation rate and the speed of agglomeration the H_2O:DMSO ratio is varied in the same way as described in section

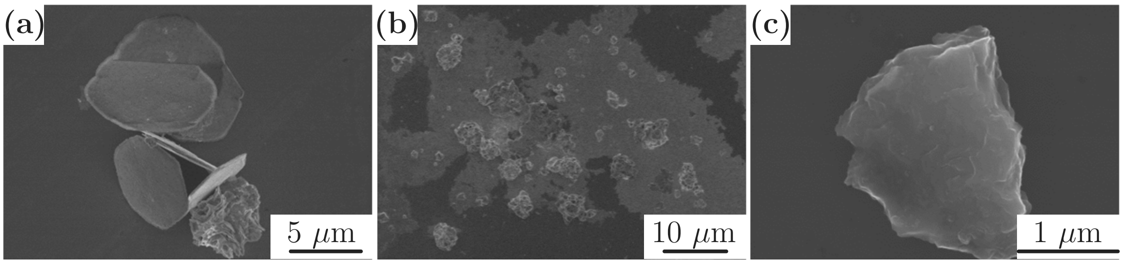

Figure 5.6.: ***Concentration dependent formation of Au:PbS supracrystals.*** *Higher concentrations (9 μmol, a) leads to hexagonally shaped plates. Lower concentrations (3 μmol, b and 1 μmol, c) show only small but more three-dimensional agglomerates.*

4.2.1. and the effect of the relative changes in the amount of DMSO is the same as described there. The amount of non-solvent should be high enough to influence the destabilisation of the nanoparticles. Small amounts only entail the normal agglomeration between the oppositely charged nanoparticles.

Adjustment of the pH value from 10 to 13 effected a higher agglomeration rate

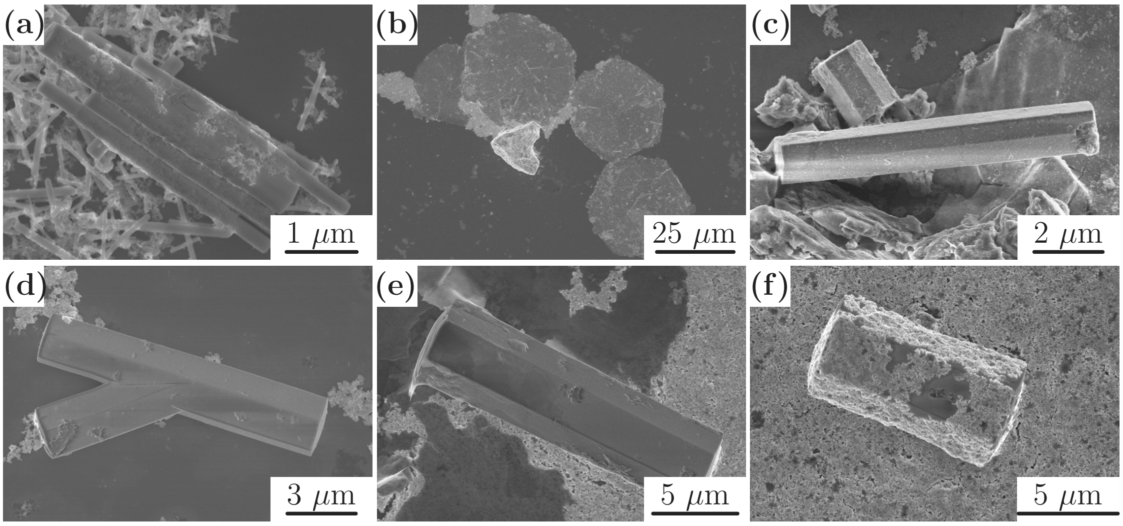

Figure 5.7.: ***SEM images of Au:PbS supracrystals with a variation of the Au-MUA-core and Au-TMA-core concentration at pH 13.*** *Without cores elongated hexagonal structures are formed (a). Addition of 0.1 μmol MUA-cores results in thin hexagonal plates (b), above this concentration MUA-core addition leads to highly symmetrical hexagonal prisms (0.2 μmol, c). Au-TMA-cores destabilise the solution with increasing amount of cores. Furthermore, the amount of amorphous side products increase with higher core concentration (d 0.1 μmol, e 0.3 μmol and f 0.5 μmol)*

and also bigger agglomerates due to the stronger effective electrostatic interaction. Surprisingly increasing pH induces the formation of elongated hexagonal structures in the size range of 5 μm in length and a maximum width of 250 nm (Figure 5.7). The resulting shapes are uniform and only different in their size with only a small amount of amorphous structures observed as a side product. Combining the pH change with the influence of the polydispersity by using Au-TMA-cores and Au-MUA-cores the size and the uniformity of the supracrystals can be enhanced. The Au-MUA-cores added to the reaction solution stabilises the PbS-TMA nanoparticles and slows down their precipitation (Figure 5.7). The amount of Au-MUA-cores influences the self-assembly only slightly because for a given core concentration (0.2 μmol) the reaction time is constant and the resulting supracrystals similar with respect to each other. Smaller concentrations lead to 2D planar hexagonally shaped sheets. In contrast to the stabilising effect of AU-MUA-cores, the TMA analogue destabilises the PbS-TMA nanoparticles. Increasing the concentration of the cores decreases the stability of the solution. This is also observable from the SEM images because the amount of amorphous side products also rises and the supracrystal length decreases.

5.3.3. PbSe:PbS, PbS:PbSe, Au:PbS and PbSe:Au and PbS:Ag

It was also tried to optimise the conditions for the different combinations of MUA- and TMA-capped nanoparticles but in contrast to Au:PbS and PbS:Au only in few cases were highly ordered symmetrical supracrystals formed, see Figure 5.8. Especially, the combinations with PbS and PbSe particles and the lower stability in comparison to the metal nanoparticles and the agglomeration of MUA-species always results in porous, amorphous structures without near-field or long-range ordering. For the combinations of metal nanoparticles the same behaviour as reported for Au:PbS and PbS:Au is observed. Higher concentrations induce more 2D hexagonal structures and lower concentrations leads to 3D arrangements which are more or less symmetrical. Furthermore the variation of the H_2O:DMSO ratio increases the destabilisation as the amount of non-solvent increases. Due to the resulting supracrystals being small and the large amount of experiments required employing highly expensive chemicals further optimisation was not attempted.

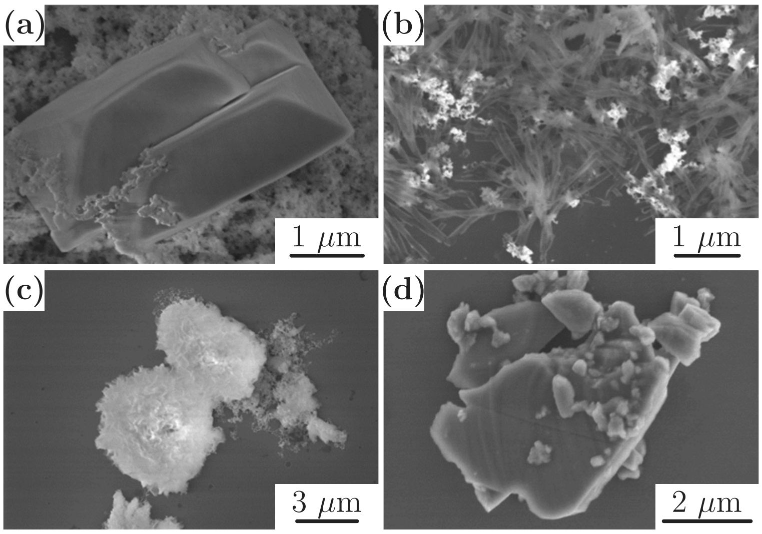

Figure 5.8.: ***Different compositions of supracrystals.*** *(a) shows PbS:Ag, (b) PbSe:Au, (c) PbS:PbSe and (d) Au:PbSe*

5.4. Internal arrangement of Au:PbS supracrystals and mechanistic investigations on destabilisation process

At first, the structure and the nanoparticular arrangement inside the supracrystals need to be determined. Therefore, HRSEM images were taken to investigate the outer structure. The low conductivity of the samples often results in charging effects on the crystal surface so that high resolution images are difficult to obtain. On such images the nanoparticles as building units can be determined. The surface of the resulting supracrystals is obviously not flat so that statements concerning the nanoparticle arrangement are difficult to make (Figure 5.9). The ordering compared to a hexagonal dense packed layer of nanoparticles differs a lot. To probe the elemental composition of gold and lead sulfide inside the structure elemental mapping was done. As shown in Figure 5.10, the elemental mapping found oxygen, lead and sulphur, but the structure does not contain gold. This means that only lead sulphide nanoparticles arrange into the hexagonal structure without incorporating gold nanoparticles. Additional SAXS measurements were made and Figure 5.9 shows the broad peak of scattered light. An internally highly ordered crystal structure would cause relatively small peaks with their position depending on the unit cell parameter and the crystal structure. The presence of a broad peak re-

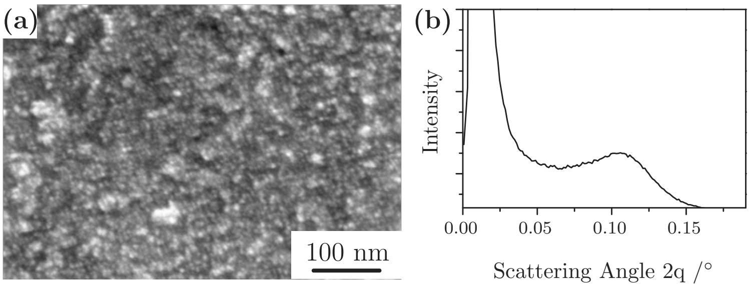

Figure 5.9.: ***HRSEM image and SAXS measurements of Au:PbS supracrystal.*** *The SEM image presents the surface structure of the supracrystal and SAXS measurements show the scattering of the unordered crystal structure. Both measurements indicate missing long-range interaction between the building blocks.*

flects a lower ordering with only near-field arrangements being present i.e. without long-range order. The surface structure visualised with HRTEM indicates that this long-range order is indeed missing. One may conclude therefore that in the Au:PbS supracrystals the building blocks are only PbS-TMA units that agglomerate generating a near-field ordering without long-range interactions. The parameters of destabilisation probably influence the outer hexagonal shape.

To shine some light onto the formation process, additional experiments were carried out where the influence of temperature and the Au-MUA nanoparticles were focused upon. The initial point for the supracrystal formation is the low stability of the PbS-TMA nanoparticle solution. After ligand exchange the TMA capped PbS-nanoparticles have enough charged ligands to be soluble in aqueous media, but the low amount of surface charges leads to agglomeration which takes place over one day. Additionally, the surface charge of the as-synthesised nanoparticles is so low that highly charged Au-MUA nanoparticles do not arrange with these particles but they increase the amount of crystalline PbS agglomerates as a consequence of the increasing stability of the whole solution. Increasing the concentration of OH- ions by increasing the pH value leads to faster precipitation because charges of the ligand shell are screened by these ions. Equivalent to this Au-MUA-cores screen the PbS-TMA nanoparticles with higher efficiency than the OH- ions. In contrast to that stable Au-TMA nanoparticles also induce crystal formation of the PbS-TMA nanoparticles. They increase the agglomeration rate of the unstable PbS nanoparticles due to their surface charge analogous to salting out effects. This also explains the increasing destabilisation rate by increasing the Au-TMA-core concentration. The PbS-TMA nanoparticles were excluded from solution because of the repulsive

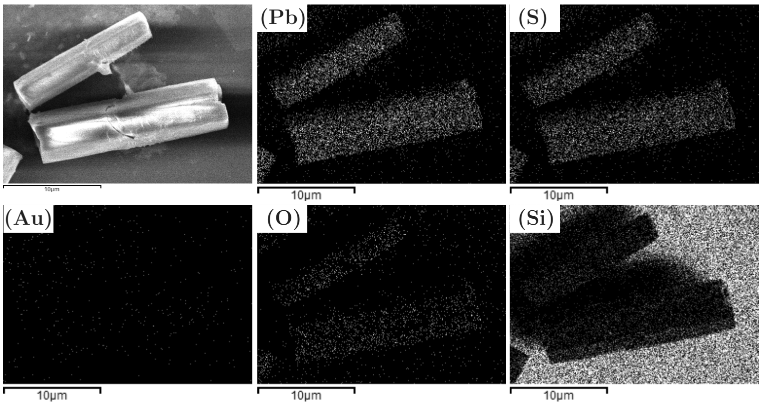

Figure 5.10.: ***Elemental mapping of a Au:PbS supracrystal.*** *The supracrystal contains solely lead and sulfur. Gold nanoparticles are only statistically distributed over the silicon wafer.*

interactions of the Au-TMA-cores. Experiments regarding reaction temperature and Au-TMA-core depending precipitation were done with removing the Au-MUA nanoparticles and observe the supracrystal formation. In the absence of Au-MUA nanoparticles hexagonal supracrystals are also formed, see Figure 5.11. Reducing the temperature of the system to room temperature, the agglomeration is slowed down and only amorphous structures are formed. Probably the reduction of the Brownian motion and so lower mobility of the nanoparticles inhibit the formation of these hexagonal structures.

In some ways this is like the salting out effect but it does not describe the formation of highly symmetrical crystalline structures. This would only describe the faster precipitation rate and in the case of Au-MUA nanoparticles the slower destabilisation rate, but additionally the Au-TMA and Au-MUA ligands have a highly charged surface. This effect induces enhanced interactions through the charged PbS nanoparticles so that it is possible that the PbS nanoparticles overcome the weak repulsive interactions between other PbS nanoparticles and they agglomerate so that the organic ligands left on the surface stick together. The effects induced by the excluded solvent holds the particles together so that they crystallise in a densely packed hexagonal structure with the result that every nanoparticle has the lowest contact to the solution and is surrounded by the highest amount of possible particles. Concentration and temperature influences this reaction mechanism. If the concentration is to low then there are only a small number of particles which can agglomerate. Consequently, the agglomerates formed are smaller and less symmetrical. Temperature is also important for the solubility of the interacting ligands

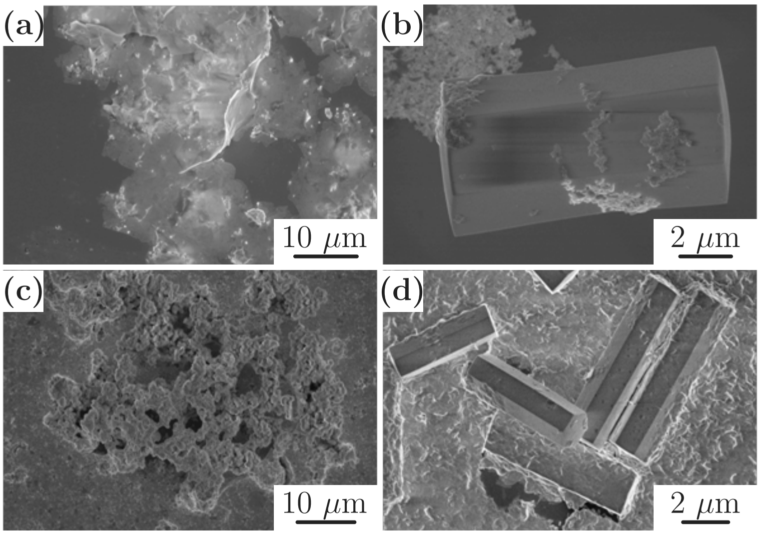

Figure 5.11.: ***Supracrystals formed by variation of the added core concentration and reaction temperature.*** *(a) PbS-TMA with Au-MUA without seeds at 65°C, (b) PbS-TMA with Au-MUA and Au-TMA seeds at 65°C, (c) PbS-TMA with Au-MUA and Au-TMA seeds at RT and (d) PbS-TMA with Au-TMA at 65°C.*

on the PbS surface. It was shown for the system of oleic acid-capped PbS nanoparticles that ordered arrangements of nanoparticles in a solvent/non-solvent system are only formed at temperatures higher than the melting temperature of the surface ligands. The same phenomenon could take place during the self-assembly of MUA- and TMA-capped nanoparticles because the melting point of these substances is around 50°C.

5.5. Résumé

Non-classical crystallisation with electrostatic interactions was presented using metal and semiconductor nanoparticles as building blocks. Thereby, the building units are capped with the surface ligand molecules 11-mecaptoundecanoic acid and N,N,N-trimethyl(11-mercaptoundecyl)ammonium chloride. The ligand exchange and the resulting nanoparticles, which are soluble in aqueous media, are shown for semiconductor nanoparticles. The agglomeration of the charged semiconductor-MUA species can be reduced by higher pH values. By contrast the semiconductor-TMA species stay separately in solution but over time the zeta potential of the nanoparticular units decreases and this induces agglomeration. After the characterisation of the building blocks the optimisation of different material combinations is presented. Higher concentrations always lead to more 2D and hexagonal arrangements. Additionally, it was shown that the pH induces faster precipitation of the lead chalcogenide component by forming more symmetrical supracrystals. Moreover an influence of polydispersity of one component was observed. Small and charged nanoparticles can stabilise the reaction solution by screening the oppositely charged nanoparticles. The material combination Au:PbS with addition of Au-TMA-cores is destabilised by this addition. The PbS nanoparticles are salted out of the solution. Consequently, the supracrystals formed solely contain PbS nanoparticles. The internal ordering of these crystals shows only short-range order without long-range interactions during the formation process. In addition, it was determined that only Au-TMA-cores are necessary to form these supracrystals i.e. they occur without the presence of oppositely charged gold nanoparticles. Hence, the small Au-TMA-cores induce a fast self-assembly of PbS nanoparticles. Temperature is also an important parameter during this process because the surface ligands have melting points around 50°C. Below this temperature the precipitate is always amorphous because of ligands that become caught and so rearrangement is not possible. This effect was also observed during non-classical crystallisation in organic media with oleic acid and oleylamine ligands.

5.6. References

1. Maier, S. a., Kik, P. G., *et al.* Local detection of electromagnetic energy transport below the diffraction limit in metal nanoparticle plasmon waveguides. *Nature materials* **2,** 229–32 (2003).
2. Grunes, J., Zhu, J., *et al.* Ethylene Hydrogenation over Platinum Nanoparticle Array Model Catalysts Fabricated by Electron Beam Lithography: Determination of Active Metal Surface Area. *The Journal of Physical Chemistry B* **106,** 11463–11468 (2002).
3. Zayats, M., Kharitonov, A. B., *et al.* Probing photoelectrochemical processes in Au-CdS nanoparticle arrays by surface plasmon resonance: application for the detection of acetylcholine esterase inhibitors. *Journal of the American Chemical Society* **125,** 16006–14 (2003).
4. Hoinville, J., Bewick, A., *et al.* High density magnetic recording on protein-derived nanoparticles. *Journal of Applied Physics* **93,** 7187 (2003).
5. Nagel, M, Hickey, S. G., *et al.* Synthesis of Monodisperse PbS Nanoparticles and Their Assembly into Highly Ordered 3D Colloidal Crystals. *Zeitschrift für Physikalische Chemie* **221,** 427–437 (2007).
6. Grzybowski, B. a., Winkleman, A., *et al.* Electrostatic self-assembly of macroscopic crystals using contact electrification. *Nature materials* **2,** 241–5 (2003).
7. Shevchenko, E. V., Talapin, D. V., *et al.* Structural diversity in binary nanoparticle superlattices. *Nature* **439,** 55–9 (2006).
8. Saunders, A. E. & Korgel, B. a. Observation of an AB phase in bidisperse nanocrystal superlattices. *Chemphyschem : a European journal of chemical physics and physical chemistry* **6,** 61–5 (2005).
9. Redl, F. X., Cho, K.-S., *et al.* Three-dimensional binary superlattices of magnetic nanocrystals and semiconductor quantum dots. *Nature* **423,** 968–71 (2003).
10. Rogach, A. L. Binary superlattices of nanoparticles: self-assembly leads to "metamaterials". *Angewandte Chemie (International ed.)* **43,** 148–9 (2004).

11. Kalsin, A. M., Fialkowski, M., *et al.* Electrostatic self-assembly of binary nanoparticle crystals with a diamond-like lattice. *Science (New York, N.Y.)* **312,** 420–4 (2006).

12. Bishop, K. J. M. & Grzybowski, B. "Nanoions": fundamental properties and analytical applications of charged nanoparticles. *Chemphyschem : a European journal of chemical physics and physical chemistry* **8,** 2171–6 (2007).

13. Bishop, K. J. M. Beyond Colloids : Interparticle Forces at the Nanoscale and their Application to Self-Assembly (2009).

14. Kowalczyk, B., Kalsin, A. M., *et al.* Size selection during crystallization of oppositely charged nanoparticles. *Chemistry (Weinheim, Germany)* **15,** 2032–5 (2009).

15. Kolny, J., Kornowski, A. & Weller, H. Self-Organization of Cadmium Sulfide and Gold Nanoparticles by Electrostatic Interaction. *Nano Letters* **2,** 361–364 (2002).

16. Leunissen, M. E., Christova, C. G., *et al.* Ionic colloidal crystals of oppositely charged particles. *Nature* **437,** 235–40 (2005).

17. Bartlett, P. & Campbell, A. Three-Dimensional Binary Superlattices of Oppositely Charged Colloids. *Physical Review Letters* **95,** 128302 (2005).

18. Rabani, E., Reichman, D. R., *et al.* Drying-mediated self-assembly of nanoparticles. *Nature* **426,** 271–4 (2003).

19. Sharma, C. V. K., Broker, G. a., *et al.* Self-assembly of freebase- and metallated-tetrapyridylporphyrins to modified gold surfaces. *Chemical Communications,* 1023–1024 (2000).

6. Nanoparticle arrangements in organic matrices and biological systems

In this chapter the focus is on the arrangement of nanoparticles into hybrid functional materials, in particular, two such systems are described. In the first section, the preparation strategy for low-bandgap, organic-inorganic composites containing functional polymers as ligands and PbS nanoparticles as inorganic core material are presented. Furthermore, ligand exchange of oleic acid ligands for thiophene-based macroligands is done in order to use the conjugated hybrid material for photovoltaic applications. The resulting hybrid materials have been characterised *via* optical and FT-IR spectroscopy, as well TEM measurements. Additionally, the photovoltaic properties have been measured. The second part of this chapter deals with a new approach to implement a Förster resonance energy transfer (FRET) over a liquid-liquid interface. Up to now, FRET has been restricted to the presence of both components into the same phase. The new construction kit containing fluorescing nanoparticles, hydrophobins as phase mediator and turbo red fluorescent protein (tRFP) as acceptor works as a model system by which to prove the general concepts. The illumination of the semiconductor CdSe nanoparticles result in excited states, which directly transfer the energy over the phase boundary to the tRFP, which is connected to the phase boundary with the help of the hydrophobins. The tRFP is used only in the model oil/water system as proof of concept and can be exchanged with other biological or water soluble proteins and living cells to use it for further applications. For this reason, the stability over time, the concentration depending on FRET efficiency and the arrangement of the components in the system were investigated.

6.1. Preface

Beside nanoparticle arrangements, hybrid materials composed of nanoparticles and organic or biological molecules are also of great interest especially for optoelectronic, biotechnological and medical applications.[1–7]

Blends of polymers and inorganic nanoparticles offer access to a large number of applications in the field of organic electronics. The nanoparticles act as a light harvesting centre and show higher efficiencies in comparison to macroscopic bulk materials because the size tuneable absorption and emission wavelength makes it possible to use the highly energetic part of the suns spectrum and the IR region additionally, where normal bulk materials cannot absorb light efficiently. The generated electron-hole pair must then be separated before recombination takes place. Directly attached semiconductor polymers like thiophene based structures with a lower conduction band than the nanoparticle band edge can transport the electron to an electrode interface. After recombination of the remaining hole with an induced electron, the process starts from the beginning and electric energy can be produced.

Polythiophenes are an especially important class of electrically conductive polymers which have been widely used in conductive plastics, batteries, transistors, OLEDs and sensors.[8] In 1980 the first synthesis of unsubstituted polythiophenes was published[8,9] and electrochemical synthesis of these materials has been possible since 1981.[10] Typical conductivities of polythiophenes are below 1000 S/cm, with conductivities above 1000 S/cm been observed only in a small number of cases, but this does not affect their usage in optoelectronics.[11] Unsubstituted polythiophenes are highly insoluble and infusible so that side chain substitution with long alkyl groups are necessary to increase their solubility for later processing.[8,12–15]

Moreover, nanoparticle hybrid materials are also of great interest for life sciences.[16] Of course, the size tuneable optical, electronic and magnetic properties are the main reason for the use of nanomaterials and in combination with biomolecules and their optimised binding specificity and functionality this opens up new areas of applications in cancer therapy or in in vivo single cell stimulation.[4,17–21] However, the different solubility properties of the nanoparticles and the biomolecules are challenging. Normally, ligand exchange reactions transfer the highly monodisperse nanoparticles from the organic into the aqueous media. Unfortunately, surface defects can potentially be introduced during this procedure, with the result that the quantum yield of the quantum dots (QDs) decreases dramatically. Also the chemical stability and photostability of the single nanoparticles decrease in aqueous media depreciating the quality of the as-synthesised quantum dots. Metal nanoparticles were not influenced by their transfer into organic solvents or were directly synthesised in aqueous media. Studies with gold nanoparticles showed their ability to act as targeted contrast agents for photothermal cancer therapy or to serve as scaffolds for increasingly potent cancer drug delivery to mention only few examples of these hybrid structures.[4,18]

6.2. Near-infrared absorbing conjugated polymer-nanocrystal hybrid systems*

In the literature, low cost materials for photovoltaic cells, photodetectors, light emitting diodes and other devices have often been mentioned in combination with conjugated polymer-nanocrystal hybrid systems.[1,2,23–31] For the preparation of these hybrid materials, thiophene based copolymers are especially well suited because the synthesis *via* palladium catalyzed cross coupling along the synthetic routes of Stille[32] or Suzuki[29] are well known. Additionally, it has been shown in the literature, that thiophene based polymers can be applied in hybrid functional materials[29,33,34] and are also suitable as low bandgap copolymers.[35,36] As the inorganic component in the hybrid material semiconductor nanoparticles are favoured because of their size dependent optical and electronic properties.[37] Especially lead sulphide nanoparticles with their advantageous exciton Bohr radius[38,39] are synthetically relatively easy to size tune resulting in changing bandgap energies in the near infrared region. Also the simple electronic and vibrational spectra of the nanoparticles allows their application in IR laser technologies, IR detectors, solar energy panels, bio-assays and window coatings.[38,40,41] The bandgap of the as-synthesised PbS nanoparticles produced *via* the hot-injection method can be varied between 800-1800 nm.[42–45] The combination of the conjugated polymer and the nanoparticles is favourable for photovoltaic applications because of the properties of these new functional materials, but also their film preparation *via* spin-coating would be a low cost and efficient industrial preparation method.

For the preparation of the above mentioned functional material two components are

---

[*] Parts of this section have already been published.[22]

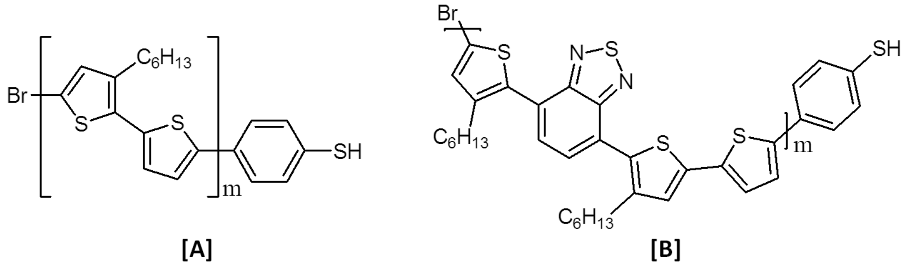

Figure 6.1.: ***Chemical structure of the received polymers.*** *Both polymers have a thiophene based backbone and show 4-bromobenzenethiol as an end group functionalisation to bind effectively at the nanoparticle surface. Polymer [A] represents a donor-donor structure and polymer [B] a donor-acceptor-donor structure.*

necessary. One is lead chalcogenide nanoparticles which absorb the incoming light and the other component is the polymer chains which should be directly bound to the nanoparticle surface to transport the excited electron over a conjugated backbone away from the nanoparticles to the electrode back contact. Therefore, the size tuneable properties of the lead chalcogenide nanoparticles are important because the conduction band of the nanoparticles can be shifted to energetically match the conduction band of the polymer *via* size variation to enable the electron flow from particle to polymer. The lead chalcogenide nanoparticles are prepared *via* a hot-injection method[38] and the size is adjustable over the reaction time. The particles are sterically stabilised with oleic acid as ligand molecules which keep the nanoparticles stable in organic solvents. The polymers which were synthesised by the working group of Professor Holder at University Wuppertal have two different structures that cause different electronic behaviour. In Figure 6.1 the chemical structure of both polymers are shown. Polymer [A] is a donor-donor structure and is based on thiophene and 3-hexylthiophene building blocks. Polymer [B] is a donor-acceptor-donor copolymer which consists of thiophene and 4,7-bis-(3-hexylthiophen-2-yl)-benzo-[1,2,5]-thiadiazole. Both polymer structures are end-capped with 4-bromobenzenethiol, which introduces a surface active thiol function into the polymer as binding site for connecting to the nanoparticle.[23,30,46]

The weight-average molecular masses of the polymers are around 14900-16000 g/mol, corresponding to a polydispersity index between 1.82 and 2.03. To verify the molecular weights obtained from gel permeation chromatography (GPC) and to determine the uniformity of the polymers, MALDI-TOF mass spectrometry measurements were instigated.[47–49] Thereby, peaks with different degrees of poly-

Table 6.1.: Optical properties of copolymers [A] and [B].

Polymer	Abs^{a}_{sol} (nm)	Abs_{film} (nm)	Eg^{a}_{sol} (eV)	Eg^{b}_{film} (eV)
[**A**]	496	540	2.50	2.30
[**B**]	463	540	2.68	2.30

[a] in toluene solution, [b] determined on glass.

merisation are observed with peak-to-peak distances for Polymer [B] of 548.8 Da which reflects the mass of two monomer repetition units. In addition, the results of the GPC could be confirmed. Both polymers show good solubility in organic solvents and uniform thin films can be produced, which makes them good candidates for the fabrication of organic semiconductor devices.

To calculate the bandgap, measurements of the optical properties were performed and the maxima of the spectra are shown in Table 6.1 as well as the bandgaps. A red-shift is observed when the absorption of the solved polymers is compared with the polymer films. In the literature as explanation for this effect that is often given is that the interactions between the polymers in the films are higher due to their direct arrangement without lowering the interactions with the solvent molecules in between. These interactions lead to a broadening of the wave function and so the red-shift is observed. The calculated bandgaps for both polymers are nearly equal although the donor-donor polymer is electron rich in comparison to the electron-deficient benzothiadiazol group.

The ligand exchange was performed with oleic acid stabilised PbS nanoparticles and both polymers. To achieve this both components were mixed in THF and kept shaking overnight. After ligand exchange takes place addition of the non-solvent, ethanol followed by slow centrifugation precipitate the nanoparticle-polymer material. Slow centrifugation in this step is very important because unbound polymer and oleic acid can also be precipitated. as cleaning steps the materials are twice redissolved and precipitated with n-butanol to minimise the presence of unbound ligands. The resulting powders were dried under vacuum and ligand exchange was investigated using FT-IR as shown in Figure 6.2. Unfortunately, the thiol group is not visible in the FT-IR spectra because of the long polymer chain and the low intensity of the end group. So it is not clear if the bonding of this functionality to the PbS-nanoparticles takes place. But there is a peak over 3000 cm^{-1} and one at 1700 cm^{-1} which is only present in the polymer and is also observable in

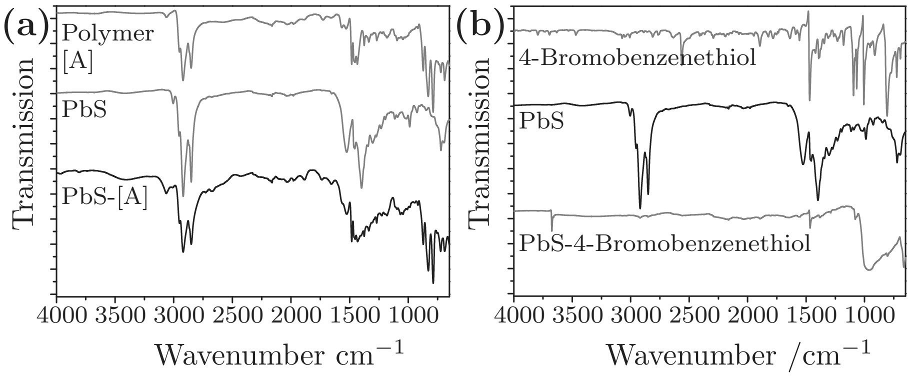

Figure 6.2.: ***FT-IR spectra of the polymer, PbS nanoparticle and composite material (a) and with the short chained reference substance 4-Bromobenzenethiol (b).*** *The present alkyl-chains in the polymer hinder the interpretation of the ligand exchange. So with a non alkyl-chain containing reference substance with the same binding behaviour the ligand exchange was determined using FT-IR measurements.*

the nanocomposite. Therefore, one cannot clearly distinguish whether the copolymer is bound to the nanoparticle surface or if it is present as a mixture of both components.

To probe the ligand exchange the sole end-capping functionality 4-bromobenzenethiol was used and FT-IR spectra were performed. From the spectra it is obvious that the CH_2- and CH_3-stretching vibration (2750-3100 cm^{-}1) of the oleic acid and also the bending vibration (1300-1600 cm^{-1}) no longer exist after ligand exchange with the end-capping thiol function. Additionally, the SH-vibration at 2564 cm^{-1} is lost in the composite which supports the assumption of binding of the SH group to the nanoparticle. The same behaviour should be shown by the polymer chains, but the presence of alkyl-chains in the polymers covers their disappearance. Assuming the same favourable binding of the thiol group of the polymer chains a covalent interconnection between the polymer and the nanoparticle to form a nanocomposite is very likely.

The optical characterisation of the nanocomposite materials in the IR region shows small red-shifts of the composites; see Figure 6.3 and Table 6.2. The observed small red-shifts can occur because of the changed binding behaviour of the ligand molecule.[30] The intensity of the single solutions is not comparable because after ligand exchange the concentration of the nanocomposite is not easily distinguished. In the IR emission the maximum in PbS-[A] is also shifted from 1326 nm to 1333

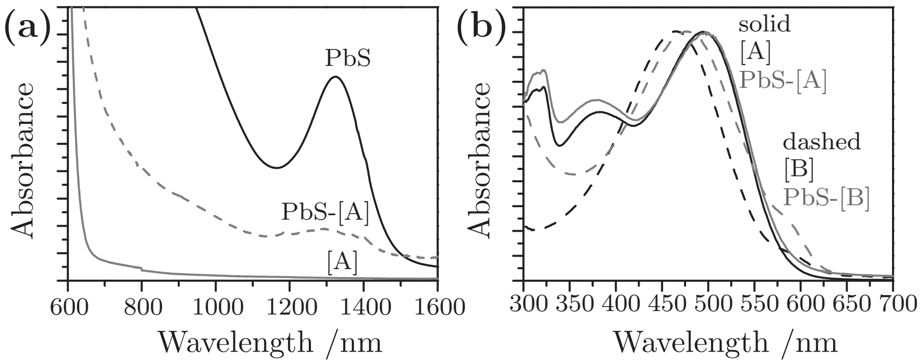

Figure 6.3.: ***Absorption spectra of the polymer, PbS nanoparticle and composite materials.*** *(a) In the IR region the absorption maximum is not affected by ligand exchange. During cleaning the PbS nanoparticle amount is not distinguishable so that the intensity loss is only a concentration effect. (b) The electron-donating binding to the PbS nanoparticle surface shifts the absorption maximum to longer wavelength. Polymer [B] with its acceptor group is affected stronger.*

nm and to 1339 nm with PbS-[B]. In UV-Vis spectra the absorption of composite [A] shifts only 2 nm to the red, but composite [B] has a red-shift of 13 nm, which corroborates the assumption of a covalent binding between the two components. The emission spectra of PbS-[B] support this assumption, but with PbS-[A] a blue-shift was determined, which cannot be explained using the ideas of covalent binding.

The colour changes in the UV-Vis spectra are also observable by eye, as is shown in Figure 6.4. Additionally, in Figure 6.4 TEM images are shownfrom which the different nanoparticle arrangements before and after ligand exchange can be determined. PbS with oleic acid ligands, which have an elongated length of 1.8 nm, form

Table 6.2.: Absorption and emission maxima of polymers [A] and [B] as well as of the composites PbS[A] and PbS[B].

Material	Abs UV-Vis^a (nm)	Abs near IR^b (nm)	Em UV-Vis^a (nm)	Em near IR^b (nm)
[A]	496	-	683	-
[B]	463	-	621	-
PbS-[A]	498	1294	673	1333
PbS-[B]	476	1297	624	1339

Solutions in toluene^a or tetrachloroethylene^b. Abs max PbSb: 1286 nm; Em max PbSb: 1326 nm.

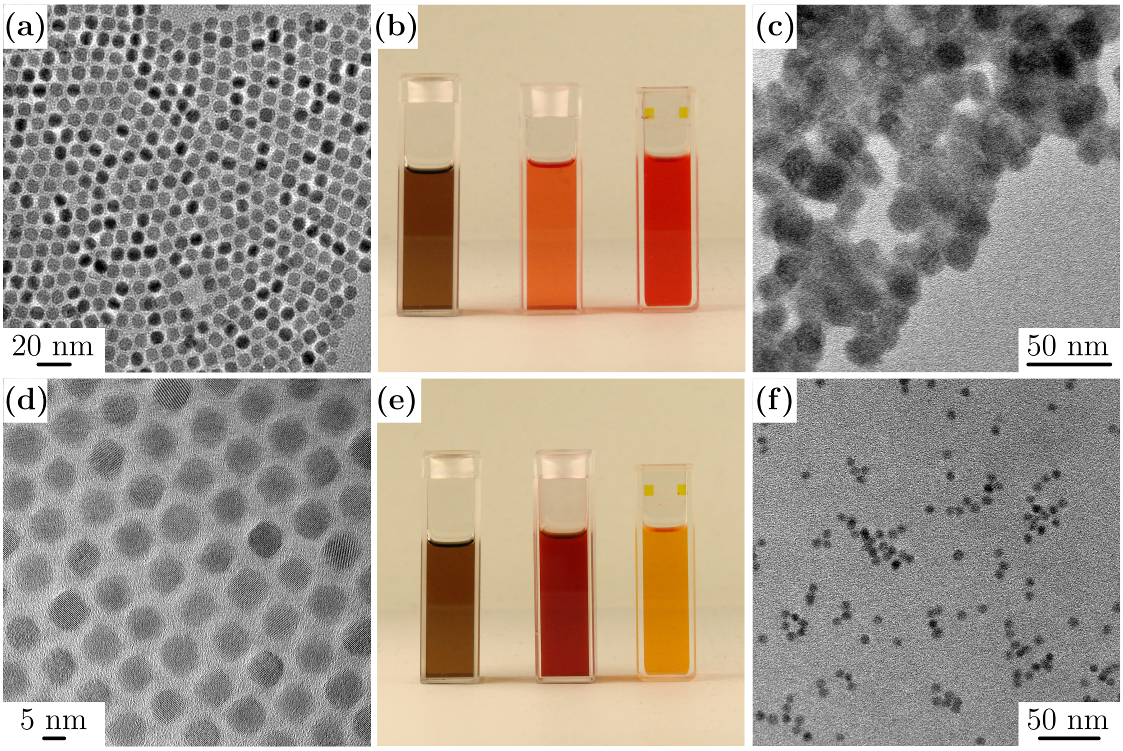

Figure 6.4.: ***TEM micrographs of PbS nanoparticles (a,d) and composite materials (c,f) and photographs of the prepared solutions (b,e).*** *(a,d) shows the 2D arrangement of oleic acid capped 6 nm sized PbS nanoparticles. (b,e) present the colour change between the PbS and polymer solution after ligand exchange has taken place and (c,f) illustrates the nanoparticles and their arrangement after ligand exchange. The longer polymer ligands remain in less ordered arrangements.*

hexagonal densely packed layers of equal interparticle distances. In comparison to that, the ligand exchanged nanoparticles do not form an ordered arrangement. Also TEM-imaging of the highly organic containing hybrid materials is difficult to realise because on the one hand the contrast of the samples is really low and on the other the organic material is not stable in vacuum under an electron beam. But the images show the higher distances between the nanoparticles and also the presence of the polymers.

The prepared nanocomposites were further characterised for their photovoltaic properties at the Light Technology Institute, Karlsruhe Institute of Technology (KIT). They determined that in the UV-Vis region the PbS nanoparticles lower the incident photon to electron conversion efficiency, but in the IR region, around 1200 nm, the PbS nanoparticles can harvest sunlight and contribute to the photocurrent generation in the solar cell.

6.3. Excitable Oil Droplets - Nanoparticle assisted FRET across a liquid-liquid phase boundary[†]

Förster Resonance Energy Transfer (FRET) is a widely used phenomenon for detection and sensor applications on the nanometer scale in one phase systems. Excitation energy is transferred between two fluorescent species, from a donor to an acceptor, through a dipole-dipole interaction i.e. without the emission and reabsorption of a photon. Subsequently, the emission of the donor fluorophore is quenched and the acceptor fluorophore becomes excited. Such systems are extremely sensitive to changes in distance between donor and acceptor and the effect decreases as the sixth power of the distance separating the two. In common FRET cascades the donor and acceptor molecules are located in one phase so that the distance over which FRET occurs is of the dimensions of the Förster radius[51,52]. When FRET occurs, the fluorescence intensity of the acceptor increases while a decrease in donor fluorescence intensity and fluorescence lifetime takes place[51].

In nature FRET is a prevalent concept to guide energy between biological molecules[53]. These well-known systems are also used in molecular biology for example to detect protein-protein-interactions[54]. FRET is not only possible between biological proteins or molecules, it is also possible to use QDs and transfer energy between different kinds of nanoparticles[55–57]. QDs are well suited for this task because they have a broad absorption spectrum and narrow emission. Furthermore, QDs show a high photostability and can be synthesised such that they possess a high quantum yield[58]. The combination of biological molecules and QDs has already been demonstrated and holds many advantages such as size tuneable absorption and emission[5,59]. Also their inherently high photostability and brightness result in an increase in the efficiency of the FRET process. Despite their many benefits, QDs are normally synthesised in organic solvents and thus have to be transferred to the aqueous phase in order to interact with biological samples[60,61]. The hydrophobic ligands on the surface of the QDs must be capped with hydrophilic ligands or exchanged in an additional post-synthetic step. Unfortunately, surface defects can potentially be introduced during this procedure, with the result that the quantum

---

[†] Parts of this section have already been submitted and are published as a patent[50].

yield of the QDs decreases dramatically. Also the stability and photostability of the single nanoparticles decrease in aqueous media which results in lower FRET efficiencies.

6.3.1. The model system

A highly stable and sensitive construction kit to transfer energy *via* FRET across a phase boundary was developed to prevent losses in quantum efficiency during phase transfer. The main advantage of this innovative construction kit is that it contains QDs in the organic phase and optically active proteins in the aqueous phase. In the present case, turbo red fluorescent protein (tRFP) was fused to a phase mediating protein, e.g. hydrophobins. Finally, the system consists of three tuneable components: donor, acceptor and phase mediator, which makes it truly adjustable in comparison to common surface bound FRET systems, where the protein or dye components are attached directly to the QD surface or indirectly *via* ligand molecules.[5–7,19,62–64] In comparison to the systems described in the literature, the system presented here is more dynamically conditioned by self-organisation. Advantageously, the components are kept in their favourable media maintaining their optimised properties, with the consequence that phase transfer of single components is no longer required. An additional advantage is the self-healing processes at the liquid-liquid interface as a result of rearrangements and flexible self-assembly. Hydrophobins possess distinct hydrophobic and hydrophilic patches so that they perfectly stabilise the oil-water emulsion by driven assembly at the phase boundary. Due to their hydropathy pattern, hydrophobins are predestined to serve as interfacial anchor domains at various interfaces. Moreover, interfacial adhesion of hydrophobin-based fusion proteins allows targeted surface functionalisation. Hydrophobins are very small proteins with average diameters of about 2.5 nm in aqueous solution.[65,66] Hence, they are able to keep the attached protein domain closely to the oil/water interface. To avoid potential interferences between two protein domains, they are separated by a randomly structured linker. The maximum length of the completely stretched linker is 2.4 nm[67]. Furthermore, the fused tRFP domain allows continuous photometric monitoring of the long-term stability of excitable oil bodies (EOBs). The red fluorescent protein is characterised by a high photo- and pH-stability[68]. For Förster resonance energy transfer the protein-mediator-complex is within its size dimension in the lower range of Förster radius so that in this context, it is only necessary to locate another fluorophore on the opposite side of the oil/water interface, which offers a suitable overlap in its emission or excitation spectrum. QDs, due to their tuneable optical properties, are suitable candidates as they meet many of the aforementioned requirements. II-IV group semiconductors especially, have been found to have high emission quantum yields and synthetic routes for their production are well known. Cadmium selenide (CdSe) QDs and cadmium sulphide/zinc sulphide (CdS/ZnS) core-shell QDs were used as reliable representatives of this group.

6.3.2. FRET in a hybrid system

The ability of hydrophobin mediated two-phase systems to support FRET at an oil/water interface were studied. CdSe QDs localised in the organic phase of the excitable oil bodies were surrounded by tRFP-labelled hydrophobins, which stabilises the oil/water interface, see Figure 6.5. An energy transfer process from QDs to proteins should be detectable due to the emission spectrum of the CdSe QDs overlapping with the excitation spectrum of the tRFP as shown in Figure 6.6. Furthermore, the fluorophore components can be separately localised due to their different emission wavelength. In fact of their excitation/emission spectra, CdSe QDs and tRFP-labelled hydrophobins are detectable using the available DAPI or DsRed specific filters, respectively (Figure 6.6). Firstly, the QD are homogeneously distributed inside the oil droplet like the uniform fluorescence shows. After a certain period of time, a pronounced fluorescent ‘corona was detectable at the oil/water interface, which leads to the assumption of QD accumulation at the oil/water interface as result of interaction with protein chimera. As expected, the tRFP fluorescence was exclusively localised at the oil/water interface, which confirms that the fusion protein containing hydrophobins and tRFP is attached to the surface of EOBs. Additionally shown in Figure 6.6 is the drop cap effect (B2.2) which is a result of the preparation technique. The light filter system and the adapted excitation/emission settings allow selective excitation of CdSe QDs as well as the simultaneous detection of the tRFP fluorescence emission. The fluorescence pattern of B1.3 and B2.3 images is identical to those resulting from protein specific excitation. The control experiment without QDs (B3.3) shows a weak fluorescence signal of the proteins. Quantitative analysis confirmed that the signal occurs as a result of weak tRFP excitation in the range of the QD excitation. Fluorescence microscopy images indicate a direct interaction between QDs and proteins which is shown by the increasing fluorescence intensity of the protein during QD excitation.

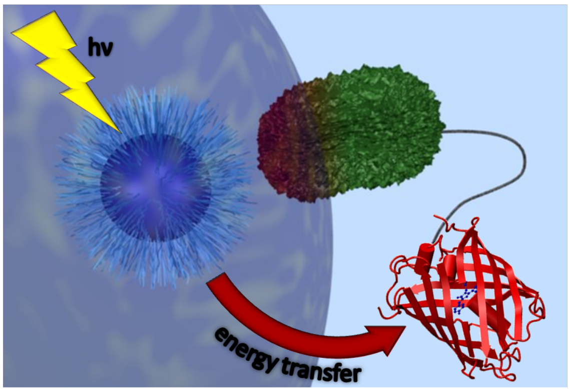

Figure 6.5.: ***Scheme of the hydrophobin mediated two-phase system to support FRET at an oil/water interface.*** *The CdSe quantum dots are soluble in organic media and can absorb incoming light. The stabilizing ligand shell of the quantum dots has the ability to interact with the hydrophobin proteins. tRFP-labelled class I and class II hydrophobins stabilise the oil/water interface and keep the tRFP localised at this position. Below the Förster radius (∼ 10 nm) energy transfer from the quantum dots to the tRFP can occur.*

A number of different parameters like the character of the protein domain, concentrations of the protein chimera and QDs, pH-value and protein stability influences the FRET phenomenon. Only the tRFP proteins exhibit constant fluorescence stability over the whole pH range in contrast to hydrophobins as fusion proteins, which reveal a decrease in fluorescence intensity at lower pH, and additionally, the fluorescence maximum is shifted to longer wavelengths. Furthermore, the QD concentration influences the EOB stability and the efficiency of the FRET process as they increasingly interact with the protein chimera which results in its enlargement. The interaction between QD and hydrophobin reduces the effective area of the hydrophobic patch of the hydrophobin and indirectly destabilises the interface. The surface activity of hydrophobins depends on a protein self-assembly process accompanied by a conformational change of the molecules at the interface[69], which does not appear to occur during QD interaction. The phenomenon of FRET manifests itself through an increase in acceptor fluorescence emission which is proportional to any increases in the donor concentration. The evaluation of the FRET efficiency of the donor/acceptor system is done by using hydrophobin stabilised 1-Octadecene-in-water emulsions containing equimolar concentrated solutions of tRFP-tagged hydrophobins and different CdSe QD concentrations (0.5-2.5%(v/v)). It was also observed that an increased QD concentration yielded an increase in the emission

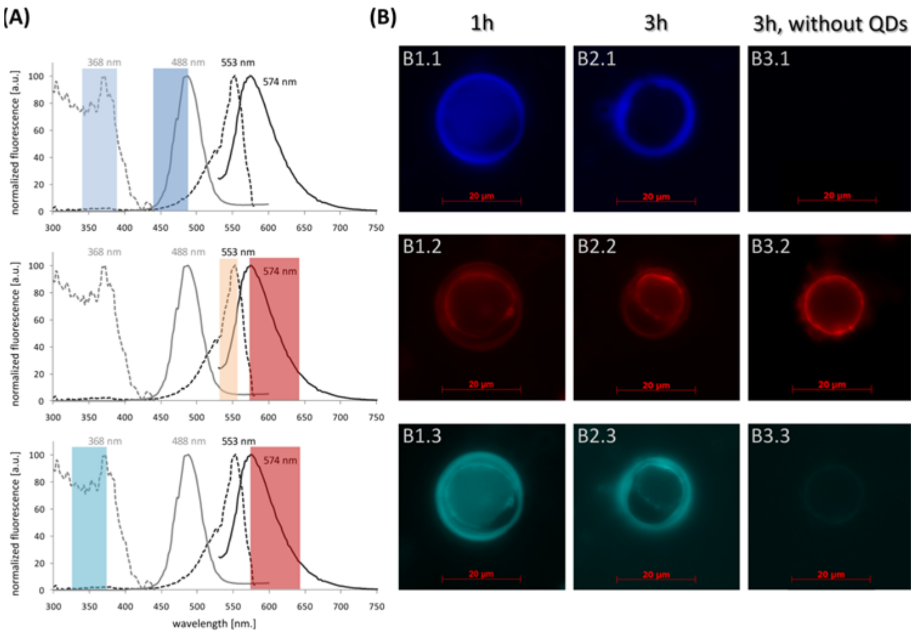

Figure 6.6.: ***Visualisation of protein/QD interactions at an oil/water interface using fluorescence microscopy.*** *(A) shows the absorption/emission spectra of the QDs (left) and proteins (right). Coloured insets schematically illustrate the applied filter sets used to match the spectral excitation/emission characteristics of the CdSe QDs (upper section), tRFP (middle) and the FRET pair (lower section). (B) Images of 0.5% (v/v) oil-in-water emulsions stabilised by Ccg2-tRFP (300 ng* L^{-1}*). Samples containing QDs in the oil phase were observed after 1 h (B1) and 3 h (B2) using three different filter sets, as illustrated in (A). The lower images are 'false-color' images. (B3.1-3.3) is the negative control with no QDs added. Samples were monitored using a Zeiss ApoTome1 confocal microscope with an exposure time of 500 ms.*

maxima of the tRFP-tagged hydrophobin. As a negative control, equimolar emulsions without QDs were prepared, which were also used to reveal the base signal. As expected the measured fluorescence intensities of hybrid systems were usually higher than the negative control. In this dynamic system the fluorescence emission of the tRFP-tagged hydrophobins increase over time in the first hour until it reaches a steady-state. The donor and acceptor fluorophore assemble during this period of time along the interface, as shown schematically in Figure 6.6, and it was observed that an increased donor to acceptor ratio gives rise to higher maxima in the fluorescence intensity, as confirmed by the FRET study. However, over time an increased donor concentration affects the stability of the EOBs, which results in a decrease in the acceptor emission after a given period of time.

6.3.3. Lifetime measurements

To show the existence of non-radiative energy transfer between the semiconductor QDs and the proteins, lifetime measurements were undertaken. The fluorescence lifetime is the time which is needed in order for the fluorescence intensity to decrease to 1/e of the initial value. The decay of the excited state of high quality CdSe QDs, which is in the range of nanoseconds, normally follows a monoexponential law. The relaxation process depends on the chemical surroundings of the fluorophore; hence, lifetime measurements can be used to detect different interactions between the fluorophore and the chemical environment. The as-synthesised CdSe and CdS/ZnS QDs have a high quantum yield and follow a non-monoexponential decay on the timescale of nanoseconds ($\sim$ 11ns) as shown in Figure 6.7. The QD relaxation processes increase drastically upon the addition of tRFP marked hydrophobin, the lifetime decreasing by a factor of 11 in magnitude, which indicates a non-radiative relaxation or energy transfer to another fluorophore. If the QDs were to act as an energy donor the emission intensity of the energy acceptor should increase. The exponential decays of the protein with and without QDs show the same results (data not shown) which indicates that the relaxation processes occurring in both are the same. However, a time dependent measurement of both reaction systems shows the increased fluorescence of the protein in the presence of the QDs. The formation rate of the acceptor fluorescence is nearly the same as the degradation

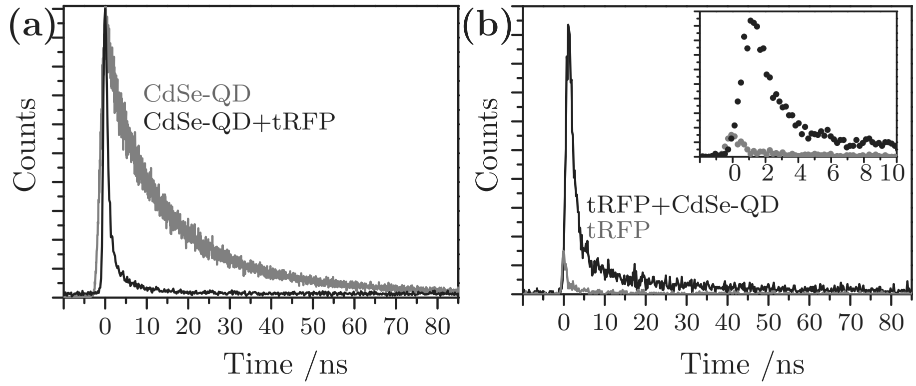

Figure 6.7.: ***Lifetime measurements.*** *Emission decay traces of CdS/ZnS QDs (0.5% (v/v)) with and without Ccg2-tRFP (300 ng L^{-1}) in an oil/water emulsion (a). Lifetime of Ccg2-tRFP in the presence or absence of CdS/ZnS QDs (right) using a 403 nm laser for excitation (b).*

rate of the QD fluorescence which is an additional indication of FRET. As a result, it may be concluded that energy must be transferred from the QDs *via* a non-radiative process to the proteins (FRET) due to the fact that the fluorescence intensity of the protein increases while the lifetime of the QDs decreases.

6.3.4. Long-term measurements

With particular regard to the application of prospective interfacial FRET systems, a long durability of EOBs must be guaranteed. The fluorescence intensity of the tRFP-tagged hydrophobin steadily declines over time. In contrast to this the hybrid system reaches the fluorescence maximum after two hours which can be explained with the ‘corona effect described above. After the arrangement of nanoparticles on the phase boundary the fluorescence declines as was observed by the tRFP-tagged hydrophobin sample. The fluorescence of the tRFP-tagged hydrophobin in the hybrid system was approximately six times higher than that of the negative control, without the addition of QDs, after three days of observation. Results of initial long-term measurements confirm functional FRET after several days. Extension of the lifetime can be achieved by the careful synchronisation and optimisation of the system components.

6.3.5. Perspective applications

As previously mentioned, the EOB setup consists of three adjustable components that provide several advantages in comparison to the common setups. Applications in biological systems generally require water-soluble QDs. Therefore, a variety of techniques, often of a high degree of complexity, have had to be developed to transfer QDs into the aqueous phase. Unfortunately, this usually leads to a dramatic decrease in their fluorescence quantum yield. A phase transfer becomes unnecessary, when both donor and acceptor can be kept in their favoured medium whilst at the same time fulfilling their required roles. The new setup introduced here allows the tailoring of EOBs to particular individual needs, e.g. by exchanging components to increase selectivity. Hence, tailored EOBs can be exploited as effective signal transducers for the dynamic monitoring of processes or environmental conditions (e.g. nutrition concentration, pH value or salt content). With regard to applications in bioanalytics, the possibility to interchange donor and acceptor could be applied for the in vitro quantification of micronutrients. Another key advantage of EOBs is their long-term stability, which is necessary for near-line and long-term monitoring applications. Zampieri *et al.* reported on the formation of highly stable hydrophobin coatings, which can be used to improve the biocompatibility of materials.[70] At the same time, encapsulation of EOBs in hydrophobin matrices inhibits the leakage of QDs from the oil phase, which is advantageous when using EOBs in an aqueous surrounding. More importantly, the toxicity of the QDs is trapped from environment. For this reason, it is in principle feasible to apply EOBs in biological systems, e.g. for a wide range of medical applications. Considering applications in biolabelling, this novel technique represents an efficient amplifier tool for photothermal cancer therapy[17,18] using directed cell irradiation or focused cell heating. Moreover, EOBs represent microstructured two-phase systems, which offer further advan-tages. The high surface-to-volume ratio of EOBs is advantageous in terms of high mass and heat transfer rates, as well as a narrow residence time distribution[71]. A faster system response time improves process control and product yields. Small-sized systems are also characterised by lower material and energy consumption[72], which is important for technical applications in industry. Development of artificial systems is an appealing strategy for producing sustainable fuels[73]. Unfortunately, biomimetic alternatives possess several disadvantages: first, synthetic electron mediators are often based on precious and water-unstable metal compounds[74]. Secondly, many synthetic materials have low electron transfer rates, which lead to relatively low efficiencies[75]. The lower the efficiency the larger the surface area required for light harvesting. EOBs can offer a promising alternative for efficient, cell-free hydrogen production. Based on artificial self-assembling peptides and proteins, size-optimised oil-anchoring domains can provide a near-zero distance between donor and acceptor. Such customised setups enable relatively short electron transfer fluxes from reaction centres in aqueous solution to synthetic catalysts, located in the oil phase, and vice versa. Therefore, light could be harvested and concentrated by QDs of a different size[76]. The captured radiant energy enables the separation of charges across the oil/water interface, whereby an excited electron is transferred to a reaction centre[74]. As an example, water could be oxidised by the accumulated positive charges of QDs and, in addition, the remaining negative charges of the reaction centre can reduce chemical compounds to generate sustainable fuels. Hence, this new methodology has the potential to impart a significant and positive impact on many of todays important technological challenges.

6.4. Résumé

All in all two functional hybrid systems containing inorganic nanoparticles as light harvesting part and organic and biological molecules for electron or energy transfer have been presented. Surface modified PbS nanoparticles capped with thiophene-based polymer ligands have been synthesised. The end-functionalisation with 4-bromobenzenethiol introduces a binding site into the polymers, which attaches to the nanoparticle surface. FT-IR measurements of reference substances confirm the surface bond of the thiol-group. Measurements of the photovoltaic properties show the potential application in optoelectronics and photocurrent generation in solar cells in the IR region. Additionally, the easy handling of the polymer-nanoparticle solution and the simple processing with spin-coating make these materials attractive for industrial low cost mass production. In comparison to the direct coupling of the polymer on the nanoparticle surface Förster resonance energy transfer over liquid-liquid interface without direct binding of proteins on the nanoparticle surface is reported for the first time. The results of the energy transfer clearly show that it is possible to transfer energy *via* FRET from semiconductor nanoparticles to biological molecules over a phase boundary. Therefore, a test setup containing CdSe QDs, hydrophobin as a phase mediator and tRFP as an optical active protein, was examined. These excitable oil droplets show long-term stability and a high quantum efficiency of the energy transfer. This research has demonstrated that it is possible to overcome the disadvantages of nanoparticle phase transfer, which has been reported in the literature, to produce such hybrid structures. In future projects the model system developed here can be optimised for further applications by easily changing the components. In this connection perspective applications can be found in numerous fields e.g. bioanalytics in case of direct monitoring of environmental conditions, photothermal cancer therapy with focused cell heating and modern fuel production.

6.5. References

1. Saunders, B. R. & Turner, M. L. Nanoparticle-polymer photovoltaic cells. *Advances in colloid and interface science* **138,** 1–23 (2008).
2. Zhao, L., Pang, X., *et al.* Organic-inorganic nanocomposites by placing conjugated polymers in intimate contact with quantum rods. *Advanced materials* **23,** 2844–9 (2011).
3. Lutich, A. A., Jiang, G., *et al.* Energy transfer versus charge separation in type-II hybrid organic-inorganic nanocomposites. *Nano letters* **9,** 2636–40 (2009).
4. Dreaden, E. C., Alkilany, A. M., *et al.* The golden age: gold nanoparticles for biomedicine. *Chemical Society reviews* **41,** 2740–79 (2012).
5. Clapp, A. R., Medintz, I. L., *et al.* Fluorescence resonance energy transfer between quantum dot donors and dye-labeled protein acceptors. *Journal of the American Chemical Society* **126,** 301–10 (2004).
6. Suzuki, M., Husimi, Y., *et al.* Quantum dot FRET biosensors that respond to pH, to proteolytic or nucleolytic cleavage, to DNA synthesis, or to a multiplexing combination. *Journal of the American Chemical Society* **130,** 5720–5 (2008).
7. Bouchonville, N., Le Cigne, A., *et al.* *Controlled FRET efficiency in nano-bio hybrid materials made from semiconductor quantum dots and bacteriorhodopsin* in *Spie* **8460** (2012), 84600.
8. Fichou D. *Handbook of Oligo- and Polythiophenes* (Wiley-VCH, Weinheim, 1999).
9. Lin, J. W.-P. & Dudek, L. P. Synthesis and properties of poly(2,5-thienylene). *Journal of Polymer Science: Polymer Chemistry Edition* **18,** 2869–2873 (1980).
10. Tourillon, G & Garnier, F. Structural effect on the electrochemical properties of polythiophene and derivatives. *Journal of Electroanalytical Chemistry and Interfacial Electrochemistry* **161,** 51–58 (1984).

11. McCullough, R. D., Tristram-Nagle, S., *et al.* Self-orienting head-to-tail poly-(3-alkylthiophenes): new insights on structure-property relationships in conducting polymers. *Journal of the American Chemical Society* **115,** 4910–4911 (1993).

12. Elsenbaumer, R., Jen, K. & Oboodi, R. Processible and environmentally stable conducting polymers. *Synthetic Metals* **15,** 169–174 (1986).

13. Hotta, S., Rughooputh, S. D. D. V., *et al.* Spectroscopic studies of soluble poly(3-alkylthienylenes). *Macromolecules* **20,** 212–215 (1987).

14. Hotta, S. Electrochemical synthesis and spectroscopic study of poly(3-alkylthienylenes). *Synthetic Metals* **22,** 103–113 (1987).

15. Hotta, S., Soga, M. & Sonoda, N. Novel organosynthetic routes to polythiophene and its derivatives. *Synthetic Metals* **26,** 267–279 (1988).

16. Niemeyer, C. Nanoparticles, proteins, and nucleic acids: biotechnology meets materials science. *Angewandte Chemie (International ed.)* **40,** 4128–4158 (2001).

17. Choi, W. I., Sahu, A., *et al.* Photothermal cancer therapy and imaging based on gold nanorods. *Annals of biomedical engineering* **40,** 534–46 (2012).

18. Dreaden, E. C., Mackey, M. a., *et al.* Beating cancer in multiple ways using nanogold. *Chemical Society reviews* **40,** 3391–404 (2011).

19. Medintz, I. L., Uyeda, H. T., *et al.* Quantum dot bioconjugates for imaging, labelling and sensing. *Nature materials* **4,** 435–46 (2005).

20. Wang, S., Mamedova, N., *et al.* Antigen/Antibody Immunocomplex from CdTe Nanoparticle Bioconjugates. *Nano Letters* **2,** 817–822 (2002).

21. Morin, J. G. & Hastings, J. W. Energy transfer in a bioluminescent system. *Journal of cellular physiology* **77,** 313–8 (1971).

22. Zhang, J., Bahrig, L., *et al.* Preparation of near-infrared absorbing composites comprised of conjugated macroligands on the surface of PbS nanoparticles. *Polymer* **54,** 5525–5533 (2013).

23. Liu, J., Tanaka, T., *et al.* Employing end-functional polythiophene to control the morphology of nanocrystal-polymer composites in hybrid solar cells. *Journal of the American Chemical Society* **126,** 6550–1 (2004).

24. Palaniappan, K., Murphy, J. W., *et al.* Poly(3-hexylthiophene)CdSe Quantum Dot Bulk Heterojunction Solar Cells: Influence of the Functional End-Group of the Polymer. *Macromolecules* **42,** 3845–3848 (2009).

25. Skompska, M. Hybrid conjugated polymer/semiconductor photovoltaic cells. *Synthetic Metals* **160,** 1–15 (2010).

26. Aldakov, D., Jiu, T., *et al.* Hybrid nanocomposites of CdSe nanocrystals distributed in complexing thiophene-based copolymers. *Physical chemistry chemical physics : PCCP* **12,** 7497–505 (2010).

27. Zhao, L., Pang, X., *et al.* Semiconductor anisotropic nanocomposites obtained by directly coupling conjugated polymers with quantum rods. *Angewandte Chemie (International ed.)* **50,** 3958–62 (2011).

28. Reiss, P., Couderc, E., *et al.* Conjugated polymers/semiconductor nanocrystals hybrid materials–preparation, electrical transport properties and applications. *Nanoscale* **3,** 446–89 (2011).

29. Holder, E., Tessler, N. & Rogach, A. L. Hybrid nanocomposite materials with organic and inorganic components for opto-electronic devices. *Journal of Materials Chemistry* **18,** 1064 (2008).

30. Kanelidis, I., Altintas, O., *et al.* Microparticles of phosphonate-functionalized copolymers and their composites with CdTe nanocrystals prepared by sonication-precipitation. *Polymer Chemistry* **2,** 2597 (2011).

31. Kanelidis, I., Ren, Y., *et al.* Arylamino-functionalized fluorene- and carbazole-based copolymers: Color-tuning their CdTe nanocrystal composites from red to white. *Journal of Polymer Science Part A: Polymer Chemistry* **49,** 392–402 (2011).

32. Hoyos, M., L. Turner, M. & Navarro, O. Recent Advances in Polythiophene Synthesis by Palladium-Catalyzed Cross-Coupling Reactions. *Current Organic Chemistry* **15,** 3263–3290 (2011).

33. Milliron, D., Alivisatos, A., *et al.* Electroactive Surfactant Designed to Mediate Electron Transfer Between CdSe Nanocrystals and Organic Semiconductors. *Advanced Materials* **15,** 58–61 (2003).

34. Locklin, J., Patton, D., *et al.* Conjugated Oligothiophene-Dendron-Capped CdSe Nanoparticles: Synthesis and Energy Transfer. *Chemistry of Materials* **16,** 5187–5193 (2004).

35. Loewe, R. S., Ewbank, P. C., *et al.* Regioregular, Head-to-Tail Coupled Poly(3-alkylthiophenes) Made Easy by the GRIM Method: Investigation of the Reaction and the Origin of Regioselectivity. *Macromolecules* **34,** 4324–4333 (2001).

36. Noone, K. M., Strein, E., *et al.* Broadband absorbing bulk heterojunction photovoltaics using low-bandgap solution-processed quantum dots. *Nano letters* **10,** 2635–9 (2010).

37. Forrest, S. R. The path to ubiquitous and low-cost organic electronic appliances on plastic. *Nature* **428,** 911–8 (2004).

38. Nagel, M, Hickey, S. G., *et al.* Synthesis of Monodisperse PbS Nanoparticles and Their Assembly into Highly Ordered 3D Colloidal Crystals. *Zeitschrift für Physikalische Chemie* **221,** 427–437 (2007).

39. Lifshitz, E, Brumer, M, *et al.* Air-stable PbSe/PbS and PbSe/PbSexS1-x core-shell nanocrystal quantum dots and their applications. *The journal of physical chemistry. B* **110,** 25356–65 (2006).

40. Rogach, A. L., Eychmüller, A., *et al.* Infrared-emitting colloidal nanocrystals: synthesis, assembly, spectroscopy, and applications. *Small (Weinheim, Germany)* **3,** 536–57 (2007).

41. Schaller, R. & Klimov, V. High Efficiency Carrier Multiplication in PbSe Nanocrystals: Implications for Solar Energy Conversion. *Physical Review Letters* **92,** 186601 (2004).

42. Hickey, S. G., Gaponik, N. & Eychmüller, A. Synthesis and characterisation of NIR-emitting nanocrystals for photonic and optoelectronic applications. *Photonics and Nanostructures - Fundamentals and Applications* **5,** 113–118 (2007).

43. Dutta, A. K., Ho, T., *et al.* Nucleation and Growth of Lead Sulfide Nano- and Microcrystallites in Supramolecular Polymer Assemblies. *Chemistry of Materials* **12,** 1042–1048 (2000).

44. Wise, F. W. Lead Salt Quantum Dots: the Limit of Strong Quantum Confinement. *Accounts of Chemical Research* **33,** 773–780 (2000).

45. Hines, M. & Scholes, G. Colloidal PbS Nanocrystals with Size-Tunable Near-Infrared Emission: Observation of Post-Synthesis Self-Narrowing of the Particle Size Distribution. *Advanced Materials* **15,** 1844–1849 (2003).

46. Kanelidis, I., Elsner, V., *et al.* Synthesis and characterization of amino-functional, blue light-emitting copolymers and their composites with CdTe nanocrystals. *Polymer* **51,** 5669–5673 (2010).

47. Enders, C., Tanner, S. & Binder, W. H. End-Group Telechelic Oligo- and Polythiophenes by Click? Reactions: Synthesis and Analysis via LC-ESI-TOF MS. *Macromolecules* **43,** 8436–8446 (2010).

48. Langeveld-Voss, B. M. W., Janssen, R. a. J., *et al.* End-group modification of regioregular poly(3-alkylthiophene)s. *Chemical Communications,* 81–82 (2000).

49. Brouwer, F., Alma, J., *et al.* Using bis(pinacolato)diboron to improve the quality of regioregular conjugated co-polymers. *Journal of Materials Chemistry* **21,** 1582 (2011).

50. Gruner, L. J., Bahrig, L., *et al. pat.* 13191563.9-1361 (2014).

51. Th. Förster. Zwischenmolekulare Energiewanderung und Fluoreszenz. *Annalen der Physik* **2** (1948).

52. Badali, D. & Gradinaru, C. C. The effect of Brownian motion of fluorescent probes on measuring nanoscale distances by Förster resonance energy transfer. *The Journal of chemical physics* **134,** 225102 (2011).

53. Morise, H, Shimomura, O, *et al.* Intermolecular energy transfer in the bioluminescent system of Aequorea. *Biochemistry* **13,** 2656–62 (1974).

54. Stryer, L. Fluorescence energy transfer as a spectroscopic ruler. *Annual review of biochemistry* **47,** 819–46 (1978).

55. Kagan, C., Murray, C. & Bawendi, M. Long-range resonance transfer of electronic excitations in close-packed CdSe quantum-dot solids. *Physical Review B* **54,** 8633–8643 (1996).

56. Kagan, C., Murray, C., *et al.* Electronic energy transfer in CdSe quantum dot solids. *Physical review letters* **76,** 1517–1520 (1996).

57. Wolf, A., Lesnyak, V., *et al.* Quantum-Dot-Based (Aero)gels: Control of the Optical Properties. *The Journal of Physical Chemistry Letters* **3,** 2188–2193 (2012).

58. Reiss, P., Protière, M. & Li, L. Core/Shell semiconductor nanocrystals. *Small* **5,** 154–68 (2009).

59. Eychmüller, A. Structure and Photophysics of Semiconductor Nanocrystals. *The Journal of Physical Chemistry B* **104,** 6514–6528 (2000).

60. Park, J., Joo, J., *et al.* Synthesis of monodisperse spherical nanocrystals. *Angewandte Chemie (International ed.)* **46,** 4630–60 (2007).

61. Murray, C. B., Norris, D. J. & Bawendi, M. G. Synthesis and characterization of nearly monodisperse CdE (E = sulfur, selenium, tellurium) semiconductor nanocrystallites. *Journal of the American Chemical Society* **115,** 8706–8715 (1993).

62. Halpert, J. E., Tischler, J. R., *et al.* Electrostatic Formation of Quantum Dot/J-aggregate FRET Pairs in Solution. *The Journal of Physical Chemistry C* **113,** 9986–9992 (2009).

63. Liu, W., Howarth, M., *et al.* Compact biocompatible quantum dots functionalized for cellular imaging. *Journal of the American Chemical Society* **130,** 1274–84 (2008).

64. Algar, W. R. & Krull, U. J. Towards multi-colour strategies for the detection of oligonucleotide hybridization using quantum dots as energy donors in fluorescence resonance energy transfer (FRET). *Analytica chimica acta* **581,** 193–201 (2007).

65. Kisko, K., Szilvay, G. R., *et al.* Self-assembled films of hydrophobin proteins HFBI and HFBII studied in situ at the air/water interface. *Langmuir* **25,** 1612–9 (2009).

66. Macindoe, I., Kwan, A. H., *et al.* Self-assembly of functional, amphipathic amyloid monolayers by the fungal hydrophobin EAS. *Proceedings of the National Academy of Sciences of the United States of America* **109,** E804–11 (2012).

67. Megeed, Z., Winters, R. M. & Yarmush, M. L. Modulation of single-chain antibody affinity with temperature-responsive elastin-like polypeptide linkers. *Biomacromolecules* **7,** 999–1004 (2006).

68. Merzlyak, E. M., Goedhart, J., *et al.* Bright monomeric red fluorescent protein with an extended fluorescence lifetime. *Nature methods* **4,** 555–7 (2007).

69. Wang, X., Graveland-Bikker, J. F., *et al.* Oligomerization of hydrophobin SC3 in solution: from soluble state to self-assembly. *Protein science : a publication of the Protein Society* **13,** 810–21 (2004).

70. Zampieri, F., Wösten, H. a. B. & Scholtmeijer, K. Creating Surface Properties Using a Palette of Hydrophobins. *Materials* **3,** 4607–4625 (2010).

71. Mills, P. L., Quiram, D. J. & Ryley, J. F. Microreactor technology and process miniaturization for catalytic reactionsA perspective on recent developments and emerging technologies. *Chemical Engineering Science* **62,** 6992–7010 (2007).

72. Moharana, M. K., Peela, N. R., *et al.* Distributed hydrogen production from ethanol in a microfuel processor: Issues and challenges. *Renewable and Sustainable Energy Reviews* **15,** 524–533 (2011).

73. Listorti, A., Durrant, J. & Barber, J. Artificial photosynthesis: Solar to fuel. *Nature materials* **8,** 929–30 (2009).

74. Cogdell, R. J., Brotosudarmo, T. H., *et al.* Artificial photosynthesis solar fuels: current status and future prospects. *Biofuels* **1,** 861–876 (2010).

75. Zhao, Y., Swierk, J. R., *et al.* Improving the efficiency of water splitting in dye-sensitized solar cells by using a biomimetic electron transfer mediator. *Proceedings of the National Academy of Sciences of the United States of America* **109,** 15612–6 (2012).

76. Makhal, A., Yan, H., *et al.* Light Harvesting Semiconductor CoreShell Nanocrystals: Ultrafast Charge Transport Dynamics of CdSeZnS Quantum Dots. *The Journal of Physical Chemistry C* **114,** 627–632 (2010).

7. Summary and Conclusion

The objectives of this thesis were to shine some light onto the process of metal and semiconductor mesocrystal formation and to find new pathways of non-classical crystallisation so as to form highly symmetrical meso- and supracrystals. Therefore, first of all the principles of non-classical crystallisation and the driving forces for self-assembly were distinguished and an overview of the presently known pathways and their driving forces were presented.

From this point on, first of all the building blocks for later self-assembly were described. The optimisation with respect to narrow size distributions and reproducibility of the nanoparticle synthesis coupled with high yields were focused on. The monocomponential nanoparticle syntheses provided monodisperse building blocks that show highly ordered 2D arrangements. In contrast to the single crystalline semiconductor nanoparticles these have a preferred alignment with the noble metal nanoparticles having twinned morphologies with various habitus. Consequently, the 2D arrangement is merely a hexagonal dense packing without preferred orientation or alignment of the single building units. The stabilisation of the monocomponential nanoparticles is realised with oleic acid or oleylamine, which only differ in their to the nanoparticle binding head group. Hence, the stability of the nanoparticles is nearly equal in solution and also during heat treatment up to 600°C. At higher temperatures the core material stability influences the behaviour after the ligand removal.

In comparison to the high yield and narrow size distributions of the monocomponential nanoparticle syntheses the preparation of core-shell materials results, in the case of PbSe-PbS nanoparticles, in monodisperse nanoparticles but the low amount of material produced impedes their use for mesocrystal formation. In the case of Au-PbS nanoparticle synthesis an optimised synthetic route was developed which provided the opportunity for Janus or core-shell particle production, but the quality and structural unity of the particles is low so that arrangements of these particles into highly ordered 3D structures results in many defects and imperfections. The multicomponential nanoparticles are inappropriate for the formation of highly ordered 3D arrangements, but are suitable for film production or gel formation as well.

Slow destabilisation of the monocomponential nanoparticles using the gas phase destabilisation method leads to highly ordered and symmetrical mesocrystals after optimisation of the parameters, i.e. temperature, concentration, solvent/non-solvent combination etc. Mechanistic investigations using dynamic light scattering to investigate the agglomeration process show the lower solubility of the ligand shell with increasing amount of non-solvent and the resulting size reduction. Then ligand stripping follows and after this agglomeration and precipitation takes place. The advantage of the gas phase destabilisation technique is the slow interdiffusion of non-solvent into the nanoparticle solution that induces slow agglomeration so that during agglomeration ordered assembly is possible. Temperature drastically influences the flexibility of the single ligands, which was also measured with dynamic light scattering. Reduced temperature increases ligand stiffness which causes entanglements and less ordered agglomeration. Additionally the uniformity of the nanoparticle cores affects the resulting structure. Atomistic arrangement of the semiconductor mesocrystals shows their ordered long-range alignment, forming mesocrystals up to 350 μm diameter. In comparison, metallic mesostructures only form smaller crystalline structures with a higher amount of defects presumably caused by the varying morphology of the building units. Furthermore, electrostatic interactions between oppositely charged nanoparticles were used to arrange mixed systems. The low stability of the phase transferred lead sulphide nanoparticles leads to fast agglomeration of monocomponential supracrystals only. The ordering of the agglomeration and the destabilisation rate increases with increasing amount of equally charged gold seeds. It appears to work similarly to a salting out of the less stable PbS nanoparticles. Additionally the increasing pH enhances the stability of the mixed nanoparticle solutions by higher amount of ordered arrangements. The internal ordering of the PbS supracrystals is lower than the alignment of the PbS building units in mesocrystals. Small angle X-ray scattering experiments show only a broad peak so that a definitive crystal structure cannot be determined. Also with HRSEM experiments only a short-range alignment can be observed. In contrast to the slow mesocrystal formation, the supracrystal arrangement is finished after one hour.

Moreover, the assembly of nanoparticles with organic and biological material was investigated. Hybrid materials where the nanoparticles act as a light harvesting system were self-assembled. PbS nanoparticles were coupled with conductive polymers via thiol groups as the binding functionality. Spin coating films were produced and first experiments show their ability to convert infrared light to an electric signal. Another energy transfer, this time of UV light to biological proteins, was shown to occur across a liquid-liquid phase boundary from organic media to the aqueous solution containing the biological sample. The protein is coupled to a phase mediated protein that stabilises the liquid-liquid interface and the nanoparticles are located in a small oil droplet. The advantage of this system is the separation of the nanoparticle and the protein and the lower degree synthetic effort required due to being able to omit a phase transfer, which additionally allows one to keep the high quantum yield of the nanoparticles. In future projects the model system developed here can be optimised for further applications by simply and easily changing the components. In connection with this id that perspective applications can be found in numerous fields e.g. bioanalytics for direct monitoring of environmental conditions, photothermal cancer therapy using focused cell heating and modern fuel production.

A. Appendix
Experimental Section

A.1. Materials

Acetontirile (anhydrous, 99.8%), ammonia (NH_3, 28-30%), cadmium(II)oxide (99.5%), decanoic acid (natural, 98+%), deuterium oxide (D_2O, 99.9% atom D), dichloromethane (≥99.8%), didodecyldimethylammonium bromide (98%), dimethylsulfoxide (DMSO, ≥99.5%), dodecylamine (≥99%), N,N-dimethylformamide (DMF, 99.8%, anhydrous), gold(III) chloride trihydrate (99.9%), hydrazine (98%), hydrazine hydrate (reagent grade), lead acetate trihydrate (99.999%), lead chloride (99.5%), lead(II)oxide (≥99%), 11-mercaptoundecanoic acid (MUA, 95%), 1-octadecene (techn.), oleic acid (90%), oxalic acid (98%), silver acetate (purum, ≥99%), trioctylphosphine oxide , tetrabutyl ammonium borohydride (98%), tetrachlorethylene (TCE, anhydrous, 99%), tetrahydrofuran (THF, anhydrous, 99%), 1,2,3,4-tetrahydronaphthalene (tetralin, 99%), tetramethylammonium hydroxide (25%wt. solution in methanol), n- trioctylphosphine oxide (99%) and thioacetamide (TA, 99%) were purchased from Sigma-Aldrich.

Acetone (p.a.), chloroform (p.A.), 1,2-Dithiolethane (≥99%), ethanol (p.a.), n-hexane (p.a.), methanol (p.a.), n-propanol (p.a.), 2-propanol (p.a.), toluene (p.a.) and octane (p.a.) were obtained from Merck.

Oleylamine (OlAm, 80-90%) was purchased from Acros. Acetic acid (99%) and formic acid (>98%, p.A.) were purchased from Roth. ChemPur supplied the Selenium powder (99.99+%), Alfa Aesar the 1,4- Dithiolbenzene (97%), ProChimia Surfaces the N,N,N-trimethyl(11-mercaptoundecyl)-ammonium chloride (TMA, >95%) and ABCR the tert-butylamine-borane-complex (TBAB, 97%).

Bis(trimethylsilyl)sulfide (TMS_2S, purum), diphenylether (DPE, >98%), hexadecylamine (>99%) 1,6-hexanedithiol (97%) and tri-n-octylphosphine (TOP, 90%) were purchased from Fluka.

All reagents were used as received with the exception of the tri-n-octylphosphine and hydrazine hydrate, which were first distilled.

A.2. Nanoparticle Synthesis

A.2.1. Synthesis of monodisperse PbS quantum dots

7-10 nm sized PbS nanoparticles were synthesised according to a modified approach as reported by Nagel *et al.*[1]. In a typical synthesis, lead acetate trihydrate (1.14 g, 3 mmol), oleic acid (3.5 ml, 11 mmol), distilled tri-n-octylphosphine (5 ml, 11.2 mmol), and diphenylether (10 ml, 63 mmol) were placed into a three-necked flask, heated under vacuum at 80°C for 1 h, and subsequently under argon atmosphere to 135°C for 1 h. After temperature stabilization, a first solution, consisting of thioacetamide (0.08 g, 1.1 mmol), N,N-dimethylformamide (0.4 ml, 5.1 mmol), and tri-n-octylphosphine (6 ml, 13.5 mmol) is injected. After 10 min, a second solution, consisting of thioacetamide (0.02 g, 0.3 mmol), N,N-dimethylformamide (0.1 ml, 1.3 mmol), and tri-n-octylphosphine (0.9 ml, 2 mmol) is injected. The reaction mixture is quenched after an additional 10 min and the as-synthesised nanoparticles are precipitated and subsequently washed two times with 1-butanol. Afterward, the nanoparticles are redissolved in an organic solvent.

PbS nanoparticles with a size of 4-7 nm were synthesised using tri-n-octylphosphine and oleic acid as stabilizing agents. Typically, a mixture of 0.78 g lead acetate trihydrate (2 mmol), 1.5 ml oleic acid (4.7 mmol), 4 ml distilled tri-n-octylphosphine (9 mmol) and 6 ml diphenylether (38 mmol) were heated under vacuum for 1 h at 80°C. The sulfur-precursor solution, comprising 0.05 g thioacetamide (0.67 mmol), 0.25 ml N,N-dimethylformamide (3.3 mmol) and 6 ml tri-n-octylphosphine (13.5 mmol) was injected at 150°C under argon and the reaction was quenched after 5 minutes. Subsequently, the particle solution was cleaned by precipitation from 1-butanol. The precipitate was washed two times with 1-butanol and afterwards redissolved in an organic solvent.

PbS nanoparticles with sizes below 4 nm were synthesised analogous to the procedure of Hines *et al.*[2]. In a 25 ml three-necked flask 0.08 g lead oxide (0.35 mmol) were mixed with 4 ml oleic acid under vacuum at 80°C for 1 h. Under argon atmosphere the solution was cooled down to 40°C and a mixture containing 40 μl (0.2 mmol) TMS_2S and 2 ml 1-octadecene was injected. Upon injection of the sulphur source, the colour of the solution changed instantly to black. After a growth time of 10 minutes the solution was quenched with 1-butanol and cleaned up by using the precipitation procedure described above.

For spectroscopic investigations tetrachloroethylene or toluene were used as solvents.

A.2.2. Synthesis of monodisperse PbSe quantum dots

The PbSe nanoparticle synthesis was undertaken using the same experimental set-up as mentioned above and was modified from both the works of Houtepen *et al.*[3] and Brumer *et al.*[4]. 0.76 g lead acetate trihydrate (2 mmol), 1.5 ml oleic acid (4.7 mmol), 8 ml distilled tri-n-octylphosphine (18 mmol) and 2 ml diphenylether (12.6 mmol) were added to a three-necked flask and heated to 80°C under vacuum for 1 hour. After raising the temperature of the mixture to 150°C under argon atmosphere the selenium precursor, containing 1.7 ml 1 M tri-n-octylphosphine selenium (1.7 mmol) and 10 ml diphenylether (63 mmol) was quickly injected. After 10 minutes, the reaction was quenched and the clean-up procedure as described for the PbS synthesis above was applied. To vary the nanoparticle size the injection temperature and/or the reaction time was altered.

A.2.3. Synthesis of Au nanoparticles for organic solvents

Gold nanoparticles were synthesised with a modified method from Peng *et al.*[5]. In a 100 ml three-necked flask 0.25 mmol $HAuCl_4 \cdot 3H_2O$ (100 mg) were added and flushed for 5 minutes with argon. Additionally 11 ml of tetralin and 11 ml of oleylamine was added. The flask is heated using a double-walled glass beaker for at least 20 min at 20°C. The reduction solution containing 43.5 mg (0.50 mmol) of tert-butylamine-borane (TBAB), 1 ml of tetralin and 1 ml oleylamine was injected under vigorous stirring to the reaction solution. 60 ml of acetone were used to quench the particle growth and afterwards the particles are centrifuged, washed twice with acetone, and redispersed in toluene.

A.2.4. Synthesis of Au and Ag nanoparticles for aqueous solvents

Synthesis of **2-4 nm sized Au-dodecylamine nanoparticles** analogue to Jana *et al.*[6]

47.2 mg (0.12 mmol) $HAuCl_4 \cdot 3H_2O$ was dissolved by sonication in 13.2 ml toluene and 444.2 mg (2.396 mmol) dodecylamine and 554.2 mg (1.198 mmol) didodecyldimethylammonium bromide. In a separate vial, fresh solution of 117.1 mg (0.455 mmol) tetrabutyl ammonium borohydride mixed with 221.7 mg (0.479 mmol) didodecyldimethylammonium bromide in 5.7 ml toluene were prepared by sonication and rapidly injected to the gold salt solution. Immediately colour change to dark purple occurs. The reaction mixture was stirred at room temperature over night.

Synthesis of **5.5 nm sized Au-dodecylamine nanoparticles** analogue to Jana *et al.*[6]

The growth solution containing 446.1 mg (1.0 mmol) $HAuCl_4 \cdot 3H_2O$, 113.4 ml toluene, 5.248 g (28.306 mmol) dodecylamine and 2.095 g (4.529 mmol) didodecyldimethylammonium bromide was mixed by sonication. Furthermore, the as-prepared gold nanoparticle seeds (2-4 nm sized Au-dodecylamine nanoparticles) were added to the growth solution and a reduction solution, containing 289.9 mg (9.059 mmol) anhydrous hydrazine, 2.095 g (4.529 mmol) didodecyldimethylammonium bromide and 43.8 ml of toluene prepared by sonication, was added dropwise (~30 min) to the reaction solution and stirred at room temperature over night.

Synthesis of **5 nm sized Ag-dodecylamine nanoparticles** analogue to Jana *et al.*[6]

1.720 g (10 mmol) decanoic acid was dissolved in 100 ml of toluene and 32 μL of anhydrous hydrazin (1.0 mmol) was dissolved by sonication. The solution was then mixed with 1.0 ml of tetrabutyl ammonium borohydride solution containing 5.1 mg of tetrabutyl ammonium borohydride dissolved in 20 ml of toluene. A solution of 167 mg (1.0 mmol) silver acetate and 371 mg (2.0 mmol) dodecylamine in 10 ml of toluene was poured into the prepared solution upon stirring. The color proceeds from milky white within seconds to yellow, orange, and then to a very deep reddish brown. The reaction is left for 2-4 hours with stirring and then for

2 days without stirring. The final solution contains 4-6 nm NPs, and some larger NPs that precipitate.

A.2.5. Synthesis of PbSe/PbS core-shell nanoparticles

In a 25 ml three-necked flask, 0.78 g (2 mmol) lead acetate trihydrate, 1.5 ml (4.7 mmol) oleic acid , 8 ml (18 mmol) TOP and 2 ml of 1-octadecene were heated under vacuum to 80°C. 0.74 ml of this solution were mixed with 5 ml 1-octadecene, $4.2 \cdot 10^{-8}$ mol PbSe core nanoparticles (concentration determined with absorption spectra) in chloroform and 2% lead chloride (molar ratio) and heated up under vacuum to 60°C. Then every monolayer formed is produced by injecting the calculated amounts of thioacetamide and TOP and growth time of 10 minutes (calculation see reference[7]). This operation is repeated until the desired number of injections have been carried out. After ten minutes of growth of the last monolayer, the reaction is stopped by cooling and the cleaning procedure is applied.

A.2.6. Synthesis of Au/PbS core-shell nanoparticles

In a three-necked flask 115.2 g (304 mmol) lead acetate trihydrate were dispersed in 5 ml 1-octadecene and 5 ml (15.7 mmol) oleic acid. After purging with argon, the solution is heated under vacuum to 150°C and kept at this temperature for 1 h. Gold solution, described in A.2.3 is diluted to the point when 10 μl sample dispersed in 3 ml of toluene shows a measured absorption of 0.68 at 520 nm. The sulfur precursor consists of 39 μl (0.185 mmol) TMS_2S in 1 ml 1-octadecene. After cooling the reaction solution to 100°C under an argon atmosphere and the addition of 0.75 ml of the prepared gold nanoparticles solution (after removal of toluene) the reaction is started by the slow addition (over 15 seconds) of the sulfur precursor solution. After one hour, the solution is quenched by the addition of 6 ml ethanol and the accompanying temperature drop. The obtained particles are centrifuged, washed with ethanol and redispersed in TCE. For the synthesis of Janus hybrid particles, the amounts of the corresponding precursors used are 76.6 mg (202 mmol) of lead acetate trihydrate, 1 ml Au nanoparticle solution and 26 μl (0.123 mmol) TMS_2S.

A.2.7. Synthesis of CdSe nanoparticles for FRET

In a typical synthesis 4 ml of a 4 mmol cadmium oxide, 6.3 ml oleic acid (20 mmol) and 40 ml 1-octadecene stock solution were loaded with 2 g of trioctylphoshineoxide (5 mmol) and 2 g of hexadecylamine (8.3 mmol) into a three-necked flask, heated under vacuum for 1 hour at 100°C and subsequently the temperature raised to 270°C under argon. After the temperature stabilised, 2 ml ODE, 1.6 ml trioctylphosphine and 0.4 ml trioctylphosphine mixed with Selenium powder (1 M) were injected. The reaction solution was quenched after 10 seconds and the as-synthesised nanoparticles were precipitated and subsequently washed twice with methanol and 2-propanol. Afterwards the nanoparticles were redissolved in 1-octadecene.

A.3. Ligand exchange

A.3.1. Ligand exchange on metal nanoparticles

11-mercaptoundecanoic acid

The toluene solution of Au-dodecalamine or Ag-dodecylamine NPs (50 ml) was precipitated with 50 ml methanol (takes 2 h). The precipitate formed was allowed to settle down and the supernatant was removed. The precipitate was dissolved in toluene (30 ml) and 1 mmol MUA thiol in 20 ml CH_2Cl_2 was added. The NPs precipitated from the toluene were let to settle out during ∼2 h. Solvents were then removed and the precipitate was washed 3x with 20 ml CH_2Cl_2. After this, the addition of tetramethylammonium hydroxide (100μL, 25%wt. solution in methanol) caused precipitation of deprotonated NPs. The solvents were removed and the solid was washed with 50 ml acetone and methanol. Finally, the product was dried and dissolved in ∼10 ml of deionised water.

N,N,N-trimethyl(11-mercaptoundecyl)-ammonium chloride

The toluene solution of Au-dodecalamine or Ag-dodecylamine NPs (50 ml) was precipitated with 50 ml methanol (takes 2 h). The precipitate formed was allowed to settle out and the supernatant was removed. The precipitate was then dissolved in 10 ml toluene and precipitated with 100 μmol TMA thiol in 20 ml CH_2Cl_2. The solvents were removed and the precipitate was washed 3x with 20 ml CH_2Cl_2.

After this, the nanoparticles were precipitated with 50 ml acetone, washed with acetone and dried before they are dissolved in ∼10 ml of deionised water.

A.3.2. Ligand exchange on semiconductor nanoparticles

11-mercaptoundecanoic acid

For the modification of the nanoparticles with MUA 1 ml of a solution containing 0.2184 g MUA, 5 ml methanol and with the pH adjusted to >10 with NH_3 was mixed with 100 μl PbS or PbSe nanoparticle solution (standard synthesis dessolved in 3 ml toluene). After briefly shaking, the solution was centrifuged and the resulting sediment redispersed in methanol and again centrifuged. The precipitate was shortly dried in air flow and then dissolved in 500 μl deionised water.

N,N,N-trimethyl(11-mercaptoundecyl)-ammonium chloride

The toluene solution of PbS or PbSe NPs, containing 10 μmol PbS or PbSe, was mixed with 50 μmol TMA thiol, 3 ml methanol and 3 ml hexane. After intense shaking and addition of 100 μl acetic acid, the precipitate formed was allowed to settle out and supernatant was removed. The precipitate was washed 3x with 20 ml CH_2Cl_2. After this, the nanoparticles were washed with acetone and dried before they are dissolved in 5 ml of deionised water with 2.5 μl tetramethylammonium hydroxide (25%wt. solution in methanol).

A.3.3. Ligand exchange with conductive polymers

In general, PbS-copolymer composites PbS-[A] and PbS-[B] were synthesised by treatment of PbS nanoparticles with [A] and [B]. First, the PbS nanoparticles (5 mg) were mixed in 1 ml of a solution of THF with the thiol-functionalised polymer (10 mg/ml) and stirred overnight. After precipitation with ethanol, washing two times with n-butanol and centrifuged slowly to separate the nanocomposite from unbound polymer. After drying under vacuum, two nanocomposite-like materials PbS-[A] and PbS-[B] were obtained as powders.

A.4. Mesocrystal formation

The crystallization of semiconductor and metal nanoparticles was carried out using a gas phase destabilization technique. 1 ml of concentrated nanoparticle solution (0.25-15.0 mg/ml) was placed in a 3 ml glass vial containing a vertically standing silicon wafer. This set up was then placed into a second snap cap vial filled with 2 ml of a non-solvent such as acetone, methanol, ethanol, 2-propanol, n-propanol or n-butanol. This allows for a slow destabilization to take place via a gas phase diffusion process the rate of which could be further controlled by the application of different temperatures (-23°C, 10°C, 25°C and 45°C). All apertures were sealed and kept in the dark in a faraday cage during the time that the destabilization was taking place.

A.5. Supracrystal preparation

In a typical procedure, solution of TMA-capped nanoparticles (0.5-9 μM) was added to a MUA-capped nanoparticle solution (0.5-9 μM). The mixture of the aqueous solution were adjusted to specific pH and a DMSO aliquot was added to the mixture which was then heated in an open vial immersed in a 65°C water bath until a black precipitate was formed. DMSO was decanted and the precipitate washed several times with acetonitrile. The mixture of crystals was then analysed by TEM and SEM and also small angle X-ray diffraction.

A.6. Preparation of EOBs

In preparation for constructing excitable oil droplets, a protein solution in Tris buffer (50 mM, pH 8.5) was sonicated (2:2, 4 cycl., 75%, 4°CC) for 20s to break multiple protein structures. Semiconductor quantum dots, dissolved in octadecene were placed at the bottom of an Eppendorf tube. One third of the total protein solution was added, followed by ultrasonication (5 cycl., 75%) for 20s. To stabilise the EOBs, a further third of the protein solution was added and mixed well. The sample was allowed to cool down for 5 minutes. Afterwards, the sonication was repeated one more time, before adding the remaining protein solution.

A.7. Characterisation

A.7.1. Optical absorption measurements

NIR absorption spectra of the lead chalcogenide quantum dots were collected using a Cary 5000 spectrophotometer from Varian. For spectroscopic investigations of the as-synthesised particles, TCE solutions of the nanoparticles were used. Subsequent to the ligand exchange, deuterium oxide was used as solvent. UV/Vis absorption spectra of the CdSe, metal nanoparticles and the polymer were collected using a Cary 50 spectrophotometer from Varian and a UV-1650 PC from Shimadzu and the as-synthesised particles were dispersed in toluene. The ligand-exchanged particles were characterised using water as solvent.

A.7.2. Fluorescence measurements

Fluorescence measurements were performed using a FluoroMax-4 spectro-fluorometer (Horiba Jobin Yvon Inc., Edison, NJ) with an excitation wavelength of 320 nm. All spectra were recorded at room temperature and gap widths of excitation and emission monochromator of 2 nm.

Fluorescence intensity of purified proteins and EOBs was quantitatively determined as arbitrary units (a.u.) by spectrophotometry using a TECAN Infinite M200 microplate reader (TECAN Group Ltd., Switzerland). For statistical significance three 100 μL aliquots of each prepared sample were distributed on a black 96-well plate. Excitation/emission wavelength and the gain depends on the fluorophore to be detected but were kept constant during any one experiment. Due to the excitation/emission bandwidth, applied values were set at least 30 nm apart from each other.

For microscopy of the EOBs, samples were mounted on a microscopy slide and covered with a cover slip. Bright field and fluorescence microscopy images were acquired with an Axio Observer.Z1 (Carl Zeiss Microimaging GmbH, Germany) inverted microscope using FS49 DAPI and FS43 DsRed filters. For confocal analysis of EODs, spectra were acquired on an ApoTome1 microscope (Carl Zeiss Microimaging GmbH, Germany) using the same filters as well as a specially adapted DAPIExc-Cy3Em filter. Image overlays and z-stack merge were performed using the BZ Analyzer or Zeiss AxioVision software platform.

A.7.3. Lifetime measurements

Emission spectra and lifetimes of purified proteins, QDs and EODs were measured with a Fluorlog-3 spectrofluorimeter from HORIBA Jobin Yvon employing NanoLEDs emitting at 403 nm and 470 nm. All measurements were performed at room temperature.

A.7.4. Fourier Transformation-Infrared spectroscopy

The absorption properties in the infrared region were determined using a Nicolet 8700 FT-IR spectrometer from Thermo Scientific Company with a Smart iTR diamond plate attenuated total reflectance (ATR) accessory. Sample preparation of liquid samples is done via drop casting of the dispersion onto the ATR crystal and evaporation of the solvent. Solid samples are directly placed on top of the ATR plate. All measurements were carried out with a resolution of 4 cm^{-1} and 50 cycles.

A.7.5. Thermogravimetric analysis

Thermogravimetric analysis was performed using a TGA/DSC 1 STAR*e* system from Mettler Toledo. The samples were heated from 25°C up to 1100°C under argon with a heating rate of 5 K/min. All experiments were performed using 70 μl Al_2O_3 crucibles.

Heat treatment of mesocrystal substrates was done directly on top of the silicon wafer, where the crystals are located. The substrate was heated up to 200°C, 350°C and 500°C with a heating rate of 10 K/min and kept at this constant temperature for 10, 20 or 30 minutes.

The coupled measurements with MS were performed on an STA 409 CD from Netzsch. The samples were also heated from 25°C up to 1100°C and back to 200°C with a ramp of 5 K/min and a gas flow of 100 ml/min argon. As sample chamber a Knudsen cell with Al_2O_3 crucibles was used.

The TEM grids were sealed in an ampoule with argon and kept for their heat treatment in a normal oven.

A.7.6. Mass spectroscopy

The mass spectroscopy is coupled to the TGA STA 409 CD from Netzsch with skimmer and Quadrupol MS QMG 422 from Pfeiffer Vacuum. The analog scan was performed from 0-300 amu using ionisation energy of 70 eV.

A.7.7. Dynamic light scattering

All samples and solvents were filtered through Millipore membranes (0.2 μm pore size) before the measurements. The experiments were done with a DelsaTM Nano C Particle Analyzer from Beckman Coulter or a Zetasizer Nano-ZS from Malvern Instruments having a He-Ne laser at a wavelength of 632 nm. The zeta potential is measured using a DIP cell kit and all DLS experiments are performed using the backscattering detector. All solvents and samples are thermostated before measurement for 10-15 minutes to guarantee a constant temperature during measurement.

A.7.8. Transmission electron microscopy

Low-resolution TEM images were carried out on a Libra R 120 and a Libra R 200 MC from Zeiss and a TECNAI T20 from FEI operating at 200 kV. High-resolution measurements were recorded on a Tecnei F20Cs from FEI with a LaB_6 source at 200 kV. Samples for TEM imaging were prepared by drop casting diluted nanocrystal colloids in toluene or water onto copper grids coated with a thin carbon film and subsequent evaporation of the solvent. HRTEM experiments on the samples were carried out at the Special Laboratory Triebenberg for Electron Holography and High-Resolution Microscopy at the TU Dresden. A field-emission microscope CM200 FEG/ST-Lorentz (FEI company, Eindhoven, NL) equipped with a Gatan 1x1 k slow-scan CCD camera was used. The analyses of the TEM images were realised by means of the Digital Micrograph software (Gatan, USA). TEM diffraction and middle resolution images were performed by using a FEI Tecnai 10 electron microscope (FEI company, Eindhoven, NL) with an LaB_6 source at 100 kV. Images were recorded with a Tietz slow-scan CCD F224HD TVIPS camera (2kx2k pixels, pixel size 24 mm, digitisation 16 bit) with an active area of 49 mm x 49 mm (Tietz Video and Image Processing Systems GmbH, Gauting, Germany).

A.7.9. Scanning electron microscopy

SEM investigations were performed by means of an ESEM FEI Quanta 200 FEGi system operated in low-vacuum (60 Pa) as well as in high-vacuum mode ($2{\cdot}10^{-4}$ Pa) at acceleration voltages between 15-25 kV (FEI company, Eindhoven, NL). For investigation under high vacuum, the samples were coated by a thin gold layer (for 30 seconds) in order to obtain a conductive surface. Both, back scattered and secondary electron images were recorded. Additionally SEM investigations were recorded using an SEM DSM 982 GEMINI with a field emission gun from Zeiss, Oberkochen, Germany at 3 kV in order to avoid charging. All measurements on the supracrystals were performed with the SU8030 from Hitachi with the use of ultra-high performance, semi-inlens SEM with cold field emission source. Additionally all EDX measurements were investigated using this SEM.

A.7.10. Powder X-ray Diffraction

Powder X-ray diffraction of quantum dots was performed on a STOE STADI-P diffractometer using Cu-Kα or Co-Kα radiation in transmittance mode and a PSD detector and a Ge(111) monochromator. All calculations were done with the help of WinXPow software.

A.7.11. Small angle X-ray Scattering

SAXS measurements were investigated with the help of a Bruker Nanostar. As source Cu-Kα radiation in transmittance mode coupled with a Hi-Star detector was used. The samples are prepared in such a way that only single mesocrystals and supracrystals were measured.

A.7.12. Single crystal X-ray Diffraction

In order to investigate the orientational order of the nanoparticles within the complete volume of a colloidal nanocrystal assembly, single-crystal XRD measurements were performed. An octahedrally shaped specimen of the PbS organic mesocrystal was mounted on a glass capillary. The X-ray diffraction images were collected along [111] of an octahedrally shaped specimen by use of a Rigaku AFC7 & Saturn 724+ CCD Detector with Mo-Kα-radiation (l = 0.71073 $\mathring{A}$).

A.7.13. Focused ion beam cut

For TEM investigations, focused ion beam (FIB) thin cuts of the aggregates were prepared by means of an FEI Quanta 200 3D dual beam device (FEI company, Eindhoven, NL). For this purpose, selected particles from an ethanol suspension were deposited onto a copper half-ring and the selected region was covered with a protective layer of platinum (thickness 12 mm, acceleration voltage 30 kV, current 0.3 nA). After these preparations, the particles were thinned down to electron transparency (thickness of 100-200 nm) by use of the FIB system at 30 kV acceleration voltage. Currents of 30.05 nA were used for the Ga^+-beam.

A.7.14. Conductivity measurements

One method for contacting the mesocrystals is by using interdigitated gold-electrodes with distances below 50 μm and with macroscopic contacts. The mesocrystals are suspended in a methanol solution to remove some of the surface ligands and then drop cast from solution on top of the electrodes. Methanol evaporates and only the mesocrystals are left on top of the gold contacts. To enhance the binding between crystals and the gold electrode linker molecules were utilised. 25 μmol 1,2-Dithiolethane, 1,6-Dithiolhexane and 1,4- Dithiolbenzene in 5 ml toluene (15 minutes) are used to cover the gold electrode with dithiols.

On a Metrohm Autolab potentiostat/galvanostat PGSTAT 128N cyclic voltammetry was carried out. The initial potential was 0 V and the maximum potentials scanned to are 1 V and -1 V. The scan rate was 0.1 V/s with a potential step of $2.44 \cdot 10^{-3}$V. The contacts and electrodes are realised with thin tungsten wires that are connected to micrometer screws.

A.8. References

1. Nagel, M, Hickey, S. G., *et al.* Synthesis of Monodisperse PbS Nanoparticles and Their Assembly into Highly Ordered 3D Colloidal Crystals. *Zeitschrift für Physikalische Chemie* **221,** 427–437 (2007).
2. Hines, M. & Scholes, G. Colloidal PbS Nanocrystals with Size-Tunable Near-Infrared Emission: Observation of Post-Synthesis Self-Narrowing of the Particle Size Distribution. *Advanced Materials* **15,** 1844–1849 (2003).
3. Houtepen, A. J., Koole, R., *et al.* The hidden role of acetate in the PbSe nanocrystal synthesis. *Journal of the American Chemical Society* **128,** 6792–3 (2006).
4. Brumer, M, Kigel, A, *et al.* PbSe/PbS and PbSe/PbSe$_x$S$_{1-x}$ Core/Shell Nanocrystals. *Advanced Functional Materials* **15,** 1111–1116 (2005).
5. Peng, S., Lee, Y., *et al.* A facile synthesis of monodisperse Au nanoparticles and their catalysis of CO oxidation. *Nano Research* **1,** 229–234 (2008).
6. Jana, N. R. & Peng, X. Single-phase and gram-scale routes toward nearly monodisperse Au and other noble metal nanocrystals. *Journal of the American Chemical Society* **125,** 14280–1 (2003).
7. Schade, E. *Synthese und Charakterisierung von Blei(II)-Selenid/ Blei(II)-Sulfid-Kern/Schale-Nanopartikeln und deren Anordnung in Überstrukturen* 2012.

List of publications

Patents

Patentnumber 13191563.9-1361 (european Patent)
L. J. Gruner, L. Bahrig, K. Ostermann, S. G. Hickey, A. Eychmüller, G. Rödel
Verfahren und System zum direkten, strahlungslosen Energietransfer über flüssige Phasengrenzen **2014**

Patentnumber 10 2012 220 083.5 (german Patent)
L. J. Gruner, L. Bahrig, K. Ostermann, S. G. Hickey, A. Eychmüller, G. Rödel
Verfahren und System zum direkten, strahlungslosen Energietransfer über flüssige Phasengrenzen **2013**

Publications in scientific journals and conference proceedings

11.
Excitable Oil Droplets - FRET across a liquid-liquid Phase Boundary
L.J. Gruner, L. Bahrig, K. Ostermann, S.G. Hickey, A. Eychmüller, G. Rödel
submitted

10.
Interconnection of Nanoparticles within 2D Superlattices of PbS/ Oleic Acid Thin Films
P. Simon, L. Bahrig, I.A. Baburin, F. Röder, P. Formanek, J. Sickmann, S.G. Hickey, A. Eychmüller, H. Lichte, R. Kniep, E. Rosseeva
accepted Advanced Materials, DOI: 10.1002/adma.201305667

9.
Preparation of near-Infrared Absorbing Composites Comprised of Conjugated Mac-

roligands on the Surface of PbS Nanoparticles
J. Zhang, L. Bahrig, A. Puetz, I. Kanelidis, D. Lenkeit, S. Pelz, S.G. Hickey, M.F.G. Klein, A. Colsmann, U. Lemmer, A. Eychmüller, E. Holder
Polymer 2013, 54(21), 5525-5533

8.
A versatile approach for coating oxidic surfaces with a range of nanoparticulate materials
J. Poppe, S. Gabriel, L. Liebscher, S. G. Hickey, A. Eychmüller
Journal of Materials Chemistry C **2013**, 1(7), 1515

7.
PbS-Organic-Mesocrystals: The Relationship Between Nanocrystal Orientation and Superlattice Array
P. Simon, E. Rosseeva, I.A. Baburin, L. Liebscher, S.G. Hickey, R. Cardoso-Gil, A. Eychmüller, R. Kniep, W. Carrillo-Cabrera
Angewandte Chemie **2012**, 51, 10776-10781

6.
Synthesis and characterization of near-infrared absorbing composites of conjugated macroligands on the surface of PbS nanoparticles
I. Kanelidis, J. Zhang, L. Liebscher, S.G. Hickey, A. Eychmüller, E. Holder
Polymer Preprints **2011**, 52, 789-790

5.
New aspects in the hot injection synthesis to provide large scale high quality quantum dots
C. Waurisch, L. Liebscher, E. Sperling, S. G. Hickey, A. Eychmüller
Proceedings of the International Conference Nanomeeting (Physics, Chemistry and Application of Nanostructures) **2011**, 329-332

4.
Amplified spontaneous emission of surface plasmon polaritons and limitations on the increase of their propagation length
P.M. Bolger, W. Dickson, A.V. Krasavin, L. Liebscher, S.G. Hickey, D.V. Skryabin,

A.V. Zayats
Optics Letters **2010**, 35 (8), 1197-1199

3.
The use of nanocrystals with emission in the visible or near infrared and their applications for photonics and optoelectronics
S. G. Hickey, V. Lesnyak, L. Liebscher, S. Miao, S. Tscharntke, C. Waurisch, N. Gaponik, A. Eychmüller
Proceedings of SPIE **2009**, 7469 (746908) 1-11

2.
White emitting CdS quantum dot nanoluminophores hybridized on near-ultraviolet LEDs for high-quality white light generation and tuning
S. Nizamoglu, E. Mutlugun, O. Akyuz, N. Kosku Perkgoz, H. Volkan Demir, L. Liebscher, S. Sapra, N. Gaponik, A. Eychmüller
New Journal of Physics **2008**, 10(2), 23026

1.
White CdS Nanoluminophore based Tunable Hybrid Light Emitting Diodes
S. Nizamoglu, E. Mutlugun, O. Akyuz, N. K. Perkgoz, H. V. Demir, L. Liebscher, S. Sapra, N. Gaponik, A. Eychmüller
Lasers and Electro-Optics Society **2007**, 602-603

Acknowledgement

This thesis is the result of three and a half years of work and would not have been possible without the help and support of many people, who I would now like to thank.

The first thankful words go to my supervisors Prof. Dr. Alexander Eychmüller and Dr. Stephen Hickey for the provision of this very interesting topic and the constant encouragement throughout the whole time. I thank them also for the opportunity to continue and deepen the topic of my Bachelor and Master theses and the countless new ideas and techniques to advance my research possibilities in this field. Additionally, I want to thank them for the very fruitful, critical and instructive mentoring during this time.

Special thanks are owed to my office mates in 003 for motivation, brainstorming and a lot of scientific and non-scientific discussions. Especially, I would like to thank Anne-Kristin Herrmann and Jan Poppe for the nice times we had during our Bachelor and Master studies, the great cooperation in experimental work and all the fruitful discussions before exams. Additionally I am glad, that since 3^{rd} semester we have been working together in the Eychmüller group and undertaken our Bachelor, Master and now also the PhD theses in parallel. Stefanie Gabriel I would like to thank for the wonderful time we had discussing about lead chalcogenides and the fact that also black materials have the ability to emit light and thank you for sharing your knowledge and experiences about lead chalcogenides with me while at the same time always finding a way of keeping our close research topics separated. I also thank Dr. Christian Waurisch and Dr. Zoran Popovic for the great ideas and tips concerning hot-injection reactions and core-shell growing procedures.

I would like to express my appreciation for the work of my bachelor and master students B.Sc. Elke Schade and M.Sc. Danny Haubold, who also supported my work as SHK students.

Furthermore, I am gratefully thankful to Dr. Paul Simon, Dr. Elena Rosseeva,

Dr. Igor Baburin and Dr. Wilder Carrillo-Cabrera for the wonderful cooperation that has allowed us to shine some light into the internal structure of mesocrystals. Also to Dr. Leopold Gruner, Dr. Kai Ostermann and Prof. Dr. Gerhard Rödel I would like to express my thanks for the cooperation and the possibility to extend my knowledge in the direction of biochemistry and working with proteins and cells. Dr. Jinming Zhang, Prof. Dr. Elisabeth Holder and Dr. Karin Sahre I thank for the collaboration concerning the conductive polymers and their hybrid structures. Moreover, my thanks go to Dr. Falk Röder and the members of the Triebenberg Laboratory for Electron Microscopy and Electron Holography for their HRTEM measurements as well as to Dr. Petr Formanek from the Leibniz Institute of Polymer Research Dresden. Ellen Kern and Susanne Goldberg I thank for the SEM images and EDX measurements and the introduction to the SEM and the possibility to measure my samples on my own. Anja Bensch and Markus Klose I thank for the XRD diffractograms, Lars Borchard for the SAXS measurements, and Anne-Kristin Herrmann, Susanne Leubner and Danny Haubold for the TEM measurements.

The research training group *Nano- and Biotechnologies for Packaging of Electronic Systems* and the DFG I would like to thank for funding and additionally for the great discussion that took part within this interdisciplinary group and their new ideas for collaborations and new experiments and also for the supply of measurement equipment and knowledge. I wish to express my appreciation for the chance the funding gave me to go to Northwestern University to expand my research field in the group of Prof. Bartosz Grzybowski.

Prof. Bartosz Grzybowski I would like to thank for the wonderful time in his working group and Dr. Pramod Pillai, Dr. Scott Warren and Tarik Baytekin I thank for the support concerning experiments at Northwestern University. Additionally, I want to thank Jared Incorvati, Aaron Oppenheimer, Gary Wilk, Sabil Huda and Monika Makurath for the pleasant atmosphere and the intercultural impressions.

Many thanks also go to all of the members of the Eychmüller group for the lovely time with more or less scientific conversations and discussions and the tea and coffee times, as well as the diverse activities, that always guaranteed fun.

My deepest gratitude goes to my friends and my family. Without your support, patience and motivation this work would not have been possible. I thank you for the love and the encouragement you gave to me every day and the willing ear in difficult situations as well as the happy moments you shared with me.

Erklärung

Hiermit versichere ich, dass ich die vorliegende Arbeit ohne unzulässige Hilfe Dritter und ohne Benutzung anderer als der angegebenen Hilfsmittel angefertigt habe; die aus fremden Quellen direkt oder indirekt übernommenen Gedanken sind als solche kenntlich gemacht. Die Arbeit wurde bisher weder im Inland noch im Ausland in gleicher oder ähnlicher Form einer anderen Prüfungsbehörde vorgelegt.

Diese Dissertation wurde an der Professur für Physikalische Chemie der Fachrichtung Chemie & Lebensmittelchemie der Fakultät Mathematik und Naturwissenschaften an der Technischen Universität Dresden unter wissenschaftlicher Betreuung von Prof. Dr. rer. nat. habil. Alexander Eychmüller angefertigt. Ich versichere weiterhin, dass bislang keine Promotionsverfahren stattgefunden haben.

Ich erkenne die Promotionsordnung der Fakultät Mathematik und Naturwissenschaften an der Technischen Universität Dresden in der Fassung vom 23.02.2011 an.

Dresden, den

Lydia Bahrig